TESLA Technical Design Report

PART IV
A Detector for TESLA

March 2001

Editors: T.Behnke, S.Bertolucci, R.D.Heuer, R.Settles

Authors

G. Alexander[51], F. Badaud[2], M. Battaglia[7,15], T. Behnke[9], M. Berggren[45], S. Bertolucci[10], F. Bieser[19], G.A. Blair[21], W. de Boer[16], G. Bohner[2], S. Borghi[28], B. Bouquet[39], I. Bozovic–Jelisavcic[9], J.–C. Brient[44], G. Bruni[4,5], K. Büsser[9], H. Burkhard[7], P. Burrows[41], A. Busata[44], P. Bussey[12], J. Butterworth[22], M. Caccia[8], R. Campagnolo[28], C. Carimalo[45], R.C. Carnegie[6], N. Cavallo[34,35], P. Checchia[42,43], P. Cloarec[2], I. Cohen[51], P. Colas[48], C.J.S. Damerell[46], M. Danilov[31], F. Le Diberder[45], M. Dixit[6], V. Djordjadze[9], M. Doucet[9], M. Dracos[50], P. Le Du[48], J. Dubeau[6], V. Eckardt[33], G. Eckerlin[9], M. Elsing[7], P.F. Ermolov[32], C. Fanin[42,43], E. Fernandez[3], P. Mora de Freitas[44], B. Gastineau[48], P. Gay[2], U. Gensch[9], R. Gerhards[9], Y. Giomataris[48], Y. Gornushkin[50], P. Grabiec[52], T. Greenshaw[20], M. Gruwé[9,a], M. Hamann[9], S.M. Xella Hansen[46], K. Harder[9], M. Hauschild[7], J. Hauschildt[9], R. Hawkings[9,a], C. Hensel[9], R.–D. Heuer[13], C.A. Heusch[49], D.J. Jackson[40], L. Jönsson[23], J. Kaminski[16], F. Kapusta[45], A. Karar[44], D. Karlen[6], F. Kircher[48], M. Klein[9], V. Klioukhine[48,b], U. Kötz[9], H. Kolanoski[9], V. Korbel[9], W. Kucewicz[18], P. Laurelli[10], J. Lecocq[2], M. Leenen[9], V. Lepeltier[38], L. Lista[34], S. Lotze[1], P. Lutz[48], T. Lux[13], J. Marczewski[52], M. Margoni[42,43], G. Martin[39], J.–P. Martin[30,6], M.M. Merkin[32], H. Mes[6], N. Meyners[9], D.J. Miller[22], J. Mnich[1], S. Monteil[2], K. Mönig[9], V. Morgunov[31], G. Morinaud[44], T. Müller[16], R. Nania[4,5], O. Napoly[48], T. Naumann[9], R. Orava[14], D. Orlando[44], Y. Pabot[48], M. Paganoni[28], M. Piccolo[10], D. Pinheiro[44], K. Piotrzkowski[9,17,c], M. Pohl[11,36], G. Quast[24], D. Reid[37], F. Richard[39], J.–P. Richer[39], M. Ronan[19], S. Roth[1], E. Rulikowska[18], M. Sachwitz[9], D.P.C. Sankey[46], V. Saveliev[26], A.A. Savin[32,d], H.J. Schreiber[9], S. Schreiber[9], H. Schröder[47], K.P. Schüler[9], D. Schulte[7], R. Schulte[1], M. Schumacher[9], R. Settles[33], W. da Silva[45], F. Simonetto[42,43], K. Sinram[9], T. Sjöstrand[23], P. Steffen[9], H. Steiner[19], W. Struczinski[1], C. de la Taille[39], K. Tammi[14], F. Terranova[29,27], N. Tesch[9], J. Timmermans[37], M. Tonutti[1], C. Trouilleau[2], R. Turchetta[46], H. Videau[44], H. Vogt[9], A. Wagner[9], G. Wagner[47], N. Walker[9], M. Walter[9], D. Wicke[7], G. Wilson[25], M. Winter[50], A. Zalewska[17], K. Zapfe[9]

Convenors

M. Battaglia, T. Behnke, S. Bertolucci, G.A. Blair, J.-C. Brient, J. Butterworth, P. Checchia, P. Colas, C. Damerell, P. Le Du, G. Eckerlin, R.-D. Heuer, F. Kircher, M. Leenen, K. Mönig, O. Napoly, M. Piccolo, R. Settles, S. Schreiber, N.J. Walker

[1] RWTH Aachen, Germany
[2] Université Blaise Pascal, Aubière, France
[3] Universitat Autònoma de Barcelona, Spain
[4] INFN, Sezione di Bologna, Italy
[5] Università degli Studi di Bologna, Italy
[6] Carleton University, Ottawa, Canada
[7] CERN, Genève, Switzerland

[8] Università degli Studi dell'Insubria, Como, Italy
[9] DESY, Hamburg and Zeuthen, Germany
[10] INFN, Laboratori Nazionali di Frascati, Italy
[11] Université de Genève, Switzerland
[12] University of Glasgow, UK
[13] Universität Hamburg, Germany
[14] Helsinki Institute of Physics, Finland
[15] University of Helsinki, Finland
[16] Universität Karlsruhe, Germany
[17] INP, Kraków, Poland
[18] University of Mining and Metallurgy, Kraków, Poland
[19] LBNL, University of California, Berkeley, CA, USA
[20] University of Liverpool, UK
[21] Royal Holloway and Bedford New College, University of London, UK
[22] University College London, UK
[23] University of Lund, Sweden
[24] Johannes–Gutenberg–Universität Mainz, Germany
[25] University of Manchester, UK
[26] Moscow Engineering and Physics Institute, Russia
[27] INFN, Sezione di Milano, Italy
[28] Università degli Studi di Milano, Italy
[29] Università degli Studi Milano–Bicocca, Italy
[30] Université de Montreal, Canada
[31] ITEP, Moscow, Russia
[32] M.V. Lomonosov Moscow State University, Russia
[33] Max Planck Institut für Physik, München, Germany
[34] INFN, Sezione di Napoli, Italy
[35] Università degli Studi della Basilicata, Napoli, Italy
[36] Katholieke Universiteit Nijmegen, The Netherlands
[37] NIKHEF, Amsterdam, The Netherlands
[38] IPN, Orsay, France
[39] LAL, Orsay, France
[40] Osaka University, Japan
[41] Oxford University, UK
[42] INFN, Sezione di Padova, Italy
[43] Università di Padova, Italy
[44] Ecole Polytechnique, Palaiseau, France
[45] Universités Paris VI et VII, France
[46] RAL, Oxon, UK
[47] Universität Rostock, Germany
[48] DAPNIA–CEA, Saclay, France
[49] University of California, Santa Cruz, CA, USA
[50] IReS, Strasbourg, France
[51] Tel Aviv University, Israel
[52] Institute of Electronic Materials Technology, Warszawa, Poland

[a] now at CERN, Genève, Switzerland
[b] now at FNAL, Batavia, IL, USA
[c] now at Université catholique de Louvain, Louvain–la–Neuve, Belgium
[d] now at University of Wisconsin–Madison, WI, USA

Contents

1 The Detector Concept **1**
1.1 Concept . . . 1
1.2 Design . . . 3
1.3 Detector R&D . . . 4
1.4 Backgrounds and rates . . . 6
1.5 Summary . . . 6
Bibliography . . . 8

2 Tracking System **11**
2.1 Vertex Detector . . . 14
2.1.1 Performance goals . . . 15
2.1.2 Machine-related issues . . . 16
2.1.3 Detector features . . . 16
2.1.4 Technology options and conceptual designs . . . 18
2.1.5 Generic detector performance . . . 23
2.1.6 R&D programme . . . 24
2.1.7 Cost estimate . . . 27
2.2 Intermediate Tracking System . . . 28
2.2.1 Technologies . . . 30
2.2.2 Conceptual design . . . 30
2.2.3 Cost estimate . . . 33
2.3 The Central Tracking Detectors . . . 34
2.3.1 Conceptual design of the TPC . . . 34
2.3.2 Conceptual design of the forward chambers . . . 47
2.3.3 Performance studies . . . 49
2.3.4 Cost . . . 52
2.3.5 R & D projects . . . 52
2.4 Performance of the Tracking System . . . 53
2.4.1 Track reconstruction . . . 53
2.4.2 Tracking resolution . . . 53
2.4.3 Flavour tagging . . . 54
2.4.4 Conclusion . . . 58
Bibliography . . . 59

3 Calorimetric Detectors **63**
3.1 Calorimeter Overview . . . 63
3.2 The SiW Electromagnetic Calorimeter . . . 65
3.2.1 The mechanical structure . . . 66
3.2.2 The detection slab . . . 68
3.2.3 The front-end electronics . . . 69
3.2.4 Calibration . . . 70
3.2.5 Performance . . . 70
3.2.6 Cost estimate . . . 71
3.2.7 R&D . . . 73
3.3 The Shashlik Electromagnetic Calorimeter . . . 73
3.3.1 Conceptual design. . . . 74
3.3.2 Performance . . . 74
3.3.3 Cost . . . 78
3.4 The Hadronic Calorimeter . . . 78
3.4.1 The tile hadronic calorimeter . . . 78
3.4.2 A digital hadronic calorimeter . . . 85
3.5 Forward Calorimetry . . . 87
3.5.1 Low angle tagger LAT . . . 87
3.5.2 Luminosity calorimeter LCAL . . . 89
Bibliography . . . 94

4 Coil **99**
4.1 Magnet Specifications . . . 99
4.1.1 Magnet layout . . . 99
4.1.2 Magnetic field . . . 102
4.2 Technical Aspects . . . 102
4.2.1 Conductor . . . 102
4.2.2 Yoke . . . 103
4.2.3 Ancillaries . . . 103
4.3 Magnet Assembly and Interface with Subdetectors . . . 104
4.4 Costs . . . 104
4.4.1 Manpower requirements . . . 104
4.4.2 Planning . . . 105
4.5 Conclusion . . . 105
Bibliography . . . 106

5 Muon System **107**
5.1 Technologies . . . 109
5.2 Conceptual design . . . 110
5.3 Performance . . . 113
5.4 Cost . . . 115
Bibliography . . . 116

6 Data Acquisition System **117**
6.1 Technologies . . . 118
6.2 Conceptual Design . . . 118
6.3 Performance . . . 121
6.4 Cost estimate . . . 123
Bibliography . . . 125

7 Machine Detector Interface **127**
7.1 Backgrounds and the Mask . . . 127
7.1.1 Motivation for the mask . . . 127
7.1.2 Design of the mask . . . 129
7.1.3 Background in the detector . . . 130
7.1.4 Background summary . . . 138
7.1.5 Cost . . . 138
7.2 Polarimeter . . . 138
7.2.1 Compton polarimeter . . . 140
7.2.2 Møller polarimeter . . . 142
7.3 Energy Spectrometer . . . 143
7.3.1 Requirements . . . 143
7.3.2 Magnetic spectrometer . . . 144
7.3.3 Møller (Bhabha) scattering . . . 145
7.3.4 Cost . . . 146
Bibliography . . . 147

8 Detector Integration **149**
8.1 Detector Mechanical Concept . . . 149
Bibliography . . . 155

9 Detector Performance **157**
9.1 Simulation Tools . . . 157
9.2 Momentum Resolution . . . 157
9.3 Flavour Tagging . . . 158
9.4 Energy Flow . . . 160
9.5 Hermeticity . . . 162
9.6 Other Topics . . . 163
9.7 Conclusions . . . 165
Bibliography . . . 168

List of Figures

1.1.1 View of one quadrant of the TESLA Detector. Dimensions are in mm. 4

2.0.1 General layout of the tracking system 12
2.0.2 Material distribution (a) as a function of the radius for $\theta = 90°$ and (b) as a function of the polar angle up to the end of the different subdetectors. For the line labelled TPC the material up to the end of the sensitive volume is shown. 13
2.1.1 Cross-section of CCD-based vertex detector. 18
2.1.2 General layout of the barrel section of the hybrid pixel-based vertex detector. 19
2.1.3 Charge collection within a CMOS pixel, indicating the potential barriers which induce efficient diffusive charge-collection. 20
2.1.4 General layout of CCD-based vertex detector. 21
2.1.5 Layout of components at end of ladder in CCD-based detector. 21
2.1.6 Material budget for CCD-based detector, as function of polar angle (from the bottom up the different contributions shown are from the beampipe, each of 5 the layers, the support shell and the cryostat). . . 22
2.1.7 Material budget for hybrid pixel-based detector, as function of polar angle (from the bottom up the different contributions are the beampipe, then each of the 3 layers). 23
2.1.8 Track impact parameter resolution in $r\phi$ vs momentum for $\theta_p = 90°$, for the CCD option. 24
2.1.9 Layout of the upper corner of hybrid pixel detector test structure, with $50\,\mu$m implant and $200\,\mu$m readout pitch. 26
2.2.1 General layout of the SIT and FTD 29
2.2.2 Conceptual layout of the SIT and FTD support structure. The space frame and the support ring consist of light e.g. carbon fibre struts. The support shell and the support legs are made from composite materials. 31
2.2.3 Layout of one FTD pixel module. The large trapezoid indicates the detector while the small rectangles are the readout electronics 32
2.2.4 Layout of an FTD strip module. The dashed lines indicate the orientation of the strips. 32
2.2.5 Material in units of radiation lengths as a function of the polar angle up to the end of the vertex detector and the SIT/FTD. 33
2.3.1 General layout of one quarter of the central tracking. 35

2.3.2 Sketch of the GEM principle (not to scale: distance between holes is $\mathcal{O}(0.1)$ mm, pad size is $\mathcal{O}(1-5)$ mm). Electric field map near the GEM holes shown in the small inset taken from [40]. 37
2.3.3 Gain in a two-GEM structure [41]. 38
2.3.4 a) Layout of the "Chevron" shaped pads, with a track superimposed to illustrate the sharing of charge between different pads. The circles indicate a typical size of the charge cloud arriving on the pads. Dimensions are in mm. b) Simulated resolution in $r-\phi$ as a function of the drift length in the TPC, for different pad geometries and two gas mixtures (Ar:CH_4=(90-10) % and Ar-CH_4-$C0_2$=(93-5-2) %) for minimum ionising particles [44]. 39
2.3.5 Schematic layout of a Micromegas. 40
2.3.6 3-D view of the TPC (not to scale). The inner and the outer fieldcage are illustrated in the small insets. 41
2.3.7 a) One possible layout of the TPC end plate for GEMs or Micromegas. On sector is shown with the mechanical frame. The length scale is in cm. b) Perspective view of one sector mounted on the TPC vessel. The drawing is not to scale. 43
2.3.8 a) Exploded view of one GEM "tower" to show the individual components. b) Photograph of a prototype module built for the COMPASS experiment illustrating the use of the spacer frame to separate the two GEMs [48]. 43
2.3.9 Measured ion-feedback and electron transparency in a double GEM structure as a function of the drift field [41]. 45
2.3.10 Orientation of the FCH wires. 48
2.3.11 Simulated separation power between pions and kaons as a function of the momentum of the particles [50]. An error of $0.2-0.3\%$ due to calibration was assumed in this figure. The top curve is for isolated tracks, the bottom one for tracks inside hadronic jets. 49
2.3.12 z-resolution measured in a GEM equipped TPC prototype [54]. 50
2.3.13 a) Gain in a two-GEM TPC prototype structure measured as a function of the different potentials applied. b) Gain measured as a function of position across a GEM over a distance of 3 cm. Errors include systematic effects. No attempt has been made to equalise the response through a pad-calibration. The gas used for both plots [54] was a Ar-CH_4-CO_2 mixture (93-5-2)%. 51
2.3.14 Measured resolution in $r-\phi$ determined using induced signals. The distribution has been measured using a X-ray source [43]. The width of the distribution is around 40μm. The gas used was a Ar-CO_2 mixture (70-30)%. 51
2.4.1 Efficiency to reconstruct tracks from charged particles in the tracking system, as a function of the polar angle. 54

2.4.2 Momentum resolution a): for 250 GeV/c muons as a function of the polar angle, for TPC and VTX, after the addition of the FTD, and for the complete system including the FCH. b): Momentum resolution as a function of the momentum for a polar angle $\theta = 90°$. The dashed curve is for the VTX and the TPC only, the solid one for the complete tracking system. 55
2.4.3 Polar angle resolution for 200 GeV muons as a function of the polar angle including the TPC and the forward chambers and with silicon tracking only. 56
2.4.4 Efficiency and purity for tagging a heavy flavour jet in Z decays. 56
2.4.5 Efficiency to tag an unwanted flavour as function of the bottom tag efficiency, for three different jet energies. 57
2.4.6 Efficiency to tag an unwanted flavour as function of the charm tag efficiency, for three different jet energies. 58

3.1.1 Quadrant view of the calorimeter system 64
3.2.1 View of the barrel calorimeter modules in the xy-plane (left) and detail of the overlap region between two barrel modules, with the space for the front-end electronics (right). 66
3.2.2 The structure of the ECAL showing the alveoli, the structural tungsten slabs, and the detection slabs. 68
3.2.3 Schematic view of the detection slab, with the read-out lines. 69
3.2.4 Photon energy resolution. The two straight lines are fits for the low energy and the high energy part. 71
3.2.5 Angular resolution for pointing photons. 72
3.3.1 Module, Row of modules (top) , and layout of the barrel part of the calorimeter (bottom). 75
3.3.2 Measured time distribution for fast and slow scintillators. 76
3.3.3 Test beam results [17]: a): Energy deposited in the slow scintillator versus total energy for electrons at 30 and 50 GeV/c and pions at 30 GeV/c. b): Pion contamination versus energy for 98.5% electron efficiency. . . . 76
3.3.4 Simulated energy resolution for $\tau \to \rho\nu_\tau$ decays for τ energies of 100 and 150 GeV, respectively. 77
3.4.1 View of the calorimeter system of the TESLA detector with open endcap calorimeters. 79
3.4.2 One barrel (left) and one endcap (right) HCAL module 81
3.4.3 Sampling structure of the hadronic calorimeter. 81
3.4.4 Schematic view of 2 tile plates with long fibre readout. 83
3.4.5 Energy resolution using energy deposited in the scintillator (blue triangle), using pad multiplicity(green square) and eventually using more informations from digital pattern (red dots). 86
3.5.1 Design of the forward angle calorimeters. The sampling calorimeters (LAT and LCAL, shown in black) are integrated into the tungsten shield of the mask. 88

3.5.2 Response of the LAT to 250 GeV electrons 89
3.5.3 Design of the LCAL. The segmentation in z direction consists of 63 planes of tungsten and sensors (not shown in this figure). 90
3.5.4 a): Energy deposited per bunch crossing and b): yearly radiation dose as a function of the plane number. The plane number runs from 1 to 63 between the plane closest and the plane farthest from the interaction point. On each figure, the lowest curve corresponds to the outer ring and the highest curve to the inner ring of the LCAL. 91
3.5.5 a): Intrinsic energy resolution of the calorimeter versus the polar angle for 250 GeV electrons. b): Detection capability of the LCAL. Shown is the 90% CL energy vs. the polar angle, see text for explanation. 93

4.1.1 Cross-section of one quarter of the magnet and the iron return yoke. . . 100
4.1.2 Calculated maximum magnetic integral field homogeneity. 102

5.0.1 Distribution of max. hit density (#/cm^2) at the front face of the muon identifier for $b\bar{b}$ events: one entry per event is plotted in the histogram. 108
5.0.2 Identification efficiency for single μ's in the barrel region. The threshold at ≈ 5 GeV/c comes from the amount of material in front of the muon identified (essentially calorimeters and coil), from the magnetic field and the radial dimensions of the device. 109
5.0.3 Spread in x (a) and y (b) at the front face of the muon identifier for muons of 20 GeV/c emitted into the forward direction at 10°. 110
5.0.4 Energy spectrum, at the front face of the muon system, for tracks that release energy in the iron. 111
5.2.1 RPC module filling of an end-cap slot: each plane is completely filled with 14 modules; RPCs with circular boundaries have already been successfully produced 112
5.3.1 a): Efficiency vs. momentum for $b\bar{b}$ final state in the barrel region for the 12 barrel/11 end cap module configuration described in the conceptual design section. b): Ratio of the $b\bar{b}$ final state muon identification efficiency to single particle identification efficiency. 113
5.3.2 Calorimetric energy resolution for the muon system versus energy at its front face, using the algorithm for energy measurement described in the text. 114

6.2.1 Overall view of the trigger and DAQ concept. 119

7.1.1 xy profile of pairs at z=220 cm 128
7.1.2 Layout of the mask 129
7.1.3 Pairs from beamstrahlung hitting mask 131
7.1.4 Hits in vertex detector (CCD option) resulting from pair background . 132
7.1.5 Origin of photons entering the TPC volume 133
7.1.6 Photon energy leaking out of cylindrical tungsten mask. 134
7.2.1 Plan layout of the Compton polarimeter 140

7.2.2 Energy spectrum, spin asymmetry and scattering angles of Compton scattered electrons and photons 141

7.3.1 Magnetic spectrometer 144

7.3.2 Møller Spectrometer 145

8.0.1 View of the detector hall with the detector in the parking position. The beam line is shielded with concrete blocks, so that the machine operation and the detector work can proceed in parallel. 150

8.1.1 View of the detector in the service position in the beam line. The yoke has been opened, and the endcap HCAL has been removed with special tooling. The TPC has been moved in the direction of the beam to clear the inner detectors and to allow access to them. 152

8.1.2 Top: View of the mask and its support and cantilever structure. Bottom: Results from a finite-elements calculation showing the deformation of the mask during normal running operations. Scales are in mm. The mask is shown in the running position, where it is suspended from the tip and at the base. 153

8.1.3 View of the detector in the beam position. 154

9.2.1 a): Generated and reconstructed Z-mass and b): recoil-mass for $e^+e^- \to ZH \to \ell^+\ell^-H$ events at $\sqrt{s} = 350$ GeV ($m_H = 120$ GeV/c^2). 158

9.3.1 Efficiency versus purity of the b- and c-tagging for jets from Z-decays. The green triangles are for the natural flavour composition. For the blue bullets the uds-background has been suppressed artificially to indicate the tagging performance in the Higgs branching ratio measurement. The green stars show the working points of the SLD R_b, R_c analyses [7]. . 159

9.3.2 Possible precision of the Higgs branching ratio measurement as a function of the Higgs mass. For details see Part III, Chapter 2. 159

9.4.1 Mass resolution for hadronic Z-decays at rest. 160

9.4.2 Distance variable for signal and background assuming a): $\Delta E/E = 60\%(1 + |\cos\theta_{jet}|)/\sqrt{E}$ or b): $\Delta E/E = 30\%/\sqrt{E}$. For details see text. 161

9.4.3 162

9.4.4 Reconstructed masses for $e^+e^- \to \nu\overline{\nu}WW$ events and $e^+e^- \to \nu\overline{\nu}ZZ$ events for a) $\Delta E/\sqrt{E} = 30\%$ and b) $\Delta E/\sqrt{E} = 60\%$. 163

9.4.5 Dilution factor d for $e^+e^- \to \nu\overline{\nu}WW$ and $e^+e^- \to \nu\overline{\nu}ZZ$ as a function of the cut on the average invariant mass for $\Delta E/\sqrt{E} = 30\%$ and $\Delta E/\sqrt{E} = 60\%$. 164

9.4.6 Directional resolution of the Calorimeter for isolated photons as a function of the energy. 164

9.5.1 Reconstructed transverse momentum distribution for muon pairs from smuon production with a small mass difference, Δm, to the lightest neutralino compared to the background from two–photon interactions with different angle cuts on the outgoing electron. The simulation was done with $\sqrt{s} = 189$ GeV and $m_{\tilde{\mu}} = 90$ GeV. However all cross sections follow approximately the same scaling if $\Delta m/m$ and $m_{\tilde{\mu}}/\sqrt{s}$ are kept constant. 165
9.6.1 Differential luminosity reconstructed in the forward region in the ideal case, including detector effects and beam energy spread. 166
9.6.2 Identification efficiency for isolated electrons (a) and hadrons (b) with the ECAL and muons (c) and hadrons (d) with the HCAL. 167
9.6.3 Two particle invariant mass spectrum assuming the pion mass for $B^0 \to \pi^+\pi^-$ and $B^0 \to K^+\pi^-$ decays without (a) and with (b) a cut on dE/dx in the TPC. 167

List of Tables

1.3.1 Detector performance goals for physics analyses for $\sqrt{s}$ up to $\sim 1\,\mathrm{TeV}$. 5
1.4.1 Table of some machine properties and related backgrounds. 6

2.1.1 Key parameters of the CCD-based vertex detector design. The penultimate column lists the background occupancy integrated over the individual data read out time per layer. 20
2.2.1 Main mechanical parameters of the SIT and the FTD. 29
2.3.1 List of main mechanical parameters of the TPC. 36
2.3.2 Main parameters of the CDR wire-chamber readout solution for the TPC (from [45, 46]). 41
2.3.3 Material budget for the TPC field cage. 42
2.3.4 List of the main mechanical parameters of the FCH. 48
2.3.5 Summary of key performance figures of the central tracker from a full simulation. 50
2.3.6 Cost of the TPC and the FCH Systems. 52

3.2.1 Cost estimate for the Si-W electromagnetic calorimeter. 72
3.3.1 Cost estimate for a shashlik-based barrel ECAL. 78
3.4.1 The structure of the hadronic tile calorimeter. 82
3.4.2 Cost of the tile version of the hadronic calorimeter. 84
3.4.3 The cost estimate for the digtal hadron calorimeter. 87
3.5.1 Cost estimate for the LAT 89
3.5.2 Cost estimate for the LCAL 93

4.1.1 Main parameters of the magnet. 101
4.4.1 Table of the cost of the detector magnet. The manpower costs listed are those for external manpower only. 104

6.3.1 Expected event rates at 500 GeV. 121
6.3.2 Expected background rates at 500 GeV. 122
6.3.3 Data Volume expected at TESLA 122
6.3.4 cost estimate for the data acquisition system 123

7.1.1 Pairs produced in one BX 128
7.1.2 Charged hits in tracking detectors 131
7.1.3 Photons in the TPC 133
7.1.4 Hits in the ECAL from pairs 134

7.1.5 Hadronic reactions from beamstrahlung 135
7.1.6 Summary table for 500 GeV backgrounds 137
7.1.7 Cost estimate for the mask elements 139
7.2.1 Compton Polarimeter Parameters 142
7.2.2 Cost of Compton Polarimeters 143
7.3.1 Cost estimate for energy spectrometers 146

1 The Detector Concept

The anticipated particle physics programme at TESLA has been presented in detail in Part III of this TDR. The anticipated programme encompasses the wide kinematic range of centre-of-mass energies ($\sqrt{s}$) from the Z peak to ∼1 TeV and a large physics assortment from discovery to very high precision measurements. It presents a formidable task for the detector, the software and the subsequent analysis. Some of the topics most demanding for the design of the detector are described in the following.

Understanding electroweak symmetry breaking gives a prime example. If a light elementary Higgs particle exists, as predicted by the Standard Model and indicated by the LEP data, precise measurements of the properties of this new boson demand experiments at $\sqrt{s}$ from 250 GeV up to 800 GeV. TESLA will provide several ab^{-1} of data and probe the mechanism of mass generation. For $M_{\mathrm{H}} = 120\,\mathrm{GeV/c^2}$ the Higgs couplings to fermions and to massive gauge bosons are best determined in ZH associated production at $\sqrt{s} \simeq 250\,\mathrm{GeV}$, the Higgs triple coupling in ZHH at 500 GeV and the Higgs-top Yukawa coupling in $\mathrm{t\bar{t}H}$ at 800 GeV. Since the Higgs mechanism predicts these couplings to scale with the particle masses, excellent identification capabilities of parton flavour and of gauge-boson type are mandatory. This requires careful layout of the detector's vertexing, tracking, energy flow and hermeticity, as will be detailed below.

Discovery and precision physics will proceed hand-in-hand via the detection of deviations from Standard Model expectations. Examples of precision experiments are those mentioned in the Higgs sector (Part III, Chapter 2), and measurements of the $\mathrm{t\bar{t}}$ threshold, anomalous gauge boson couplings and of Z-boson properties (Part III, Chapter 5). Direct discovery of an extended Higgs structure, of Supersymmetry or the manifestation of other new physics (Part III, Chapters 3 and 4) will compel further precision experiments. In the opposite situation that no light Higgs is found, the GigaZ experiment, 10^9 Zs produced at $\sqrt{s} = 91\,\mathrm{GeV}$ with polarised beams, will shed light on the electroweak symmetry breaking mechanism. If this mechanism is realised by heavy or composite Higgs particles, the study of fusion processes of the kind $\mathrm{e^+e^-} \to \mathrm{VV}\nu_{\mathrm{e}}\bar{\nu}_{\mathrm{e}}\,(\mathrm{V} = \mathrm{W}, \mathrm{Z})$ at the highest TESLA energy is expected to provide distinctive signals.

1.1 Concept

The detector will have to deal with a large dynamic range in particle energy, complexity of final states and signal-to-background ratio. The average jet multiplicity in hadronic events doubles from $\sqrt{s} \sim 100$ to 1000 GeV because of the increasing cross section for

multiple gauge boson production and harder gluon radiation; $t\bar{t}H$ or charged Higgs boson pair production will result in spectacular multi (8 or more) parton final states. The track densitiy in collimated jets can be as high as one per mm^2 at a radius of 1.5 cm, and the accelerator induced backgrounds produce typical hit densities of the order of $0.03/mm^2$ per bunch crossing (BX) at a radius of 1.5 cm, and $0.003/cm^2$ per BX at a radius of 30 cm. The diversity of physics signatures anticipated at TESLA and the characteristics of the bunch timing suggest a data acquisition scheme with continual read-out having no trigger and no dead time for maximum data logging efficiency.

As noted the physics requirements affect four main detector benchmarks which must be substantially better than at LEP/SLC: i) track momentum resolution, ii) jet flavour tagging, iii) energy flow and iv) hermeticity.

i) Track momentum resolution. The analysis of the di-lepton mass in the process $HZ \to H\ell^+\ell^-$ provides the means to analyse the Higgs production independent of its decay properties via the recoil mass to the di-lepton system. Requiring the measuring error on $M_{\ell^+\ell^-}$ and on the mass recoiling to the $\ell^+\ell^-$ system to be small reduces significantly the combinatorial background. This places a stringent requirement on the momentum resolution, which will be achieved by a large tracking volume and high magnetic field.

ii) Vertexing. The potential in investigating electroweak symmetry breaking must be met by a detailed study of the decay properties of the Higgs to complement the aforementioned production studies: distinguishing between a light Higgs boson decaying into $b\bar{b}$, $c\bar{c}$, gg and $\tau\bar{\tau}$ pairs represents a major challenge for the vertex detector system. An extended Higgs sector will most likely manifest itself via the production and the decay of pairs of heavy Higgs particles by processes such as $e^+e^- \to H^+H^- \to t\overline{b}\,\overline{t}b$ or $e^+e^- \to H^0A^0 \to b\overline{b}b\overline{b}b$ that can be discriminated from the multi-fermion background thanks to their distinctive signatures with multiple b jets. If supersymmetry exists, for example the scalar top will produce complex final states such as $\tilde{t}_1 \to b\tilde{\chi}_1^+ \to bW^+\tilde{\chi}_1^0$ for which both b and charm tagging are important. Standard model processes such as $t\bar{t} \to bW^+\overline{b}W^-$ provide equally challenging requirements. As final example, possible anomalies in the gauge boson self-couplings will be probed by using high energy WW production in which one W decays leptonically and the other hadronically to cs, an analysis which will profit strongly from high charm tag efficiency and purity.

The vertexing performance will be given by a multilayered Si-based pixel detector with a minimum of material, an innermost layer as close as possible to the interaction point (IP) and a large solenoidal field to confine the background generated in the interaction of the colliding bunches.

iii) Energy flow. Most signatures of new physics are expected from hadronic final states where intermediate states, such as $t \to bW$, $W \to q\bar{q}'$ or $Z \to q\bar{q}$, must be detected in the cascade decays to efficiently suppress the Standard Model backgrounds. The effect of beamstrahlung and initial state radiation (ISR), the complexity of the signal final states and the presence of missing energy in fusion processes and in reactions involving SUSY particles reduce the applicability of kinematic constraints to enhance the di-jet mass resolution, thus requiring excellent performances in terms of accuracy on the energy and direction of partons. Some SUSY models demand sensitivity to

non-pointing tracks and photons, and good τ identification is vital for multi-τ final states in supersymmetric scenarios with large values of tanβ.

The experience at LEP and SLC has shown that such multi-parton final states are best analysed using an energy flow measurement, where the demand for unprecedented performance is opening new avenues of approach and technical innovations.

The energy flow technique combines the information from tracking and calorimetry to obtain an optimal estimate of the flow of particles and of the original parton four-momenta. This works best if besides the tracking system also both calorimeters are located inside the coil. This keeps the amount of inactive material in front of the calorimeters low and allows to optimise the calorimetric measurement. Electrons below 150 GeV/c, muons and charged hadrons are best measured in the tracking detectors, electrons above 150 GeV/c and photons by the electromagnetic calorimeter and neutral long-lived hadrons by the combined response of the electromagnetic and hadronic calorimeters. The subdetectors must have excellent 3-D granularity to enable an energy flow algorithm which resolves energy depositions of almost overlapping particles, combines redundant measurements properly (e.g. of electrons in tracking and the electromagnetic calorimeter or of charged pions in tracking and calorimetry) and performs other corrections (e.g. calorimeter software compensation). Good particle identification and good coverage for long-lived particles will add valuable information for each event.

iv) Hermeticity. Hermeticity and particle detection capabilities at small angles are required since missing energy is the main expected signature for the production and decay of supersymmetric particles and for other processes of interest, such as $e^+e^- \rightarrow WW\nu_e\bar{\nu}_e$, which are forward peaked. Excellent missing energy resolution will increase the sensitivity to supersymmetry in those cases with small mass difference ΔM between the lightest and the next lightest SUSY particle. Missing energy is also a signature for many extra-dimension scenarios.

Hermeticity requires having good coverage of and measurement capability in the forward direction; this is also essential to allow a precision determination of the luminosity spectrum.

1.2 Design

The detector for e^+e^- physics up to $\sqrt{s} \sim 1$ TeV has been evolving during two series of workshops in europe [1]- [7] and internationally [8]- [12]. Large, lower-field and small, higher-field detector options were compared [2], and the large version was found to have better overall performance because the tracking can be more precise and efficient, the effective calorimeter granularity is better if further from the IP, both electromagnetic and hadronic calorimeters can be inside the coil for better energy flow measurement and the sensitivity to long-lived particles is increased. The Fig. 1.1.1 shows the detector layout and dimensions [1].

[1]The coordinate system used in the this document is a right handed system, with the z-axis in the direction of the electron beam, and the y-axis pointing upwards. The polar angle θ and the azimuthal angle ϕ are defined w.r.t. z and x, respectively, while r is the distance from the z-axis.

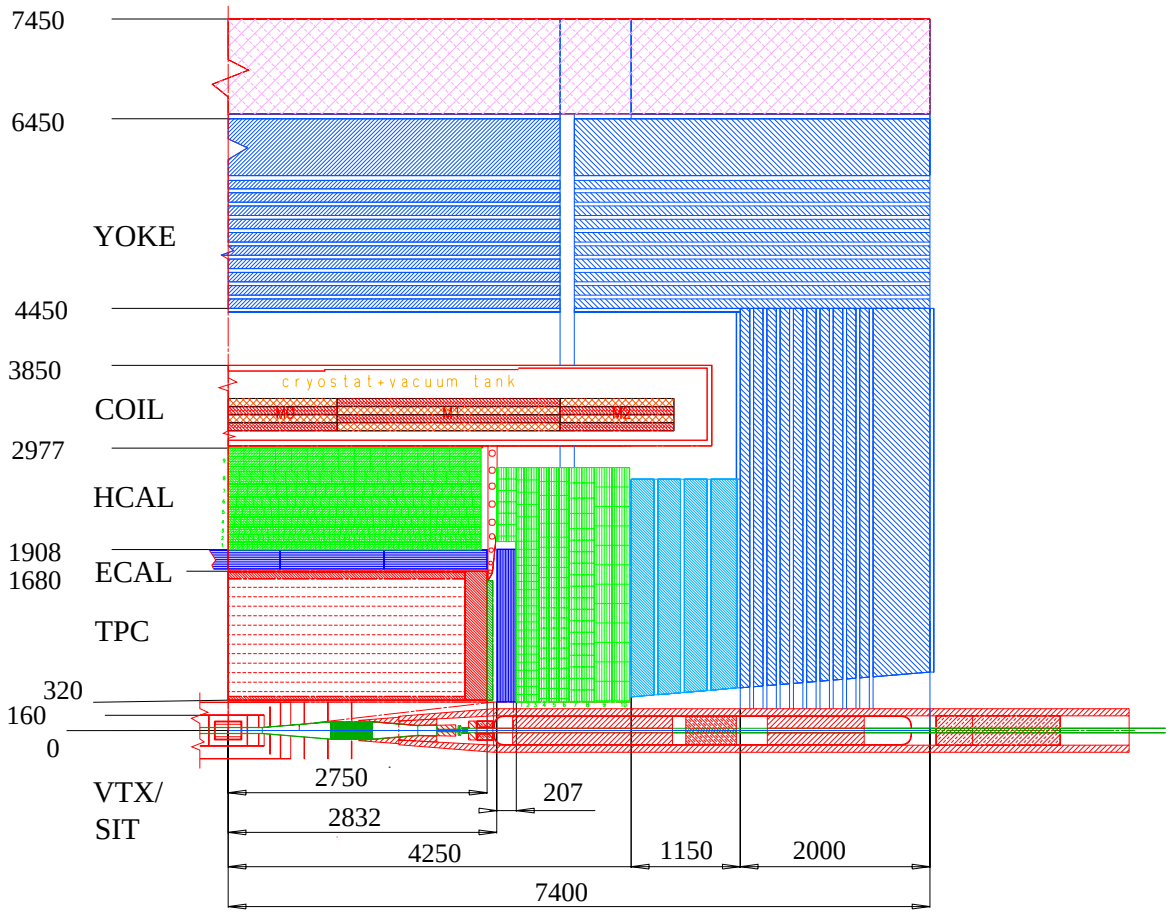

Figure 1.1.1: *View of one quadrant of the TESLA Detector. Dimensions are in mm.*

A coherent design of the subdetectors will make it possible to acquire as many details of each event as possible, so that Monte Carlo corrections to the data and thus systematic errors are as small as possible and the sensitivity for discovery and precision physics is as large as possible.

The performance goals are summarised in Table 1.3.1. They are backed up by a decade of world studies [2] -[27].

1.3 Detector R&D

While the detector technology and read-out solutions largely profit from the LEP/SLC experience as well as from R&D programmes for applications such as the LHC, many areas remain where specific TESLA applications need to be addressed by novel, dedicated R&D activities. This has warranted the launching of new detector R&D programmes, for example within the present ECFA/DESY study (see [3]).

Subdetector	Goal	Technologies
Vertex Detector (VTX)	$\delta(IP_{r\phi,z}) \leq 5\,\mu\text{m} \oplus \frac{10\,\mu\text{m GeV}/c}{p\sin^{3/2}\theta}$	CCD, CMOS, APS
Forward Tracker (FTD)	$\frac{\delta p}{p} < 20\,\%, \delta_\theta < 50\,\mu$rad for p=10-400 GeV/c down to $\theta \sim$100 mrad	Si-pixel/strip discs
Central Tracker (TPC)	$\delta(1/p_t)_{\text{TPC}} < 2{\cdot}10^{-4}(\text{GeV/c})^{-1}$ $\sigma(dE/dx) \leq 5\%$	GEM, Micromegas or wire readout
Intermediate Tracker (SIT)	$\sigma_{point} = 10\,\mu$m improves $\delta(1/p_t)$ by 30%	Si strips
Forward Chamber(FCH)	$\sigma_{point} = 100\,\mu$m	Straw tubes
Electromag. Calo. (ECAL)	$\frac{\delta E}{E} \leq 0.10\,\frac{1}{\sqrt{E(\text{GeV})}} \oplus 0.01$ fine granularity in 3D	Si/W, Shashlik
Hadron Calo. (HCAL)	$\frac{\delta E}{E} \leq 0.50\,\frac{1}{\sqrt{E(\text{GeV})}} \oplus 0.04$ fine granularity in 3D	Tiles, Digital
COIL	4 T, uniformity $\leq 10^{-3}$	NbTi technology
Fe Yoke (MUON)	Tail catcher and high efficiency muon tracker	Resistive plate chambers
Low Angle Tagger (LAT)	83.1–27.5 mrad calorimetric coverage	Si/W
Luminosity Calo. (LCAL)	Fast lumi feedback, veto at 4.6–27.5 mrad	Si/W, diamond/W
Tracking Overall	$\delta(\frac{1}{p_t}) \leq 5 \cdot 10^{-5}(\text{GeV/c})^{-1}$ systematics $\leq 10\,\mu$m	
Energy Flow	$\frac{\delta E}{E} \simeq 0.3\,\frac{1}{\sqrt{E(\text{GeV})}}$	

Table 1.3.1: *Detector performance goals for physics analyses for $\sqrt{s}$ up to $\sim$ 1 TeV.*

Centre of mass energy		TESLA Parameters 0.5 TeV	0.8 TeV
Beam properties			
$\mathcal{L}$	$[10^{34}\,\mathrm{cm^{-2}s^{-1}}]$	3.4	5.8
Trains/s		5	4
Bunches/train		2820	4886
Interbunch spacing	[ns]	337	176
Bunch sizes			
σ_x/σ_y	[nm]	553/5	391/2.8
σ_z	[mm]	0.3	0.3
Backgrounds			
$\gamma\gamma$ ev./BX ($p_T^{min} = 2.2\,\mathrm{GeV/c}$)		.02	0.1
Physics events			
Bhabha ($\theta > 20$ mrad)	$[s^{-1}]$	350	240
W^+W^-	$[h^{-1}]$	930	810
$q\bar{q}$	$[h^{-1}]$	330	210
$t\bar{t}$	$[h^{-1}]$	70	54
$\nu\nu H_{SM}$ ($M_{H_{SM}} = 120$ GeV/c^2)	$[h^{-1}]$	10	35
ZH_{SM} ($M_{H_{SM}} = 120$ GeV/c^2)	$[h^{-1}]$	7	4

Table 1.4.1: *Table of some machine properties and related backgrounds.*

1.4 Backgrounds and rates

Backgrounds for the detector arise from beam-beam interactions (e^+, e^- and γ), from synchrotron radiation and from upstream or downstream sources (μ and n). Particles from beam-beam interactions produced at the interaction point that cannot be shielded from the detector volume are responsible for much of the background in the detector. Table 1.4.1 gives an overview of some machine properties and related background and physics rates.

The $\gamma\gamma$ interaction can produce background particles in addition to those of a real physics event and may also come from a different bunch-crossing (BX) in the train, depending on the time resolution of the subdetector. The row labelled "$\gamma\gamma$ ev./BX, $p_T^{min} = 2.2$ GeV" gives a measure of the probability of having particles from a $\gamma\gamma$ event in the same BX.

1.5 Summary

The detector must be optimised specifically for the following requirements:

- track momentum determination to measure the recoil mass to $Z \to \ell\ell$ decays,
- vertex resolution for flavour identification,

- energy-flow measurement for the multitude of multijet topologies, implying fine 3-D granularity in tracking and calorimetry, with both being inside the coil,
- hermeticity implying good forward detectors, for measuring missing energy and/or the luminosity spectrum,
- data acquisition with continual, triggerless and deadtimeless readout for maximum efficiency,
- coping with high machine induced backgrounds, meaning a high $\vec{B}$ field and a minimum of material in front of the electromagnetic calorimeter.

These points lead to challenging detector issues which are presented in the following sections. They will motivate intensive detector design and R&D work in future.

Bibliography

[1] R. Brinkmann, G. Materlik, J. Rossbach, and A. Wagner (eds.). *Conceptual Design of a 500 GeV e^+e^- Linear Collider with Integrated X-Ray Laser Facility*. DESY, 1997. http://tesla.desy.de/TTF_Report/CDR/TTFcdrTab.html.

[2] ECFA/DESY Study of Physics and Detector for a Linear Collider. http://www.desy.de/conferences/ecfa-desy-lc96.html.

[3] 2nd ECFA/DESY Study of Physics and Detector for a Linear Collider. http://www.desy.de/conferences/ecfa-desy-lc98.html.

[4] P. M. Zerwas (ed.). *e^+e^- Collisions at 500 GeV: The Physics Potential, Part A& B*. DESY 92-123A,B, 1992.

[5] P. M. Zerwas (ed.). *e^+e^- Collisions at 500 GeV: The Physics Potential, Part C*. DESY 93-123C, 1993.

[6] P. M. Zerwas (ed.). *e^+e^- Collisions at 500 GeV: The Physics Potential, Part D*. DESY 96-123D, 1995.

[7] R. Settles (ed.). *e^+e^- Linear Colliders: Physics and Detector Studies, Part E*. DESY 97-123E, 1996.

[8] R. Orava, P. Eerola, and M. Nordberg (eds.). *Proceedings of Workshop on Physics and Experiments with Linear Colliders, Finland, 1991*. World Scientific, 1992.

[9] F. A. Harris, S. L. Olsen, S. Pakvasa, and X. Tata (eds.). *Proceedings of Workshop on Physics and Experiments with Linear e^+e^- Colliders, Vols. I and II, Hawaii*, 1993. World Scientific.

[10] *Proceedings of 3rd Workshop On Physics and Experiments with e^+e^- Linear Colliders (LCWS95), Japan, 1995*. World Scientific, 1996.

[11] E. Fernandez and A. Pacheco (eds.). *Physics and Experiments with Future Linear e^+e^- Colliders*. ISBN 84-490-1977-X. Universitat Autònoma de Barcelona / IFAC, 2000.

[12] *Physics and Experiments with Future Linear e^+e^- Colliders: LCWS2000*. American Institute of Physics, 2001. To be published.

[13] J. H. Mulvey (ed.). *Proceedings of the Workshop on Physics at Future Accelerators, La Thuile, Italy and Geneva, Switzerland, Jan 7-13, 1987*, 1987. CERN 87-07.

[14] S. Jensen (ed.). *Proceedings of the Summer Study on High Energy Physics in the 1990s, Snowmass, 1988*. World Scientific, 1989.

[15] J. Rogers (ed.). *Electroweak Symmetry Breaking at Colliding Beam Facilities: December 11-12, 1992, University of California, Santa Cruz, California*. 1993. Proceedings of the 1992 Workshop on High-Energy Physics with Colliding Beams.

[16] The proceedings of the studies in the USA by "DPF Long Range Planning" working groups are available under
http://fermi.pha.jhu.edu/dpf/cltp/index.html.

[17] Zeroth Order Design Report for the Next Linear Collider: Volume 1,2. SLAC-R-0474-VOL-1.
http://www-project.slac.stanford.edu/lc/ZDR/nlc_zeroth.htm.

[18] C. Ahn et al. Opportunities and Requirements for Experimentation at a very High-Energy e^+e^- Collider. *SLAC-0329*.

[19] C. A. Heusch (ed.). *The Electron Electron Linear Collider. Proceedings, Workshop, Santa Cruz, USA, September 5-6, 1995*, vol. A11. 1996.

[20] C. A. Heusch (ed.). *Electron Electron Linear Collider. Proceedings, 2nd Workshop, Santa Cruz, USA, September 22-24, 1997*, vol. A13. 1998.

[21] JLC-I. *KEK Report 92-16 (1992)*, 1992.
http://www-jlc.kek.jp/JLC.proposal-e.html.

[22] The three workshops on the Japan Linear Collider (1989,1990,1992) that resulted in Ref. [21] have been followed up with yearly workshops; more information may be found at http://acfahep.kek.jp/.

[23] A. Sessler (ed.). *Proceedings of the $\gamma-\gamma$ Collider Workshop, Berkeley, March 28-31, 1994*, vol. A355. 1995.

[24] V. Telnov (ed.). *Proceedings of the International Workshop on High Energy Photon Colliders, Hamburg, June 14-17, 2000*. To be published,
http://www.desy.de/~gg2000.

[25] A Study of the Physics and Detectors for Future Linear e^+e^- Colliders,
http://lcwws.physics.yale.edu/lc/america.html.

[26] *International Linear Collider Technical Review Committee Report 1995*, SLAC-R-95-471, G. Loew/SLAC(Chair) and T. Weiland/TH Darmstadt (Secreteriat),
http://www.slac.stanford.edu/xorg/ilc-trc/ilc-trchome.html.

[27] Worldwide Study of the Physics and Detectors for Future Linear e^+e^- Colliders.
http://lcwws.physics.yale.edu/lc/.

2 Tracking System

In the previous chapter the physics goals of TESLA and the requirements they and the linear collider environment impose on the detector have been outlined. For the tracking system this means:

- excellent momentum resolution ($\Delta(1/p) = 5 \cdot 10^{-5}\,(\mathrm{GeV/c})^{-1}$) in the central region to measure recoil masses with optimal precision;
- very high b- and c-tagging capabilities to identify multi-b final states like ZHH and $t\bar{t}H$ and to separate $H \to c\bar{c}$ events from $H \to b\bar{b}$ decay;
- good momentum resolution in the forward region to identify charges unambiguously down to lowest angles and up to highest momenta and very good angular resolution in this region to measure the luminosity spectrum from the acolinearity of Bhabha-events;
- very good pattern recognition capabilities to find tracks in high-energy jets with a very high local track density;
- minimal material to be able to measure also electrons and to avoid additional background to the calorimeters.

A detector which has been optimised to fulfil these requirements will be described in the following. Its components are

- a large Time Projection Chamber (TPC) ($r = 170\,\mathrm{cm}$, $\mathrm{L} = 2 \times 273\,\mathrm{cm}$) with ~ 200 readout points in the radial direction;
- a multi-layered pixel micro-vertex detector (VTX) between $r = 1.5\,\mathrm{cm}$ and $r = 6\,\mathrm{cm}$;
- an additional silicon tracking detector between the vertex detector and the TPC, consisting of cylinders in the barrel (SIT) and discs in the forward region (FTD);
- a precise forward chamber located behind the TPC endplate (FCH).

The complete tracking system is immersed in a magnetic field of 4 T. The general layout of the system is shown in Fig. 2.0.1. Fig. 2.0.2 shows the material in units of radiation lengths as a function of the radius at polar angle $\theta = 90°$ and as a function of θ for the different detectors.

The vertex detector is primarily optimised to reconstruct secondary vertices in b- and c-decays. An optimal resolution requires to build the first layer of the detector as close as possible to the interaction point. To be able to work with backgrounds from e^+e^--pairs of order 0.03 hits per mm^2 and beam crossing a pixel technology is mandatory. The LEP and SLD experience has shown that for an efficient b- and c-tag

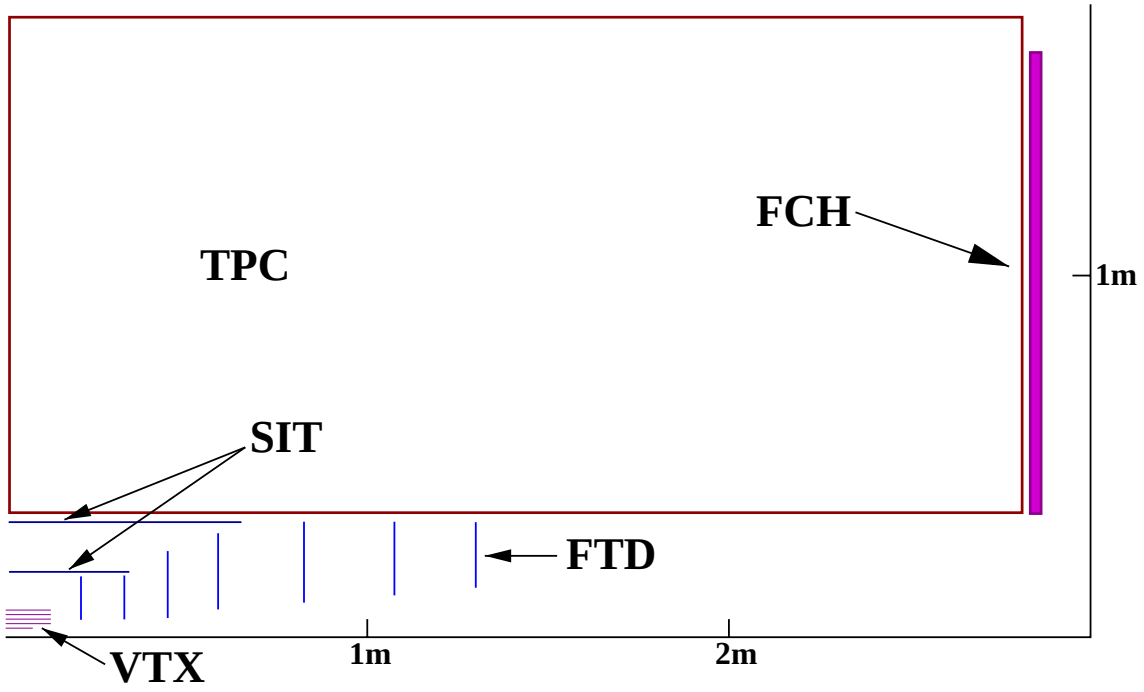

Figure 2.0.1: *General layout of the tracking system*

the determination of the invariant mass of the charged particles originating at the secondary decay vertex is essential. To measure this mass precisely not only very good resolution is needed but also a very high track reconstruction efficiency. For a precise measurement down to low momentum particles, it is important to have a minimal amount of material in the vertex detector itself and in the beampipe. Several technologies are under study to optimise the resolution and minimise the material. To obtain a good reconstruction efficiency at least three detector layers are proposed so that, together with the SIT, at least five silicon layers inside the TPC are available. In addition to the good impact parameter resolution the vertex detector provides also a very precise space point and slope of a charged particle trajectory close to the interaction point that contributes significantly to the momentum resolution.

The TPC is chosen as the central tracking device because it has a number of advantages compared to other options. A TPC allows a large number of measurements along a track, providing both spatial coordinates and information about the energy loss of the particle along its path in a large volume while presenting a minimum amount of material to the particles. This compensates the comparatively moderate point resolution and double-hit resolution. A TPC measures three-dimensional space-points directly, so that no ambiguities are created by matching different projections, and tracking is simple with high efficiency. The large radius of the central tracker ensures a good momentum resolution and, with the many space point measurements, it enables an efficient pattern recognition to be maintained even in a dense jet environment or with large backgrounds. Also because of the large radius, the decay products of long lived particles can be reconstructed with high efficiency and good precision. The measure-

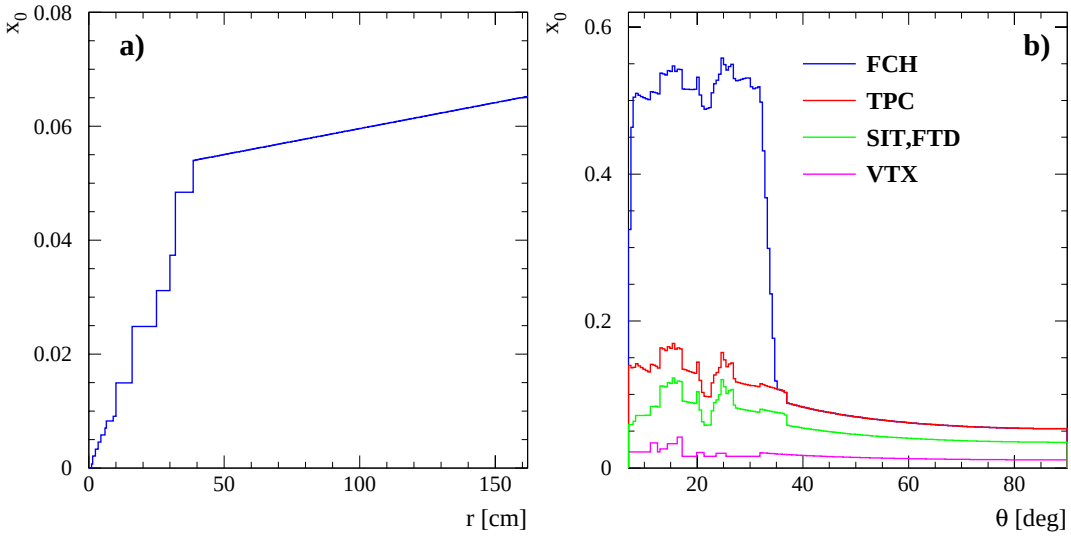

Figure 2.0.2: *Material distribution (a) as a function of the radius for $\theta = 90°$ and (b) as a function of the polar angle up to the end of the different subdetectors. For the line labelled TPC the material up to the end of the sensitive volume is shown.*

ment of the specific energy loss in the TPC will be used for particle identification. Kaons and pions will be separated in the 2-20 GeV/c momentum range, and electron identification will be improved compared to what can be done with the calorimeters alone, especially for low momenta, where a calorimetric identification is difficult. A TPC is also well suited to operate in a high magnetic field. Since the particle drift is along the magnetic field lines, there is no Lorentz angle involved and the diffusion is suppressed by the B-field. However because of the long drift distance the field must be very homogeneous and mapped to better than 10^{-3}. Finally a TPC is relatively easy to maintain since all sensitive parts are concentrated at the endplate which can be accessed and serviced if necessary.

Once the TPC tracks are matched with tracks in the intermediate silicon tracker or the vertex detector the timing resolution is about 2 ns, which is by far sufficient to identify the bunch crossing for every single track.

The overall momentum resolution is improved by 30% by adding a cylindrical silicon detector just inside the TPC. A second cylinder at $r = 16$ cm improves the track reconstruction efficiency, mostly for long lived particles [1]. The Silicon discs (FTD) in the forward region are needed for two reasons. Since the combined vertex detector and TPC resolution degrades at low polar angle θ due to a shorter projected track length, additional information provided by the silicon discs decreases significantly the momentum error. In addition these discs improve the polar angle resolution in this area. This is particularly important for electrons which are used to measure the luminosity spectrum from the acolinearity of Bhabha events. Since the TPC inner cylinder is traversed at very shallow angles in this region and electrons radiate a lot while crossing it, the polar angle resolution has to be provided by the silicon-tracking, before the

electrons enter the TPC.

Below $\theta = 12°$, where no vertex detector layer is crossed anymore, the momentum resolution deteriorates due to the decreasing lever-arm, even with the silicon discs present. This problem is addressed by the addition of the forward chamber (FCH). This improves the momentum resolution in that region which allows an unambiguous determination of the particle charge up to highest momenta and down to the edge of the tracking system given by the mask, at θ=5°. At larger polar angles, above $\theta = 12°$, the FCH assists the TPC in the pattern recognition, can be used to help the calibration of the TPC, and serves as a preshower detector for showers initiated in the TPC endplate.

The chosen layout is not only optimised for track resolution but also for track finding efficiency. A very high track finding efficiency inside jets is needed in order to have optimal resolution on the energy and direction of hadronic jets. There are ~ 200 space points per track measured in the TPC, and depending on the technology choice, ≥ 5 or ≥ 7 silicon planes, many of them being pixels. This allows for two independent local pattern recognition systems, one in the silicon detectors and one in the TPC. By combining both a very high overall track finding efficiency can be reached.

2.1 Vertex Detector

The physics motivation for the vertex detector (VTX) has been discussed in the Detector Concept section of this report. Section 2.1.1 indicates how this leads to performance goals for the detector and Section 2.1.2 discusses the machine-related issues which constrain the vertex detector design. Combining the performance goals with the restrictions from the machine leads to an acceptable compromise for the detector features, as discussed in Section 2.1.3, as are other points which are common to all the technology options. Section 2.1.4 discusses the three technology options which are currently considered for the vertex detector, namely charge-coupled devices (CCDs), CMOS pixels and hybrid pixel sensors.

How well does a detector which can be built, accessed and serviced satisfy the physics goals? The generic detector performance is discussed in Section 2.1.5. The more detailed aspects of the performance are mentioned in the Tracking System Performance section, while the global performance in terms of b- and c- tagging is presented in the Detector Performance section. The conclusion from these studies is that, by careful control of backgrounds, the interaction region can be made particularly favourable for the construction of a vertex detector of unprecedented performance, well-matched to the physics goals of the TeV e^+e^- regime.

All three detector options are the subject of active R&D programmes, which are discussed in Section 2.1.6. Cost estimates for the R&D and eventual production are given in Section 2.1.7.

2.1.1 Performance goals

At first sight, the average impact parameter of a B decay product, approximately $300\,\mu$m (independent of boost for $\beta\gamma \gtrsim 3$) suggests that modest detector performance may suffice. However, this is misleading for several reasons. Firstly, the average impact parameters for τ and charm particle decay products are 3-4 times smaller. Equally importantly, in recent years the physics advantages have been established of detector systems which permit the correct assignment of nearly all tracks to primary, secondary or tertiary vertices. Determination of the vertex mass and charge are examples which permit greatly improved b/c separation and the classification of jets as b or $\bar{b}$, c or $\bar{c}$. The importance of the vertex detector in many physics analyses which go beyond simple b-tagging increases at higher collider energies with more complex events, each containing a larger number of jets of various flavours.

The impact parameter resolution of a detector is a convolution of the point measurement precision, lever arms, mechanical stability and multiple scattering effects. One might hope that higher energy colliders would permit a relaxation of the concerns regarding multiple scattering, but this is not the case. Even in a 1 TeV e^+e^- collider, the average energy of particles in jets (depending on the physics process) is in the region 1-2 GeV. The most interesting events will probably have high jet mutiplicity, where multiple scattering effects are worst. Consequently, the detector design still needs to be pushed to the limit as regards layer thickness.

Whatever performance is achieved for jets which are optimally oriented with polar angle $\theta \approx 90^\circ$, the impact parameter precision degrades at small polar angles due to the increased distance of the first hit from the IP, and the increased thickness of material traversed by the oblique tracks. For lower energy colliders, it was reasonable to restrict the analysis to say 90% of the solid angle. At TESLA, this will no longer be the case, firstly because in events with high jet multiplicity there is a significant probability that one of the jets is found in the extreme forward or backward region, and secondly because much of the physics relies on having spin-polarised electrons and/or positrons, where the significance of events becomes weighted in favour of the forward-backward direction.

Taking account of all these effects, the ideal vertex detector would consist of a series of nested low-mass spherical shells of radii R, $2R$, $3R$,.. where $R \approx 5\,$mm (so as to track most of the parent Bs and Ds) with a point-measurement precision $\sim 1\,\mu$m, with small apertures for the entry and exit beams. The separation between layers would be sufficient to control multiple scattering effects, and the number of layers would be sufficient for stand-alone track reconstruction. Reality, in the form of machine-related constraints, mechanical supports, electrical connections and cooling systems, conspires to drive the detector design away from this ideal. Fortunately, solutions can be found which largely preserve the required physics capability.

2.1.2 Machine-related issues

The luminosity and bunch timing at TESLA, combined with the requirement of untriggered operation, impose particular constraints on the vertex detector. Data need to be stored somewhere (preferably local to the detector) through the 1 ms bunch train, then transferred to the processor selected to handle the data for that bunch train. For successive trains, data are transferred to different members of the processor farm. It is not necessary for the data from the vertex detector to correlate with a unique bunch crossing. On the contrary, it is acceptable to accumulate the signals over a number of bunch crossings (as at SLD) provided that the hit density is everywhere sufficiently low that the track fitting is not significantly compromised. Both the CCD and CMOS pixel options take advantage of this important tradeoff, which favours high granularity and moderate readout speed. The optimal solution depends on the magnitude of the machine background. In TESLA, the dominant e^+e^- pair background from the beam-beam interaction is confined radially by the 4 T magnetic field in the detector solenoid. Consequently, the background is strongly peaked in layer-1, and falls rapidly beyond; thus the readout of layer-1 needs to be the fastest. Due to constraints on the design of the machine collimation system, it is necessary to set the beampipe radius at 14 mm. The pair background in a vertex layer just outside this beampipe produces about 0.03 hits mm^{-2} per bunch crossing (BX), which is acceptable for the foreseen readout systems.

Apart from the question of hit density due to the background particle flux, one has also to consider the question of radiation damage to the detector. The dominant background (pair-produced electrons which penetrate the VTX inner layer) imposes a requirement on radiation hardness of about 100 krad for a 5 year life, which is easily achieved with modern silicon technology. Potentially more serious for the CCD option is the neutron background. This is currently estimated to be of the order of 10^9 1 MeV-equivalent neutrons cm^{-2} $year^{-1}$, which is acceptable with current CCD designs, and there is scope for major improvements in their resistance to bulk radiation damage. The hybrid and CMOS pixel options have large safety factors as regards radiation tolerance.

2.1.3 Detector features

Since the inner layer needs to be as close as possible to the IP, the optimal design for this layer will certainly be cylindrical, just outside the beampipe, extending in length to cover the required polar angle range. With a radius of 15 mm defined by the machine, it has been demonstrated [2] that a pixel-based detector with pixels of the smallest possible size is required in order to avoid confusion (cluster merging) within the cores of high energy jets.

Beyond layer-1, there are essentially two options. For sufficiently thin detectors, the optimal arrangement is to continue with a series of cylindrical layers with the same polar angle coverage as layer-1, stepped approximately equally in radius similarly to the ideal spherical system referred to in Section 2.1.1. However, if the layer thickness

exceeds $\sim 0.5\%\,X_0$, the penalty in material thickness at small polar angles becomes excessive, and shorter barrels supplemented by conical endcaps become preferable.

A design which profits from thin layers is shown in Fig 2.1.1. The inner 3 layers extend to $|\cos\theta| = 0.96$, with 5-layer coverage to $|\cos\theta| = 0.9$. The forward coverage is extended by the FTD to $|\cos\theta| = 0.995$, but this is without useful flavour ID capability. The outer 4 VTX layers are used for stand-alone track reconstruction. The advantages of stand-alone reconstruction in tracking sub-detectors are well-established; they include internal alignment optimisation, efficiency monitoring of the other tracking systems (notably the FTD/SIT/TPC) and vice versa, optimal identification of photon conversions within the vertex detector and optimal rejection of 'bad' hits due for example to cluster merging between signal and background hits.

Having found the tracks in layers 2-5 (and rejected a low level of fake tracks by linking to the SIT and TPC) the layer-1 hits are used to refine the track extrapolation to the IP, which is particularly important for low momentum particles.

Figure 2.1.1 shows the CCD-based detector inside its low-mass foam cryostat, used to permit an operating temperature of around 200 K. Not shown in the figure is the high precision mechanical support structure (a closed beryllium cylinder) which is mounted off the beampipe inside the cryostat. Being outside the volume used for the precision measurements and extrapolation to the IP, this cylinder can be extremely robust (approximately 2 mm wall thickness). It serves the additional role of clamping the two sections of beampipe rigidly together (clamps at z about $\pm$ 15 cm) so that the critical inner cylindrical section of beampipe of length 12 cm and radius 14 mm can be made extremely thin: 0.25 mm wall thickness beryllium is considered possible. Striplines and optical fibres are routed along the beampipe below the polar angle range used for tracking, connecting to inner electronics mounted in the form of a thin shell on the outer surface of the synchrotron radiation mask assembly.

Other than the cryostat, this general description may apply equally to the CMOS pixel option.

The layout based on the somewhat thicker hybrid pixel sensors is shown in Fig 2.1.2 and consists of a three-layer cylindrical detector surrounding the beampipe complemented by forward cones and disks extending the polar acceptance to small angles, following a solution successfully adopted in the DELPHI Silicon Tracker. The three barrel layers have a polar acceptance down to $|\cos\theta| = 0.82$, with the forward detectors extending the 3-hit coverage to $|\cos\theta| = 0.995$. The transition from the barrel cylindrical to the forward conical and planar geometries optimises the angle of incidence of the particles onto the detector modules in terms of the point resolution and the multiple scattering contribution. Overlaps of neighbouring detector modules provide a useful means of verifying the relative detector alignment.

The vertex detector will be an extremely sophisticated part of the detector. Along with other elements of the inner detector system (everything inside the TPC inner radius) it will potentially need periodic maintenance and upgrades. For this reason, there needs to be a clear plan for carrying out such operations without a major impact on other delicate equipment such as the final focus magnet system. A procedure for avoiding such interference has been devised, and is based on a strategy of rolling the

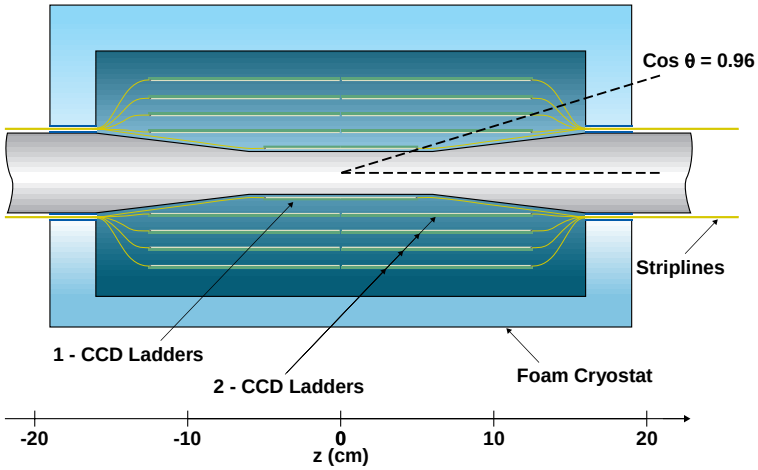

Figure 2.1.1: *Cross-section of CCD-based vertex detector.*

TPC along the beamline by about 5 m, to provide access to the inner detector. This is discussed further in the Detector Integration section.

2.1.4 Technology options and conceptual designs

Detailed technical reports on the three options are to be found in [3], [4] and [5].

2.1.4.1 CCD and CMOS pixels

Both these options rely on a charge-collection region of thickness 10–20 μm, which is partly depleted and in part of which the charge is collected by diffusion, as indicated in Fig 2.1.3. These features lead to coordinate measurements which are precise and robust (relatively free of the effects of δ electrons and fluctuations in charge deposition) in both the rϕ and z components down to small polar angles. Use of small pixels ($\sim 20\times20\mu$m^2) permits coordinate measurements with precision 1.5 - 3 μm by centroid fitting.

The essential difference between these two options is the method of sensing the signal after collection. The CCD design shown in Fig 2.1.4 restricts the material within the fiducial volume to the thin silicon alone. The CCDs are attached to 'ladder blocks' and tensioned so as to achieve excellent mechanical stability. These devices with their inactive pixels dissipate very little power in the fiducial volume ($\sim$ 10 W in total for 800 Mpixels), and can be cooled by a gentle flow of nitrogen gas. Outside this volume, as well as the mounting blocks, each ladder carries a driver IC and a readout IC, as shown in Fig 2.1.5. The driver chip generates the waveforms which shift the stored signals row by row down the device. The readout chip receives the analogue signals from all columns in parallel as they are shifted out of the active area to buffer amplifiers. This chip incorporates analogue-to-digital conversion, correlated double

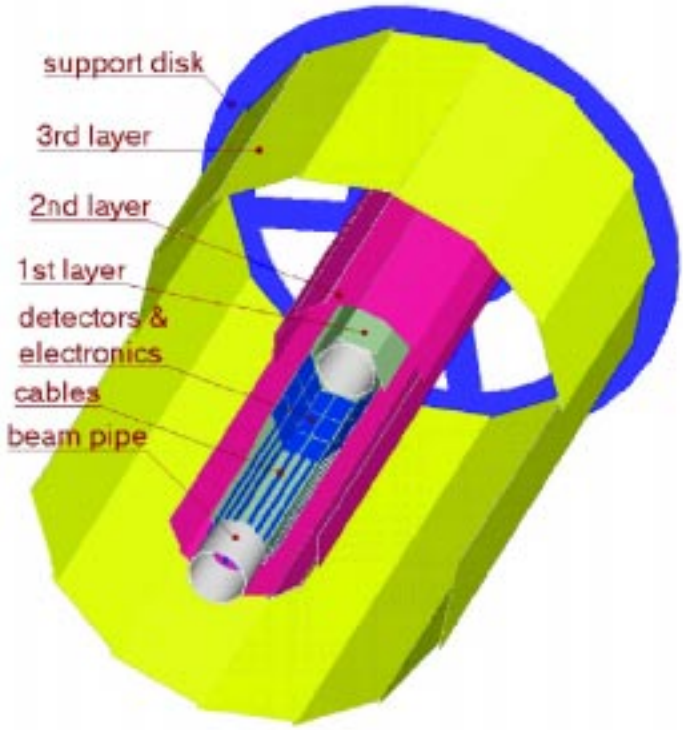

Figure 2.1.2: *General layout of the barrel section of the hybrid pixel-based vertex detector.*

sampling, data sparsification by a sequence of pixel- followed by cluster-comparators, and data storage.

Some of the key parameters associated with this detector design are listed in Table 2.1.1. The material budget for this option is shown in Fig 2.1.6. With 0.06% X_0 per layer, the potential for precise tracking to very low momentum is established. Processed data ($\sim$ 8 MB) are stored in the readout ICs during the bunch train, and read out via a few optical fibres between trains.

This design philosophy, while it minimises the material in the tracking volume, imposes the need for an environment in which fast, efficient transfer of signal charge in the CCD buried channel (transport through as much as 12.5 cm of silicon) is established and preserved throughout the life of the detector.

In the case of the CMOS pixels, the plan is also to measure the signal charge in every pixel, on a row-by-row basis. However, the charges are now sensed where they are collected, and the rows of sensing transistors are successively switched on by means of gating lines controlled by a shift register. The analogue signals are then transmitted to the edge of the active area by means of a set of readout lines, one per column. From this point, the signal processing proceeds approximately as in the CCD option. To achieve the required noise performance and readout rate, it will be desirable to introduce logic for correlated double sampling inside the unit cell; space for this is probably available without enlarging the pixels. Whether CMOS pixel devices can be constructed with the required performance in the full length needed for an unsupported-silicon detector

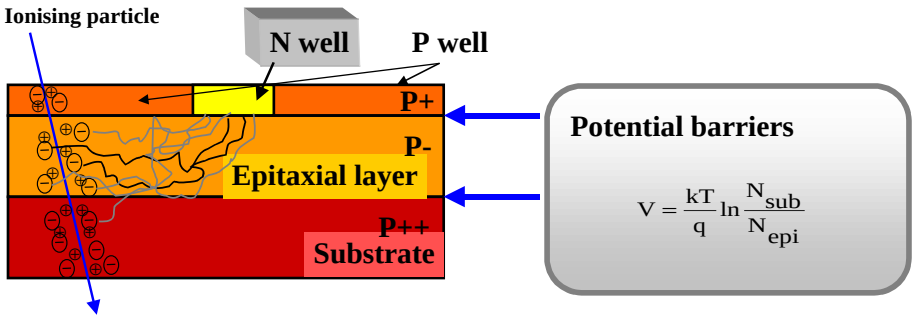

Figure 2.1.3: *Charge collection within a CMOS pixel, indicating the potential barriers which induce efficient diffusive charge-collection.*

architecture is an open question. If not, a solution (which would substantially increase the material budget) would be to tile a substrate (possibly diamond-coated carbon fibre) with a number of these devices, so as to make up the full ladder length. In this case, the planned cooling (by conduction along the substrate) would need to take account of the full power dissipation including the readout sections of the chips. Here there are many open issues to be investigated, including the possible use of pulsed power.

Layer	Radius	CCD L×W	CCD size	Ladders & CCDs/lddr	Row clock fcy & Readout time	Bgd occup.	Integr. bgd
	mm	mm^2	Mpix			Hits/mm^2	khits/Train
1	15	100 × 13	3.3	8/1	50 MHz/50 μs	4.3	761
2	26	125 × 22	6.9	8/2	25 MHz/250 μs	2.4	367
3	37	125 × 22	6.9	12/2	25 MHz/250 μs	0.6	141
4	48	125 × 22	6.9	16/2	25 MHz/250 μs	0.1	28
5	60	125 × 22	6.9	20/2	25 MHz/250 μs	0.1	28

Table 2.1.1: *Key parameters of the CCD-based vertex detector design. The penultimate column lists the background occupancy integrated over the individual data read out time per layer.*

2.1.4.2 Hybrid pixels

Silicon hybrid pixel detectors have been developed and successfully applied to track reconstruction in high energy physics experiments in the last decade. In particular, DELPHI at LEP was the first collaboration adopting hybrid pixel sensors for a tracking detector at a collider experiment [6]. They have been further developed for ALICE [7], ATLAS [8], and CMS [9] to meet the experimental conditions of the LHC collider.

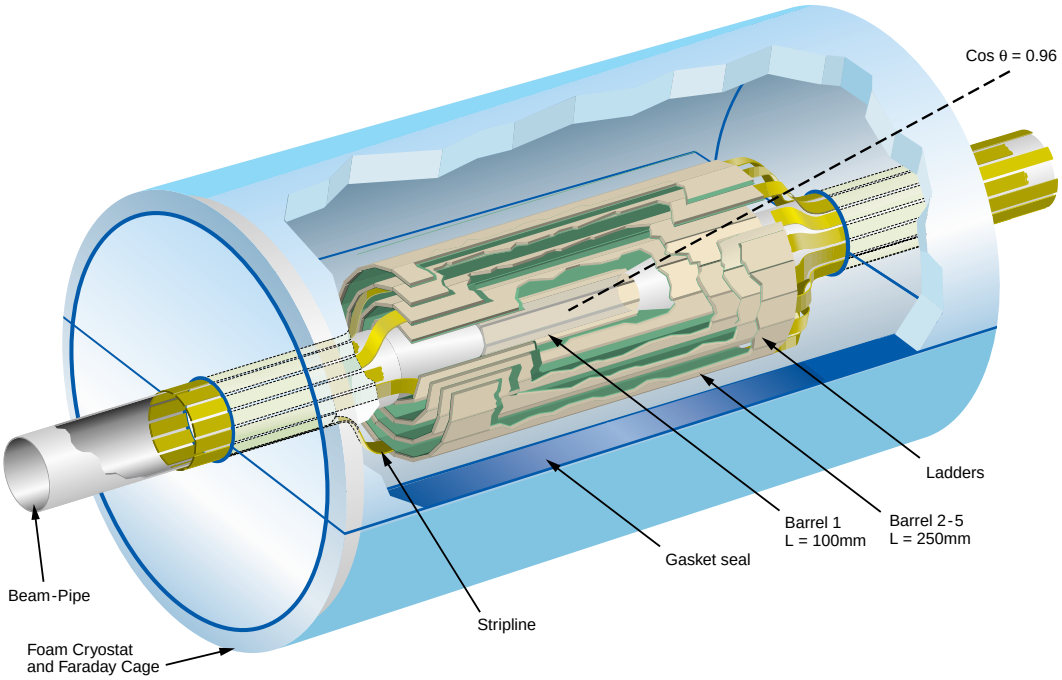

Figure 2.1.4: *General layout of CCD-based vertex detector.*

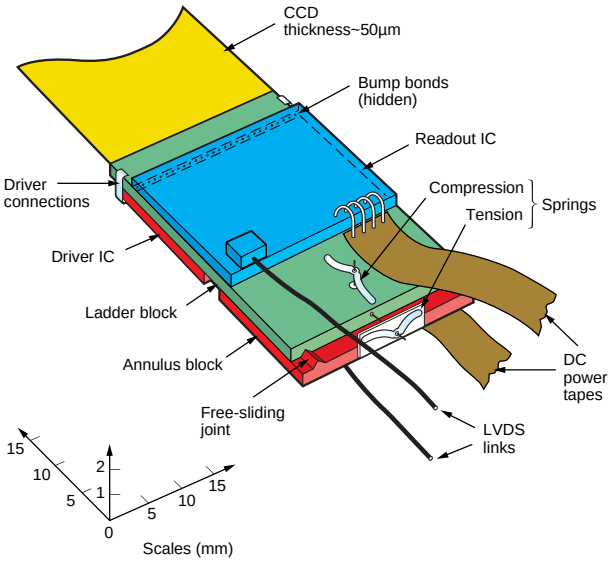

Figure 2.1.5: *Layout of components at end of ladder in CCD-based detector.*

These R&D activities have demonstrated the feasibility of fast time stamping (25 ns) and sparse data scan readout, and the operability of hybrid pixel detectors exposed to neutron fluxes well beyond those expected at the linear collider.

The spatial resolution requirements may be achievable by localised collection of the signal charge and by interpolating the signals of neighbouring cells using less highly

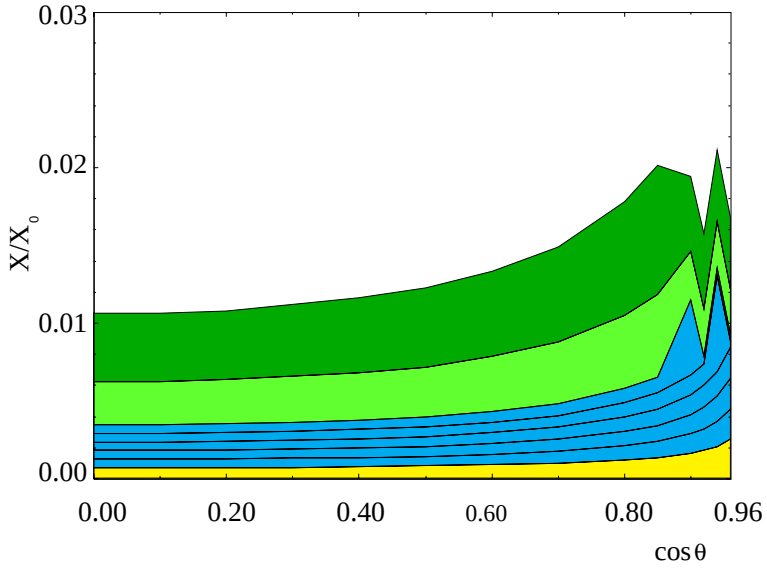

Figure 2.1.6: *Material budget for CCD-based detector, as function of polar angle (from the bottom up the different contributions shown are from the beampipe, each of 5 the layers, the support shell and the cryostat).*

segmented analogue readout. This requires a pitch of the charge-collection electrodes of not more than 25 μm, exploiting the capacitive coupling between neighbouring pixels and arranging a readout pitch n times larger than the implant pitch. Recent tests on a microstrip sensor with 200 μm readout pitch have achieved a 10 μm resolution with a layout having three interleaved strips [10]. Similar or better results are to be expected for a pixel sensor, taking into account both the lower noise because of the intrinsically smaller detector capacitance and the charge sharing in two dimensions, setting the target single point resolution to $\leq$ 7 μm. Reducing the readout density without compromising the achievable space resolution is also beneficial in limiting the power dissipation and overall costs.

The material budget can be optimised by adopting 200 μm thick detectors and back-thinning of the readout chip to 50 μm, corresponding to 0.3 % X_0, plus a light support structure. The estimated material budget, shown in Fig 2.1.7 corresponds to 1.6 % X_0 for the full tracker. The present concept for the mechanical structure envisages the use of diamond-coated carbon fibre detector support layers acting also to conduct the heat dissipated by the readout electronics so that it becomes uniformly distributed over the whole active surface of the detector. Assuming a power dissipation of 40 μW/channel, the total heat flux is 530 W, corresponding to 1750 W/m^2, for a readout pitch of 150 μm. Preliminary results from a finite element analysis show that pipes circulating liquid coolant must be placed every 5 cm along the longitudinal coordinate except for the innermost layer where they can be placed only at the detector ends, minimising the amount of material. Signals can be routed along the beampipe to the repeater electronics installed on the forward masks which shield the detector from

background.

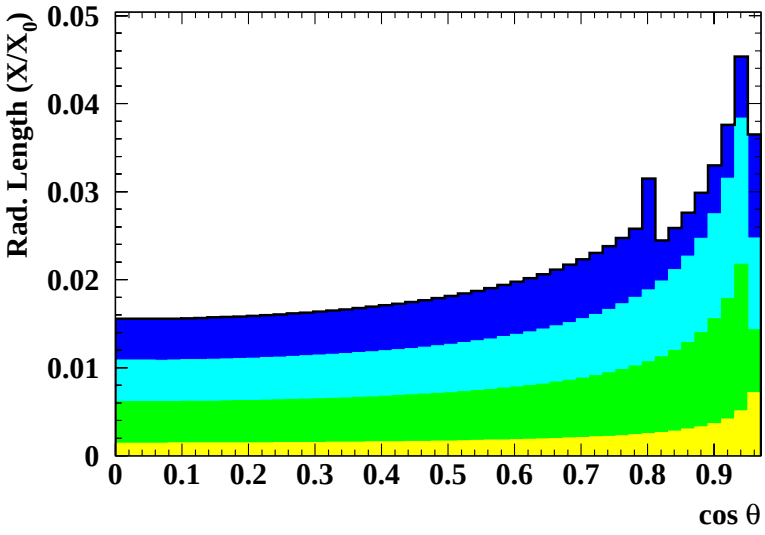

Figure 2.1.7: *Material budget for hybrid pixel-based detector, as function of polar angle (from the bottom up the different contributions are the beampipe, then each of the 3 layers).*

2.1.5 Generic detector performance

This section, and the Tracking System and Detector Performance sections, discuss simulations for the CCD-based option, since this has the best-defined geometry and material budget, and also has the highest established performance in terms of precision over a wide range of incident angles, for devices of the dimensions needed for this application (tens of cm^2). Details of these simulation studies are reported in [11]. This work is an update of studies carried out with an earlier detector description [12].

It must be emphasised that one of the other technology options for the vertex detector may eventually reach or exceed these performance figures. Furthermore, CCDs might be ruled out due to unexpectedly large neutron or other hadronic backgrounds. There is still time for completely new ideas to emerge. For these reasons, the detector architecture to be selected remains completely open. However, it can be expected that the detector which is eventually installed will deliver at least the performance represented by these simulations.

The figure of merit for any pixel-based vertex detector can be expressed by the precision with which one measures the track impact parameter to the IP, separately in the rϕ and rz projections. For a set of cylindrical detectors, this resolution can be

expressed as

$$\sigma = \sqrt{a^2 + \left(\frac{b}{p \sin^{\frac{3}{2}} \theta}\right)^2} \; .$$

The constant a depends on the point resolution and geometrical stability of the detectors and b represents the resolution degradation due to multiple scattering, which varies with track momentum p and polar angle θ. For the present detector design, the values of a and b are similar for both projections, and take the values $4.2\,\mu$m and $4.0\,\mu$m respectively. An example is plotted in Fig 2.1.8. These calculations are based on a full GEANT3 description of the TESLA detector, and use the BRAHMS detector simulation program. The solenoid field is set to 4 T.

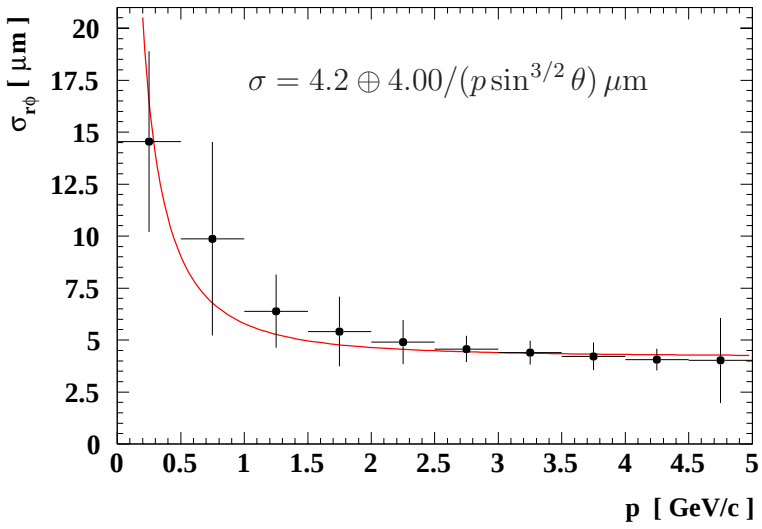

Figure 2.1.8: *Track impact parameter resolution in $r\phi$ vs momentum for $\theta_p = 90°$, for the CCD option.*

2.1.6 R&D programme

For the CCD option, the proposed detector with 799 Mpixels is a reasonable evolution from the successful SLD vertex detector of 307 Mpixels [13], which operated reliably for several years in hostile background conditions. However, there are challenges which push the design well beyond the performance required for SLD.

In terms of the mechanical design, the most ambitious aspect is the move to stretched silicon, which reduces the layer thickness from $0.4\%\,X_0$ (achieved with excellent mechanical stability in SLD) to $0.06\%\,X_0$. This is the subject of an active R&D

programme using thin silicon ladder replicas. Using the system of tensioning the silicon via ladder blocks (Fig 2.1.5), the sagitta was repeatedly measured after major mechanical disturbances (releasing the tension, so the ladder sagged visibly). On re-establishing the spring tension, the ladder recovered its shape with a repeatability in the sagitta of better than $3\,\mu$m.

Regarding the CCD dimensions, the active area of up to $125 \times 22\,\mathrm{mm}^2$ is standard for companies with at least 6 inch wafer processing. The column-parallel architecture is intrinsically simple, since the readout register is omitted. However, the layout of the single stage source followers on a $20\,\mu$m pitch needs detailed design. The major challenge is in the clocking rate. Recent SPICE simulations have highlighted the areas needing development, notably a reduction in the resistance of the drive buslines and of the imaging gate electrodes. Both are achievable using existing IC technology. However, care needs to be taken to minimise inductances in the drive circuitry.

The complexity of the drive electronics depends on the minimal gate voltage required for efficient charge transfer. This is a major development area in the field of commercial CCDs for video cameras, where power minimisation is critical. Recent progress has been spectacular. Given the small well capacity required to transport signals from minimum-ionising particles, there is a good chance that 1 V clock pulses will suffice. This issue will need a significant R&D programme, which must also consider the question of radiation effects. As previously noted, the hardness of CCDs with respect to the neutron background at TESLA may well be sufficient. Nevertheless, much can be done to improve the performance by modern design procedures. Since this question is of inter-disciplinary interest, it forms part of the R&D programme of the CCD community working towards TESLA.

The readout IC represents a reasonable step beyond the circuitry already integrated on CMOS APS devices for optical imaging [14]. The goal of 4 bit ADCs running at 50 MHz with associated comparators and clustering logic on a pitch of $20\,\mu$m will become achievable due to ongoing reductions in feature size. Nevertheless, the design work will be challenging. Fortunately, the column-parallel CCD architecture with readout speed enhanced by about a factor 100 is of considerable inter-disciplinary interest. The IC design work will be pursued as part of a generic imaging detector development programme.

The use of the column-parallel approach certainly lends itself to pulsed power (most of the system being switched off between bunch trains) and to 2-phase CCD clocking with sinusoidal drive pulses. Even so, a careful minimisation of the power dissipation at the ends of the ladders may be needed. If gas cooling were to be insufficient, it would be quite convenient in these locations to use the evaporative cooling technique which worked reliably on the NA32 experiment at CERN [15].

CMOS pixels for the detection of minimum-ionising particles have emerged recently. Excellent performance has been established with structures of area few mm^2. It will now be important to establish the unit cell design appropriate for large-scale devices. A correlated double sampling circuit will be needed to reduce reset noise, either at the sensor periphery or within the $20\,\mu$m square pixel. The output capacitive load represented by the column line which overlays all the row lines needs to be established,

and hence the requirement for the transconductance of the output FET in order to achieve the necessary signal risetime. The need for higher transconductance could increase the required pixel size. The peripheral logic to perform the data sparsification needs to be designed; in some respects it can be similar to that of the CCD option.

Putting these pieces together will establish the scaling law for these devices (width and length) and hence the practical limit for this application. If it turns out to be feasible to work with $> 12{\times}2\,\mathrm{cm}^2$ read from only one end at the required frequency, then the unsupported silicon option will be equally promising for this detector architecture. If not, the degree of tiling necessary will become apparent. If one or more readout sections need to be situated inside the active volume of the detector, this will increase the cooling requirements and hence the material budget.

The question as to whether the APS option is amenable to pulsed power operation is of considerable importance. To some extent, circuit features such as correlated double sampling can protect against the effects of baseline drift.

Hybrid pixel sensors have been adopted at LEP, heavy ion experiments and at the LHC. The HEP community has acquired considerable experience with these detectors and addressed important issues related to reliability, radiation hardness and timing capabilities. The linear collider application now requires R&D aimed to improve the achievable single point resolution to better than $10\,\mu$m and to reduce the layer thickness.

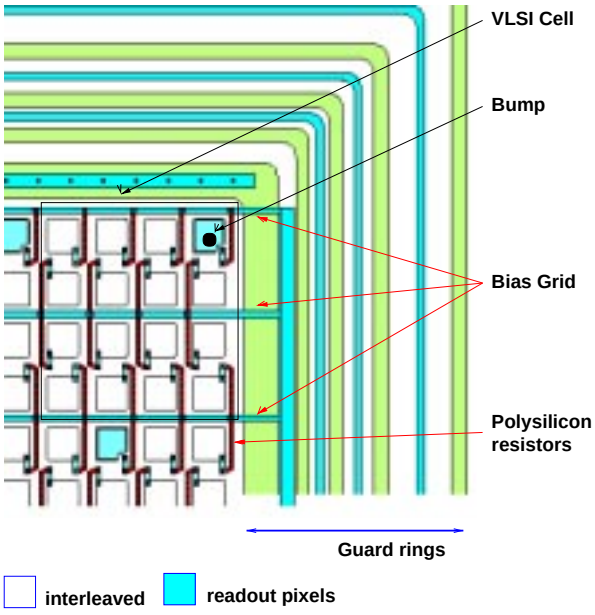

Figure 2.1.9: *Layout of the upper corner of hybrid pixel detector test structure, with 50 μm implant and 200 μm readout pitch.*

In these devices the ultimate readout pitch is constrained by the front-end electronics that must be integrated in a cell. At present, the most advanced readout circuitry

has a minimum cell dimension of $50 \times 300\,\mu\mathrm{m}^2$ which would not be suitable for finely segmented charge sampling. Developments in VLSI and recent studies [16, 17] on intrinsic radiation hardness of deep submicron CMOS technology will permit a sizeable reduction in the cell dimensions. However, sensor designs without such limitations are worth exploring. A possible solution is to exploit the capacitive coupling of neighbouring pixels and to have a readout pitch n times larger than the implant pitch [18]. The proposed sensor layout is shown in Fig 2.1.9 for n=4. In this configuration, the charge carriers created underneath an interleaved pixel will induce a signal on the capacitively coupled readout nodes. The ratio of the signal amplitudes on the readout nodes at both sides is related to the particle position. The resolution is expected to be better than (implant pitch)/$\sqrt{12}$ for an implant pitch of 25 μm or smaller. The ratio between the inter-pixel capacitance and the pixel capacitance to backplane plays a crucial role, as it defines the signal amplitude reduction at the output nodes and therefore the maximum number of interleaved pixels. In order to verify the feasibility of this scheme a dedicated R&D program has started [19]. Prototype sets of sensors with interleaved pixels and different choices of implant and readout pitch have been already designed, produced and characterised [20, 21].

After 20 years of developing pixel-based vertex detectors, it is clearly the unforeseen problems which become the most threatening for any next generation detector. It is also clear that while one can make coherent plans for individual parts of the detector, the system aspects are less predictable. It is true for all options that convergence on the ambitious goals will be challenging. Serious support for the various ongoing R&D programmes is essential. It is fortunate that all options already have applications as imaging devices in other fields of science. Developments aimed for a TESLA vertex detector will not all find a home there, but are almost certain to be picked up elsewhere, possibly including some of the challenging X-ray imaging applications required for the TESLA FEL science programme.

2.1.7 Cost estimate

Regarding the CCD option, the column-parallel CCD design concept has sparked interest from several scientific disciplines, so the development costs may be shared between them. Based on the SLD experience, an estimate for these costs would be 600kEUR, with smaller amounts for each of the drive and readout ICs. The mechanical R&D work is manpower-intensive, but not overly expensive in equipment, beyond the infrastructure already built up for other projects. An overall figure for the R&D phase of 1MEUR seems reasonable.

Once in production, the cost of manufacturing the CCDs will be modest, as with other IC devices. What can enormously increase the cost, as happens in astronomy projects, is the requirement for detailed performance evaluation by the manufacturer. It was demonstrated in SLD that accepting devices required only to produce a good image from an illuminated test card at room temperature resulted in a high yield for cold operation in the detection of far smaller signals, such as those from minimum ionising particles. Based on this experience, an average unit cost of around 5000 EUR

would be sufficient, giving a total CCD cost of 600kEUR.

The cost of the custom drive and readout ICs might be in the region of 300kEUR. The off-detector electronics is modest, cost maybe 100kEUR.

The mechanical systems (tooling etc.) for the unsupported silicon assembly will be of similar complexity to those used for SLD, where the relative simplicity of the ladders was offset by the more compressed geometry (radial separation between layers). The beryllium support structure (two half-shells, plus 5 annuli for separately mounting each layer) is larger and contains more parts than at SLD. An approximate cost estimate is 1.2MEUR. The system of cooling gas/liquid nitrogen is estimated at around 35kEUR. The detector cryostat would be around 6kEUR.

Thus, the overall production cost of a CCD-based vertex detector for TESLA, after the R&D phase, is approximately 2.3MEUR.

For the CMOS pixels, continued R&D for 4-5 years is assumed, with a typical rate of 2 multiproject submissions (small test structures mainly for electronics development) and 1 engineering run (large devices for the detector development) per year. A multi-project submission costs about 10-12kEUR and an engineering run about 70-100kEUR, which leads to a total cost estimate for the R&D of about 500kEUR.

For the detector production, assuming the CMOS devices can be produced with similar sizes to those for the CCD option, one envisages a total of 120 detectors. The cost will of course be driven by the yield, but the use of standard industrial processing (or close to it) gives reason for optimism that the production yield will be high. For a relatively large production run, a wafer cost of 3–4kEUR is estimated. On this basis, the cost of the complete set of devices is estimated at 500kEUR, including spares.

The cost of the external electronics and of the mechanics is estimated to be similar to that of the CCD option. This brings the cost estimate for the CMOS option to about 500kEUR R&D and 1.9 MEUR for the production.

A fairly detailed cost estimate for the hybrid pixel option has also been made. R&D amounts to 450kEUR, sensor production 1.4MEUR, mechanics and readout electronics 1.5MEUR, translating in a total production cost of 2.9 MEUR.

Experience with the two SLD pixel-based vertex detectors suggests that one can hope to build a detector of high reliability needing almost no maintenance. The reason for insisting on convenient access would be primarily to permit the installation of upgrade detectors in the future. At LEP, SLD and the Tevatron, the need for enhanced physics reach, combined with advances in detector technology, have led to the installation of upgrade detectors with substantially improved physics performance every few years. This trend is likely to continue for the future, but long term upgrades do not form part of the cost estimate of the start-up detector.

2.2 Intermediate Tracking System

In the space between the vertex detector and the beampipe on the inside and the TPC on the outside further silicon detectors are positioned consisting of two cylinders in the barrel (SIT) and of seven planes perpendicular to z in each of the two endcaps (FTD).

The three planes closest to the interaction point will consist of active pixel sensors while the remaining four are silicon strip detectors with modest resolution. The setup of the proposed system is shown in Fig. 2.2.1. and the exact parameters are listed in table 2.2.1.

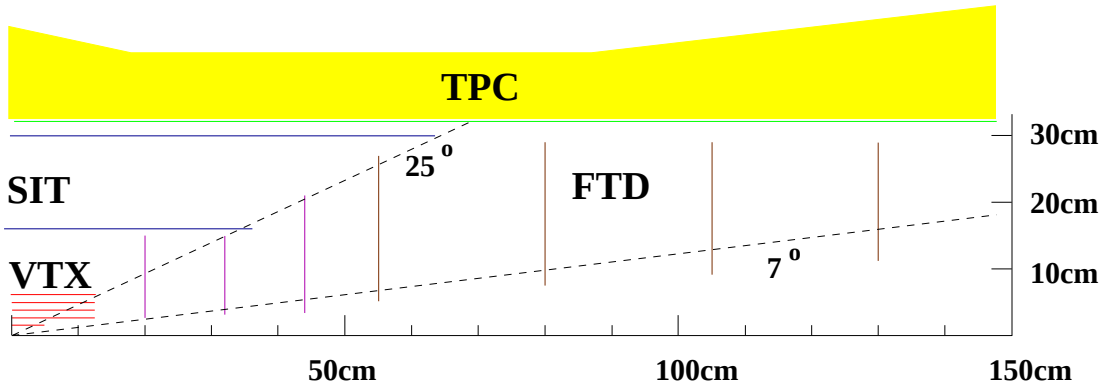

Figure 2.2.1: *General layout of the SIT and FTD*

module	type	r,z	z,r_{min}	z,r_{max}	technology
SIT1	cylinder	16 cm	-36 cm	36 cm	strips
SIT2	cylinder	30 cm	-64 cm	64 cm	strips
FTD1	plane	20 cm	2.9 cm	14 cm	pixels
FTD2	plane	32 cm	3.2 cm	14 cm	pixels
FTD3	plane	44 cm	3.5 cm	21 cm	pixels
FTD4	plane	55 cm	5.1 cm	27 cm	strips
FTD5	plane	80 cm	7.2 cm	29 cm	strips
FTD6	plane	105 cm	9.3 cm	29 cm	strips
FTD7	plane	130 cm	11.3 cm	29 cm	strips

Table 2.2.1: *Main mechanical parameters of the SIT and the FTD.*

The main role of these detectors is to improve the momentum resolution by the addition of a few very precise space points at comparatively large distance from the primary interaction point, and to help the pattern recognition in linking the tracks found in the TPC with tracks found in the vertex detector, and vice versa. In addition the SIT in particular fills the rather large gap between the vertex detector and the TPC, thus helping in the efficient reconstruction of long-lived particles.

With rather small modifications the outer Silicon layer of the SIT could also serve as a photon detector for a TRD (transition radiation detector) setup. The space between the two SIT layers could be filled with a radiator medium. Because of the excellent

resolution of the SIT, the small lever-arm between the radiator and the outer SIT layer is large enough to get a decent resolution and a good electron - pion separation [22].

2.2.1 Technologies

The SIT will consist of two cylinders of double sided silicon strip detectors. The required resolution in rϕ is 10 μm. Such detectors, using a strip pitch of 25 μm and a readout pitch of 50 μm have already been used successfully for example in the microvertex detector of DELPHI [23]. The z measurement of the SIT is mainly needed to improve the track finding efficiency. For this purpose a resolution of 50 μm is largely sufficient [1].

The FTD will consist of pixel detectors in the first three layers and strip detectors in the last four. For the pixel detectors the technology of the ATLAS pixels, with a pixel size of $50 \times 300\,\mu\text{m}^2$ can be used [8]. For the strip layers the requirements are somewhat less stringent than for the SIT. The resolution requirement is 25 μm. This can be reached with a strip pitch of 90 μm and a readout pitch of 270 μm.

2.2.2 Conceptual design

A conceptual layout of a possible mechanical support structure is shown in Fig. 2.2.2. The SIT and FTD will be mounted around the beampipe after the vertex detector is installed. Together with the vertex detector, the SIT and the FTD will form the inner detector, which is mechanically independent of the TPC.

The most challenging part of the SIT design will be to make the whole detector as thin as possible, while at the same time ensuring that it is mechanically very rigid. The most promising solution at the moment is a "space-frame"-like structure as pioneered e.g. by ATLAS [8] or CMS [24]. This structure will support both SIT layers. The SIT support frame is held by two light, composite material cylinders, one on each side, which are used to support the FTD layers 5, 6, and 7. These cylinders themselves are supported by another space-frame like structure from the tungsten-mask tips on either side of the experiment. It is important that the inner detector part is mechanically independent from the TPC vessel, so that the whole TPC can be withdrawn from the detector. Care has to be taken that small movements of the tips of the Tungsten mask, which are expected when the detector is opened, do not transmit undue stresses into these structures.

With a typical width of an individual Silicon detector of around 6 cm, the outer layer of the SIT will consist of approximately 33 detectors in ϕ for the outer layer, and around 17 detectors in ϕ for the inner layer, where it has been assumed that a small overlap of 3 mm between neighbouring detectors is needed. To enable the simple dismounting of the detector it should be split into at least two half shells. Longitudinally the system is split in two halves, each made from six detectors for the inner and ten detectors for the outer layer which are read out together. Since the readout pitch in z can be a factor six larger than in rϕ the number of channels in both coordinates per module is approximately equal, making the routing of the signals much

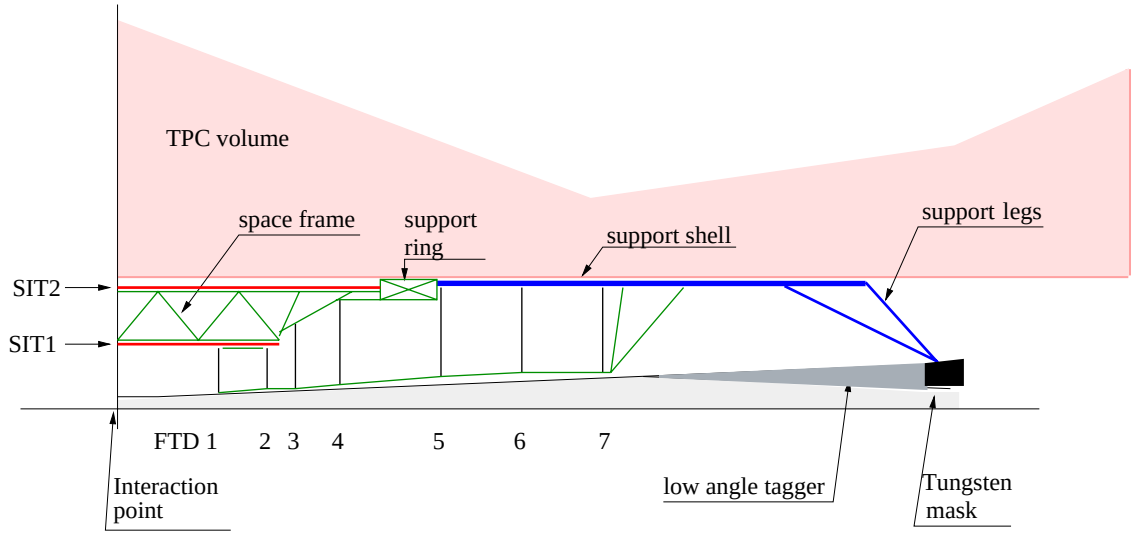

Figure 2.2.2: *Conceptual layout of the SIT and FTD support structure. The space frame and the support ring consist of light e.g. carbon fibre struts. The support shell and the support legs are made from composite materials.*

easier. In a recent measurement it has been shown that the Lorentz angle in silicon causes a broadening of the clusters of $\sim 180\,\mu$m for electrons and $\sim 40\,\mu$m for holes for $300\,\mu$m thick detectors and a magnetic field of 4 T if the strips are parallel to the B-field [25]. Not to be limited by this effect one has to use the p-side of the detectors for the rϕ-measurement and the n-side for z.

In this scheme the read-out electronics will be situated at the very end of the SIT layers, in order to minimise the material in front of the TPC.

The pixel planes of the FTD can be very similar to the ones of ATLAS. In this technology electronic detectors of $\sim 0.5\,\mathrm{cm}^2$ are bonded to a detector chip allowing great flexibility in the layout of the modules. If a chip size of $0.5 \times 1\,\mathrm{cm}^2$ is chosen one pixel layer can be easily subdivided into 24 modules, one of which is shown in Fig. 2.2.3. To make optimal use of the pixel resolution in the first and third layer the pixels are oriented radially, so the the resolution in the rϕ-direction is $50\,\mu\mathrm{m}/\sqrt{12}$ and in the r-direction $300\,\mu\mathrm{m}/\sqrt{12}$ while in the second layer they are oriented tangential, so that the high resolution is in the r-direction and the lower one in rϕ.

The power consumption is about $40\,\mu$W per pixel or $270\,\mathrm{mW/cm}^2$. In the case of ATLAS the cooling is done with C_4F_{10}. The size of the two first FTD discs is basically identical to an ATLAS disc, so that also here 12 tubes should be sufficient. Also the cabling can be basically identical, which means around 70 power cables and 200 readout fibres per disc. The third module is about twice as large, so that these numbers have to be doubled.

To minimise the material the strip discs are preferably built with double sided double metal detectors [23]. A possible module is built of five trapezoidal detectors as shown in Fig. 2.2.4. The outer two detectors are daisy-chained where the p-side of one is

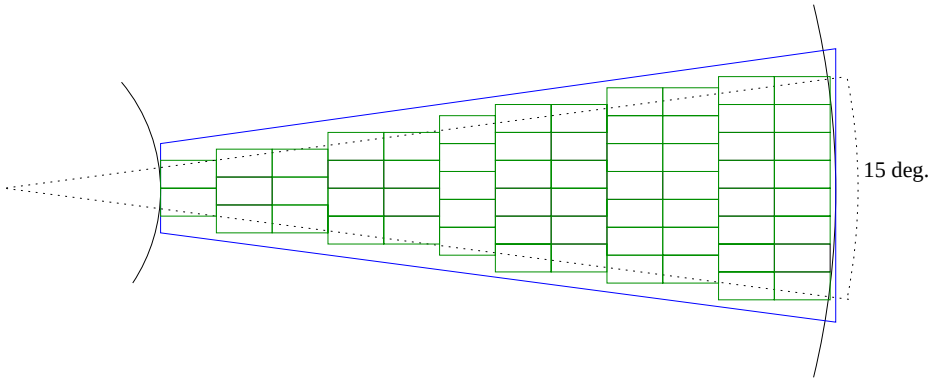

Figure 2.2.3: *Layout of one FTD pixel module. The large trapezoid indicates the detector while the small rectangles are the readout electronics .*

connected to the n-side of the other. This flipping technique was pioneered by DELPHI and allows to resolve the ambiguity between the two modules. The strips measuring the radial coordinate (r-strips) will run parallel to the inner and outer detector boundary, while the ones measuring the azimuthal coordinate (rϕ-strips) are parallel to one of the two side boundaries. The modules are then installed such that every module is flipped with respect to the preceding one, so that the rϕ-strips actually have a small stereo angle. In this way ghost hits, created by several tracks passing one module, will not line up to tracks in the different planes.

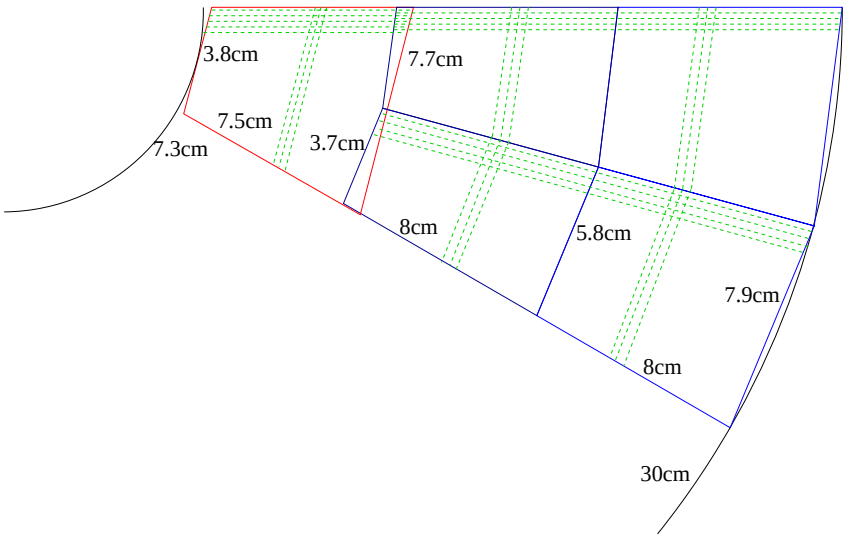

Figure 2.2.4: *Layout of an FTD strip module. The dashed lines indicate the orientation of the strips.*

The material budget as a function of the polar angle up to the end of the SIT/FTD is shown in Fig. 2.2.5. At $\theta = 90°$ the SIT contributes roughly 2.5% of a radiation length while the FTD contributes about 8% in the region where all seven planes are crossed.

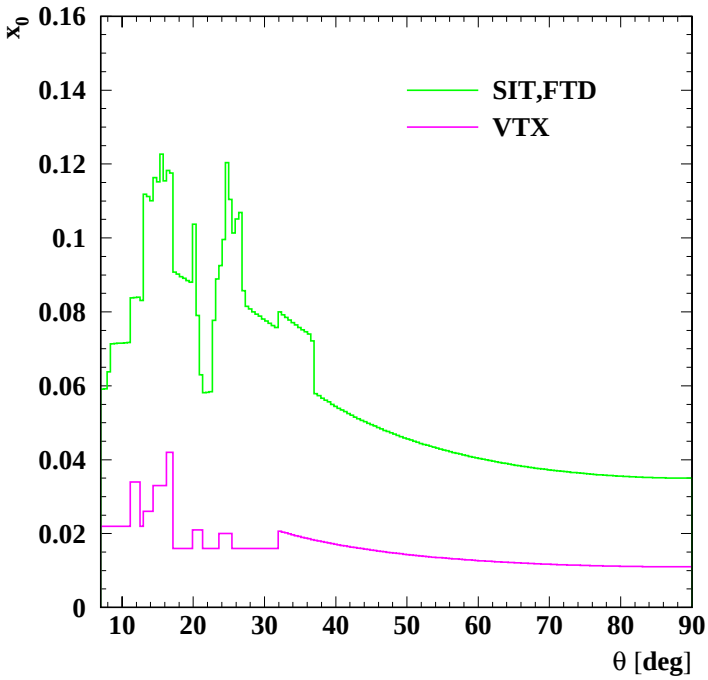

Figure 2.2.5: *Material in units of radiation lengths as a function of the polar angle up to the end of the vertex detector and the SIT/FTD.*

2.2.3 Cost estimate

For the FTD pixels the cost can be extrapolated from ATLAS. For the ATLAS pixels most of the costs is in the modules, so that a simple scaling by area should be sufficient. The total pixel area is $0.56\,\mathrm{m}^2$ yielding a total cost of 2.2 MEUR.

For the FTD strips the total area is about $2\,\mathrm{m}^2$. Due to the relatively large difference between the size of the ATLAS system and the system presented here the extrapolation is somewhat more uncertain. A cost of $50\,\mathrm{EUR/cm}^2$ has been used which is in between the ATLAS estimate and the cost of the present H1 forward silicon tracker. This estimate gives a total cost of 1 MEUR for the FTD strips.

The total area of the SIT is around $1.7\,\mathrm{m}^2$, very similar to the FTD strip area. Therefore the price of around 1 MEUR should also be a reasonable estimate for this part of the detector. A significant addition to the cost will be the support structure, for which no detailed design exists at this point. However, based on the cost estimate

for CMS pixel detector and their silicon tracker [24], which are similar to the proposed space-frame structure, a cost of 0.5 MEUR should be sufficient.

Based on these assumptions the total cost of the combined SIT and FTD system is expected to be around 5 MEUR.

2.3 The Central Tracking Detectors

The central tracking system consists of two gas-filled chambers, a large volume time projection chamber (TPC) [26] and a forward tracking chamber (FCH) located between the TPC endplate and the endcap calorimeter. The motivation for choosing a TPC as central tracker system has been presented at the beginning of Section 2. The TPC has to meet a number of stringent boundary conditions. The system has to be able to operate continuously throughout one TESLA train of 1 ms, which requires a new gating scheme. The amount of dead material in the TPC should be minimised to not compromise the capabilities of the calorimeter. The system has to cope with high backgrounds. The overall performance must be significantly better than for existing TPCs, and systematic effects in the TPC track reconstruction must be kept below the 10 μm level in order to guarantee the overall precision of the tracking measurement.

The TPC will play a central role in both finding and measuring the charged particles. To ensure good solid angle coverage, good track resolution, and simultaneously good determination of the specific energy loss (dE/dx) of particles a large number of points needs to be measured along each track. This dictates that the chamber should be rather large, both radially and longitudinally.

In the forward direction the performance of the TPC degrades because of decreasing lever-arm and reduced number of hits. On the other hand some high cross section processes such as W-pair production peak in this region, and the forward backward asymmetries in fermion pair production, sensitive to new physics such as a Z$'$ or extra dimensions, are largest there. To improve the momentum resolution for tracks in this region the precise FCH was positioned between the TPC and ECAL endcaps.

2.3.1 Conceptual design of the TPC

The concept for the TPC presented here is based on the recent design of the STAR [27, 28] and ALICE [29] TPCs and draws from the large experience collected at LEP experiments [30, 31, 32]. The requirements for the TPC at TESLA are slightly different from those at STAR or ALICE. The total number of tracks per event is comparatively small, but the time between bunch crossings is short, so that events from many bunch crossings are superimposed in one TPC "picture". The TPC also has to be sensitive for many consecutive "pictures". The timing information from the TPC has to be sufficiently precise to disentangle events from different bunch crossings. In addition it is important that the amount of material introduced by the TPC is as small as possible. Therefore the emphasis of the concept has been in the area of new readout systems, the minimisation of the amount of material in the endcap of the chamber, and the gating

scheme, to enable continuous TPC operation throughout one train.

The overall layout of the central tracking system can be seen in the cross section view of the detector in Fig. 2.3.1, and the main mechanical parameters are listed in Table 2.3.1. The inner radius is given by the size of the mask system (see Chapter 7),

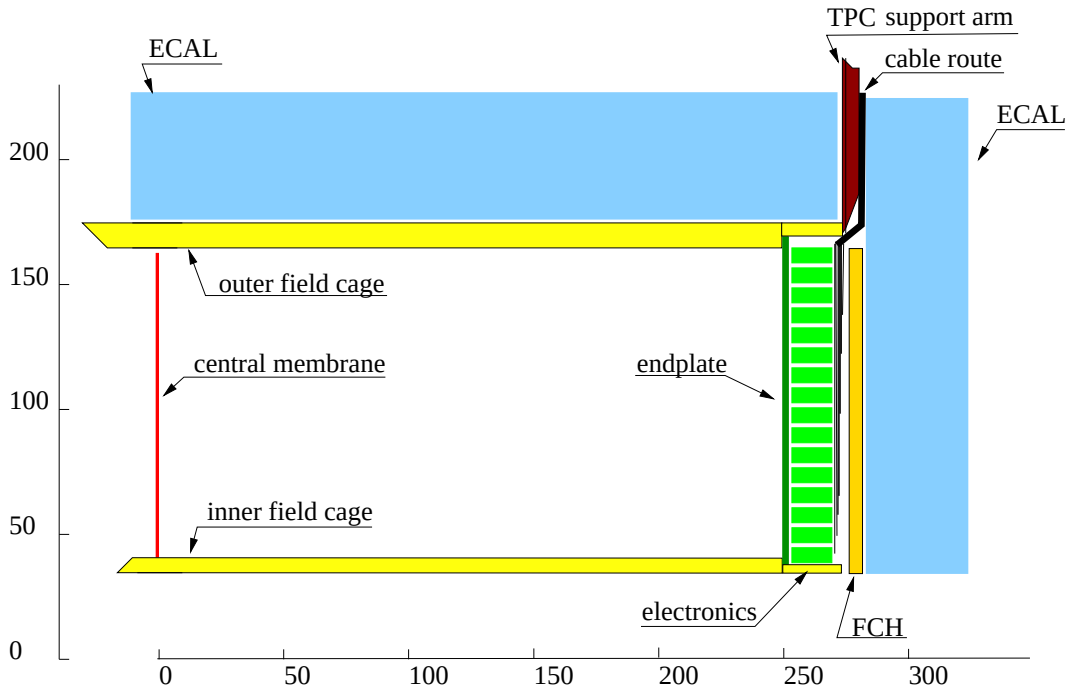

Figure 2.3.1: *General layout of one quarter of the central tracking.*

which extends to inside the TPC bore and which in turn is given by the dimensions of the final focus quadrupoles. The outer radius comes from the requirement that the calorimeters fit inside the coil and that the desired momentum resolution of $\delta p_t/{p_t}^2 < 2 \cdot 10^{-4}(\mathrm{GeV/c})^{-1}$ (TPC only) and a dE/dx resolution of $< 5\%$ be reached. The design of the TPC, while demanding better performance than has been achieved previously, however represents a reasonable extrapolation of existing technology.

2.3.1.1 Gas

The choice of the gas impacts many areas of the TPC design. It influences not only the performance, but different gases may also require different electrical designs of the field cage, the endcap and the readout electronics. The choice also depends on a number of external boundary conditions, in particular on the level of background expected. At the same time the gas should be easy to use, should be stable and insensitive to small impurities.

The gas which at the moment is considered a good candidate is a three component mixture of Ar-CO_2-CH_4 (93-2-5)%. A rather comprehensive summary of the properties

TPC	
Mechanical radii	320 mm inner, 1700 mm outer
Overall length	2×2730 mm
Radii of sensitive volume	362 mm inner, 1618 mm outer
Length of sensitive volume	2×2500mm
Weight	~ 4 t
Gas volume	38 m^3
Radiation length	~ 0.03 X_0 to outer field cage

Table 2.3.1: *List of main mechanical parameters of the TPC.*

of this and many other gas mixtures may be found in [33, 34]. This gas mixture has an acceptable drift field of 230 V/cm for a drift velocity of 4.6 cm/μs, thus limiting the total voltage at the cathode to around 60 kV, while the time to completely empty the drift volume is around 55 μs, or 160 bunch crossings in TESLA. The diffusion coefficient for this mixture is $D_{L(T)} = 300\,(70)\,\mu\mathrm{m}/\sqrt{\mathrm{cm}}$ at a magnetic field of 4 T. This results, as will be discussed in more detail in section 2.3.3, in an average spatial resolution of 150μm in the transverse direction, and in the possibility to use moderately small pad sizes in the readout with a width between 1 and 2 mm. Better resolutions around 100 μm can be achieved, with the same readout structure, if a gas like $(90-10)\%$ Ar-CH_4 is used, which has a smaller diffusion coefficient.

One advantage of using a three component mixture is that the neutron cross section can be smaller than for a two component mixture based solely on hydrocarbons as quenchers (18 barn for this mixture vs 34 barn for Ar-CH_4 (90-10)%), thus reducing the number of spurious hits in the TPC from neutron background (see Chapter 7). The aging properties for gases with small hydrocarbon concentrations are also better than for those with large ones [35], though at the levels of backgrounds expected at TESLA this is not expected to be of major concern. Quenching properties of this gas mixtures are acceptable, though not as good as for pure Ar-CH_4 mixtures (see for example [35]).

2.3.1.2 Readout technologies

The electrons, produced by ionisation of the TPC gas when a charged particle traverses the TPC volume, will drift under the electric field (applied parallel to the magnetic field) to the end plates.

In conventional TPCs the number of drifting electrons is amplified by avalanche multiplication in high electric fields generated near thin wires, and the signals are read out with a system of pads. The wires are arranged in planes at the end of the TPC drift volume, and neighbouring wires are typically a few mm apart. Close to the wires the electric field is no longer parallel to the magnetic field, and electrons drifting in this region experience a significant transverse movement. In a strong magnetic field this can result in a broadening of the electron cloud and worsening of the resolution. Thus the wires define a preferred direction along which also the separation of close-by hits

depends on the projected angle between track and wires [30]. In addition the width of the signal induced on the pads depends on the so-called "pad response function" (given by pad-to-wire distance and pad size), which is generally a few times broader than the cloud of arriving electrons and limits the overall granularity of the TPC.

An attractive alternative to a wire chamber readout is based on recently developed gas avalanche micro detectors such as Gas Electron Multipliers (GEM)[36] or Micromegas [37]. Here the amplification elements themselves are only of the order of $100\,\mu$m apart, limiting the transverse movement of the cloud of electrons due to the $\vec{E} \times \vec{B}$ effect to $\mathcal{O}(50\mu\text{m})$. Also these systems do not have a preferred direction, so that the intrinsic resolution and double hit separation is expected to be more uniform. Together a reduction of the systematic effects from this by about one order of magnitude can be expected.

One problem which any TPC has to face is that the positive ions produced during the avalanche multiplication will migrate back into the drift region and, if not removed, distort the electric field. Most gas avalanche micro detectors show a natural suppression of this so-called ion feedback, thus reducing the size of the problem. However an additional gating system can be employed to reduce the ion feedback to near zero.

GEM

One well studied type of gas avalanche micro detector is the Gas Electron Multiplier, GEM. GEMs were developed at CERN [36] and are currently used in a number of experiments [38, 39]. A GEM consists of a thin polymer foil, metal coated on both

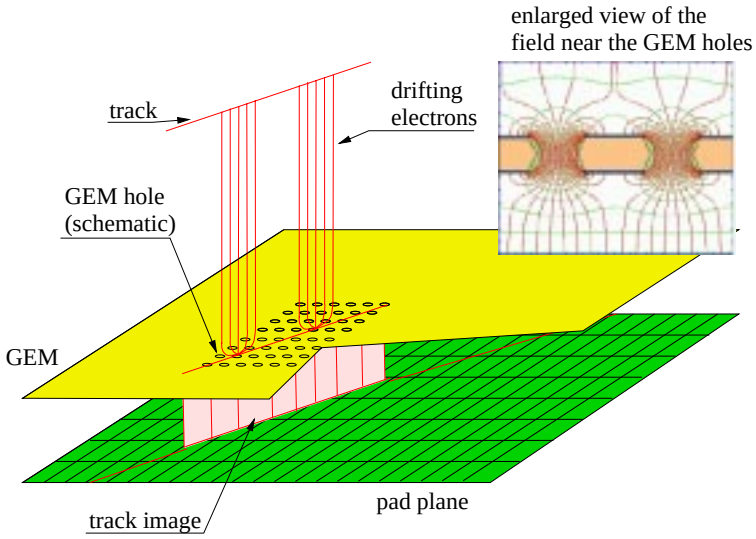

Figure 2.3.2: *Sketch of the GEM principle (not to scale: distance between holes is $\mathcal{O}(0.1)$ mm, pad size is $\mathcal{O}(1-5)$ mm). Electric field map near the GEM holes shown in the small inset taken from [40].*

sides, and perforated by a high density of small holes, typically $\mathcal{O}(100\,\mu\text{m})$ apart. An

appropriate potential difference between the two conducting sides generates a strong field, typically 80 kV/cm, in the small holes where avalanche amplification of the drifting electrons occurs. Nearly all electrons drifting to the GEM from the TPC volume are funnelled into these holes, amplified and transferred by the electric field to the readout electrodes. A schematic view of a GEM and how it could be used in a TPC is shown in Fig. 2.3.2.

Gains of up to a few times 10^3 have been achieved with a single GEM. It is often advantageous to cascade two GEMs to obtain a higher gain at lower operating voltages and have more stable operating conditions. The performance of such a system [41] is shown in Fig. 2.3.3.

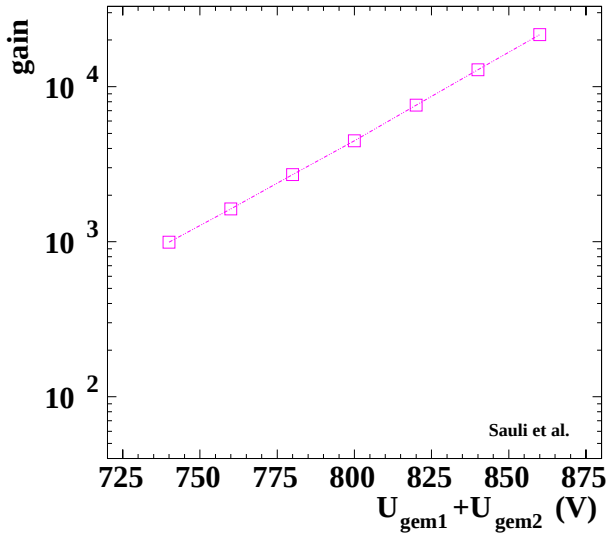

Figure 2.3.3: *Gain in a two-GEM structure [41].*

The charge produced in the avalanche in the GEMs is collected by readout pads located typically 1-5 mm behind the last GEM. Since for practical reasons the number of pads is limited, the distance between pad centres (for example 2 mm) is large compared to the size of the electron avalanche (typically a few to several 100 μm). The charge from a track after amplification in the GEMs is therefore sometimes collected on a single rectangular pad. In this case the expected point resolution is around $2\,\mathrm{mm}/\sqrt{12}$.

With a conventional wire chamber readout the signals induced on neighbouring pads are used to significantly improve this resolution, by averaging the signals. In a GEM based readout system only very small induced signals are present on neighbouring pads, which, in addition, are significantly shorter than the direct signals. Recent R&D [42, 43] has shown that nevertheless these induced signals can be measured and used to obtain very good spatial resolution.

Without the induction signal good spatial resolution can be achieved by using narrow pads or specially shaped pads, e.g. either as diamonds or "chevrons" (see Fig 2.3.4 a). Simulations have shown that with chevron pads of overall size of 2×6 mm^2 spatial resolutions around 150 μm in a three component mixture as Ar-CH_4-CO_2 are

possible with only small dependence on drift length [44]. This is shown in Fig. 2.3.4 b) for a simulation study.

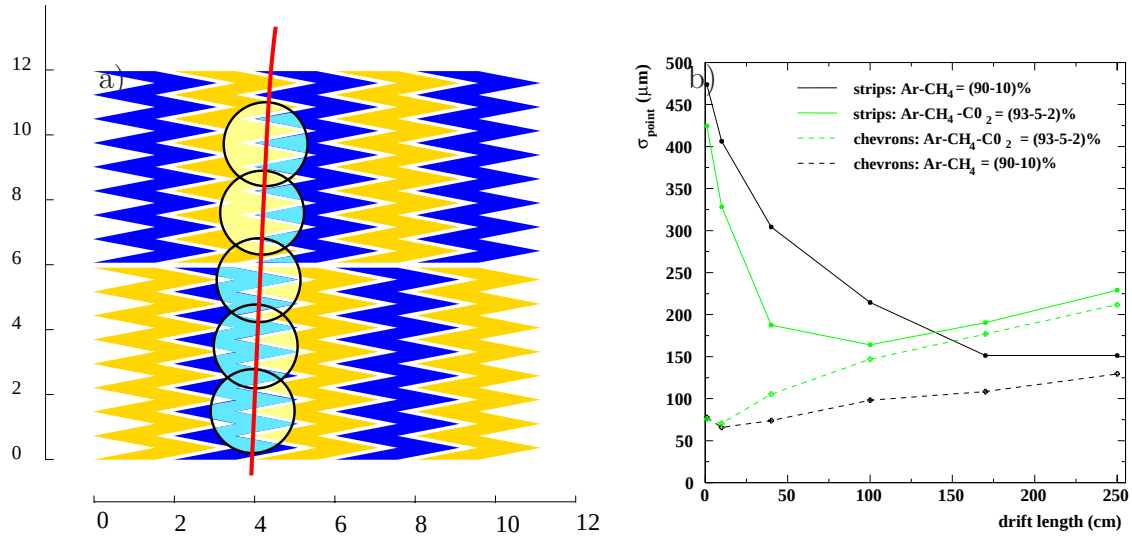

Figure 2.3.4: *a) Layout of the "Chevron" shaped pads, with a track superimposed to illustrate the sharing of charge between different pads. The circles indicate a typical size of the charge cloud arriving on the pads. Dimensions are in mm. b) Simulated resolution in* $r - \phi$ *as a function of the drift length in the TPC, for different pad geometries and two gas mixtures (Ar:*CH_4*=(90-10) % and Ar-*CH_4*-*$C0_2$*=(93-5-2) %) for minimum ionising particles [44].*

Micromegas

An alternative technology to GEMs is that of Micromegas [37]. A uniform high-field is produced between a thin metallic mesh stretched at a distance of $50 - 100\,\mu$m above the readout pad-plane and held by dielectric supports. With a very high field across the gap, typically 30 kV/cm, electrons arriving from the TPC drift volume are collected and multiplied in the gap. Regularly spaced supports ensure that the gap is uniform, at the expense of small localised loss of efficiency. Gains in excess of 10^4 have been obtained with such structures [40].

A micromegas has similar advantages to a GEM as far as simplicity of construction, low cost and efficiency of ion collection are concerned. It has an excellent potential for dE/dx resolution due to the fact that the gain is independent of the gap thickness to first order. Moreover it is robust and can be built at least in part using commercially available components. In Fig. 2.3.5 a) schematic view of a Micromegas is shown.

A Micromegas can be used as a readout chamber in a TPC readout in a fashion similar to the one described above for the GEM, with the same advantages. As in a GEM the spatial resolution can be improved by using chevron shaped pads. The

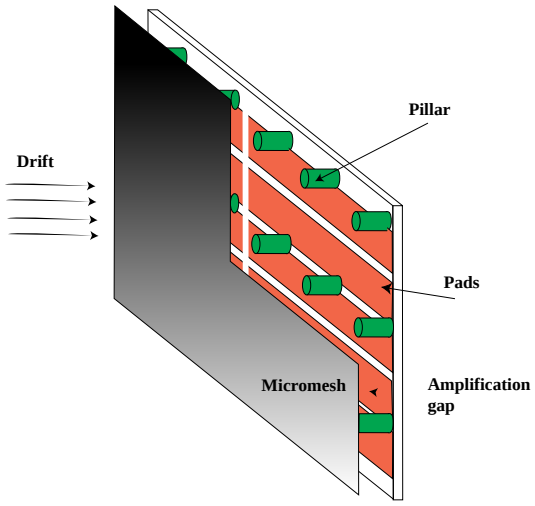

Figure 2.3.5: *Schematic layout of a Micromegas.*

induction signal on neighbouring pads would probably be too small to be usable since the gas-gain region is even closer to the pads than it is for the GEM solution.

Wire chamber readout

The wire chamber version was already presented in the Conceptual Design Report [45, 46]. This is considered as a back-up in case unforeseen difficulties arise with the new technologies described above.

To summarise briefly, the chambers were arranged in two rings, with a total of 36 sectors, where the cracks between the inner modules are such as to not point to the vertex. The characteristics are listed in Table 2.3.2.

2.3.1.3 Field cage design

With the gases considered the field cage should be able to withstand electric potentials of up to 100 kV, while at the same time introduce only little material into the detector. A cross section of a conceptual design of the inner and outer field cage is shown in Fig. 2.3.6. Drawing from experience gained at LEP [47] and recent developments for the STAR [27] and ALICE experiments [29] the inner and the outer wall are made of a very light, composite structure. The field gradient is generated by a set of Al potential strips on a 50 μm thick Mylar foil followed by a second set of Al strips shifted relative to the first set by half a period. A layer built up of 20 Mylar foils each 75 μm thick, shields the field gradient present in the material of the wall effectively from the TPC drift volume. Mechanical rigidity is achieved by a sandwich structure built up of two layers of high-tensile strength material impregnated with epoxy (prepreg) and a roughly 70 mm (40 mm for the inner fieldcage) thick layer of closed cell structural foam such as Rohacell. On the inside of the inner cylinder another layer of pre-preg completes the structure. On the outside an approximately 10 mm thick composite structure of prepreg - Nomex - honeycomb - prepreg provides high mechanical strength

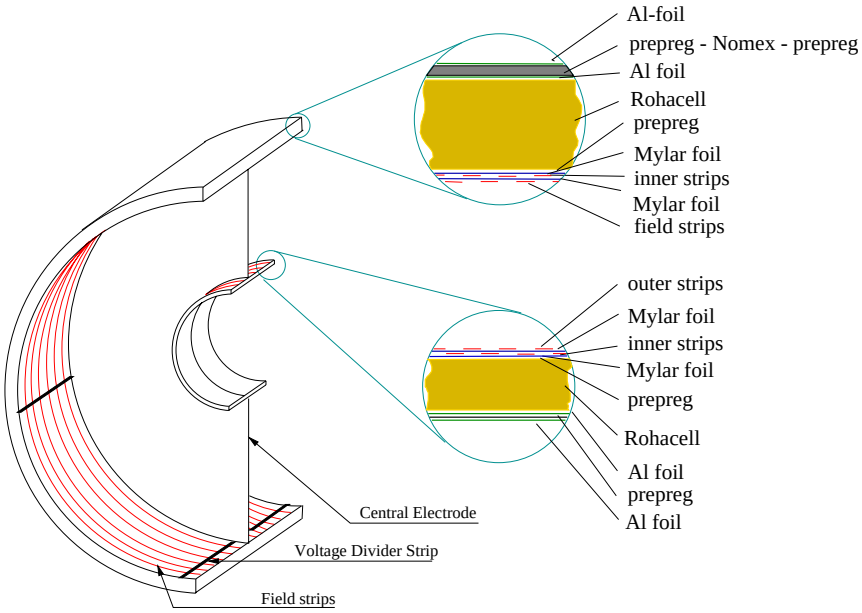

Figure 2.3.6: *3-D view of the TPC (not to scale). The inner and the outer fieldcage are illustrated in the small insets.*

and rigidity to the system. Electrically both the inside of the inner and outside of the outer cylinder are covered completely with a thin (50 μm) grounded Al-foil.

The thickness of both fieldcages together at 90° is approximately 3% of a radiation length (see Table 2.3.3). R&D will be needed to make sure that the proposed structure can operate at potentials of up to 100 kV at the cathode.

Number of sectors	36
Number of sense wires	24000
Sense grid	20 μm W-Rh wires, 2 mm pitch, distance to pad plane: 1 mm, width of pad response function: 1.4 mm, σ_{point} = 0.16 mm for 0° crossing.
Number of pad rows	64 + 54 (outer and inner sectors)
Number of pads	506k + 214k (outer and inner)
Cathode grid	76 μm Cu-Be wires, 1 mm pitch, distance to pad plane = 2 mm.
Gating grid	76 μm Cu-Be wires, 2 mm pitch, distance to pad plane $\simeq$ 20 mm.

Table 2.3.2: *Main parameters of the CDR wire-chamber readout solution for the TPC (from [45, 46]).*

Material	inner FC μm	inner FC % X_0	outer FC μm	outer FC % X_0
Aluminium	50	0.056	50	0.056
Prepeg	200	0.103	200	0.103
Nomex-Honeycomb	–	–	10000	0.070
Prepeg	–	–	200	0.103
Aluminium	50	0.056	50	0.056
Rohacell	40000	0.320	70000	0.561
Prepeg	200	0.103	200	0.103
Mylar	20×75	0.520	20×75	0.520
Aluminium	50	0.056	50	0.056
Mylar	50	0.017	50	0.017
Aluminium	50	0.056	50	0.056
Sum		1.3		1.7

Table 2.3.3: *Material budget for the TPC field cage.*

2.3.1.4 Endplate design

The end plate of the TPC has to support the readout modules and the electronics, and to seal the gas in the TPC volume. The design proposed is a very modular one. It is based on the experience of the ALEPH experiment, where the possibility to selectively remove parts of the end plate, both for repair of the end plate itself and for access to the field cage, has proven to be extremely useful [47].

To match the TPC segmentation to that of the electromagnetic calorimeter, an eight-fold symmetry in ϕ has been adopted. One possible layout of the end plate geometry is shown in Fig. 2.3.7 a). The end plate is separated into eight approximately wedge-shaped sectors. Boundaries between sectors are straight so that gas-sealing and handling will be easier. The boundaries are non-pointing to the primary interaction point, to obviate the need for complicated geometries.

The gas amplification modules within one sector will be arranged according to sizes of GEMs or Micromegas available when the detector is built. Each of the eight sectors supports the GEM or Micromegas modules on the inside, the pad plane, and the readout electronics on the outside. The sector is attached to a frame and has a system of stiffening ribs to ensure its mechanical rigidity. It connects mechanically the outer and the inner field-cage cylinders, as indicated symbolically in Fig. 2.3.7 b). The frame must be designed to make the gas seal for the TPC volume. In case of failure of a GEM or Micromegas module, the sector can be removed using a special handling tool. The readout pads are etched into a printed circuit board which is the size of the sector. This will be a multilayer board which routes the pad signals to the readout electronics.

In Fig. 2.3.8 a conceptual design of one GEM module is shown. It is based on a technology developed at CERN for the COMPASS [39, 48] experiment. The GEMs are mounted on a fiberglass frame, which is glued to the top and the bottom GEM. A

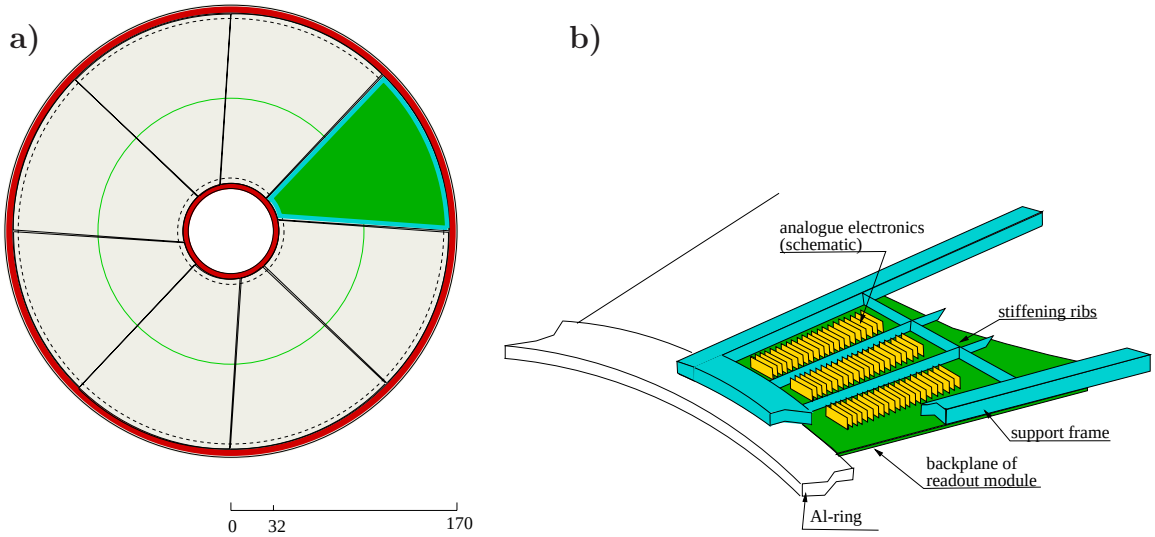

Figure 2.3.7: *a) One possible layout of the TPC end plate for GEMs or Micromegas. On sector is shown with the mechanical frame. The length scale is in cm. b) Perspective view of one sector mounted on the TPC vessel. The drawing is not to scale.*

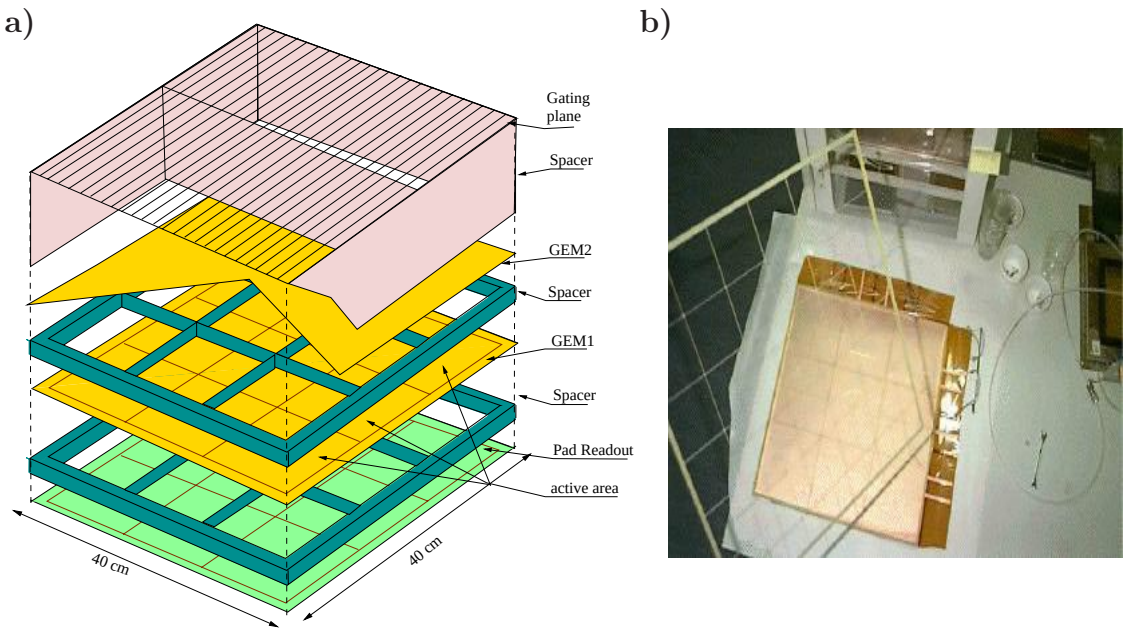

Figure 2.3.8: *a) Exploded view of one GEM "tower" to show the individual components. b) Photograph of a prototype module built for the COMPASS experiment illustrating the use of the spacer frame to separate the two GEMs [48].*

second frame is glued to the inner GEM (labelled GEM 1 in the figure) and is used to position the tower on the readout board. To enable a fast exchange of a single GEM tower on a readout board, each tower is bolted to the board with four plastic screws located in the corners of the tower. On the side of the GEM tower facing the drift volume a very light structure is glued to the GEM which may support a third GEM at approximately 2 cm distance. This gating GEM may be used to suppress ions drifting back into the gas volume of the TPC.

An alternative solution to the end plate layout sketched above would be to follow the proven strategy of ALEPH, STAR or ALICE, and to separate the end plate into smaller, independent sectors by another division in radius between the inner and outer field cages. In this scenario a separate frame connects the inner and outer field cages and guarantees the gas seal of each sector. This solution has the advantage that smaller sectors have to be handled, and that the gas seal is simpler. The disadvantage is that most likely more material will be present in the end plate, and that the dead-space between sectors will be larger.

Gating scheme

As has been discussed above the positive ions produced in the avalanche will migrate back into the drift volume, and distort the fields, if they are not removed. Using GEMs or Micromegas will reduce the problem due to the natural suppression of the ion feedback [41]. In Fig. 2.3.9 the measured ion feedback is plotted as a function of the drift voltage applied. Using a double GEM structure a suppression to around 2% of the original amount of charge is expected.

A further suppression can be realised with a gating plane in front of the amplification structure. This plane can be used as a gate to change from near total transparency for electrons to total opacity for the positive ions produced by the gas avalanche. If it is constructed from a GEM itself, this can be achieved quite simply by switching the voltage across the GEM by about 50 volts. Since the drift velocity of the ions is approximately a factor 10^{-4} smaller than the electron drift velocity, the ions will drift throughout one full train only about 1 cm. If this gate as seen in Fig. 2.3.8 is placed approximately 2 cm from the amplification region and is switched to ion-opacity during the time between TESLA trains, it will absorb all the positive ions produced during the 1 ms TESLA bunch train and eliminate positive ion build up in the TPC volume.

An irreducible source of charge in the drift volume is from primary ionisation. During one bunch train the volume of the TPC will be filled with positive ions from the primary ionisation. Due to the much smaller drift velocity of the ions it will take approx. 500 ms to empty the TPC volume completely of these ions, so that on average for a train frequency of 5 Hz the charge from 2.5 trains is accumulated in the TPC volume. For the levels of background expected this corresponds to roughly 50 ions/cm^3, which is similar to what is expected for the STAR experiment [28], and should not present any problem to the operation of the TPC.

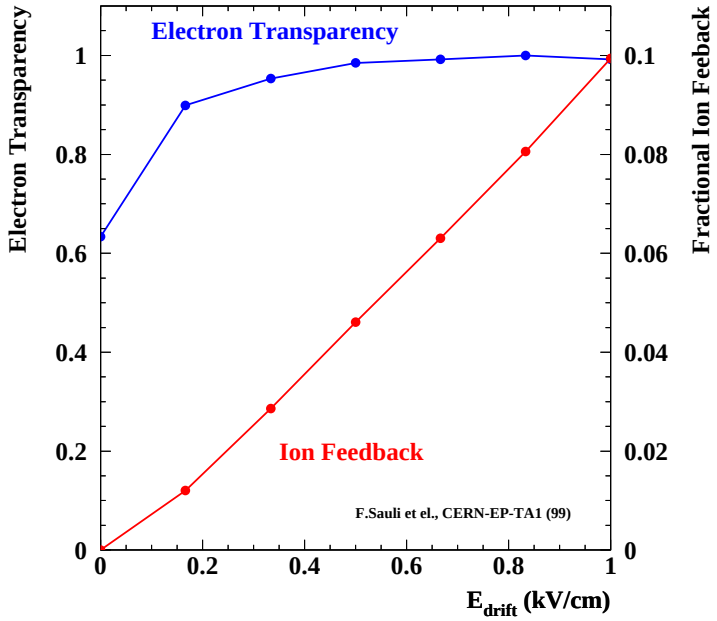

Figure 2.3.9: *Measured ion-feedback and electron transparency in a double GEM structure as a function of the drift field [41].*

2.3.1.5 Readout and electronics

The readout electronics has to meet a number of stringent constraints. The longitudinal diffusion in a 4 T field in the three-component gas is around $300\,\mu\mathrm{m}/\sqrt{\mathrm{cm}}$, or around 3 mm for an average drift distance of 1 m. In order to make sure that the two track resolution is limited by the gas diffusion rather than by the sampling speed of the electronics the TPC signals should be digitised with at least 20 MHz. The system has to be able to accumulate data for the full 1 ms of one TESLA train. At the same time the electronics should be very compact, with all analogue components and the digitisation module mounted directly on the chamber end-plate, to minimise the number of cables needed to read out the full system.

Two different approaches are possible.

- If only the total charge collected is to be measured, a charge amplifying electronics as developed e.g. for the STAR experiment[27, 28] is suitable. Such electronics has been realised in high density packages, with low power consumption of 60 mW/channel, which can be reduced further as explained below.

- If the induction pulse should be measured in addition, a faster electronics, sampling of order 100 MHz, is needed with 8 bit resolution. Such systems are available on small scales [49], but do not yet exist in highly integrated and inexpensive packages suitable for a large scale application. Development of such an option has started.

Since extensive development is needed before the readout of the induction signal can be used in large scale experiments, the conventional measurement of the total charge will be discussed as the base-line option in the following.

To limit the number of electronics channels, large pads are preferred. As explained above in Section 2.3.1.2, chevron pads with a width of 2 mm are found to be sufficient [44] to achieve an average spatial resolution of around 150 μm. To meet the goal that the momentum resolution in the TPC alone be better than $2 \cdot 10^{-4}$, at least 100 space points are needed, however an optimal dE/dx resolution requires more points. Simulations have shown that for realistic conditions about 200 pads rows are optimal [34, 50]. This results in a final pad size of $2 \times 6\,\mathrm{mm}^2$, or 0.6 million pads per TPC readout side. Then a dE/dx resolution of 4.3 % is attained and $\delta(1/\mathrm{p_t})$ is $\simeq 1.5 \times 10^{-4}\,\mathrm{GeV/c}^{-1}$, where in both cases systematic effects are not included.

The analogue frontend consists of a fast, high bandwidth pre-amplifier, and a digitization part. Two approaches are under investigation. Following the example of STAR, the analogue signals for one full train are stored in an anlogue pipeline, before they are digitised with a relatively modest number of FADCs. The recognition of a charge cluster signal on a pad triggers a switched capacitor array chip to store the content of this pad. If needed the immediate neighbours can also be included. If only the central pad is used, up to 1024 time buckets can be stored, together with a time stamp per bucket. The clusters would be digitised with 9-bit FADCs in roughly 10 ms, well within the time between two trains.

An alternative approach would be to equip each channel with a low-cost 20 MHz FADC, and to do the pulse handling, zero suppresion and pipelining of the data digitially. In this case a two-stage pipelining scheme can be envisioned, where the memory per pad is kept to a minimum, to save space and power, and where data from groups of pads are stored together in a larger buffer memory unit, before being transmitted to the outside DAQ.

Assuming a total occupancy of the TPC including background of around 1% (see Chapter 7) the total data volume to be moved is below 500 MB/s per side. If the readout system is split along sectors and each sector is read out individually, data rates around 60 MB/s are expected per readout module. These data rates are well within that available today using commercial electronic components.

One of the major challenges will be to design the readout electronics for 0.6 million pads per TPC side and, at the same time, keep the end plate reasonably thin. This corresponds to an electronic packing density of $\sim$ 10 times that of STAR [27, 28], which was at the maximum when it was designed eight years ago. However with the advances in technology (e.g. 0.3 μm or smaller printed-circuit traces now compared with 1.2 μm then) and expected further developments in this field, the factor of eight to ten appears possible but is definitely a challenge.

Another important consideration is the cooling. A typical power consumption per channel, which seems easily achievable in the near future, might be around 30 mW. The pulse-train structure of TESLA however lends itself to a pulsed operation of the power, which would result in a power reduction, by at least a factor of 10. With 0.6 million channels per side, this results in a power of $\approx$ 2 kW per side, including additional

power consumed by the readout and multiplexing electronics. This amount of cooling has been solved in existing experiments.

2.3.1.6 Calibration

One of the main differences of this TPC compared to existing ones is that the anticipated performance is significantly improved (10 × better than existing TPCs). This requires that the chamber be extremely well calibrated and that the degree of calibration be constantly monitored.

Following the experience at LEP one of the main tools for the calibration will be the data themselves. Events recorded at special runs at center-of-mass energies at the Z-mass will give excellent handles on many calibration constants. In particular the spatial alignment of the endplates against each other and the local distortions must be determined from such data to better than $10\,\mu$m (3 × better than at LEP), which is another challenge. Similarly the TPC will be aligned relative to the other subdetectors using these events [51].

Of importance for a uniformly excellent momentum resolution is the exact knowledge of the $\vec{E}$ and $\vec{B}$ field and of possible local field distortions. As pointed out in Section 4, the field will have to be homogeneous and mapped to an accuracy of 10^{-3} in order to ensure a momentum resolution of $1.5 \cdot 10^{-4}\,(\mathrm{GeV/c})^{-1}$ for the TPC alone. The stability of the calibration will be monitored by analyzing events of the type $\mathrm{Z} \rightarrow \mu^+\mu^-$.

The monitoring of the drift–velocity in the TPC is another very important point. Several methods exist for this. Tracks which cross the central cathode can be used to directly measure the drift velocity, based on the known drift distance from the cathode to the readout modules. To monitor the drift velocity throughout a run, one can use beam-gas events which produce tracks crossing the central membrane. For the primary calibration where a large number of events are needed, it might be conceivable to do a dedicated calibration run where the primary vertex has been shifted by a few mm, thus allowing stiff 45 GeV/c muons to cross the cathode. Once the inner Si-detectors are well calibrated, tracks extrapolated from the Si detectors into the TPC can also be used to calibrate the TPC and to determine the drift velocity, a method effectively used at LEP.

An alternative solution which is possible for the calibration of the drift velocity might be a system of UV-laser beams, inserted into the TPC volume. Such system is being used at STAR [28] and a similar one proposed for the ALICE TPC [29].

2.3.2 Conceptual design of the forward chambers

The forward chambers (FCH) are implemented as straw-tubes similar to the ones developed for the ATLAS experiment [52]. The FCH extends radially from the inner radius of the TPC to just below the outer radius of the TPC field cage and is approximately 6 cm thick. The system consists of 6 planes of straw-chambers, with each plane built up from two layers of straws which are shifted with respect to each other by one half of the distance between neighbouring wires, in order to help resolving the track

ambiguities. Each tube has a diameter of 5 mm. Table 2.3.4 lists some of the mechanical parameters. As shown in Fig 2.3.10, the six double planes are arranged with three

FCH	
Technology	Straw tubes with 5 mm diameter
Radii	320 mm inner, 1600 mm outer
number of samples	12 in three planes
Depth	z = ±(2730 to 2800) mm

Table 2.3.4: *List of the main mechanical parameters of the FCH.*

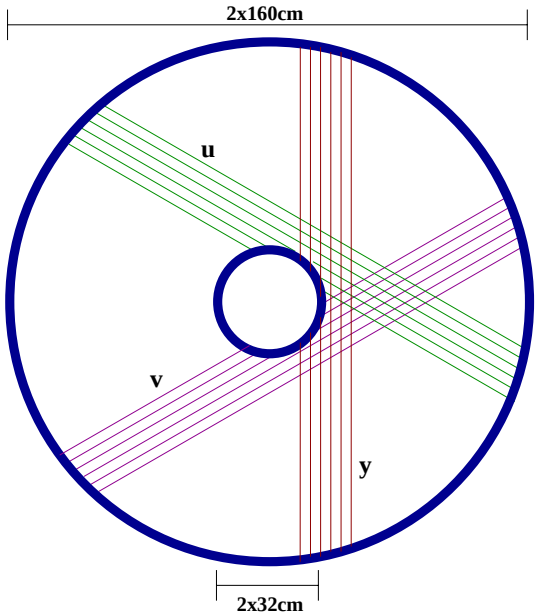

Figure 2.3.10: *Orientation of the FCH wires.*

different wire orientations $yuvyuv$, where the u, v coordinates are rotated with respect to y by $\pm 60°$. There will be about 10^4 electronic channels, and the resolution per plane will be about $100\,\mu$m.

The measurement of three different coordinates enables a stand-alone pattern recognition even with a high hit multiplicity. The twofold repetition allows for a crude measurement of the track direction which is very helpful in the combination of the track element with the rest of the detector.

The chamber is mounted on the surface of the ECAL. Since each wire has at least one end at the outer radius all services can reach the chamber from the outside. Also having the chamber radius slightly smaller than the TPC the front-end electronics

can be housed in the empty space between the TPC and the ECAL. ATLAS reaches a single plane resolution of $100-120\,\mu$m per plane, which is sufficient to get an equivalent point resolution of $50\,\mu$m for the full chamber. For this a very fast gas mixture is used ($Xe - CF_4 - CO_2$), resulting in a maximum drift time of less than 50 ns. Gases slower by a factor of 2 would still allow the unique identification of a bunch in TESLA, while improving the FCH resolution.

2.3.3 Performance studies

The central tracker has been simulated in a GEANT based Monte Carlo program [53] to evaluate its performance. The expected $r-\phi$ resolution has already been discussed in section 2.3.1.2 and is shown in figure 2.3.4 b). From the charge measurement in the TPC the specific energy loss, dE/dx, of particles traversing the TPC can be determined. With 200 measured points on a track and for the gas mixture considered the separation power between pions and kaons expected from the simulation is presented in Fig. 2.3.11 [50]. The expected resolution figures are summarised in Table 2.3.5.

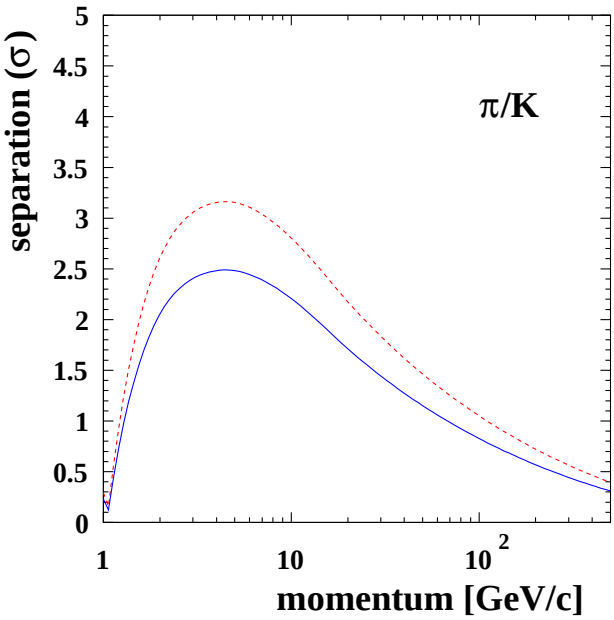

Figure 2.3.11: *Simulated separation power between pions and kaons as a function of the momentum of the particles [50]. An error of* $0.2-0.3\%$ *due to calibration was assumed in this figure. The top curve is for isolated tracks, the bottom one for tracks inside hadronic jets.*

The resolution in z measured in a test TPC equipped with a double GEM readout structure is shown in Fig. 2.3.12 [54]. The gain determined in this TPC (gas mixture $Ar - CH_4 - CO_2$ $(93-5-2)\%$) and its stability as a function across the GEM is

	Drift distance	
	10 cm	200 cm
r-ϕ –resolution	70 μm	190 μm
z –resolution	0.6 mm	1 mm
double pulse resolution in r-ϕ	$\leq$ 2.3 mm	
double pulse resolution in z	$\leq$ 10 mm	
dE/dx resolution	4.3% for 200 pad rows	
$\pi-$K separation	$> 2\sigma$ between 2 and 20 GeV/c	
momentum resolution ($\lvert\cos\theta\rvert < 0.75$)	1.4×10^{-4} (GeV/c)$^{-1}$	
momentum resolution ($\lvert\cos\theta\rvert \approx 0.90$)	3.2×10^{-4} (GeV/c)$^{-1}$	

Table 2.3.5: *Summary of key performance figures of the central tracker from a full simulation.*

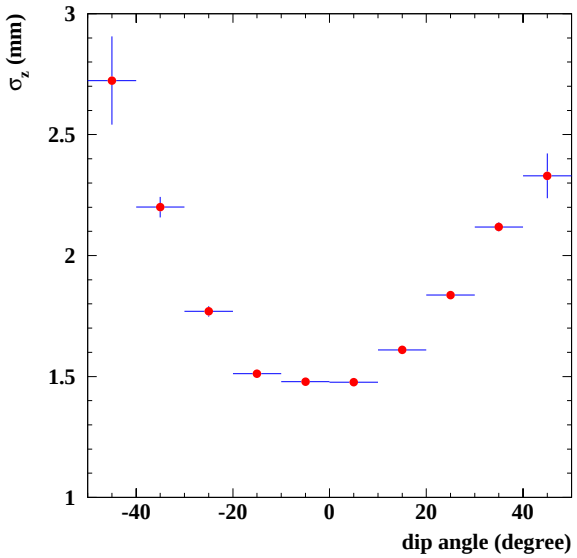

Figure 2.3.12: *z-resolution measured in a GEM equipped TPC prototype [54].*

shown in Fig. 2.3.13 [54]. Stable and reliable operation has been achieved. Different from Fig. 2.3.3 the TPC has been operated at a drift field of around 180 V/cm and low electric fields in the gaps between the GEMs and the readout plane, with a resulting reduction in gain.

First results from trying to utilise the induction signals [43] are shown in Fig. 2.3.14. The single hit resolution can be substantially improved if the induced signals on neighbouring pads are read out and included in the point-measuring algorithm. Resolutions well below 100 μm seem feasible if the readout electronics [49] can be developed for a large-scale system.

In summary all results available at the moment point in the direction that a TPC read out with gas avalanche micro detectors can be built and operated, and presents a valid option for a large chamber as needed at TESLA.

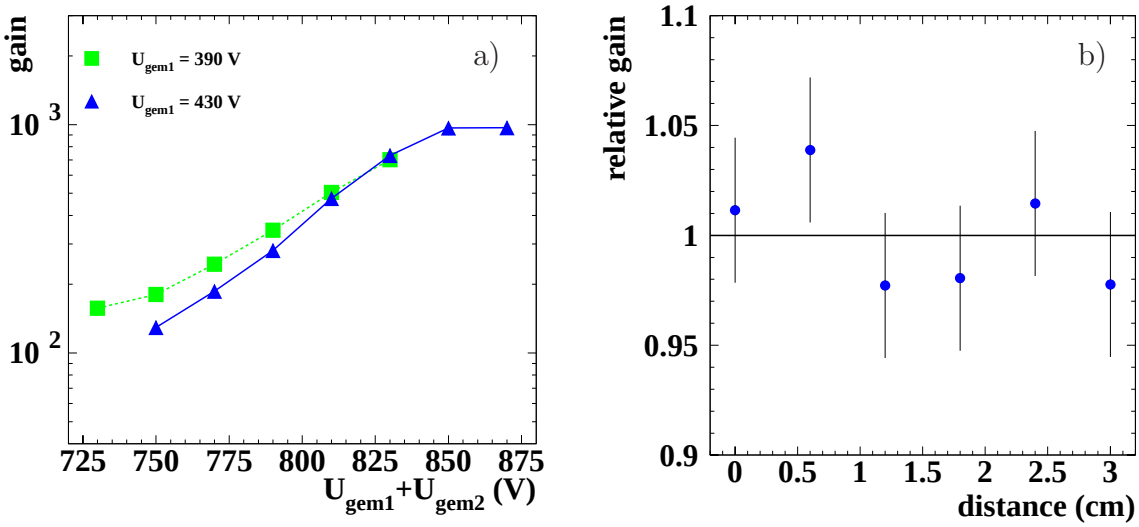

Figure 2.3.13: *a) Gain in a two-GEM TPC prototype structure measured as a function of the different potentials applied. b) Gain measured as a function of position across a GEM over a distance of 3 cm. Errors include systematic effects. No attempt has been made to equalise the response through a pad-calibration. The gas used for both plots [54] was a Ar-CH_4-CO_2 mixture (93-5-2)%.*

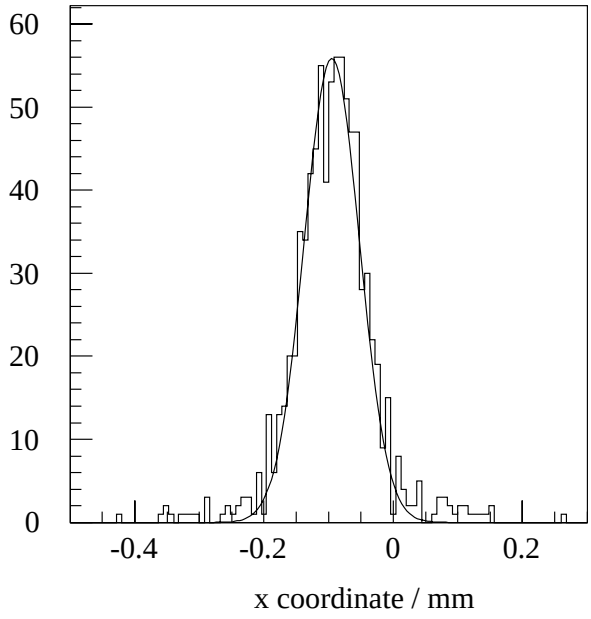

Figure 2.3.14: *Measured resolution in $r-\phi$ determined using induced signals. The distribution has been measured using a X-ray source [43]. The width of the distribution is around 40μm. The gas used was a Ar-CO_2 mixture (70-30)%.*

2.3.4 Cost

The expected costs of the TPC and FCH system are listed in Table 2.3.6. They are based on the costs of the Star TPC and the estimate for the Alice TPC. The costs of the FCH were estimated following the example of ATLAS, where a very similar system is being constructed.

Description	estimated cost in MEUR
TPC	
Outer Field Cage	4.0
Inner Field Cage	0.8
Central Membrane	0.3
Endcap Sectors	6.5
Sector Support Structure and handling tools	1.5
Laser System	1.0
Gas and Cooling System	1.8
TPC Electronics	
Front End Electronics	3.5
Readout Boards	0.5
Power Supplies	0.4
Slow Controls	0.2
TPC Sum	20.5
FCH	1.3

Table 2.3.6: *Cost of the TPC and the FCH Systems.*

2.3.5 R & D projects

Research for TPCs is carried out at a number of different locations in the world. The main topics are the further exploration of novel methods for the TPC readout, and the development of readout electronics.

System tests of TPCs equipped with gas avalanche micro detectors will have to be performed, to learn more about the operating conditions, the optimal design and the ultimate resolutions possible. A particular test will have to be the operation of such devices in large magnetic fields. As pointed out, significant work still needs to be done for the readout electronics. Low cost, low power compact systems are needed. If the induced signals should be used in addition, theses system need also a high sampling speed.

2.4 Performance of the Tracking System

In this section the combined performance of the tracking system is presented. The vertex detector with its excellent flavour tagging capabilities and the very good and efficient tracking in the combined system will together allow the reconstruction of tracks from charged particles, of secondary, and tertiary vertices from long-lived particles, with an unprecedented accuracy. Together they will provide the necessary input to the event analysis to enable an excellent measurement of the energy flow when combined with the results of the calorimeters.

2.4.1 Track reconstruction

The performance of the tracking system depends critically on the ability to find and to reconstruct tracks. The tracking system has been designed in such a way that nearly the full solid angle is covered with at least two independent sub-detectors, which allows stand alone track finding and reconstruction. This results for a high degree of redundancy and robustness of the performance of the system in a wide variety of events.

A track-reconstruction has been developed for the detector which is based largely on algorithms developed for the LEP experiments [55]. The system operates in a number of different steps. Tracks are first found in as many subdetectors as possible. In a second step the track information from the different sub-detectors is combined into single tracks. Some cleaning-up is already done at this stage, when hits which clearly do not belong to a track are dropped. In a third and final step all tracks of one event are treated together and an attempt is made to find the best overall fit to all tracks at once. The main goal of this is to resolve ambiguities which might still be present. The overall performance of this system as simulated in events of the type $Z \rightarrow d\overline{d}$ at $\sqrt{s} = 500$ GeV is shown in Fig. 2.4.1, as a function of the polar angle, $\cos\theta$. In the central region the efficiency for momenta larger than 1 GeV/c is better than 99%, and drops to 95% in the very forward direction. Overall an efficiency of 98.4% has been achieved. Very similar reconstruction efficiencies have been found in other types of events like $Z \rightarrow \tau^+\tau^-$, or heavy flavour decays of the Z. It has been checked that the system performance is essentially independent of the background for the level of background expected at TESLA (see Chapter 7 for a detailed discussion).

2.4.2 Tracking resolution

The very ambitious goal of a momentum resolution of $5 \times 10^{-5}\,(\,\mathrm{GeV}/c)^{-1}$ as laid down in section 1 can only be reached by a combination of the different subdetectors. The TPC alone achieves a resolution of $1.5 \times 10^{-4}\,(\,\mathrm{GeV}/c)^{-1}$. Using also the vertex detector $7 \times 10^{-5}\,(\,\mathrm{GeV}/c)^{-1}$ is reached. The addition of the Silicon layer at a radius of 30 cm (SIT) improves the resolution to the required precision of $5 \times 10^{-5}\,(\,\mathrm{GeV}/c)^{-1}$. This is illustrated in Fig. 2.4.2, where as a function of the polar angle the momentum resolution is shown, with and without the SIT and FCH. Below momenta of $\sim$ 20GeV the multiple scattering starts to dominate the resolution, so that the SIT does not help anymore.

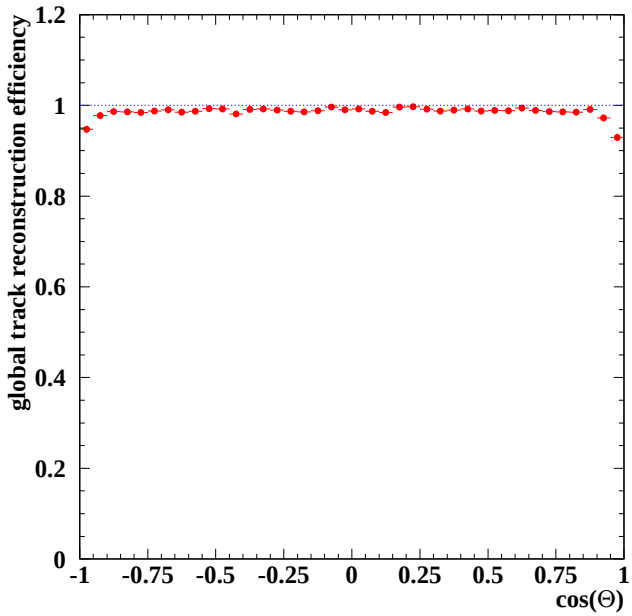

Figure 2.4.1: *Efficiency to reconstruct tracks from charged particles in the tracking system, as a function of the polar angle.*

In the forward direction it is not primarily the momentum resolution but the angular resolution which is defining the ultimate performance of the detector. The resolution achieved is shown in Fig.2.4.3. The main interest in the polar angle in the forward direction is coming from the measurement of the beamstrahlung spectrum using the acolinearity distribution of Bhabha events. For small acolinearity the experimental error on the effective centre of mass energy, $\sqrt{s'}$, is given by $\Delta\sqrt{s'/s} \approx \Delta\theta/\sqrt{2}\sin\theta$. Down to lowest angles the experimental error is significantly smaller than the beam energy spread of TESLA of $\sim 0.1\%$.

2.4.3 Flavour tagging

As already pointed out in the description of the vertex detector, it is important to be able to tag decays with bottom and charm quarks in the final state with excellent efficiency and purity. Most tracks are of low energy, so good impact parameter resolution down to small (few GeV/c) momenta are important. However due to the large average boost of heavy flavour hadrons, decay vertices might be a few cm away from the primary vertex, and therefore can be outside the innermost vertex detector layer. Therefore the system has to be extremely flexible and should be able to cope with these high boost events as well. The topological vertexing as pioneered by SLD [56] has the potential to allow efficient reconstruction of secondary and tertiary vertices for a very large range of situations.

Most of the simulations have been done using $Z\rightarrow q\bar{q}$ events generated at $\sqrt{s} =$

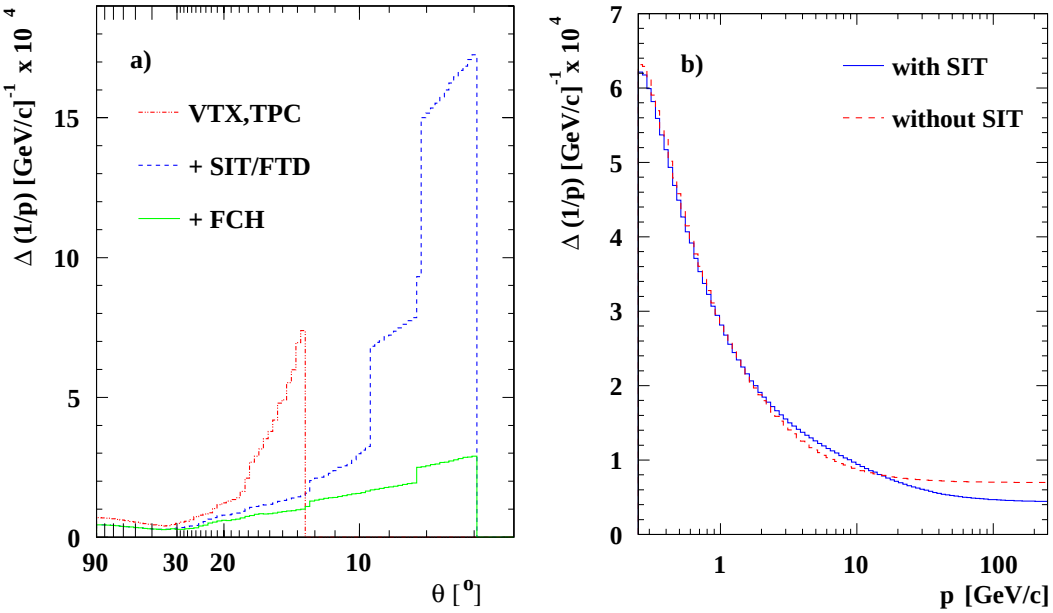

Figure 2.4.2: *Momentum resolution a): for* 250 *GeV/c muons as a function of the polar angle, for TPC and VTX, after the addition of the FTD, and for the complete system including the FCH. b): Momentum resolution as a function of the momentum for a polar angle* $\theta = 90°$*. The dashed curve is for the VTX and the TPC only, the solid one for the complete tracking system.*

m_Z with PYTHIA 6.1, since the 45 GeV jets are typical of the energies produced in more complex multijet final states at high energies, and provide a good benchmark for comparison with current experiments. These studies have then been extended to jets over a wide energy range, in order to provide a more complete overview of the generic performance [57].

The location of the primary vertex in the xy projection is found by averaging over a number of consecutive events, yielding a precision of around 1 μm. For the z position, fitting of each individual event is necessary, due to the length of the beamspot ($\sim 400\,\mu$m).

The flavour tagging is based primarily on ZVTOP, the SLD topological vertexing code [56], including updates to eliminate approximations which cease to hold adequately in the case of long-lived particles in the high magnetic field of TESLA. In addition to ZVTOP, a 1-prong charm tag and an impact parameter joint probability tag are combined in a neural net approach similar to that used by OPAL [58] to obtain the highest performance flavour tagging.

Fig. 2.4.4 shows the simulated detector performance for tagging a single heavy flavour jet in $Z \rightarrow q\bar{q}$ events. The SLD points, shown at the knee of the corresponding curves, indicate the status of flavour identification with currently existing detectors. The improvement of the charm tag relative to that available at LEP and SLD is particularly important for physics. The further enhancement in performance of the charm

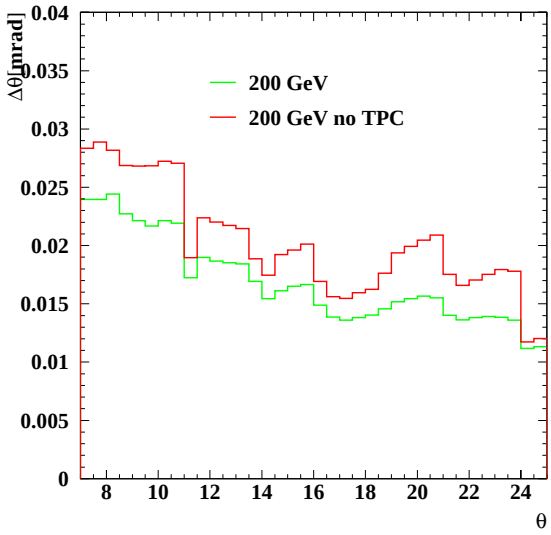

Figure 2.4.3: *Polar angle resolution for 200 GeV muons as a function of the polar angle including the TPC and the forward chambers and with silicon tracking only.*

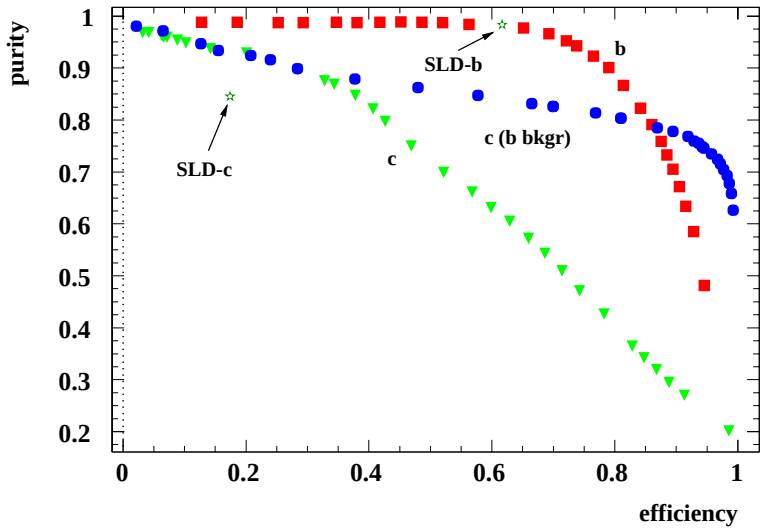

Figure 2.4.4: *Efficiency and purity for tagging a heavy flavour jet in Z decays.*

tag in events with only bottom background (labelled as b-bkgr in Fig. 2.4.4) is relevant for example to the measurement of Higgs branching ratios.

As an indication of the energy dependence of flavour tagging, a study has been made by hadronising single quarks in JETSET at various energies, distributed uniformly with $|\cos\theta| < 0.9$. For these 'monojet' events, in Fig. 2.4.5 and Fig. 2.4.6 the probability to tag an unwanted flavour as a function of the efficiency to tag the wanted flavour is shown. While these events are not representative of a specific physics process, it is encouraging that the dependence of the tagging efficiency and mis-tagging rate on the

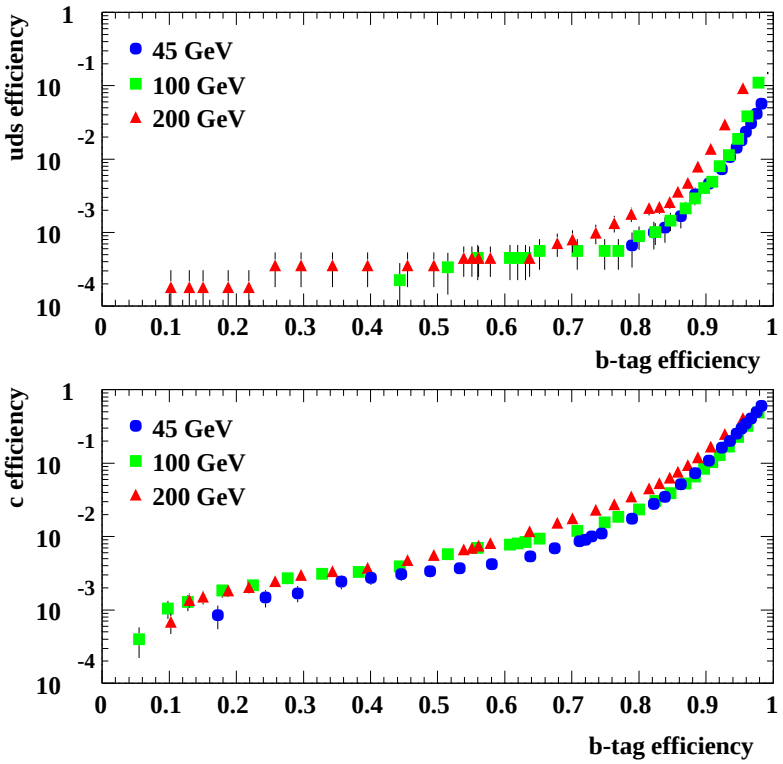

Figure 2.4.5: *Efficiency to tag an unwanted flavour as function of the bottom tag efficiency, for three different jet energies.*

jet energy is rather weak, indicating that the algorithms can be applied to a wide range of energies. As discussed in [57], there are a number of further developments to be made in the tagging algorithms. The next steps will include studies for benchmark physics and background processes, and an evaluation of the systematic errors, particularly those associated with the fragmentation in high energy jets. Eventually, internal calibration from double tagging of $q\overline{q}$ and other events at TESLA will be essential.

In many analyses it is important to know whether the quark or the anti-quark has been tagged. In semi-leptonic decays of the hadron this can be done with very good precision. The majority of jets, with non-leptonic decay, can still be classified by the reconstruction of the so-called vertex charge, which is related to the charge of the primary quark. Such an analysis places very stringent demands on the quality of the topological reconstruction, since any track which is ambiguous between the primary and secondary or tertiary vertices will significantly weaken the measurement. Given the far better impact parameter resolution achievable than at LEP or SLD, where the vertex charge has been pioneered to good effect, this information will be a valuable tool for many analyses in the multi jet environment at TESLA.

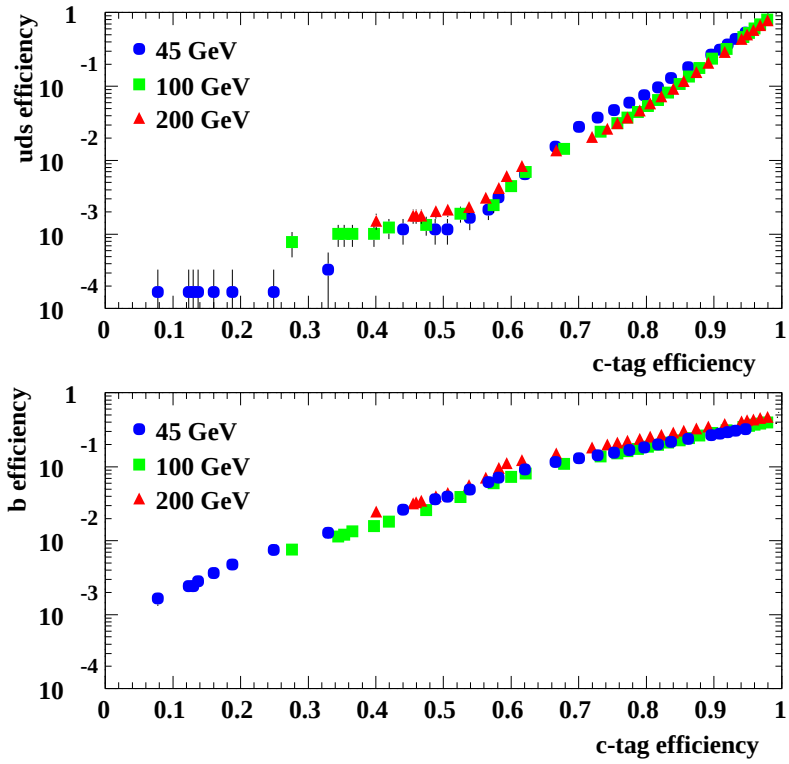

Figure 2.4.6: *Efficiency to tag an unwanted flavour as function of the charm tag efficiency, for three different jet energies.*

2.4.4 Conclusion

The system of central tracking detectors proposed offers excellent potential for tracking and vertexing. The very high demands coming from the analysis of the physics at TESLA can be fulfilled with a combination of silicon and gaseous tracking devices. The clean environment of the electron-positron collider allows the placement of the vertex detector very close to the interaction point, which, combined with the very good resolution possible with modern silicon pixel detectors, allows an unprecedented level of identification of heavy flavour jets to be reached.

Bibliography

[1] J. Hauschildt, *Studies on a Silicon Intermediate Tracker for the TESLA Detector,* LC-DET-2001-036, electronic document.

[2] C. K. Bowdery and C. J. S. Damerell. Progress Report on a CCD-based Vertex Detector Design, and some Observations on the Microstrip Detector Option. In *Workshop on Physics and Experiments with Linear Colliders, Waikoloa, Hawaii*, 773. World Scientific, 1993.

[3] LCFI-Collaboration: C. J. S. Damerell et al. A CCD-based Vertex Detector for TESLA. *LC-DET-2001-023*. http://www.desy.de/~lcnotes electronic document.

[4] G. Deptuch et al. Design and Testing of Monolithic active Pixel Sensors for charged Particle Tracking. *LC-DET-2001-017*, 2001. http://www.desy.de/~lcnotes electronic document.

[5] M. Battaglia. A Pixel based Vertex Tracker for the TESLA Detector. *LC-DET-2001-042*, 2001. http://www.desy.de/~lcnotes electronic document.

[6] DELPHI-Collaboration: P. Chochula et al. The DELPHI Silicon Tracker at LEP2. *Nucl. Instrum. Meth.*, A412:304, 1998. electronic document.

[7] F. Antinori. In *Proc of the Int Pixel Detector Workshop PIXEL98*, 41, 1998.

[8] ATLAS-Collaboration: Pixel Detector Technical Design Report. *CERN*, LHCC/98-13, 1998. http://atlasinfo.cern.ch/Atlas/GROUPS/INNER_DETECTOR/PIXELS/tdr.html.

[9] D. Bortoletto. In *Proc of the International Pixel Detector Workshop PIXEL98*, 22, 1998.

[10] M. Krammer and H. Pernegger. Signal Collection and Position Reconstruction of Silicon Strip Detectors with 200 μm readout pitch. *Nucl. Instrum. Meth.*, A397:232, 1997. electronic document.

[11] S. M. X. Hansen, D. J. Jackson, R. Hawkings, and C. J. S. Damerell. Flavour Tagging Studies for the TESLA Linear Collider. *LC-PHSM-2001-024*, 2001. http://www.desy.de/~lcnotes electronic document.

[12] R. Hawkings. Vertex Detector and Flavour Tagging Studies for the TESLA Linear Collider. *LC-PHSM-2000-021*. http://www.desy.de/~lcnotes electronic document.

[13] K. Abe et al. Design and Performance of the SLD Vertex Detector, a 307 Mpixel Tracking System. *Nucl. Instrum. Meth.*, A400:287, 1997. electronic document.

[14] F. Fossum, contribution to 8th European Symposium on Semiconductor Detectors,1998.

[15] C. J. S. Damerell. Developments in Solid State Vertex Detectors. In *Proc Physics in Collision IV*, 453, 1984. Editions Frontieres.

[16] W. Snoeys. Total Dose Behaviour of Commercial Submicron VLSI Technologies. *CERN-LHCC-97-60*, 139, 1997.

[17] M. Campbell. Proc of the Int Workshop on Vertex Detectors - Vertex 2000. In *Nucl. Instrum. Meth*, 2000. To be published.

[18] V. Bonvicini and M. Pindo. Simulating Capacitive Cross-talk Effects in DC-coupled Hybrid Silicon-pixel Detectors. *Nucl. Instrum. Meth*, A372:93, 1996. electronic document.

[19] M. Battaglia et al. *Nucl. Instrum. Meth*, A447:202, 2000. electronic document.

[20] M. Battaglia et al. Hybrid Pixel Detector Development for the Linear Collider Vertex Detector. *hep-ex/0101020*, 2001. electronic document.

[21] M. Caccia et al. Characterization of hybrid pixel detectors with capacitive charge division. *hep-ex/0101012*, 2001. electronic document.

[22] J. Chamanina, et al. Si-pixel Transition Radiation Detector with Separation of TR-Photon and Particle Track by B-Field. *LC-DET-2000-038*, 2000. http://www.desy.de/~lcnotes electronic document.

[23] DELPHI-Collaboration: P. Chochula et al. The DELPHI Silicon Tracker at LEP2. *Nucl. Instrum. Meth.*, A412:304, 1998. electronic document.

[24] CMS-Collaboration: The Compact Muon Solenoid, Technical Proposal. *CERN*, LHCC 94/38, 1994. http://cmsinfo.cern.ch/TP/TP.html.

[25] W. de Boer. Lorentz Angle Measurements in Silicon Detectors. *LC-DET-2001-028*, 2001. http://www.desy.de/~lcnotes electronic document.

[26] D. R. Nygren. The Time Projection Chamber: A New 4 Pi Detector for Charged Particles. *PEP-0144, Proceedings of Pep Summer Study, Berkeley*, 58–78, 1975.

[27] STAR-Collaboration: K. H. Ackermann et al. The Star Time Projection Chamber. *Nucl. Phys.*, A661:681–685, 1999.

[28] STAR-Collaboration: M. E. Beddo et al. STAR: Conceptual Design Report for the Solenoidal Tracker at RHIC. BNL-PUB-5347, LBL-PUB-5247.

[29] ALICE-Collaboration: Time Projection Chamber. *CERN*, ALICE TDR 7 LHCC 2000/001, 2000. http://alice.web.cern.ch/Alice/TDR/.

[30] P. S. Marrocchesi et al. The Spatial Resolution of the ALEPH TPC. *Nucl. Instrum. Meth.*, A283:573, 1989.

[31] DELPHI-Collaboration: C. Brand et al. The DELPHI Time Projection Chamber. *Nucl. Instrum. Meth.*, A283:567, 1989.

[32] DELPHI-Collaboration: P. Abreu et al. Performance of the DELPHI Detector. *Nucl. Instrum. Meth.*, A378:57, 1996. electronic document.

[33] M. Gruwé. Gas Studies for a TPC of a Detector for the Future Linear Collider TESLA. *LC-DET-1999-003-TESLA*, 1999. http://www.desy.de/~lcnotes/ electronic document.

[34] M. Gruwé. Studies of dE/dx Capabilities of a TPC for the Future Linear Collider TESLA. *LC-DET-2001-043*, 2001. http://www.desy.de/~lcnotes electronic document.

[35] S. Abachi et al. The D0 Detector. *Nucl. Instrum. Meth.*, A338:185–253, 1994.

[36] F. Sauli. GEM: A New Concept for Electron Amplification in Gas Detectors. *Nucl. Instrum. Meth.*, A386:531, 1997. electronic document.

[37] Y. Giomataris, P. Rebourgeard, J. P. Robert, and G. Charpak. Micromegas: a High Granularity Position Sensitive Gaseous Detector for High Particle Flux Environments. *Nucl. Instrum. Meth.*, A376:29, 1996. electronic document.

[38] HERA B-Collaboration: HERA-B: An Experiment to Study CP-Violation using an internal Target at the HERA Proton Ring. *DESY*, PRC-95/01, 1995. http://www-hera-b.desy.de/general/publications/proposal.

[39] COMPASS-Collaboration: G. Baum et al. COMPASS: A Proposal for a Common Muon and Proton Apparatus for Structure and Spectroscopy. CERN-SPSLC-96-14.

[40] F. Sauli and A. Sharma. Micropattern Gaseous Detectors. *Annu. Rev. Nucl. Sci.*, 49:341–388, 1999.

[41] F. Sauli. GEM Readout of the Time Projection Chamber. *CERN-EP-TA1*, 1999.

[42] L. Thompson. TPC Readout using the Gas Electron Multiplier. In *International Workshop on Micro-Pattern Gas Detectors*. Orsay, France, 1999.

[43] D. Karlen et al. GEM Space Point Resolution for a TPC Tracker. In *Linear Collider Workshop 2000*, 2000. American Institute of Physics. To be published, http://www-lc.fnal.gov/lcws2000
M. S. Dixit et. al., GEM-TPC Readout Studies, talk presented at ECFA/DESY Padova Workshop, May 2000 http://www.pd.infn.it/ecfa/.

[44] M. Schumacher. Pad Readout Geometries for a TPC with GEM Readout for the TESLA Linear Collider. *LC-DET-2001-014*, 2000.
http://www.desy.de/~lcnotes/ electronic document.

[45] R. Brinkmann, G. Materlik, J. Rossbach, and A. Wagner (eds.). *Conceptual Design of a 500 GeV e^+e^- Linear Collider with Integrated X-Ray Laser Facility*. DESY 1997-048, ECFA 1997-182. DESY,
http://tesla.desy.de/TTF_Report/CDR/TTFcdrTab.html, 1997.

[46] R. Settles (ed.). *e^+e^- Linear Colliders: Physics and Detector Studies, Part E*. DESY 97-123E, 1996.

[47] C. Bowdery (ed.). *The ALEPH Handbook*. CERN, 1995. ISBN 92-9083-072-7.

[48] S. Bachmann, A. Bressan, A. Placci, L. Ropelewski, and F. Sauli. Development and Test of large Size GEM Detectors. *IEEE Trans. Nucl. Sci.*, 47:1412–1415, 2000.

[49] For information see

http://obsidian.lbl.gov/~ronan/talks/LCTPC/TPC_FastSampling.html.

[50] M. Hauschild. Particle Identification with dE/dx at the TESLA-TPC. In *Linear Collider Workshop 2000*, 2000. American Institute of Physics. To be published, http://www-lc.fnal.gov/lcws2000.

[51] ALEPH-Collaboration: W. Wiedenmann. Alignment of the ALEPH Tracking Devices. *Nucl. Instrum. Meth.*, A323:213, 1992.

[52] ATLAS-Collaboration: Inner Detector Technical Design Report. *CERN*, LHCC(16,17), 1997. http://atlasinfo.cern.ch/Atlas/GROUPS/INNER_DETECTOR/TDR/tdr.html.

[53] T. Behnke, G. Blair, et al. BRAHMS: a Monte Carlo for a Detector at a 500/800 GeV Linear Collider. *LC-TOOL-2001-005*, 2001. http://www.desy.de/~lcnotes/ electronic document.

[54] T. Behnke, M. Hamann, and M. Schumacher. Development of a TPC with GEM Readout. *LC-DET-2001-006*, 2001. http://www.desy.de/~lcnotes/ electronic document.

[55] K. Harder, M. Elsing, et al. Track Reconstruction for a Detector at TESLA. *LC-DET-2001-029*, 2001. http://www.desy.de/~lcnotes/ electronic document.

[56] D. J. Jackson. A Topological Vertex Reconstruction Algorithm for Hadronic Jets. *Nucl. Instrum. Meth*, A388:247, 1997. electronic document.

[57] S. M. Xella Hansen, D. J. Jackson, R. Hawkings, and C. J. S. Damerell. Flavour Tagging Studies for the TESLA Linear Collider. *LC-PHSM-2001-024*, 2001. http://www.desy.de/~lcnotes electronic document.

[58] OPAL-Collaboration: G. Abbiendi et al. *Eur Phys J*, C8:217, 1999.

3 Calorimetric Detectors

3.1 Calorimeter Overview

The physics programme at TESLA mandates a detector capable of precision measurements, in order to fully exploit the discovery potential of a linear collider, where new physics can be detected either directly or by exposing deviations from the Standard Model prediction.

Many of the new physics signatures at TESLA will show up in complex hadronic final states, often proceeding through cascade decays, such as $t \to bW$, $W \to q\bar{q}'$ or $Z \to q\bar{q}$, which must be measured well in order to distinguish them from Standard Model processes.

Reconstruction of jet (parton) four-momenta with high resolution will be a key factor to comply with this task, considering also that beamstrahlung and ISR, as well as the presence of undetected particles in the final state (ν's, *ino*'s), will severely limit the applicability of constrained fit techniques to enhance di-jet mass resolution.

The above considerations call for calorimetry with unprecedented performance and translate in a set of important requirements:

- Hermeticity down to small polar angles
- Excellent energy resolution for jets (partons)
- Excellent angular resolution
- Capability to reconstruct non-pointing photons as a stand-alone device
- Good time resolution, to avoid event pile-up

Experience at LEP and SLC has shown that the best energy resolution for jets is achieved by means of energy flow algorithms, where photons are measured by the electromagnetic calorimeter, charged hadrons by the tracker, and neutral long-lived hadrons by the hadronic calorimeter, which also is used to tag muons. In addition, lepton identification down to low momenta is important in order to separate purely hadronic jets from jets containing leptonic decays.

This strategy is best realized in a dense and hermetic sampling calorimeter with a very high granularity, where one can efficiently separate the contributions of the different particles in a jet and use the best suited detector to measure their four-momenta. It must be stressed that the success of this approach will originate much more from the high segmentation (both lateral and longitudinal), than from the stochastic and constant terms in the energy resolution, which could be moderate.

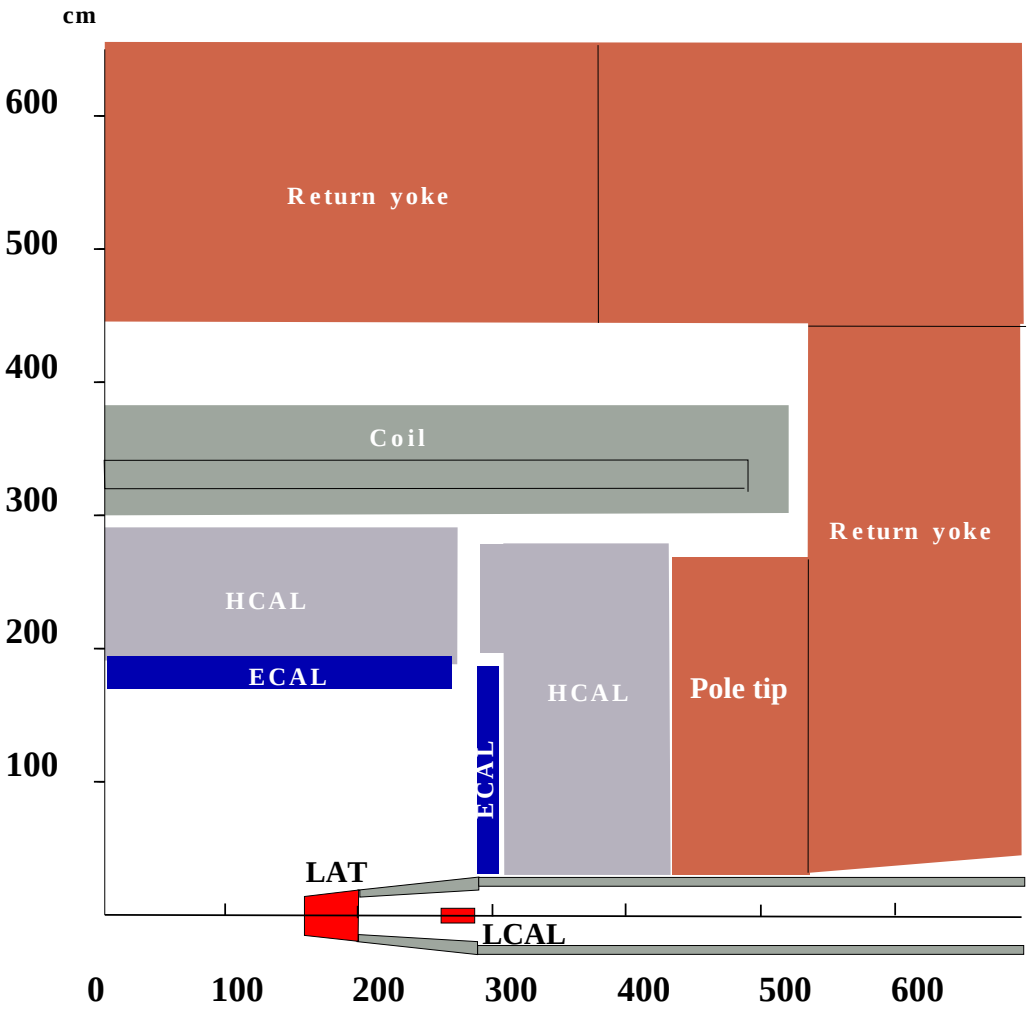

Figure 3.1.1: *Quadrant view of the calorimeter system*

The hermeticity requirement also forces the choice to include the hadronic barrel calorimeter inside the superconducting coil producing the 4T solenoidal field, which otherwise, with its considerable thickness ($\sim 1.6\lambda$), would degrade the performance of the hadronic calorimeter.

A quadrant view of the calorimeter system is shown in figure 3.1.1.

In the course of the study many possible realizations of the calorimeter system have been proposed and in parallel with the study of their technical design, their ability to fulfil the physics goals has been benchmarked using a common set of reactions (e.g. $e^+e^- \to ZHH$, $e^+e^- \to VV\nu_e\bar{\nu}_e$ ($V = W, Z$), etc.). The development of novel algorithms is needed to perform these comparisons and to achieve an accurate measurement of the energy flow in jets by exploiting the information from tracking system and calorimetry in a refined way. Although there is excellent progress in this area as indicated in the Detector Performance Section, more effort will be needed in future.

In the following, two options are presented both for the electromagnetic part as well as for the hadronic compartment.

For the electromagnetic part (ECAL), the two options are:

- a very high granularity 3D calorimeter, based on tungsten absorbers and silicon diode pads. The Si-W calorimeter, perfectly suited for energy flow measurements, has prompted an ongoing effort to produce appropriate algorithms, to fully profit from its imaging capabilities. Engineering studies indicate the feasibility to build, commission and operate a 32 million channels calorimeter at a finite, albeit rather high cost, and a strong R&D program as well as good progress in reconstruction software has started to strengthen this conviction.

- a shashlik calorimeter, an evolution of the design presented in the CDR [45], which has since undergone a successful R&D program as well as more detailed studies of its layout.

For the hadronic part (HCAL), two solutions are presented:

- an Fe/scintillating tile calorimeter with high transverse and longitudinal segmentation, to allow for software compensation,

- a fully digital calorimeter with imaging capabilities, where the active layers are gas detectors.

The system is completed by forward calorimeters (Low Angle Tagger, LAT, and Luminosity Calorimeter, LCAL), which cover polar angles down to 4.6 mrad. These calorimeters, despite their small size, have a large impact in the overall detector performance, since they enhance missing energy resolution, provide electron ID and measure single bunch luminosity.

3.2 The SiW Electromagnetic Calorimeter

In order to measure the energy flow in jets, the best way would be to get a three dimensional picture of the shower development. The spatial separation of particles depends on the distance of the calorimeter to the interaction point and on the magnetic field. Therefore a large detector with a B-field of 4 T is well suited. Within the calorimeter this separation depends on the transverse and longitudinal shower size. In a dense calorimeter the transverse shower size is small and therefore, the transverse separation of showers is good if the granularity is high enough. If the ratio of radiation length over interaction length is small, the longitudinal distance between the starting points of electromagnetic and hadronic showers is large. With many longitudinal samplings available this can be used to further separate particles. This demands a dense electromagnetic calorimeter with a cell size which is well matched to the Molière radius of the absorber and to the typical separation between particles in a jet. An attractive solution to these requirements is a calorimeter with tungsten as an absorber and thin silicon sensors.

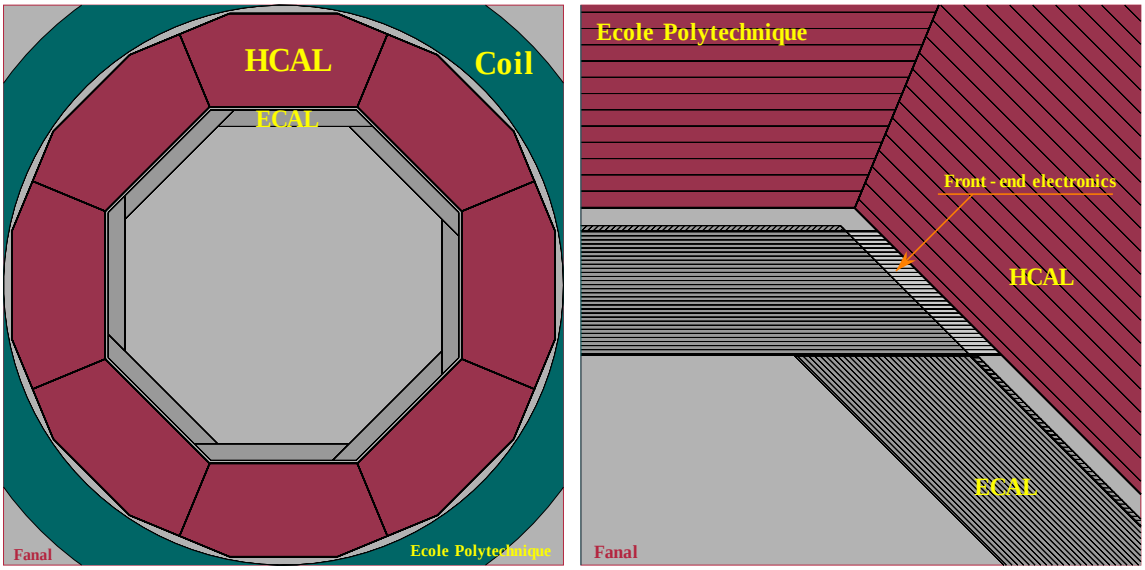

Figure 3.2.1: *View of the barrel calorimeter modules in the xy-plane (left) and detail of the overlap region between two barrel modules, with the space for the front-end electronics (right).*

3.2.1 The mechanical structure

The electromagnetic calorimeter is divided into a cylindrical barrel part and two endcaps. It is finely segmented both in the transverse and in the longitudinal direction. In depth 12 radiation lengths are filled with 30 layers of $0.4\,X_0$ thick tungsten absorbers, and another 12 radiation length are made from 10 layers of $1.2\,X_0$ thick tungsten. Transversely the calorimeter is segmented into readout cells of approx. $1\,\mathrm{cm}^2$. Since the Molière radius [1] and therefore the transverse shower shape in tungsten is of a size similar to that of a cell and since the number of longitudinal samples is very high there is no strong need for a projective arrangement of the cells, and the cells can match the mechanical constraints.

One of the requirements for the calorimeter is that it should surround the interaction point as hermetically as possible. To minimise the number of cracks a design with large modules is preferred, with boundaries not pointing back to the vertex, and a carefully designed junction between the barrel and the endcap calorimeter. As shown in Fig. 3.2.1 an eight-fold symmetry in Φ has been adopted for the barrel. One-eight of the barrel calorimeter is called a stave. Two staves overlap in such a way that no pointing cracks are produced. On the side of a stave, between the ECAL module and the HCAL (see Fig. 3.2.1), some space is left which is used to house the front-end electronics and other services like cooling and electrical power distribution. Along the beam axis, a stave is subdivided into five modules.

The design and construction of a module itself present an interesting technologi-

[1] The radiation length of tungsten is $X_0 = 3.5\,\mathrm{mm}$, and the Molière radius is $\approx 9\,\mathrm{mm}$.

cal challenge. A classical solution, assembling together the different layers with solid tie-rods or similar devices is not very attractive, since it would introduce significant dead regions. Therefore a design has been adopted where every second tungsten layer becomes part of a solid mechanical structure, by embedding it into a light composite structure made of carbon fibre reinforced epoxy. In between these plates and the carbon-fibre partitions, free spaces are left into which tungsten plates are inserted. The silicon detector layers are attached to these tungsten plates, one on the top, one on the bottom. A tungsten plate together with the two silicon detectors and the necessary connection elements will be called a detection slab in the following. The plates which are inserted into the module are cut into 9 cm wide slabs, which run across one module. In this way a sensitive plane is made up of many pieces, separated by small dead zones. Since these are small compared to the typical shower shape, they do not impact on the performance of the device.

The mechanical structure is built by wrapping the tungsten sheets with carbon fibres impregnated with epoxy. They are then stacked alternating with objects of the size of the detection slabs, until a module is complete. The full module is then put under pressure and at high temperature, to cure the epoxy. Since the thermal expansion coefficient of carbon fibre is very close to that of tungsten, distortions during the curing are small. After curing, the place holders for the detection slabs are taken out, leaving empty spaces called alveoli into which the real detection slabs can be inserted. In Fig. 3.2.2 the mechanical structure of an ECAL module is shown.

The end cap calorimeter is constructed from very similar modules as the barrel part. Each end cap consists of four modules, and is split vertically into two halfs. A particularly sensitive area is the overlap between the barrel and the endcap calorimeter. To ensure that in this region the depth of the calorimeter remains sufficient, the shape of the end cap at the outer radius follows the barrel part, and the outer radius of the endcap is extended to the outer radius of the barrel. The space between the barrel and the endcap is 10 cm wide.

The silicon diodes dissipate very little power, less than a few hundred watts for the whole calorimeter. To keep the power deposited inside the calorimeter structure low, the front-end electronics is located at the lateral side of the modules. In this area cooling is needed and can be provided by running cooling pipes in the approx. 2.5 cm of space between the ECAL and the HCAL. In the same space the power lines and the signal cables for the readout can be found.

To assemble and install the barrel calorimeter one complete stave is assembled from five modules outside the detector, and equipped with the detection slabs and the frontend electronics. The cooling pipes and power lines are mounted. Then the stave is slit into place in the detector on rails installed on the inside of the hadronic barrel calorimeter. The end caps are hung in front of the hadronic end cap calorimeter.

The different mechanical elements can be summarised as follows: The electromagnetic calorimeter is composed of a barrel and two end caps. The barrel is made of 8 staves weighing 14150 kg each. A stave is made from 5 modules weighing 2830 kg each, an end cap of 4 modules weighting 5180 kg each. A detection slab used in the first part of the calorimeter covers an area of $9 \times 150\,\mathrm{cm}^2$ and weights 4.9 kg, a detecttion

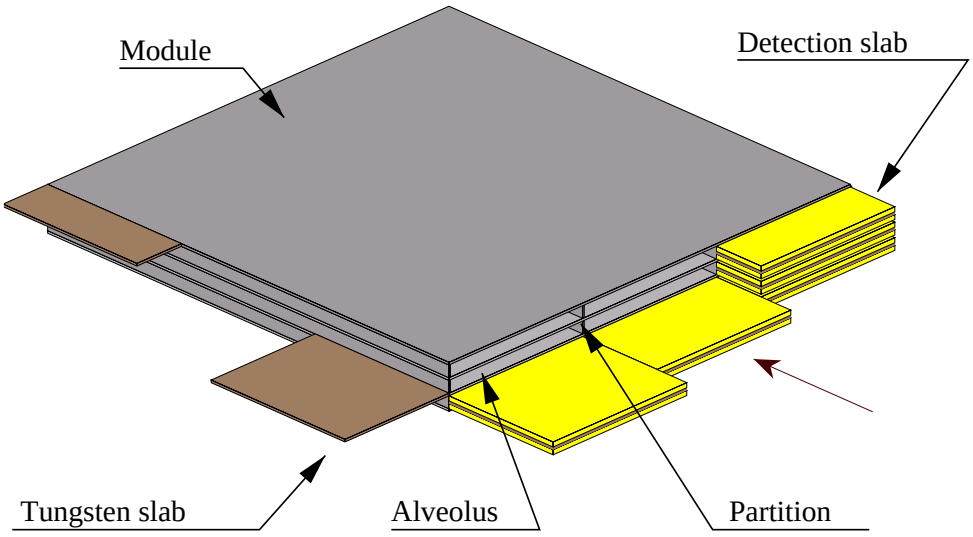

Figure 3.2.2: *The structure of the ECAL showing the alveoli, the structural tungsten slabs, and the detection slabs.*

slab from the second, coarser part covers $9 \times 130\,\mathrm{cm}^2$ and weights 10.5 kg. With the segmentation given above an inner detection slab has 2160 channels, an outer one 1860.

3.2.2 The detection slab

In Fig. 3.2.3 a schematic view of one detection slab is shown. More details can be found in [1]. The design presented in the following is based on ongoing work in close collarboration with a specialist laboratory for semiconductor technology [2].

The width of a detection slab is 9 cm, the maximum length is 160 cm. The silicon wafers are supported by pieces of 1.4 mm thick sheets of tungsten, as discussed in the previous section. Each silicon wafer is divided into 8×8 pads of size $1.15 \times 1.07\,\mathrm{cm}^2$. On top of the wafers, a printed circuit board (G10) connects the pads through metalised holes to flat cables, which carry the signals to the end of the detection slab. Within the space of 1 cm around 140 signals need to be taken out. A possible solution would be to use thin printed circuit boards. A novel very high density solution has been developed were 50 μm thin wires are embedded with a pitch of 300 μm into a plastic sheet.

The connection between the diode and the G10 board is done with conductive glue. On the diode a layer of amorphous silicon is to be deposited on the pad, and the connection will be done to this layer. In this way a resistive coupling to the diode is realised which protects the Silicon diode, and allows simple and low-cost bonding techniques to be used. The diodes are characterised as follows:

- thickness 500 μm,
- pad area around $1\,\mathrm{cm}^2$,
- capacitance per pad 25 pF,

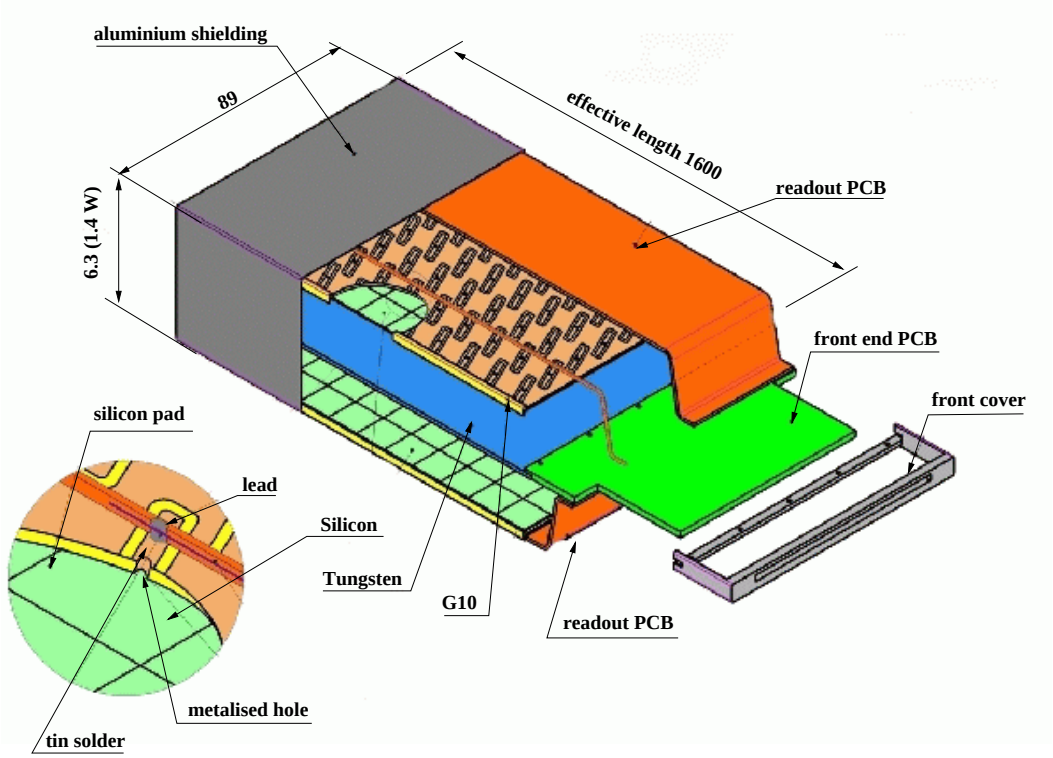

Figure 3.2.3: *Schematic view of the detection slab, with the read-out lines.*

- leakage current less than 30 nA (at 25° C),
- polarisation voltage larger than 100 V.

3.2.3 The front-end electronics

A detailed description of the front-end electronics proposed can be found in [1]. Here only a brief summary is presented.

Calling a "barrette" a row of pads along the long side of the detection slab, there is one front-end chip at the end of each barrette. At the end of each detection slab therefore these 16 front end chips have to be located in the space at the end of the alveolus behind the electromagnetic calorimeter module. Since the space available is small (about $2\times1\times0.4\,\mathrm{cm}^3$), the chip will likely have to be in a μBGA type package.

The front end chip may be characterised as follows:

- low noise pre-amplifiers with a noise around 1/10 of a signal deposited by a minimum ionising particle (MIP), for a shaping time of around 150 ns;
- dynamic range of 15 bits, realized with two different gains, each with a precision of 10 bits;
- minimum threshold around 2/3 of a MIP signal, allowing efficient zero supression;
- analogue coding of address and bunch number, (a digital solution is also studied);

- analogue storage for all signal read out by the chip, with a depth of about 1000 channels;
- low power dissipation per channel, $\sim 3\,\mathrm{mW/channel}$.

The output data format corresponds to 33 bits per channel, including the bunch number, the pad position and the amplitude for the signal.

A set of 40 detection slabs will be read out serially into one ADC, and digitised within a few ms. Thus the total number of ADCs for the whole calorimeter does not have to be larger than around 1000.

3.2.4 Calibration

Since the response of a silicon diode is very stable with time and temperature (at least up to a per–mille level), the ratio of detector response to electrons and to photons is related to the amount of tungsten in front of the detector, the silicon diode depletion length and the characteristics of the readout system like gain of the preamplifiers, etc. The first point is a constant of the detector, while the depletion length and the overall read-out system could change with time.

Measurements of the thickness and density of the tungsten slabs can be taken during the construction. Different methods are under study, however it seems feasible to make and maintain a map of the mechanical properties of the calorimeter.

The overall response of the system can be calibrated with physics events which contain isolated electrons. Prime examples are Bhabha events, W/Z decays to electrons, etc. The energy of the electron, if it is reasonably well separated from neighbouring particles, can be measured with the tracking system, and used to calibrate the response of the calorimeter cells. Thanks to the high luminosity at TESLA a calibration of every cell in the calorimeter at the level of a few per–mille can be reached within 5 years. As described in [3], cosmic ray muons can also be used to intercalibrate the cells to a precision of about 1.3×10^{-3}.

3.2.5 Performance

The performance has been evaluated in a GEANT4 [4] based simulation program, after checking the agreement with the EGS4 [5, 6] shower simulation for the energy resolution of the device. In this section the main paramaters of the calorimeter like energy resolution, position measurement precision, angular measurement precision and electron pion separation are presented.

Since the thickness of the tungsten varies between the front and the rear part of the calorimeter it is expected that the energy resolution does not scale purely like $\alpha/\sqrt{\mathrm{E}}$. This can be seen in Fig. 3.2.4 where two distinct areas are visible, at low and at large energies. The resolution found is around $11\%/\sqrt{\mathrm{E}}$ in the first energy region and around $14\%/\sqrt{\mathrm{E}}$ in the second part.

The position precision, measured as an angular resolution of photons originating at the primary interaction point, is shown in Fig. 3.2.5. It is about 2 mm for 1 GeV

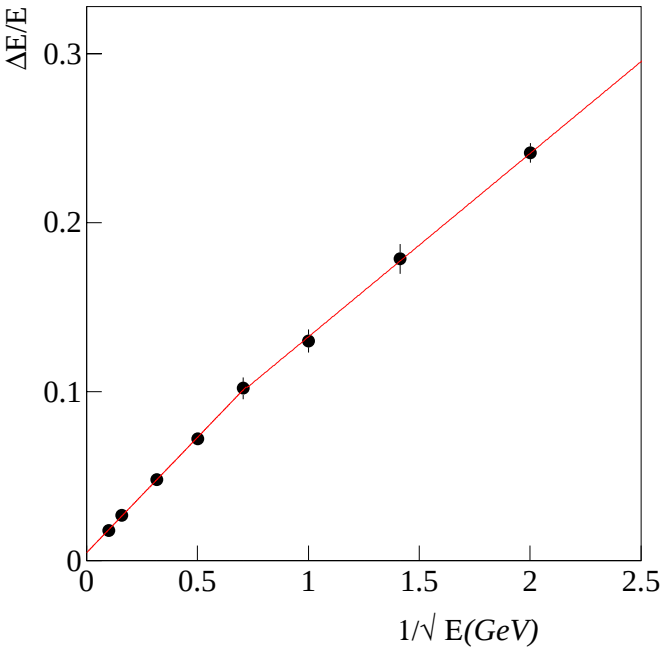

Figure 3.2.4: *Photon energy resolution. The two straight lines are fits for the low energy and the high energy part.*

photons and scales roughly as $1/\sqrt{\mathrm{E}}$. The precision with which the origin of a photon can be determined is of importance when searching for some particular models, e.g. gauge mediated supersymmetry. In these models the final state might include non-pointing hard photons. A study with a sample of photons between 3 and 30 GeV leads to a resolution of $68\,\mathrm{mrad}/\sqrt{\mathrm{E}} + 8$ mrad.

Isolated electrons and charged pions have been simulated, and the response of the ECAL, without any HCAL information, has been used to estimate the electron pion separation [7]. It has been found that electrons and pions with momentum larger than 2 GeV/c, those which reach the calorimeter, can easily be separated. An efficiency of 99.8% for the electron identification is reached, with a mistag probability to tag the electron as a pion of only a few 10^{-3}.

3.2.6 Cost estimate

In Table 3.2.1 the cost for the calorimeter is summarised. To obtain this cost estimate, the following prices have been used: 100\$/kg for the tungsten, 90\$/alveolus for the G10 sheet with metallised holes, 45\$/chip for the front-end electronics, and $3\$/\mathrm{cm}^2$ for the silicon wafers. The estimated cost for the tungsten structure includes the tungsten, but also the cutting, the composite fibre, tools, processing and manpower. It can be seen that the calorimeter cost is totally dominated by the silicon wafer contribution:

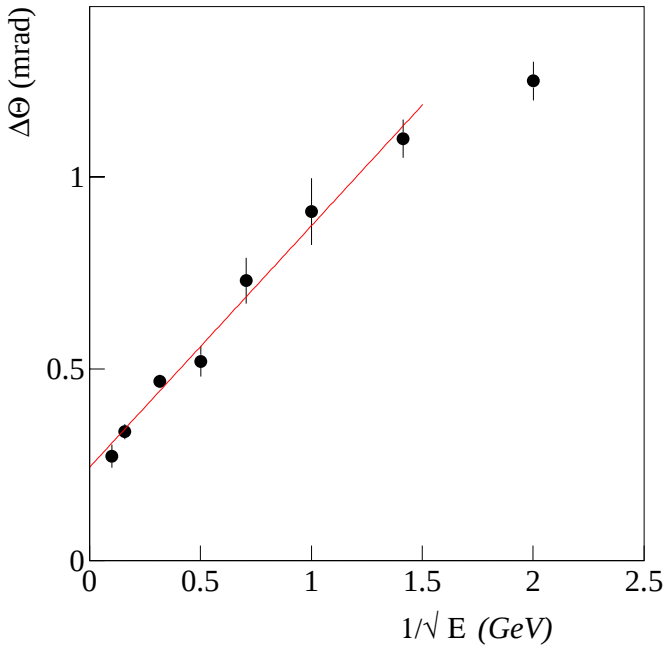

Figure 3.2.5: *Angular resolution for pointing photons.*

Sources	cost estimate (MEUR)
Tungsten structure	9.4
Tungsten active layers	7.9
G10	3.2
Wire sheets	9.2
Front-end electronics	10.0
Si wafer	93.0
TOTAL	132.7

Table 3.2.1: *Cost estimate for the Si-W electromagnetic calorimeter.*

the price per square centimetre multiplied by the detection area. However the price quoted does not take into account its expected evolution between now and the time of construction, where a significant decrease in price is expected. It is important to realize that the area of silicon detector needed is not related to the calorimeter granularity, which is of prime importance for the jet resolution, but is driven by the size of the TPC and by the density of the longitudinal sampling. This sampling is solely dictated by the choice of the electromagnetic energy resolution. For example, reducing the number of samplings by a factor of two would, but for the tungsten cost, reduce the total cost by a factor of two. It would degrade the intrinsic electromagnetic energy resolution by 40%,

but the reconstructed photon energy only by 20% and would not harm significantly the jet resolution. Therefore there is room for cost optimisation.

3.2.7 R&D

The ECAL proposed here presents significant technological challenges such as the mechanical structure, the integration of the front-end electronics, and the micro-packaging of the silicon wafers. Also the software challenges are sizeable to quantify the gain on jet energy flow with such a detector. All these features have to be studied in the coming years, first with technological prototypes. This means, for example, producing a detection slab model which would be tested with cosmic ray muons. In parallel, it is important to design and build a physics prototype, with a transverse size and a number of layers large enough to test the ECAL performances, in front of a HCAL prototype, on single particles. At the same time it will bring a proof of feasibility for such a compact device, with such a high level of integration of the components.

3.3 The Shashlik Electromagnetic Calorimeter

In recent years the "shashlik" technology has been extensively studied to assess its performance at e^+e^-, ep and pp accelerator experiments [8]-[10]. Shashlik calorimeters are sampling calorimeters in which scintillation light is read-out via wavelength shifting (WLS) fibres running perpendicularly to the converter/absorber plates [11, 12]. This technique combines the advantages of an easy assembly and operation, good hermeticity and low price.

Shashlik calorimeters are, in particular, considered to be good candidates for barrel electromagnetic calorimetry at future linear e^+e^- colliders [13]. The present shashlik technology can satisfy the requirements described in the previous sections, for a dense, highly segmented calorimeter with longitudinal sampling. A transversal segmentation of the order of 3×3 cm^2 can be easily achieved. Significant progress has been made over the last few years in the development of a shashlik-type calorimeter with longitudinal segmentation. At least two new solutions have been proposed, where either vacuum photo-diodes are inserted between adjacent towers in the front part of the calorimeter [14], to read out scintillator plates in the early part of the calorimeter, or different types of scintillator are used which have different decay times, in different parts of the calorimeter [15].

A transverse segmentation of $\sim 3\times3\,$cm^2 can be obtained in a simple way by using large (i.e. $\sim 20\times10$ cm^2) absorber and scintillator plates and confining the scintillation light inside smaller areas of the plate. This can be achieved for example by cutting grooves into the plates, which effectively keeps the light within the smaller areas. Each tile is then read out by its own bundle of fibres. This solution can only be realised with the second proposal for the longitudinal segmentation. It will be discussed in more detail in the following.

More details concerning the Shashlik calorimeter and other possible calorimeter layouts can be found in [16].

3.3.1 Conceptual design.

The smallest unit of the calorimeter is the cell. Each cell consists of 140 layers of 1 mm thick lead and 1 mm thick scintillator plates, resulting in a total depth of $25X_0$. In the first $5X_0$ the scintillator plates consist of long decay time scintillator (during development work a BC-444 scintillator from Bicron with a decay time around 250 ns was used) while the remaining plates are based on standard plastic scintillator with a decay time of less than 10 ns. For each cell the blue light produced by both scintillators is carried to the back of the calorimeter by means of 9 plastic optical wavelength shifting (WLS) green fibres. The fibre time response is fast enough (< 10 ns) not to deteriorate the separation between the fast and the slow scintillator signals. The light transmission between the plastic scintillator and the fibres is through an air-gap. Light collection is increased by aluminising the fibre end opposite to the photo-detector by sputtering. At the end of the detector the fibres are connected to clear long attenuation-length fibres in order to bring the light signal outside of the high magnetic field region where it can be read by photo-detectors (for example photo-multipliers (PM)).

One mechanical unit called a module contains 18 (3×6) cells. All the cells in a module are read independently by bundling their 9 fibres and connecting them to the same PM. The module layout is shown in Fig. 3.3.1.

The barrel part of the calorimeter is assembled from rows of 21 modules arranged to be quasi-pointing to the interaction point along the z and the ϕ coordinates (see Fig. 3.3.1). Each row covers an angular range of 112.1 mrad in ϕ. In the centre one ring of 56 modules is inserted in a way to not directly point to the interaction region. The complete barrel is assembled from 56×2 rows plus the central ring, for a total of 2408 modules corresponding to 43344 cells. The barrel detector layout is shown in Fig. 3.3.1. An endcap detector can be build based on the same idea, with modules of very similar shape.

3.3.2 Performance

A prototype consisting of 9 Pb/scintillator towers ($5 \times 5 \times 28$ cm^3) assembled in a 3×3 matrix was tested at a CERN SPS beam. Each tower consists of 29 layers of 1 mm thick lead (corresponding to 5 X_0) and 1 mm thick Bicron BC-444 slow scintillator followed by 100 layers of a lead and standard fast plastic scintillator sandwich. The light produced by both scintillators is carried to the photo-detectors by means of fast WLS fibers. The timing information from the signal is used to disentangle the layer. This is illustrated in Fig. 3.3.2 where a clear separation between the fast and the slow signal is visible. The prototype was tested using electrons ranging from 5 to 75 GeV/c and pions of 20, 30 and 50 GeV/c. In order to avoid particles from channelling through fibres or diodes, the calorimeter was tilted by 3 degrees in the horizontal plane with respect to the beam direction.

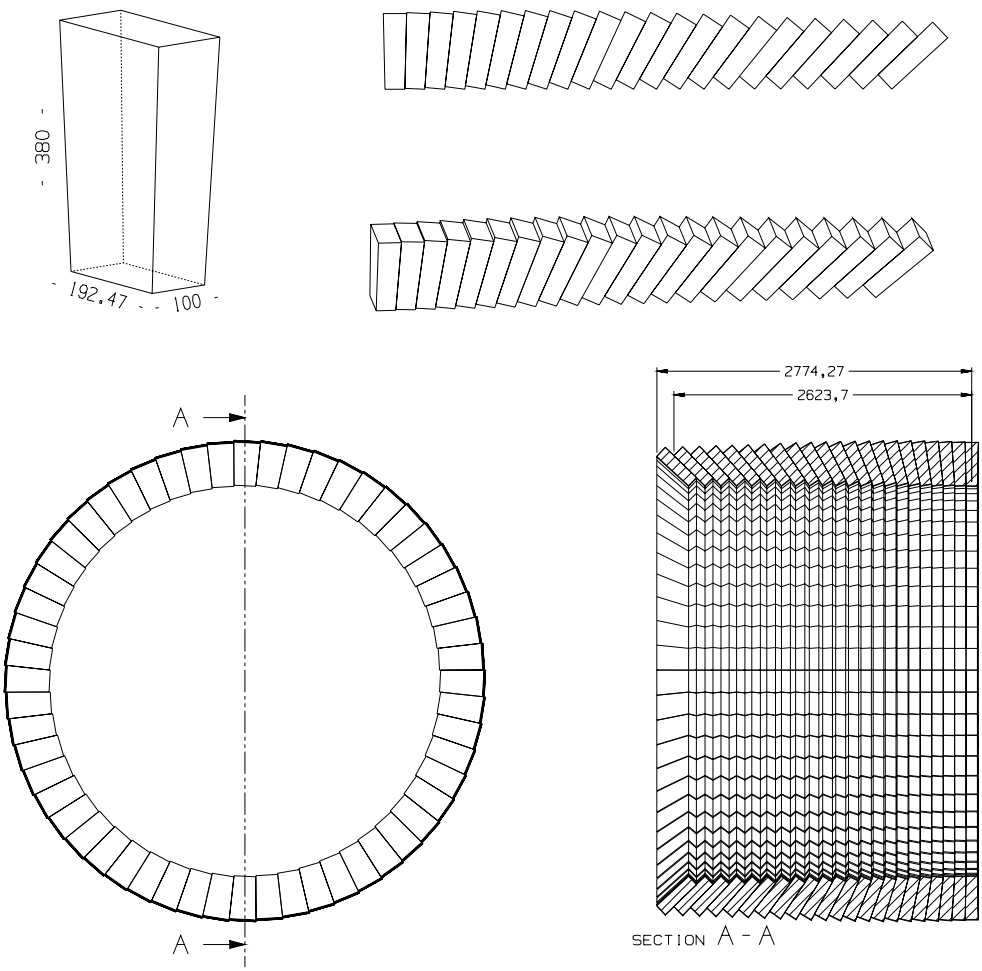

Figure 3.3.1: *Module, Row of modules (top) , and layout of the barrel part of the calorimeter (bottom).*

Preliminary results from the test beam data analysis show that the proposed technique works. The signal extracted from the slow component versus the total energy is shown in Fig. 3.3.3 for electrons and pions. The discriminating power of the E_{slow} information (Fig. 3.3.3) improves the separation capability by a factor ~ 2 w.r.t. the use of the E/p ratio alone.

The same data have been used to parametrise the energy resolution as a function of the beam energy as [17]

$$\frac{\sigma(E)}{E} = \frac{14.2\%}{\sqrt{E}} + 0.6\% \tag{3.3.1}$$

where E is expressed in GeV. The shower position reconstruction was based on centre of gravity method corrected for the detector granularity with the algorithm suggested in [18]. The barycenter $X_b = 2\Delta \sum_i i E_i / \sum_i E_i$ where Δ is the half-width of the tower and E_i the energy deposited in tower i, was modified according to $X_c =$

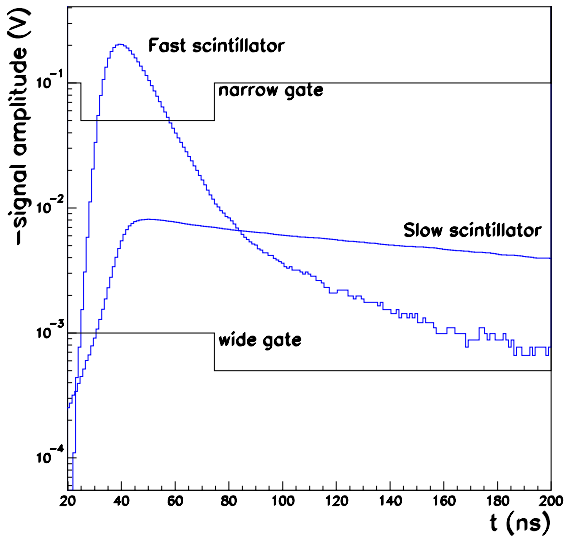

Figure 3.3.2: *Measured time distribution for fast and slow scintillators.*

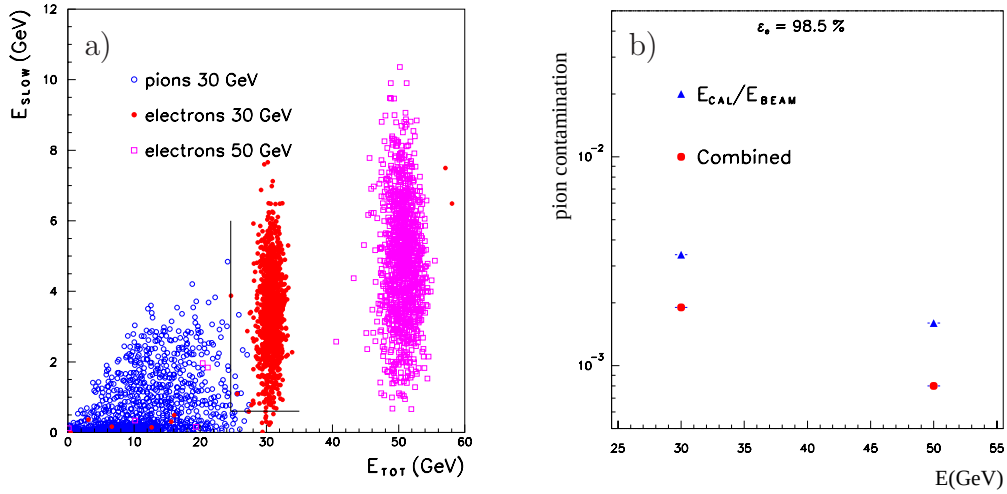

Figure 3.3.3: *Test beam results [17]: a): Energy deposited in the slow scintillator versus total energy for electrons at 30 and 50 GeV/c and pions at 30 GeV/c. b): Pion contamination versus energy for 98.5% electron efficiency.*

b arcsinh $\left(\frac{X_b}{\Delta} \sinh \delta\right)$ where b is a parameter describing the transversal shower profile and $\delta \equiv \Delta/b$.

The position resolution of the prototype at the cell centre was 1.6 mm with 50

GeV/c electrons and had the following energy dependence:

$$\sigma_X(E) \;=\; \sqrt{\left(\frac{0.9}{\sqrt{E}}\right)^2 + (0.1)^2}\ \text{cm}.$$

The two–particle separation capability with the proposed 3×3 cm^2 lateral granularity and the effects on the global energy reconstruction were studied with simulated events. Generated $\tau \rightarrow \rho\nu_\tau$ decays with an energy of 100 and 150 GeV were simulated in the proposed Shashlik barrel electromagnetic calorimeter using the BRAHMS [19] program. The total ρ energy was obtained from its decay products as the sum of the momentum of the charged pion measured in the tracking system and the energy released in the electromagnetic calorimeter by the photons from the π^0 decay. It is then necessary to disentangle the energy released by the charged pion shower in the calorimeter from the electromagnetic showers. The hadronic shower must be associated to the charged track and its contribution excluded from the total energy evaluation. A pattern recognition based on the distance from the track impact on the calorimeter and the shower centroid, on the E/p ratio, on the rate of the shower energy released in the first radiation lengths and on the shower width has been developed. The reconstructed ρ energy is compared with the generated energy in Fig. 3.3.4 and the results are satisfactory.

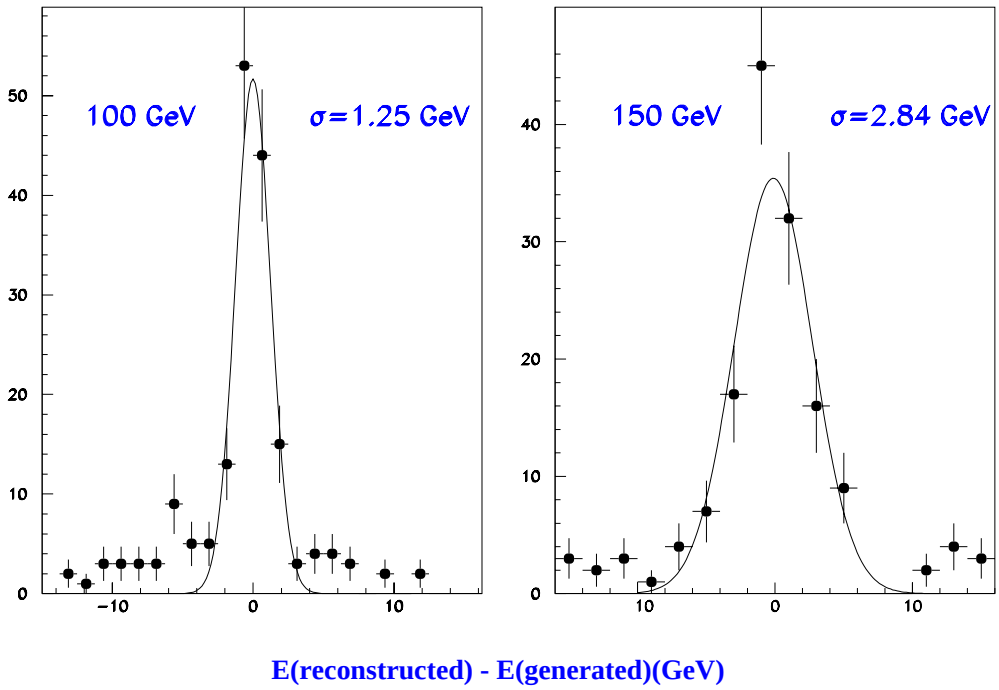

Figure 3.3.4: *Simulated energy resolution for $\tau \rightarrow \rho\nu_\tau$ decays for τ energies of 100 and 150 GeV, respectively.*

3.3.3 Cost

The proposed design consists of 2408 Modules for a total of 43344 cells corresponding to the same number of electronic channels. The cost evaluation is based on the presently available prices and is detailed in table 3.3.1. A total cost of about 15 MEUR is expected for the barrel electromagnetic calorimeter. The cost of an endcap calorimeter based on the same technique is estimated to be slightly less than 5 MEUR, so that the total cost of the complete system would be around 20 MEUR.

Item	cost per unit (EUR)	Total cost (MEUR)
Module production	3089	7.4
Fibres	170(Module)	0.4
Photo-detectors	100	4.3
R.O. Electronics	50	2.2
Total		14.3

Table 3.3.1: *Cost estimate for a shashlik-based barrel ECAL.*

3.4 The Hadronic Calorimeter

As seen from the interaction point the hadronic calorimeter (HCAL) is lined up behind the electromagnetic calorimeter (ECAL). Both together measure energy and angles of hadrons and jets and allow the tracking of minimum ionising particles (MIPs) in the calorimeter volume. To optimise the energy flow measurement the HCAL should contain the hadronic showers, allow the determination of the energy deposited with good precision, and have a sufficiently high granularity both in the transverse and in the longitudinal direction to allow the separation of close-by clusters. In addition the HCAL should be able to measure the time of events precisely, to help in the rejection of cosmic events, and to search e.g. for exotic signatures with long lived particles as they are predicted in some SUSY theories.

In this section two approaches for a hadronic calorimeter are presented. One is a tile calorimeter, of moderate segmentation and with analogue readout of the cells, the other one a highly segmented calorimeter with a purely binary readout per cell.

3.4.1 The tile hadronic calorimeter

The HCAL is constructed as a sampling calorimeter, with a material of low magnetic permeability ($\mu < 1.01$) like stainless steel or brass plates as absorbers, and scintillator plates as the active medium. The scintillator plates are subdivided into tiles. The light from the tiles is collected by loops of wavelength shifting fibres (WLS). Clear fibres are connected to these and transport the signals to the readout. Tile calorimeters with

WLS readout were first developed and used by the CDF collaboration [20, 21, 22], by OPAL [23] and later by the ATLAS [24, 25, 26] and CMS collaborations [27].

The HCAL is arranged in 2 cylindrical half barrel parts and two endcaps as shown in Fig. 3.4.1 in the opened position. The barrel HCAL fills the magnetic field volume between the ECAL and the cryostat within $191 < r < 298\,\text{cm}$.

In addition the space between the rear of the HCAL endcap and the endcap of the iron return yoke is filled with iron to guarantee the high quality of the magnetic field. This so called pole-tip will also be instrumented with a small number of sensitive planes to act as a tail-catcher in the endcap region.

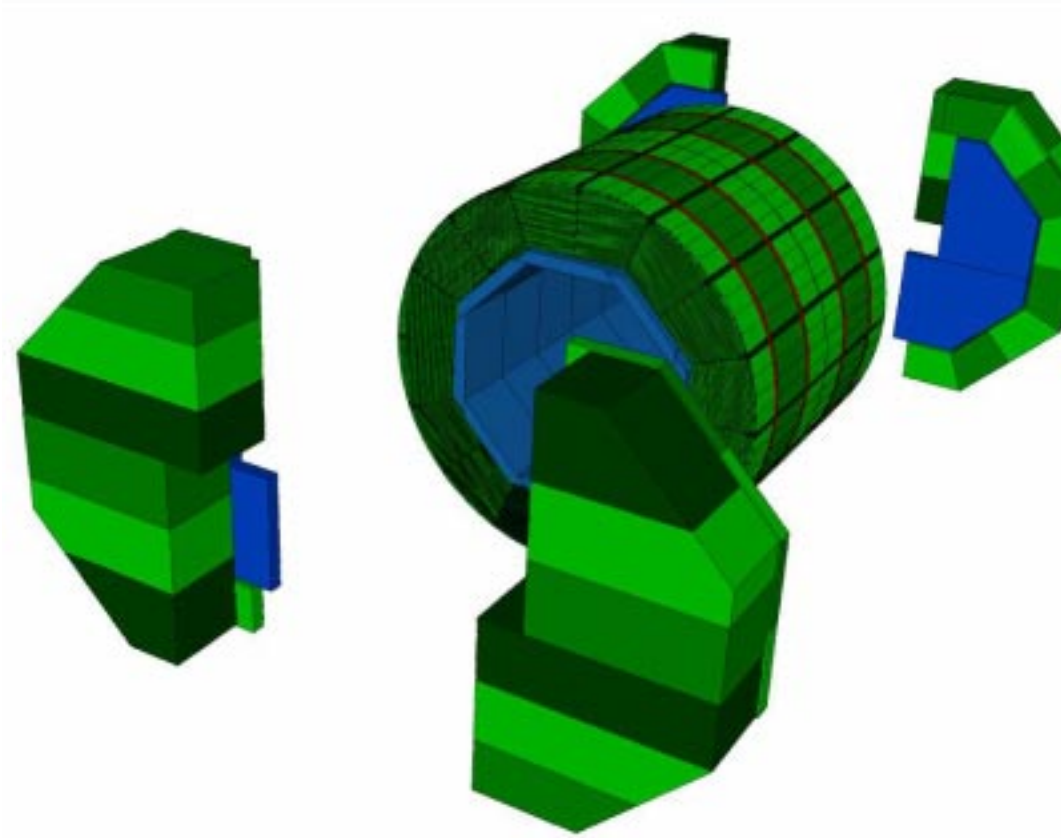

Figure 3.4.1: *View of the calorimeter system of the TESLA detector with open endcap calorimeters.*

In the magnetic field direction the barrel extends from $-267 < z < 267\,\text{cm}$. The endcaps close the barrel on either side in order to fully cover the solid angle. The gap between the barrel and the endcap is needed for support and for cables from the inner detectors, and for the readout fibres from the barrel HCAL itself.

Care has been taken to maximise the material in the space available, so that the probability for punch-through is minimised. Even though the muon system will act as

a tail catcher, the 1.6λ of the coil between the HCAL and the muon system severely limit the energy resolution for this device.

Each HCAL half barrel is subdivided into 16 modules, each of the endcaps into 4 modules. Two HCAL modules together form an octant, and support the ECAL modules in this Φ range.

3.4.1.1 The HCAL module

The basic sampling structure consists of 20 mm thick absorber plates interleaved with 6.5 mm deep gaps, into which the scintillator plates are inserted. The sampling structure is the same for barrel and for endcap modules. One barrel module has a maximum of 38, an endcap module 53 layers (see Fig. 3.4.2). Eight of these layers are arranged in a ring at the outer radius of the endcap, to fill the gap between the barrel and the endcap modules [28, 29].

One layer corresponds to 1.15 X_0, or 0.12 λ. The layers are subdivided into tiles, starting with $5 \times 5\text{cm}^2$ in the inner layer, and increasing to $25 \times 25\text{cm}^2$ at the outer radius. To reduce the number of readout channels, groups of cells are formed to get 9 longitudinal readout cells in the barrel, 12 in the endcap. The actual cell sizes in the different layers, for both barrel and endcap, are given in Table 3.4.1. This corresponds then to an actual cell depth between 0.36 and 0.84λ and a lateral cell size between $(0.22\lambda)^2$ and $(1.11\lambda)^2$. The sizes of these cells are well matched to the typical shower sizes at energies of a few GeV, which are of the order of 20 cm. Further studies however are needed to fully optimise the cell sizes in both the transverse and the longitudinal direction. Fig. 3.4.3 shows the cell arrangement in barrel and endcap modules.

Mechanically each module is held together entirely by a 3 mm thick steel skin, which connects the individual layers together. These skins cover three sides of the module. The gap between plates is maintained by 6.5 mm high strips which are fixed to the skin on the inside. The scintillator plates are inserted into these spaces. All tiles for one layer are combined into one large tile-sheet, which can be inserted into the module at once. This allows for easy installation and easy maintenance, should an intervention be needed. The thickness of the scintillator alone is 5 mm, the remainder of the space in the module gap is taken up by the wavelength shifter (WLS) loop and reflector layers, the clear readout fibres, and some room to take into account tolerances of the plates and the fibres. A detailed description of the design of the calorimeter may be found in [29, 30, 28, 31].

3.4.1.2 Scintillation light readout

The blue scintillation light produced in the tiles is transferred by frequent refraction and reflection to a wavelength shifting (WLS) fibre where it is absorbed and converted to green light. The coupling between the WLS and the tile can be done in a number of different ways, either by putting the WLS into a groove machined into the tile, by using the gap between neighbouring tiles, or by simply fixing it directly to the surface of the tile with an appropriate optical contact medium. Further R&D is needed to find the optimal solution. The fraction of light caught within the total reflection acceptance

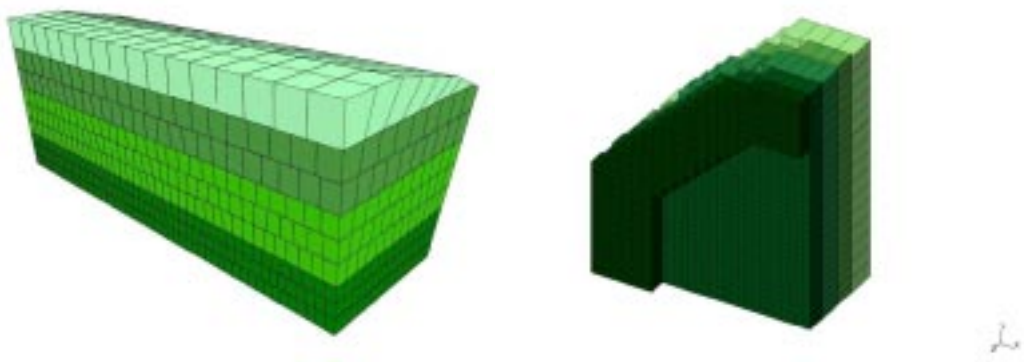

Figure 3.4.2: *One barrel (left) and one endcap (right) HCAL module*

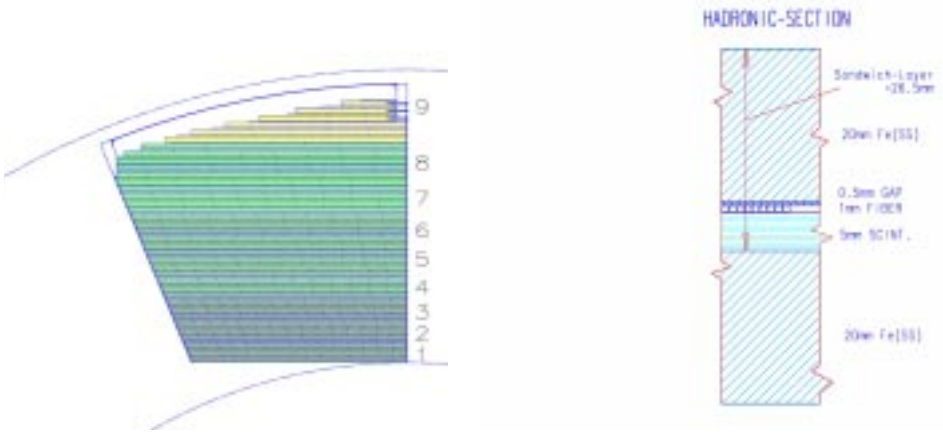

Figure 3.4.3: *Sampling structure of the hadronic calorimeter.*

of the double-clad WLS fibres is transferred via long clear plastic fibres to the photo detectors. A sketch of 2 tile plates as used in barrel front and rear gaps is shown in Fig. 3.4.4.

The light from all fibres of a cell is summed in light mixers in front of the photodetectors. The number of fibres added varies from 3 for the front cells up to a maximum of 7 fibres in the rear cells. The signal expected for a MIP passing through a small cell (3 sandwich layers) is $\approx 65 \pm 8$ photons. A detailed description of the optical scintillator-fibre light transport is given in [31].

3.4.1.3 Photodetectors

The amount of light produced in a calorimeter cell varies from ≈ 65 photons for MIPs to $\approx 3.6 \times 10^4$ photons when an energy of 50 GeV is deposited in the cell. The photodetectors will have to be able to cover a large dynamic range, and at the same time operate in the large magnetic field of 4 T: Avalanche Photodiodes (APD), Metal Resistor Semiconductor Photodiodes (MRD) or Hybrid Photodiodes (HPD) are possible

HCAL sections	barrel	endcap	pole tip
number of modules	2×16	2×4	2×4
overall dimensions (m^3):	$1.1 \times 1.1 \times 2.7$	$3.1 \times 2.5 \times 1.4$	$2.7 \times 2.7 \times 1.2$
weight/module (t):	16	42	49
polar angle coverage:	$90° - 35°$	$35° - 5°$	$30° - 5°$
Sandwich structure	barrel	endcap	pole tip
depth in cm:	101	140	115
in λ :	4.5	6.2	6.7
sandwich structure Fe/scint/Fibres (mm):	20/5/1.5	20/5/1.5	282/5/1.5
number of layers:	38	53	4
longitudinal segmentation:	9	12	4
Tile/cell structure		barrel and endcap	pole tip
tile sizes:	front	rear	
in cm^2	5×5	25×25	25×25
tiles / cell:	3	7	1
depth in λ:	0.36	0.84	1.7
in X_0:	3.5	8.1	16
number of cells:	128500	73500	2000

Table 3.4.1: *The structure of the hadronic tile calorimeter.*

choices. The most challenging part is the detection of MIPs, where a signal to noise ratio of $\geq 3\sigma$ is needed. This can be achieved e.g. with small capacity APDs having small dark current and low noise [31, 32, 33, 34].

MRDs are as small as APDs and also sufficiently radiation hard, but still are under development and so far not available in large quantities. HPDs have a larger gain than APDs and MRDs, and less noise but they need very large high voltage and thus have larger dimensions and frames. If the gain possible with APDs or MRDs will not be sufficient the light of the fibres can be brought out further to places outside the magnet yoke where only weak magnetic fields are present. There other detectors like mesh tube photomultipliers (PM) or even multianode PMs can be used.

3.4.1.4 Signal conversion

The photodetector signals have to be amplified in preamplifiers before they are sent to analog-to-digital (ADC) converters. It is foreseen to digitise these signals with FADCs running at $100 - 200\,\mathrm{MHz}$, thus allowing not only an energy measurement but also a good time resolution. Proper signal shape and appropriate dynamic range has to be

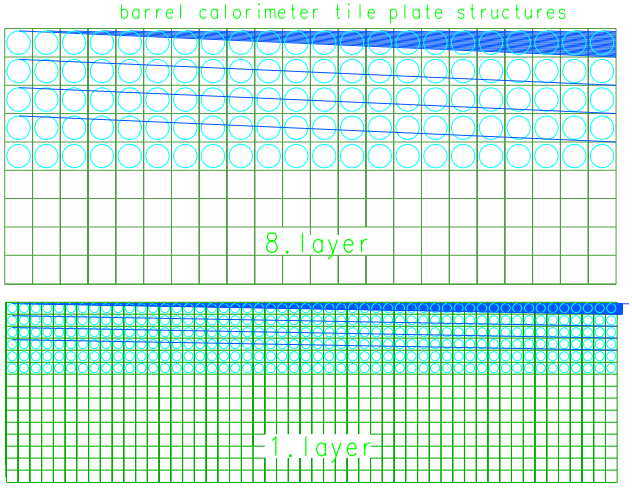

Figure 3.4.4: *Schematic view of 2 tile plates with long fibre readout.*

provided by the preamplifiers circuit with a shaped risetime of ≈20 ns (≥2 time bins) and a pulse width of ≈ 100 ns. The energy range covered between a MIP and the maximum cell signal corresponds to 9 bit. The calibration with cosmic muons requires more precision in the low energy range. Such precision can be achieved by storing the signal with 14 bit accuracy. Other options like low-cost at least 10-bit FACD used in a non-linear mode are under investigation.

A detailed description of the whole readout chain from scintillator tile to digital information of the energy deposed in individual calorimeter cells is presented in [31]. Extensive information on front end electronics is collected in [35, 36].

3.4.1.5 Performance

The depth of the HCAL varies between 4.5 λ in the barrel to 6.2 λ in the endcaps. For the total calorimetric containment 0.9 λ from the ECAL in front and 6.7 λ from the instrumented pole tip behind the endcap calorimeter have to be added. This sums up to 5.4 λ in the barrel and 13.8 λ in the endcap. With such containment the mean energy leakage is only a few % in the barrel region and is negligible in the forward region. Nevertheless for a small fraction of events, a significant amount of energy from leaking shower tails will not be observable. Such events, which might be a signature for new physics, have to be tagged with the muon system (see Section 5).

The large granularity in the HCAL is needed for compensation by software weighting as described in [37, 38, 39], for identification and separation of neutral hadrons in jets and also for muon tracking in the calorimeter volume.

The energy resolution for single hadrons is estimated from simulations of hadronic showers in both calorimeters to be $\sigma_E/E = 35\%/\sqrt{E} \oplus 3\%$, with the energy given in GeV. The large constant term in the energy resolution is partly due to the ECAL in front. The constant term will be significantly reduced when events with leaking showers are excluded and also compensation by software weighting is applied. More detailed

accounts of the performance of very similar systems can be found in [40, 41, 42, 43] and [44].

3.4.1.6 Calibration and monitoring

Good performance of the HCAL needs permanent calibration and monitoring of all calorimeter cells. Cosmic ray muons will pass through the detector continuously. Muons with momenta above 10 GeV/c will pass through the complete detector, and cross up to 9 cells on each side. Even without any other subdetectors the ECAL and the HCAL will be able to recognise such events, so that they can be used to calibrate the detector. Around 200 muons per cell are needed to reach an accuracy below a few percent. Under normal operation conditions, and if the calorimeters are only operated in between TESLA trains, such numbers are obtained within roughly one week even in the smallest cell. In the endcap where the cosmic flux is somewhat reduced muons from the beam halo could be used to calibrate the individual cells.

During collisions some charged hadrons will be available well separated from jets, with momenta well measured by the tracker system. Due to the low useful event rate of only several events per second and the huge number of calorimeter cells to calibrate, about one year of running time is required for a $\approx 3\%$ calibration. A more detailed description of possible monitoring and calibration is available [45].

The stability of the calibration will be monitored with the system of light emitting diodes (LED). Such systems have been demonstrated in the past (see for example [46]) at the required levels of accuracy. A careful monitoring of the temperatures of the different parts of the system will also be needed to maintain the apparatus in stable conditions.

Item	cost / unit [EUR]	cost [MEUR]
Iron		5.0
Scintillator, fibres		2.1
Photo detectors	25	5.5
Preamplifiers	7	1.7
FADC	30	6.5
other (pipelines, etc)		2.3
total cost		23.1

Table 3.4.2: *Cost of the tile version of the hadronic calorimeter.*

3.4.1.7 R&D

The main goal of future R&D will be to optimise the light yield of the tiles, so that when using photodetectors like APDs a good signal to noise ratio is obtained. Therefore detailed studies of the readout structure, of the coupling of the different optical elements

and of the photodetectors have to be done [47]. In addition a good time resolution of $\approx 2\,\text{ns}$, even for MIPs, has to be achieved by optimising the FADC clock frequency ($\approx$ 100–200 MHz) and the shaper signals. Similar work is under way at KEK in Japan [48, 49, 50].

3.4.1.8 Cost

An estimate of the cost of the tile hadronic calorimeter is summarised in Table 3.4.2.

3.4.2 A digital hadronic calorimeter

With an electromagnetic calorimeter as granular as the Si-W proposed in this TDR, and for the precision of the energy flow measurement attempted, a very granular hadron calorimeter is a natural choice. This will provide a refined description of the interactions, allowing a good pattern recognition in the full calorimeter. This is ideal for example in the separation of muons and pions even at low energies. However a solution as adopted for the ECAL, based on SI sensors, is excluded because of the high costs.

An alternative solution is based on the recognition, that, if cells are small enough, simply counting them provides an estimate of the shower energy. This solution has been tried in the past for electromagnetic calorimetry, for example in PEP4 [51], or in early studies for the ALEPH calorimeter; it has been also used or proposed for muon detectors. In the electromagnetic case, a reasonable cell size remains not negligible compared to the shower size and that induces a strong non linearity of the response with energy. This drawback does not concern hadron calorimeters since the hadronic showers are much wider. A number of hadronic calorimeters already have been constructed incorporating digital devices (see for example [52]). With proper analysis algorithms, a resolution very close to that of a calorimeter with the same sampling structure but analogue readout has been obtained [53].

For TESLA a design of a digital hadronic calorimeter with a $1\,\text{cm}^2$ cell size has been developed. It is based on the same mechanical structure as the tile calorimeter presented above. The absorber plates are, as for the tile calorimeter, made of stainless steel plates. The detecting medium can be made of resistive plate chambers, wire chambers operated in limited Geiger mode or even thin wire chambers like in the ALEPH electromagnetic calorimeter. The signals are collected on small pads. In the first two solutions the signal is big enough to switch shift registers, in the second an amplification is needed. The bits are read serially and, as the occupancy is small, zero suppression is applied early. For a better separation between showers the use of heavier radiator is envisaged. An important consideration is that the detector has to be sensitive to a minimum ionising particle.

The response of such a calorimeter has been simulated in detail. It has been shown that the purely digital signal, the number of cells with energy deposited, is linear in energy and that the resolution is even slighly better than the analogue one. In addition to the pure digital information of the number of cells hit, the density of cells, correlations between cells, etc. are used. Given the very large granularity, software

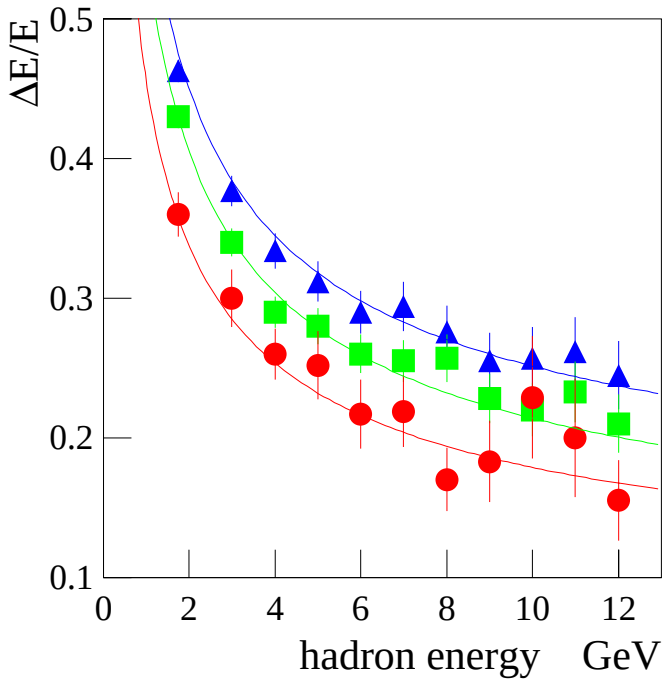

Figure 3.4.5: *Energy resolution using energy deposited in the scintillator (blue triangle), using pad multiplicity(green square) and eventually using more informations from digital pattern (red dots).*

compensation to equalise the response to electrons and hadrons can be applied readily. The energy resolution achieved for an analogue readout, a purely digital readout and one where the number of hits and the distributions of the hits are used, is shown in Fig. 3.4.5.

The performance of such a device together with the Si-W electromagnetic calorimeter has been studied as well. The two main points are the separation of muons and pions, and the jet resolution. The efficiency for isolated muons has been shown to be 99.8 % for a pion contamination of 10^{-3}, down to 2 GeV/c. The resolution for the visible energy of a jet has been shown to be better than $40\%/\sqrt{\mathrm{E}}$. A more detailed description of the performance can be found in the detector performance Chapter (Chapter 9).

3.4.2.1 Cost

An estimation of the cost is summarized in the following table. It is largely based on the cost of the ALEPH electromagnetic calorimeter.

Item	Cost (MEUR)
Stainless steel and structure	7.0
Cathode planes and electronics	9.1
Wire planes	1.6
Gas system	0.6
TOTAL	18.3

Table 3.4.3: *The cost estimate for the digtal hadron calorimeter.*

3.5 Forward Calorimetry

As pointed out in the introduction excellent hermeticity of the detector is needed for many new-physics signatures, some of which predict reactions with large missing energy signals. In addition the instrumentation of the forward region is important for the measurement of the luminosity and the luminosity spectrum.

Therefore the calorimetric coverage of the solid angle is completed by two devices in the very forward region on both sides of the interaction point, the low angle tagger, LAT, and the luminosity calorimeter, LCAL. The LAT will be used primarily to provide good calorimetric coverage in the region between 83.1 and 27.5 mrad. The LCAL covers the regime down to very small angles, to 4.6 mrad. Both devices at the same time are a part of the masking system shielding the detector from backgrounds as described in detail in section 7.1.2.

In Fig. 3.5.1 the placement of the two calorimeters in the mask structure is shown. Both devices have to exist in an area of large backgrounds. In particular the LCAL is subject to an enormous flux of background particles from the beam-beam effects in the interaction region.

3.5.1 Low angle tagger LAT

The Low Angle Tagger LAT is designed to provide an accurate measurement of electrons up to the nominal beam energy (400 GeV in the second stage of TESLA). It extends the electromagnetic calorimetry down to polar angles below 30 mrad. It is placed at the tips of the tungsten mask and serves itself as an additional shield to protect the tracking detectors from backscattered particles (see section 7.1.1).

Its design foresees a tungsten sampling calorimeter. As the beam induced background is comparatively low in the angular region of the LAT, silicon detectors can be used as active elements. The proposed design consists of 63 planes of tungsten (2.6 mm thickness) and silicon (0.5 mm thickness). The segmentation in radial direction foresees 14 segments, the azimuthal segmentation will be 15°. The calorimeter is supported by an inactive tungsten structure (compare figure 3.5.1).

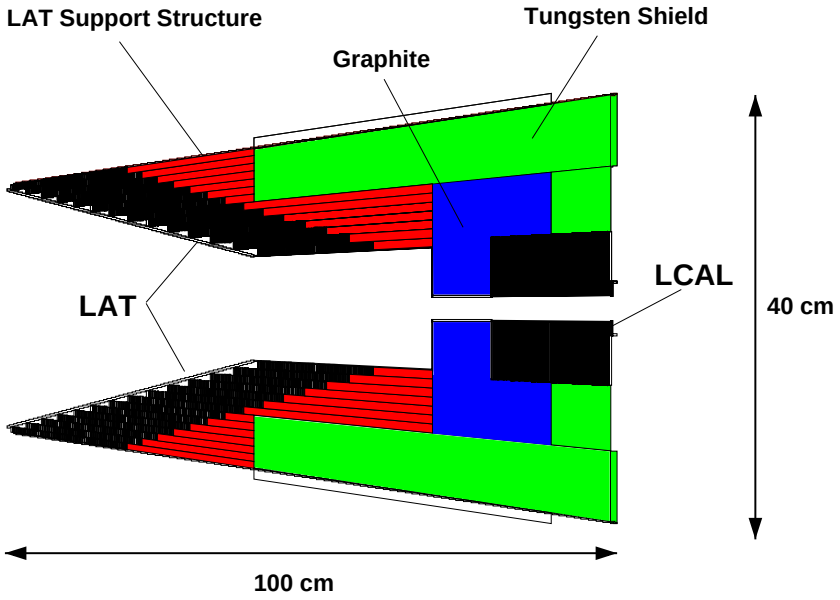

Figure 3.5.1: *Design of the forward angle calorimeters. The sampling calorimeters (LAT and LCAL, shown in black) are integrated into the tungsten shield of the mask.*

3.5.1.1 Readout

For each of the two modules, 21168 channels will have to be read out. Front-end electronics like those of vertex detectors of currently running high-rate experiments (for example HERA-B [54]) could be used. The analogue information from the cells could be buffered in order to make use of the full time interval between pulses to digitise all signals and thus minimise the number of ADC modules. A fast online subtraction of background could be foreseen, to be able to handle larger than expected backgrounds, though according to simulations this should not be strictly needed.

3.5.1.2 Detector performance

The expected performance of the LAT has been studied using its simulated response to high energetic electrons. Fig. 3.5.2 a) shows the energy which is deposited by showers from electrons with 250 GeV energy in the tungsten and silicon layers. It can clearly be seen that the energy which is leaking out of the calorimeter is below 10% and has a reasonably flat angular distribution in the range of interest.

The expected intrinsic energy resolution as calculated from simulations is shown in Fig. 3.5.2 b). A resolution of 20–25% $\times \sqrt{E\,[\mathrm{GeV}]}$, is in reach. The background from e^+e^- pairs on the LAT is comparatively small. The typically deposited energy per bunch crossing is of the order of a few GeV.

Figure 3.5.2: *Response of the LAT to 250 GeV electrons: (a) energy deposited in the LAT, the horizontal line indicates $E = 250$ GeV; (b) energy resolution vs. the polar angle θ.*

3.5.1.3 Cost estimate

The cost estimate for the LAT is given in table 3.5.1. It is based on the assumptions of a price of 100 EUR/kg for tungsten and 3 EUR/cm^2 for silicon.

Item	Cost estimate [kEUR]
Tungsten (active)	18
Tungsten (inactive)	27
Silicon	105
Electronics (incl. cables)	160
Mechanics (processing etc.)	50
Total	360

Table 3.5.1: *Cost estimate for the LAT.*

3.5.2 Luminosity calorimeter LCAL

A detector serving both as a fast luminosity monitor and as a low angle calorimeter will be placed at a distance of 220 cm on both sides of the interaction point, covering an annular surface between radii of 1.2 cm and 6.2 cm from the beam line. As a luminosity monitor, the detector will measure the amount of beam induced background particles. About $2 \cdot 10^4$ electron-positron pairs will hit the LCAL on each side of the detector per bunch crossing, carrying over 20 TeV of energy (section 7.1.3.1). The signal left by

these particles will be used to resolve luminosity variations within one bunch train. The information will be fed back to the beam delivery system to tune the beam (compare section 7.4.4 in Part II of this TDR and [55]). For this purpose, a precision of the order of 1% will have to be achieved within a response time of about 30 to 50 ns. Given the number of particles passing through the detector, a measurement of this precision should be possible. As a calorimeter, the LCAL will be used to measure electron showers in the region between around 6 mrad and 28 mrad. These showers will be used to measure low angle electrons for luminosity measurements and physics studies (see Part III, Chapter 5).

The LCAL must also serve as shielding for the rest of the detector (see section 7.1.2 for a detailed discussion). For this purpose the device is mounted behind a 10 cm thick layer of graphite, and should have a thickness of at least 30 radiation length, to efficiently shield the detector from synchrotron radiation and from particles backscattered from the final focus quadrupoles.

3.5.2.1 Experimental constraints and detector design

The current design of the LCAL foresees a sampling calorimeter with 63 planes of tungsten absorber, interleaved with 63 active layers equipped with either silicon or diamond sensors (see Fig. 3.5.3). The total length of a module is 20 cm. The sensing planes are 500 μm thick. They are divided radially into 7 rings of equal width, each subdivided azimuthally into 24 sectors. The cells thus vary from a surface of 0.3 cm^2 for the inner ring to 1.1 cm^2 for the outer ring. Each tungsten plate is about 2 mm thick, for a total of 36 radiation lengths for a complete module.

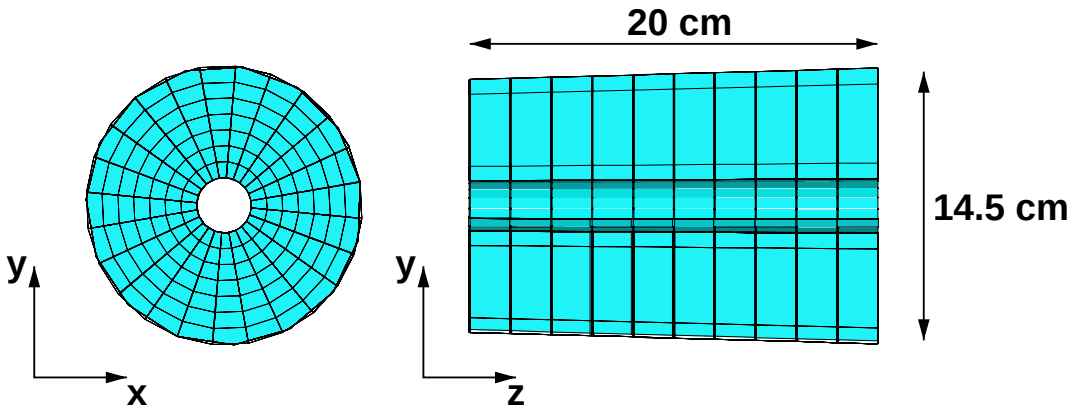

Figure 3.5.3: *Design of the LCAL. The segmentation in z direction consists of 63 planes of tungsten and sensors (not shown in this figure).*

A particular challenge for the design of the device is the high level of electromagnetic radiation present in the area where the LCAL should be installed. In the region of the

LCAL close to the beam, electromagnetic doses of the order of 1 MGy per year [1] are expected. Figure 3.5.4 shows the energy deposited per bunch and the dose per year as a function of the plane number and radial position. To operate several years without interventions, the detector should be able to sustain a dose of the order of 10 MGy. Conventional Si detectors might not survive long enough in this environment, particulary in the region close to the beam line where the background is highest. An attractive alternative to Si sensors are diamond sensors, which have been extensively studied over the last years [56, 57]. They are extremely radiation hard, and have been tested for fluences of hadronic radiation of the order of 10^{15}/year/cm^2 [58, 59]. For electromagnetic radiation dedicated tests were done to doses of up to 0.1 MGy only [60], but they are expected to be able to sustain much larger doses. Silicon detectors were tested up to gamma irradiations of 4 MGy [61]. Although standard silicon reaches space charge sign inversion at doses of about 2.5 MGy, oxygenated silicon was found to sustain the full 4 MGy without indications of any damage. Silicon detectors often need cooling, which might prove to be a hindrance given the space constraints on the LCAL.

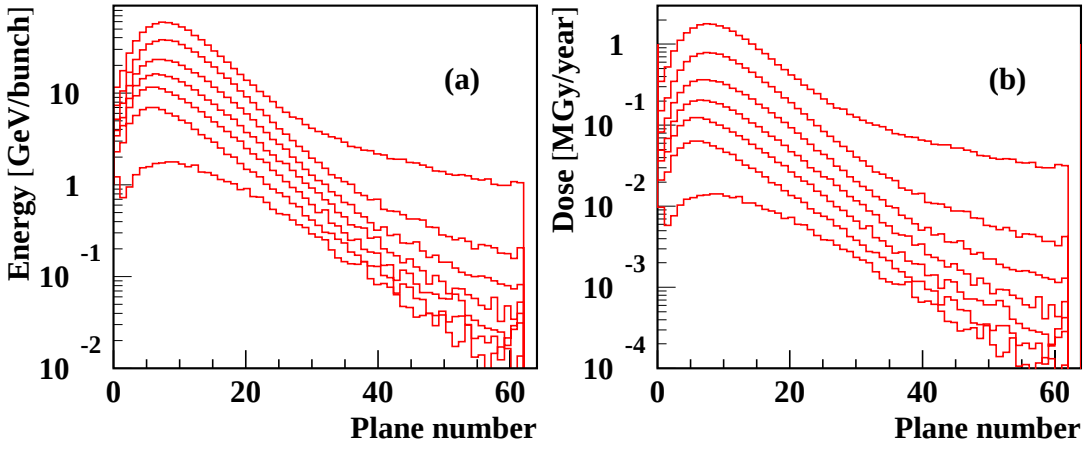

Figure 3.5.4: *a): Energy deposited per bunch crossing and b): yearly radiation dose as a function of the plane number. The plane number runs from 1 to 63 between the plane closest and the plane farthest from the interaction point. On each figure, the lowest curve corresponds to the outer ring and the highest curve to the inner ring of the LCAL.*

[1] For the current discussion, a year is defined as 2.3×10^{11} bunch crossings (6 months of running at 5 Hz and 3000 bunches per bunch train).

3.5.2.2 Readout

The readout for the LCAL could be very similar to that of the LAT. The signals for the luminosity measurement and those for the calorimetric measurements however will be treated differently. To monitor the luminosity, the first plane will be used to give a signal proportional to the number of incoming particles from the beam induced background. The sum of the analog signals of the first plane will be transfered directly to a fast acquisition system and made available to the machine.

The signals from the different planes will be used for energy measurements. To minimize data volume, background subtraction could be done after digitization using information from previous bunch crossings, and zero suppression could be applied. The treatment of the signals is currently being investigated. Energies of up to 4 GeV per bunch crossing can be deposited in some of the cells closest to the beam line. The behavior of solid state detectors under such conditions and the final choice for a readout scheme remains the topic of further research.

3.5.2.3 Performance

The energy resolution of the LCAL will not so much be determined by the intrinsic detector resolution, but rather dominated by the error introduced by the subtraction of the large background. Subtraction of the background could be done using the average signal of previous bunches. Given the very large amount of beam induced background, the error on the background energy measurement in each cell is expected to be smaller than the systematic error on the absolute level of the background calculated from previous bunches. This systematic error is expected to be at the level of the percent, corresponding to the expected variations of the luminosity from bunch to bunch.

The detector optimization was done using simulated showers from 250 GeV electrons. The number of diamond planes was chosen such that the contribution of the intrinsic resolution of the calorimeter to the total uncertainty on the energy measurement was equal to the systematic error coming from background subtraction at large angle. To minimize the energy to be subtracted, only the area of 3×3 cells in $r - \phi$ centred on the peak maximum was considered. Figure 3.5.5 shows the intrinsic resolution of the calorimeter and the total uncertainty on the energy measurement. In the central part of the calorimeter between 0.01 and 0.025 rad, we expect a resolution approximately given by:

$$\Delta E\,[\mathrm{GeV}] \simeq 10\% \cdot \sqrt{E\,[\mathrm{GeV}]} \oplus (34.0 - 1.3 \cdot \Theta\,[\mathrm{mrad}])\,.$$

Figure 3.5.5 shows the 90% CL energy for electron detection. This indicates that if an electron with more than the 90% CL energy is hitting the LCAL, the probability that the background fluctuates to the same level (which makes the background-signal separation impossible) is below 10%. The visible structure is due to border effects appearing when summing the cells in the 3×3 area of $r - \phi$ cells centred on the peak maximum. It can be seen, that the detection of electrons with more than 50 GeV should be possible down to polar angles of 5 mrad.

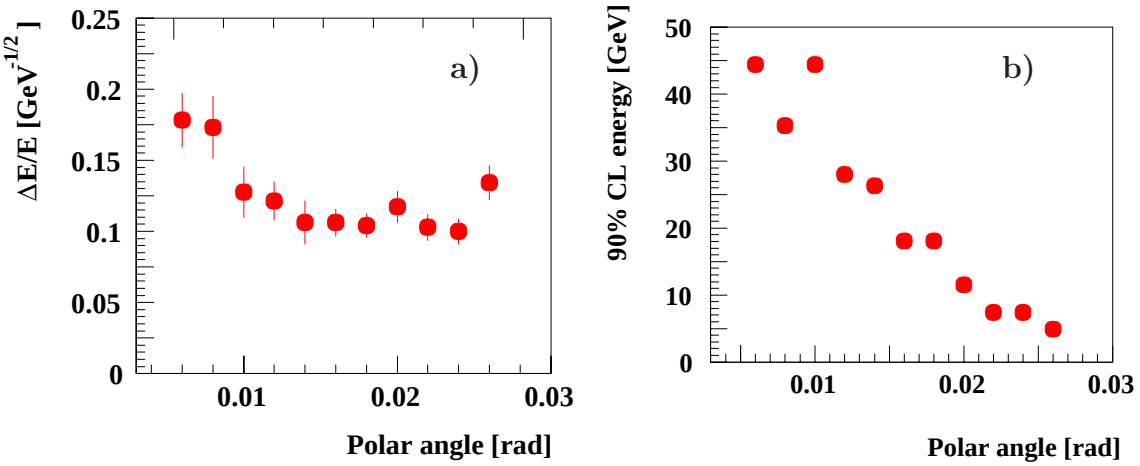

Figure 3.5.5: *a): Intrinsic energy resolution of the calorimeter versus the polar angle for 250 GeV electrons. b): Detection capability of the LCAL. Shown is the 90% CL energy vs. the polar angle, see text for explanation.*

3.5.2.4 Cost estimate

The cost of the LCAL is given in table 3.5.2. The base of the cost estimate is a price of 100 EUR/kg for Tungsten, 3 EUR/cm^2 for silicon and 5 EUR/mm^2 for diamond. If the detector would be build entirely with diamond sensors, the price would increase by $\approx$ 5MEUR. Most probably the final detector would be a combination of a few rings and layers of diamond in those areas which are subject to large radiation doses, with Si detectors for the majority of the sensors.

Item	Cost for silicon opt. [kEUR]
Tungsten (active)	5
Silicon	30
Electronics (incl. cables)	80
Mechanics (processing etc.)	50
Total	165

Table 3.5.2: *Cost estimate for the LCAL.*

Bibliography

[1] A. Karar and C. de la Taille. Silicon Diode, Readout and Front-end Electronics of the proposed W-Si electromagnetic Calorimeter. *LC-DET-2001-059*, 2000. http://www.desy.de/~lcnotes electronic document.

[2] Laboratoire de physique des interfaces et couches minces. http://www.lpicm.polytechnique.fr.

[3] J.-C. Brient. On the Calibration of the W-Si ECAL proposed for TESLA. *LC-DET-2001-057*, 2001. http://www.desy.de/~lcnotes electronic document.

[4] GEANT4-Collaboration: K. Amako. Present Status of GEANT4. *Nucl. Instrum. Meth.*, A453:455–460, 2000, and references therein. electronic document.

[5] W. R. Nelson, H. Hirayama, and D. W. O. Rogers. The EGS4 Code System. *SLAC-265*. Stanford Linear Accelerator Center, 1985.

[6] H. Hirayama, Y. Namito, and S. Ban (eds.). *EGS4. Proceedings, 8th Users' Meeting*. 1999. KEK-proceedings 99-15, Tsukuba, Japan.

[7] J.-C. Brient et al. Si-W Calorimeter Performances. *LC-DET-2001-058*, 2001. http://www.desy.de/~lcnotes electronic document.

[8] J. Badier et al. *Nucl. Instrum. Meth.*, A348:74–86, 1994.

[9] H. B. Collaboration. *HERA–B Design Report*. DESY-PRC 95/01. DESY, http://www-hera-b.desy.de/general/publications/proposal, 1995.

[10] DELPHI-Collaboration: S. J. Alvsvaag et al. The small Angle Tile Calorimeter in the DELPHI Experiment. *Nucl. Instrum. Meth.*, A425:106–139, 1999. electronic document.

[11] H. Fessler et al. *Nucl. Instrum. Meth.*, A240:284, 1985.

[12] G. S. Atoyan et al. *Nucl. Instrum. Meth.*, A320:144, 1992.

[13] R. Brinkmann, G. Materlik, J. Rossbach, and A. Wagner (eds.). *Conceptual Design of a 500 GeV e^+e^- Linear Collider with Integrated X-Ray Laser Facility*. DESY, 1997. http://tesla.desy.de/TTF_Report/CDR/TTFcdrTab.html.

[14] CALEIDO-Collaboration: A. C. Benvenuti et al. An electromagnetic Shashlik Calorimeter with longitudinal Segmentation. *Nucl. Instrum. Meth.*, A432:232, 1999. electronic document.

[15] *Poster presented by M. Margoni at 1999 IEEE Nuclear Science Symposium & Medical Imaging Conference*, Seattle, USA October 24-30, 1999, to be published in IEEE Transaction in Nuclear Science.

[16] CALEIDO-Collaboration: A. C. Benvenuti et al. Overview of an Electromagnetic Calorimeter for a Linear Collider based on the Shashlik Technique with longitudinal Segmentation. *LC-DET-2001-027*, 2001. http://www.desy.de/~lcnotes electronic document.

[17] P. Checchia et al. A Shashlik Calorimeter with longitudinal Segmentation for a Linear Collider. In *Proceedings of the IX Int. Conf. on Calorimetry in Part. Phys.*. To be published in Frascati Physics Series (2001), http://wwwlapp.in2p3.fr/Calor2000/Calor2000_Contributions.html.

[18] G. A. Akopdjanov et al. *Nucl. Instrum. Meth.*, A140:441, 1977.

[19] T. Behnke et al. BRAHMS: A Monte Carlo for a Detector at a 500/800 GeV Linear Collider. *LC-TOOL-2001-005*, 2001. http://www.desy.de/~lcnotes/ electronic document.

[20] CDF Plug Group, A scintillating Tile / Fiber System for the CDF Plug Upgrade EM Calorimeter. *Nucl. Instrum. Meth.*, A352:557, 1995. electronic document.

[21] S. Kim et al. R & D and Mass Production of a scintillating Tile / Fiber System for the CDF Plug Upgrade EM Calorimeter. *Nucl. Instrum. Meth.*, A360:206, 1995. electronic document.

[22] CDF-Collaboration: The CDF II Detector Technical Design Report. *Fermilab-Pub-96/390E*, 1996.

[23] G. Aguillion et al. Thin Scintillating Tiles with High Light Yield for the OPAL Endcaps. *Nucl. Instrum. Meth.*, A417:266, 1998. electronic document, SLACcitation =.

[24] ATLAS-Collaboration: W. W. Armstrong et al. ATLAS: Technical Proposal for a General-Purpose pp Experiment at the Large Hadron Collider at CERN. *CERN-LHCC-94-43*, 1994.

[25] ATLAS-Collaboration: ATLAS Liquid Argon Calorimeter: Technical Design Report. *CERN-LHCC-96-41*, 1996.

[26] A. Gomes. Calorimetry using Organic Scintillators. *Proceedings of the VIII. International Conference on Calorimetry in High Energy Physics*, 474, Lisbon, 1999.

[27] CMS-Collaboration: V. V. Abramov et al. The Hadron Calorimeter Project Technical Design Report. *CERN/LHCC/97-31*, 1997.

[28] C. Martens. The Mechanical Design of the HCAL Detector for TESLA. *LC-DET-2001-046*, 2001. http://www.desy.de/~lcnotes/ electronic document.

[29] P. Hassler et al. The Hadronic Tile Calorimeter for the TESLA Detector, Design, Construction, and Installation. *LC-DET-2001-049*, 2001. http://www.desy.de/~lcnotes/ electronic document.

[30] V. Korbel. The hadronic Tile Calorimeter for the TESLA Detector. *Proceedings of the Linear Collider Workshop 2000, LCWS2000, to be published*, 2000. http://www-lc.fnal.gov/lcws2000.

[31] V. Korbel. The Optical Read Out of the HCAL Tile Calorimeter. *LC-DET-2001-052*, 2001. http://www.desy.de/~lcnotes/

electronic document.

[32] K. Deiters et al. Properties of the Avalanche Photodiodes for the CMS Electromagnetic Calorimeter. *Proceedings of the VII. International Conference on Instrumentation for Colliding Beam Physics*, (223), Hamamatsu, Japan, 1999. electronic document.

[33] A. Karar, J. C. Vanel, and Y. Musienko. Characterization of Avalanche Photodiodes for Calorimetry Applications. *Nucl. Instrum. Meth.*, A428:413–431, 1999. electronic document.

[34] C. Cheshkov et al. Application of Avalanche Photodiodes as a Readout for Scintillator-Tile Fibre Systems. *Nucl. Instrum. Meth.*, (A 440):38, 2000. electronic document.

[35] C. de la Taille. Front End Electronics in Fast Calorimetry. *Proceedings of the VIII. International Conference on Calorimetry in High Energy Physics, Lisbon*, 557, 1999.

[36] Proceedings of the 6th. Workshop on Electronics for LHC Experiments, Cracow. *CERN/LHCC/2000-041*, 557, 2000.

[37] C. Issever. The Calibration of the H1 Liquid Argon Calorimeter. *Proceedings of the IX. International Conference on Calorimetry in Particle Physics*, Annecy, 2000,to be published.

[38] J. P. Kubenka et al. *H1 Internal Note*, (H1-02/94-364), 1994. electronic document.

[39] C. Issever. *H1 Internal Note*, (DESY-FH1-96-06), 1996. electronic document.

[40] J. Proudfoot. Calorimetry using Organic Scintillators. *Proceedings of the VIII. International Conference on Calorimetry in High Energy Physics*, 380, Lisbon, 1999.

[41] B. D. Girolamo. Calorimetry using Organic Scintillators. *Proceedings of the VIII. International Conference on Calorimetry in High Energy Physics*, 386, Lisbon, 1999.

[42] ATLAS-Collaboration: A. Airapetian et al. ATLAS Calorimeter Performance. *CERN-LHCC-96-40*, 1996.

[43] S. Akhmadalievet et al. *Nucl. Instrum. Meth.*, (A449):461, 2000. electronic document.

[44] W. Wu. Physics Capabilities of the CMS Hadron Calorimeter. *Proceedings of the VIII. International Conference on Calorimetry in High Energy Physics*, 394, Lisbon, 1999.

[45] V. Korbel and P. Steffen. Calibration and Monitoring of the HCAL Tile Calorimeter. *LC-DET-2001-051*, 2001. http://www.desy.de/~lcnotes/ electronic document.

[46] J. Janoth. Das Kalibrationssystem CAM fuer das neue Kalorimeter SpaCal des

Detektors H1 bei HERA und Analyse erster Daten. *Dissertation, Heidelberg, HD-IHEP 96-17*, 2000.

[47] V. Korbel, V. Morgunov, and V. Saveliev. R&D for the TESLA Tile Calorimeter HCAL. *LC-DET-2001-050*, 2001. http://www.desy.de/~lcnotes/ electronic document.

[48] Y. Fujii. Calorimetry using Organic Scintillators. *Proceedings of the VII. International Conference on Instrumentation for Colliding Beam Physics*, 237, Hamamatsu, Japan, 1999. electronic document.

[49] T. Suzuki et al. A Systematic Measurement of Energy Resolution and e/pi Ratio of a Lead/Plastic-Scintillator sampling Calorimeter. *Nucl. Instrum. Meth.*, A432:48–65, 1999. electronic document.

[50] T. Takeshita. Tile/Fibre Hadron Calorimeter Performance. *Proceedings of the Linear Collider Workshop 2000, LCWS2000, to be published*, 2000.

[51] A. Barbaro-Galtieri et al. Tests of Gas Sampling Electromagnetic Shower Calorimeter. *Nucl. Instrum. Meth.*, A213:223, 1983.

[52] ALEPH-Collaboration: D. Decamp et al. ALEPH: A Detector for Electron - Positron Annihilations at LEP. *Nucl. Instrum. Meth.*, A294:121, 1990.

[53] J.-C. Brient, talks given at ECFA/DESY workshop, May 2000, Padova.

[54] C. Bauer et al. First Experience and Results from the HERA-B Vertex Detector System. *Nucl. Instrum. Meth.*, A418:65–79, 1998. electronic document.

[55] O. Napoly and D. Schulte. Luminosity Monitor Options for TESLA. In *Proceedings of XIX International Linear Accelerator Conference, LINAC 98*, Chicago, IL, USA, 1998. http://www.aps.anl.gov/conferences/LINAC98/.

[56] W. Adam et al. Review of the Development of Diamond Radiation Sensors. In *Proceedings of International Workshop on GaAs and Related Compounds*, Praha-Pruhonice, 1998.

[57] A. Oh. Particle Detection with CVD Diamond. DESY-THESIS-1999-022.

[58] W. Adam et al. Performance of Irradiated CVD Diamond Micro-Strip Sensors. In *Proceedings of Int. Conf. Rad. Eff. on Semicond. and Mat.*, Florence, Italy, 2000. CERN-EP-2000-115 electronic document.

[59] A. Oh, M. Moll, A. Wagner, and W. Zeuner. Neutron Irradiation Studies with Detector Grade CVD Diamond. *Diamond and related Materials*, 9(11):1897, 2000.

[60] RD42-Collaboration: C. Bauer et al. Recent Results from Diamond Microstrip Detectors. *Nucl. Instrum. Meth.*, A367:202–206, 1995. electronic document.

[61] RD48(ROSE)-Collaboration: M. Moll, E. Fretwurst, and G. Lindström. Investigation on the improved Radiation Hardness of Silicon Detectors with high Oxygen Concentration. *Nucl. Instrum. Meth.*, A439:282–292, 2000. electronic document.

4 Coil

The TESLA magnet has been designed to provide a solenoidal magnetic field of 4 T along z in the central region of the detector. The tracking detectors, the electromagnetic and the hadronic calorimeter are all located inside the magnet. The iron return yoke serves as a muon detector. The TESLA magnet is based on the design for the CMS experiment [1]. This provides a solid base for the specification and design of the magnet. In addition significant time and money can be saved in the development of the magnet components. The first tests of the CMS magnet have been scheduled for the beginning of 2004. Experience gained in this work will enter into the TESLA design.

The largest difference between the TESLA and the CMS design is that TESLA has more stringent requirements on the homogeneity of the magnetic field. Therefore a novel system of correction coils has been developed, using parts of the main windings of the magnet.

4.1 Magnet Specifications

The main requests from physics for the TESLA magnet are a solenoidal central field of 4 T, in a volume of 6 m in diameter and with a high integral field homogeneity,

$$\left| \int_0^{2.5\mathrm{m}} (B_r/B_z)\mathrm{d}z \right| \leq 2\,\mathrm{mm}$$

with

$$B_r = B_x(x/r) + B_y(y/r) \ .$$

This very good homogeneity should primarily apply to the TPC volume, which is a cylinder 3.2 m in diameter and 5 m length. To accommodate the inner detectors including the calorimeters a length of 8.5 m must be clear inside the magnet aperture. The iron return yoke will have to be instrumented for muon detection.

There are no especially stringent requirements from the machine on the quality of the magnetic field. However the two final focusing quadrupole doublets will be inside the detector magnet bore, and therefore subject to high magnetic fields, which influences the design of these quadrupoles.

4.1.1 Magnet layout

The magnet consists of the solenoidal coil and of the iron yoke, subdivided between the barrel yoke and the two end-cap yokes. The coil is subdivided into five modules with four layer windings each.

Preliminary calculations have shown that a coil length of 9.2 m and an iron thickness of 1.6 m are a good choice to obtain the requested magnetic field parameters. To reach the required field accuracy, correction coils are needed at the two ends of the magnets. They have been incorporated into the main windings, by changing the current in the outermost windings. Technically this means that different power leads will feed power to the outer and the other windings separately.

A cross section of the magnet is shown in figure 4.1.1.

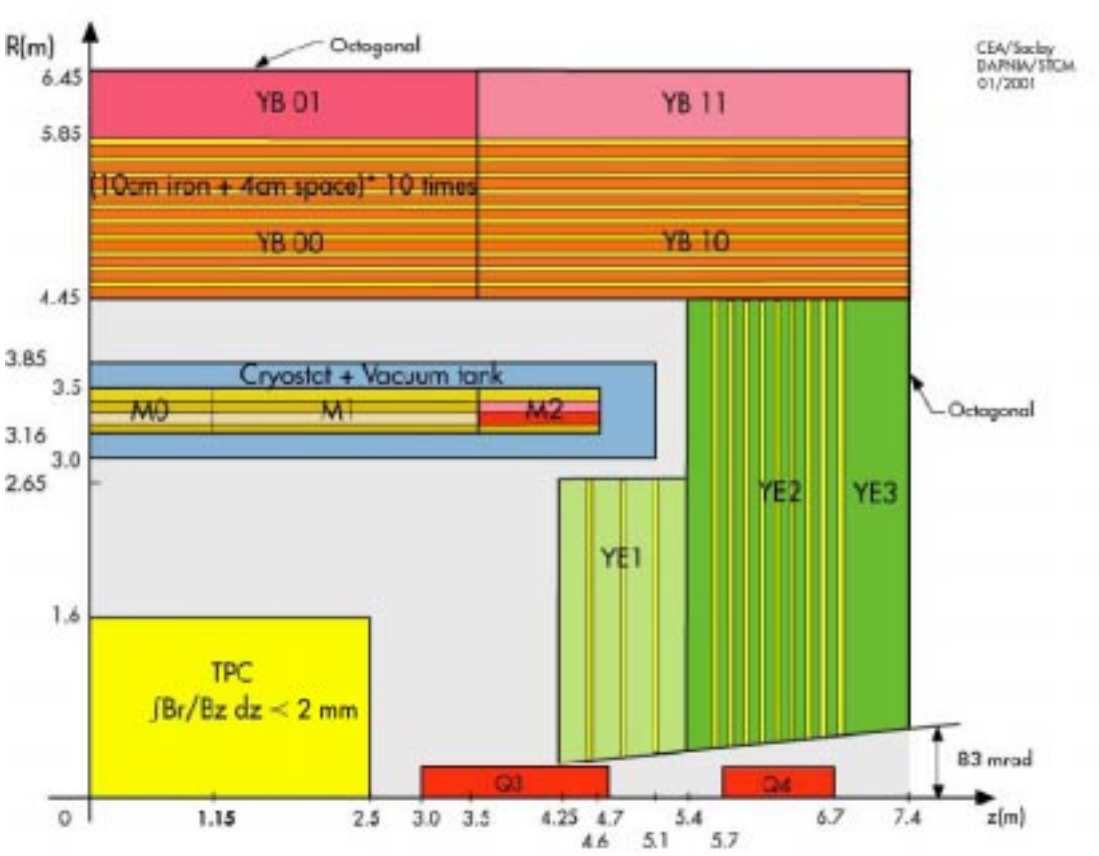

Figure 4.1.1: *Cross-section of one quarter of the magnet and the iron return yoke.*

In some detail the different parts of the magnet have the following properties:

- The coil consists of five modules, electrically and mechanically connected :
  - The three central modules are 2.35 m long each.
  - The two external modules are 1.1 m long each.
  - Each module consists of a four layer winding. The nominal main current is 18.8 kA for the central field of 4.0 T. An extra correction current of about

24.5 kA must be added to the turns of the two middle layers of the two external modules to reach the integral field homogeneity.

- The barrel yoke, of octagonal shape, has an inner radius of 4.45 m, an outer radius of 6.45 m and a total length of 7 m. Radially the yoke is subdivided into 10 layers of 10 cm iron plate and 4 cm space for muon chambers. At the outer radius the yoke is completed by a 60 cm thick layer of solid iron.
- The end cap yokes, also of octagonal shape, are each 3.9 m long. They are vertically split into two parts, to enable opening the detector without removing the beam pipe. A magnetic-iron pole tip is added in front of the end-cap, at the back of the hadronic calorimeter, inside the magnet aperture, to improve the field homogeneity.

The relevant geometric, magnetic and electric parameters of the detector magnet are given in Table 4.1.1.

	Dimensions
Cryostat inner radius (m)	3.00
Coil inner radius (m)	3.16
Coil outer radius (m)	3.50
Cryostat outer radius (m)	3.85
Barrel yoke inner radius (m)	4.45
Barrel yoke outer radius (m)	6.45
Coil length (m)	9.20
Cryostat length (m)	10.20
Yoke overall length (m)	14.80
	Magnetic field
Central field (T)	4.00
Maximum field on conductor (T)	4.70
Stored energy (GJ)	2.32
Nominal main current (A)	18 800
Nominal correction current (A)	24 500
Ampere-turns main coil (At)	298 106
Ampere-turns correction coils (At)	47 106
	Weight
Cold mass (t)	200
Barrel yoke (t)	6 400
End cap yoke (t)	2 000
Total magnet (t)	8 600

Table 4.1.1: *Main parameters of the magnet.*

4.1.2 Magnetic field

The integral field homogeneity, calculated with the nominal values of the main and correction currents, is shown in Fig 4.1.2. The field homogeneity is better than the requirement, the maximum calculated deviation being 25% smaller than the allocated one (1.45 mm vs 2 mm). It has been checked that, in the TPC volume, the stray-field

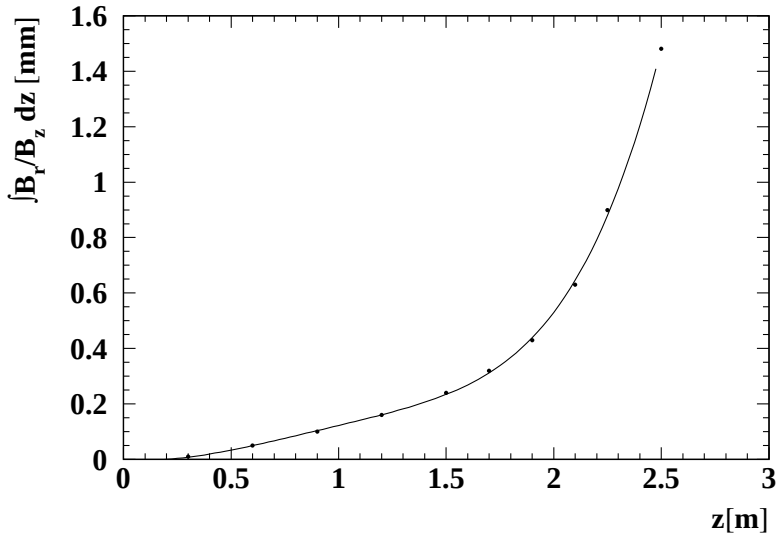

Figure 4.1.2: *Calculated maximum magnetic integral field homogeneity.*

of the quadrupole doublets has no influence on the field homogeneity of the detector magnet.

The biggest technological challenge of the magnet construction will be to actually ensure the requested magnetic field homogeneity. It implies that the B_x and B_y components of the fields have to be determined with a relative accuracy in the range of 0.2%. A device with Hall probes, an updated version of those previously used for the mapping of the ALEPH, DELPHI and H1 magnets, can meet these requirements.

4.2 Technical Aspects

In this part some technical points are summarised, which are developed in more detail elsewhere [2].

4.2.1 Conductor

The conductor design is similar to that for CMS [3]. It consists of a superconducting cable coextruded in a very pure aluminium and mechanically reinforced. Two different

conductors are necessary, one carrying the nominal current, one carrying the nominal and the extra correction current. Practically, the increase of the current capacity will be done by increasing the number and the diameter of the strands of the cable, but the overall dimensions of both conductors will be the same.

The winding will be done using a inner winding technique, similar to the CMS one [4]. Al-alloy cylinders will be used as outer mandrels for the modules. The assembly of the five modules will follow either on the DESY site or on the winding-manufacturer's site, if the transportation of the assembled coil is possible. The magnetic forces are contained both by the local reinforcement of the conductor, made of Al-alloy strips, and by the outer mandrels, thick enough to act as a mechanical support. The superconducting coil will be indirectly cooled by saturated liquid helium at 4.5 K, circulating in a thermosiphon mode.

4.2.2 Yoke

Both the barrel and end-cap yokes will be built using iron plates, the dimensions of which have been determined taking into account production and transportation requirements. The yoke assembly will not use welds, but bolts throughout, so that a trial assembly can be made before the final assembly.

4.2.3 Ancillaries

The main ancillaries required for the detector magnet are the cryogenic plant, the electrical power circuit and the control and monitoring system.

Cryogenic plant

The electrical power needed to maintain the magnet cold at 4.5 K is around 1 kW. It should be noted that with some adaptations, this cryogenics system could also be used for supplying the quadrupole doublets (foreseen to be working at 1.8 K).

The magnet cryogenic plant will include compressors, helium gas and liquid nitrogen storage containers, a cold box, the transfer lines and an intermediate cryostat for liquid helium storage in case of failure of the main refrigeration system.

Electrical power circuit

The electrical power supply will consist of :

- a main bipolar power supply (20 kA, $\pm$25 V);
- two correction bipolar power supplies (25 kA, $\pm$5 V), one for each correction winding;
- the related switch breakers, dump resistances and electrical busbars for discharge of the magnet in the case of a loss of power or quench.

A control and monitoring system will control and monitor the cryogenics and the electrical circuits and will provide the safety of the magnet.

	cost [MEUR]
Coil:	
conductor	9.5
winding operation	10.0
internal cryogenics and suspension	3.0
tooling for assembly	1.2
total for coil	23.7
Yoke and Vacuum tank	25.0
Ancillaries:	
cryogenic plant	4.3
electrical power circuit	1.9
control / monitoring system	1.3
total for Ancillaries	7.5
Miscellaneous (external manpower, test, etc.)	8.8
Total	65.0

Table 4.4.1: *Table of the cost of the detector magnet. The manpower costs listed are those for external manpower only.*

4.3 Magnet Assembly and Interface with Subdetectors

After the modules have been assembled, they will be enclosed in the vacuum tank which is the external part of the cryostat. The vacuum tank will be supported in a cantilevered way by the central part of the barrel yoke. The outer parts of the barrel yoke and the end cap yokes will be then assembled.

All the main parts of the yoke must be easily movable for opening the magnet and accessing the various detector parts. The inner tank will support the complete inner detector, including the hadronic and electromagnetic calorimeter, and the TPC.

4.4 Costs

The cost estimate is based on industrial offers for the CMS magnet. A breakdown of the main components is given in table 4.4.1. The total cost of the magnet adds up to 65 M EUR.

4.4.1 Manpower requirements

Few new developments are foreseen for the TESLA detector magnet. The laboratory manpower will be primarily needed for the final design of the project, the following of

industrial contributions, and tests. It is estimated that a total of about 200 man years are needed over the construction period of six years.

4.4.2 Planning

After approval a minimum period of six years is needed to build and test the magnet :

- one year to finalise the detailed design;
- one year to place the main orders;
- three years to produce the conductor, the modules and the yoke;
- one year to do the final assembly and the cryogenic tests.

4.5 Conclusion

The design of the TESLA detector magnet has already reached a mature state due to the fact that the magnet is similar to that of the CMS magnet. No major technical problems are foreseen, although both the absolute magnetic field of 4 T and the homogeneity requirements are a challenge to the builders of this device.

Bibliography

[1] CMS collaboration, *The Magnet Project*, Technical Design Report, CERN / LHCC 97-10, May 1997.

[2] F. Kircher, B. Gastineau, V. Klioukhine, Y. Pabot, *The TESLA Detector Magnet*, LC-DET-2001-056, 2001. electronic document.

[3] I. L. Horwath et al. ,*The CMS Conductor*, IEEE Trans. on Applied Superconductivity, vol 10,No 1, 395, March 2000.

[4] P. F. Fabbricatore et al., *Pre-industrialisation Activities Related to CMS Coil Winding*, submitted to Applied Superconductivity Conference, Virginia Beach, USA, September 2000.

5 Muon System

The basic task for a muon detector is to identify muons and provide a hardware and/or software trigger for them. A muon system should ideally also be able to perform momentum measurements for penetrating particles; however, the benign environment of e^+ e^- collisions allows the unequivocal association of muon candidates with inner detector tracks, so that momenta for charged tracks can be obtained independently from it.

Another purpose of the muon identifier is the tail catching of hadronic showers; with suitable longitudinal segmentation this device can provide calorimetric information and be used either to tag events in which a large portion of energy is not contained in the calorimeters or to add back the measured energy released in it.

The muon identifier is located behind the calorimeters and the coil. The iron of the flux return is used as an absorber and, for this purpose, is segmented in slabs whose thickness (and therefore number, as usually the overall thickness comes from magnetic flux containment) is defined by the required robustness of the μ identification performance and by the calorimetric resolution one would like to obtain in the tail catching mode. In the TESLA detector, the overall iron thickness needed to contain a 4 T solenoidal field is about 1.6 m. This figure in turn yields a hadron rejection ratio for punch-through hadrons at the level of one percent or less. The number of active detector planes must be chosen keeping in mind that muon efficiency would be better at finer segmentations as detection techniques for muons rely on measuring both total amount of traversed interaction lengths and track continuity in the interaction with a radiator material.

The area to be covered with active devices is a factor that limits the overall longitudinal segmentation of this subsystem and severely constrains the usable technologies.

Most of the complications in the design and realization of muon detectors come from the requirement that they should operate on a stand-alone basis and accomplish both μ-identification and momentum measurement for penetrating particles; detectors for high energy hadron colliders [1, 2] have also to cope with a remarkable amount of physics background, as the influx of particles coming from uninteresting processes tends to crowd the detector requiring a high sustainable local rate capability. Neither of these problems can be regarded as very serious in case of e^+ e^- collisions, at least in the region of polar angles $\geq$ 150 mrad. The muon detector, as one can see with available simulation tools, will work at a relatively low occupancy and even in the worst type scenario of very dense jets, it will always be possible with the TESLA detector geometry to match inner tracks with muon track candidates. As far as local rate is concerned, by studying the environment for dense jets, $e^+e^- \rightarrow b\bar{b}$ for instance, one can see that at the first active layer of the detector maximum local hit density is

low. (see Fig. 5.0.1)

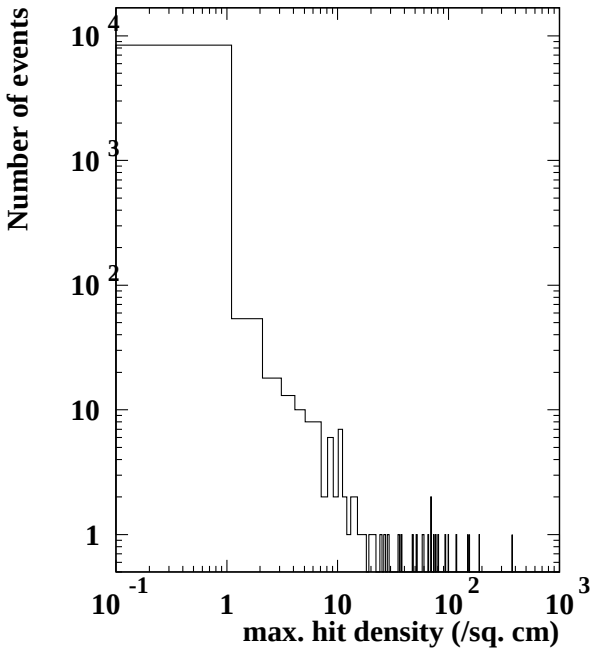

Figure 5.0.1: *Distribution of max. hit density (#/cm^2) at the front face of the muon identifier for* $b\bar{b}$ *events: one entry per event is plotted in the histogram.*

The association of inner tracks with muon track segments at the front face of the muon detector depends on two main experimental parameters: the threshold momentum and the spatial resolution of the device. Given the dimensions and the magnetic field we plan to use, full efficiency is reached above 5 GeV/c, as shown in Fig. 5.0.2.

The spatial resolution needed for the association with a track from the inner detector is constrained by multiple scattering which is relevant for relatively low energy muons inside jets, for example $e^+ e^- \rightarrow b\bar{b}$. The average momentum for this class of muons is 20 GeV/c. The spatial spread for single muons tracked through the detector is shown in Fig. 5.0.3. The width of the distribution of a few cm corresponds to an angular resolution of the order of few mrad; this value, as will be shown in detail in the following sections, is sufficient to obtain a good association of charged tracks from inner detectors.

The energy leakage one can expect out of the calorimetric system of the TESLA detector is small but still sizable on the scale of the energy resolution one would like to obtain: using $b\bar{b}$ jet events at $\sqrt{s} = 500$ GeV one finds that about 5% of charged tracks do leave some energy in the muon system. The energy spectrum, at the front face of the muon system for these events can be seen in Fig. 5.0.4.

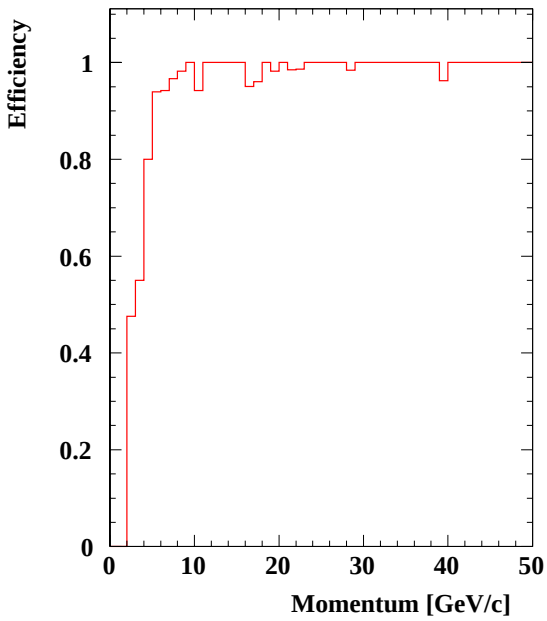

Figure 5.0.2: *Identification efficiency for single μ's in the barrel region. The threshold at $\approx 5\,GeV/c$ comes from the amount of material in front of the muon identified (essentially calorimeters and coil), from the magnetic field and the radial dimensions of the device.*

Releases greater than 20 GeV per track happen with a probability of around 0.1%; for the class of events used, the average charged multiplicity is 38 and this translates into a probability per event of having more than 20 GeV released in the muon system of the order of 4%. It is reasonable then to design a system capable of measuring this energy with a fractional precision of the order of 40%.

5.1 Technologies

Instrumenting the flux return of a general purpose detector for colliding beams brings about the problem of covering a large area with devices that will be difficult to replace in case of failure. Large dimensions also imply that output signals must be routed to collection points by means of relatively long cables. The chosen technology therefore should allow the construction of very reliable detectors which are inexpensive and which can be used to cover large areas. Large pulses would be helpful to keep the readout electronics simple. Time resolution of the device is not extremely important, given the bunch spacing one expects at TESLA, but some degree of timing would be useful to help reject background which does not come from the interaction point. Two types of detectors fulfill the requirements discussed above: Plastic Streamer Tubes (PST)[3] and Resistive Plate Chambers (RPC) [4].

The RPCs, however, do carry a number of substantial advantages: detector construction is very simple, as there is no need of stretching wires, their operation does not rely on the $1/R$ behaviour of the electric field and malfunctioning tends to be confined,

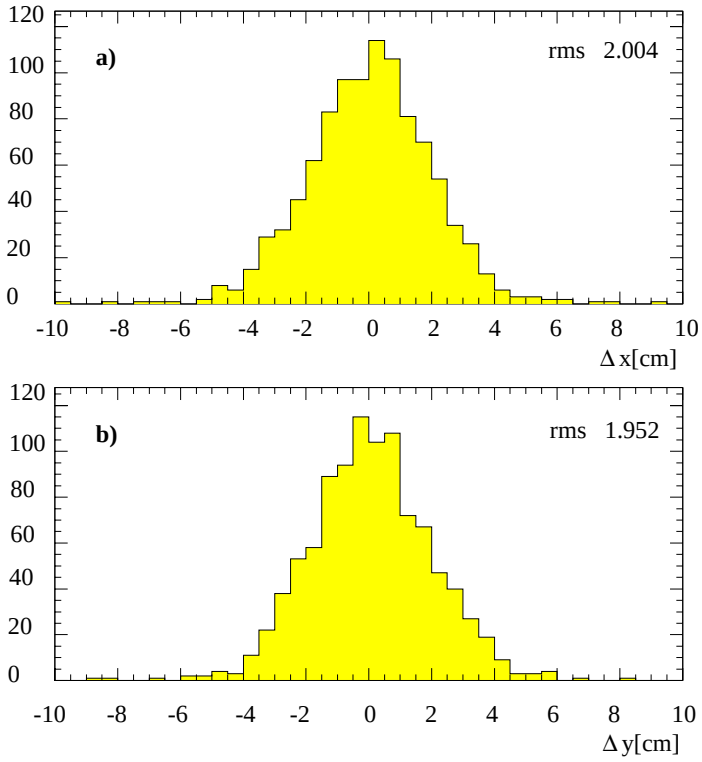

Figure 5.0.3: *Spread in x (a) and y (b) at the front face of the muon identifier for muons of 20 GeV/c emitted into the forward direction at 10°.*

unlike the PSTs in which a single non working wire might bring down a larger portion of the detector. By the same token they do not have a preferred direction that might make them vulnerable to background (*i.e.* wire direction). Last but not least RPCs can be shaped almost at will with obvious design and construction simplification [5]. The first choice for the TESLA detector muon system are RPCs while a backup solution could rely on PSTs.

Both PSTs and RPCs have been working with non-flammable gas mixtures, and, even with the non flammability constraint, operational mixtures can be adjusted to requirements. Evaluation of the neutron background rate, especially for the outer end caps planes, has to be carried out and the operating gas mixture must be tuned accordingly.

5.2 Conceptual design

As noted in the previous sections, the longitudinal segmentation of the flux return iron impacts the efficiency and robustness of muon identification as well as the overall energy resolution of the subsystem when used in the calorimetric mode. Mechanical construction and practical considerations suggest that the plate thickness should not be smaller than 10 cm: at this level of segmentation, given the overall iron thickness

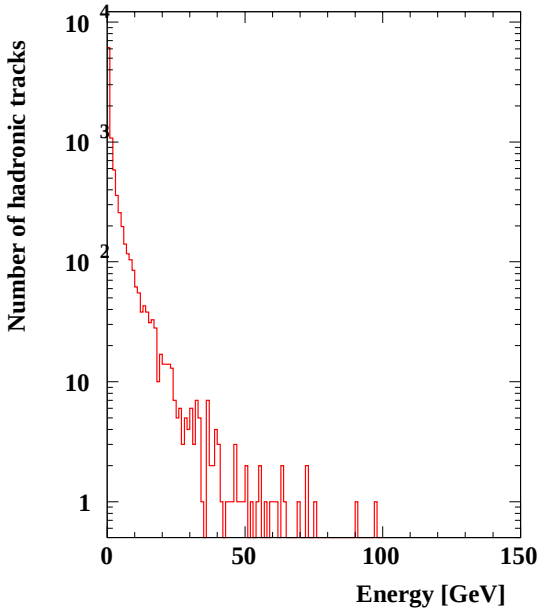

Figure 5.0.4: *Energy spectrum, at the front face of the muon system, for tracks that release energy in the iron.*

required to contain the coil magnetic field, fifteen planes of active detector could be allocated to the end caps and sixteen to the barrel. The overall active area, in this hypothesis, would be of the order of 7000 m^2. Performance in μ-identification and calorimetry have been shown not to degrade much if the number of active planes is reduced by 30%. In order to retain much of the calorimetric energy resolution, the first 10 layers are kept at a segmentation of 10 cm, and one last plane of detectors is added just outside the iron. With this choice, there are 12 layers of RPCs in the barrel and 11 layers in the end cap.

The overall detector concept of the yoke split into three parts favours a solution where the barrel parts of the two outer modules extend to the maximum z, and the end-caps are completely inside the barrel itself. With this choice the barrel part of the muon identifier would be 14.4 m long and extend radially from 380 cm to 580 cm. As previously noted there are 12 active planes for the barrel, one just in front of the iron, then 10 interspersed in gaps 4 cm wide every 10 cm of radiator, with the last one after the last 50 cm of iron. The overall length of the octagonally shaped flux return of 14.4 m, would be broken down into three pieces of 370, 700 and 370 cm in length respectively. The end caps, relatively small in this design, would have the usual pie shape and extend radially from 46 cm from the beam line up to the barrel inner radius. Longitudinally, the end caps will occupy roughly 2 m from 540 to 740 cm. RPCs can be produced in different shapes and dimensions: at the time of writing maximum dimensions are $1.3 \times 3.2\,m^2$ [5]. To fill the long (700 cm) barrel slots one might use a combination of 12 modules whose length is fixed at 115 cm and whose width varies according to the radial coordinate from 157 to 238 cm. The short (370 cm) barrel

slots can be filled with 6 modules 122 cm long and as wide as the ones for the long slots. Modules can be manufactured in tiles spanning three modules by laminating longitudinal strips or pad electrodes on one side across the total length. Long slots will be filled with 4 tiles, short ones with two. Filling of the end caps is a bit more complicated. In the framework of minimising the overall number of modules Fig. 5.2.1 gives a pictorial view of how end cap slots can be filled with 14 modules: four different shapes would be needed to fill the end-caps slots.

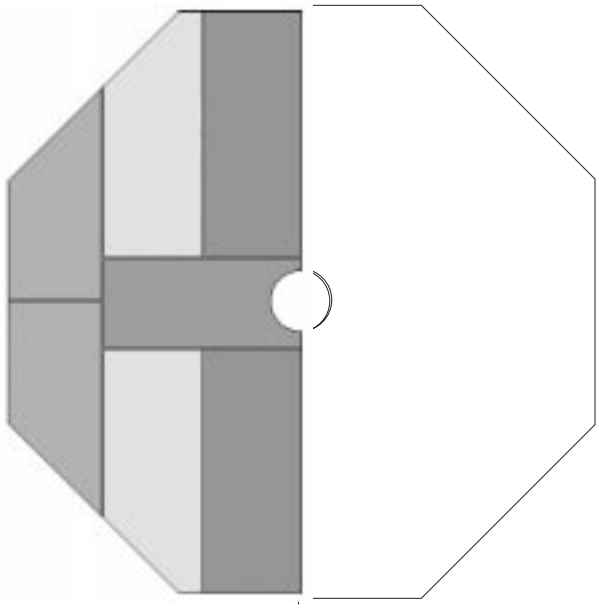

Figure 5.2.1: *RPC module filling of an end-cap slot: each plane is completely filled with 14 modules; RPCs with circular boundaries have already been successfully produced*

The pole tip iron could also be segmented, adding a few (five) planes of active detector. Details of the design depend strongly on the mechanical design of the iron. As far as the arrangement of electrodes one would use, the first 11 (10 in the end cap) layers would track muons and measure energy; strips alternating in two orthogonal directions would be glued on one side of the RPCs, on the other side one would have pads $25 \times 25\,\mathrm{cm}^2$ (at the front face). Hadronic calorimeter projective towers would thus extend into the muon system. The last layer will be equipped with crossed strips to yield a full space point. Energy measurement would not have any longitudinal segmentation: given the size of the streamer pulses, pads pertaining to various layers can be added just using a daisy chain technique. Resolution requirements set by multiple scattering determine the size of the tracking strips: an overall resolution of $\mathcal{O}(1\,\mathrm{cm})$ at the front face of the detector fixes the strip pitch to around 3 cm. In order to keep the number of electronic channels per layer in the barrel constant one might employ a sort of projectivity for the strip pitch too, widening it as radial dimensions

increase. The electronics will include a single bit information for strip location: a fixed or variable threshold discriminator would suffice, a 12 bit ADC would record the total number of tracks crossing per pad, and time measurement at granularity 16 or 32 times coarser than that of the strips would complement the overall information this system will yield.

The channel count would be ≈ 70k discriminator channels, 2.5k ADC channels and 5k or 2.5k TDC channels according to the chosen granularity.

5.3 Performance

The performance for the muon system has been evaluated using the dense jet environment of the $b\bar{b}$ final states. The calculations were done based on a full simulation of the TESLA detector [6]. The performance of the system for $b\bar{b}$ events is shown in Fig. 5.3.1. It can be seen that there is no significant loss of efficiency for muons in jets compared to isolated muons. For this plot the efficiencies of all the layers have been set at 95%, with the exception of the first layer, for which, given its pivotal role in associating tracks with muon track segments, the efficiency has been set at 99%. Such performance is readily attainable with the use of a double RPC layer.

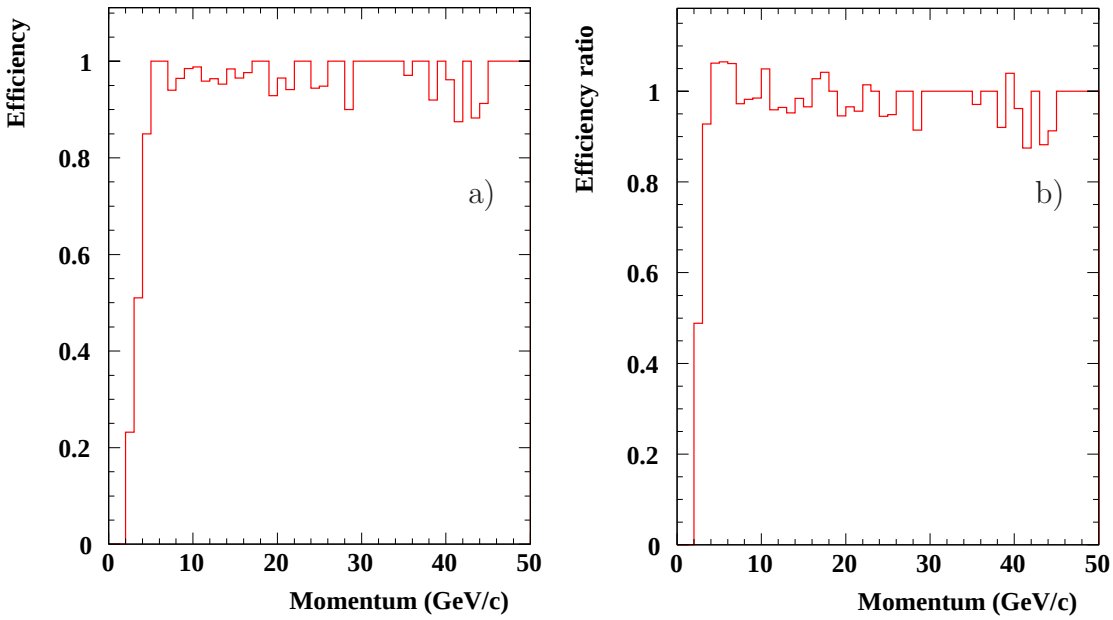

Figure 5.3.1: *a): Efficiency vs. momentum for* $b\bar{b}$ *final state in the barrel region for the 12 barrel/11 end cap module configuration described in the conceptual design section. b): Ratio of the* $b\bar{b}$ *final state muon identification efficiency to single particle identification efficiency.*

As noted in the introduction the muon system plays an important role as a tail catcher calorimeter. The amount of energy hadronic tracks deposit in the muon system is small but not negligible on the scale of the targeted energy resolution of the TESLA detector. In a $b\bar{b}$ final state 4% of events have one track that leaves 20 GeV or more in the iron of the flux return: measuring that energy with a fractional resolution of $\approx$ 40% would surely help the overall performance of the apparatus. In order to evaluate the calorimetric track-counting resolution, the total number of hits pertaining to a primary track and its secondaries were correlated with the energy of the primary track at the entrance of the muon system; the correlation plot is found to be reasonably linear. Using this simple algorithm, the overall resolution obtained as a function of the primary energy is shown in Fig. 5.3.2.

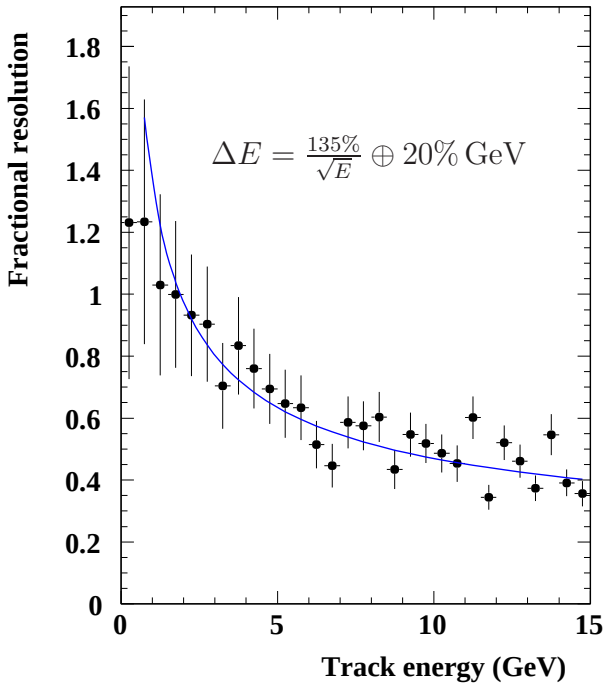

Figure 5.3.2: *Calorimetric energy resolution for the muon system versus energy at its front face, using the algorithm for energy measurement described in the text.*

In conclusion, the design with 12 active planes (11 in the end-caps) seems to yield robust performance: simulation runs reducing the detection efficiency of up to three active planes to 50% show minimal loss of overall muon-id efficiency ($\leq$10%). The expected energy resolution in the calorimetric mode will scale as $150\%/\sqrt{(E)}$ with a constant term of (20$\pm$10)%.

5.4 Cost

Scaling from costs of muon detectors already built or under construction with the same technology one arrives at the following cost breakdown:

- RPC modules construction: 150 EUR/m^2 : total cost 600 kEUR.
- Electronics: 70k ch's discrimination, 2.5kch's of ADC, 5kch's TDC: total cost 500 kEUR.
- Ancillary equipment : electrodes, cables, crates, power etc.: total cost 900 kEUR.

The total cost of the system adds up to 2.3 MEUR.

Bibliography

[1] ATLAS Collaboration: ATLAS Technical Design Report. CERN/LHCC/94-43, 1994.

[2] CMS Collaboration: CMS Technical Resign Report CERN/LHCC/94-38, 1994.

[3] E. Iarocci, Proceedings of the International Conference on Instrumentation for Colliding Beam Physics. G. Feldman, editor, Stanford , 1982.

[4] R. Santonico and R. Cardarelli, Nucl. Instrum. Meth. (A187):377 1981.

[5] BaBar Collaboration: BaBar Technical Design Report. SLAC-R-95-457.

[6] T. Behnke et al. BRAHMS: A Monte Carlo for a Detector at a 500 - 800 GeV Linear Collider. *LC-TOOL-2001-005*, 2001.
http://www.hep.ph.rhbnc.ac.uk/blair/detsim/brahms.html
electronic document.

6 Data Acquisition System

The main goal of the data acquisition (DAQ) system is highly efficient data taking of interesting physics events in the presence of several orders of magnitude higher background without losing data of a possible, yet unknown, physics process. In addition the rates of the known interesting physics processes vary as well by several orders of magnitude. These conditions drive the proposal of an event building without a hardware trigger, followed by a software based event selection.

Larger and more complex detector structures are needed to measure the physics processes with the required accuracy, resulting in subsystems having more and more readout channels. The increasing number of readout channels requires signal processing and data compression already at the detector electronics level and high bandwidth for the event building network to cope with the data flow. The currently built experiments have up to 10^8 front-end readout channels and an event building rate of a few kHz moving data with up to 500 Gbit/s.

The rapid development of fast network infrastructures and high performance computing technologies as well as the higher integration and lower power consumption of electronic components fits nicely with the requirements needed for such systems.

Furthermore it turned out that for such large systems a restriction to standardised components is vital to achieve maintainability at an affordable effort, requiring commodity hardware and industry standards to be used wherever possible.

Details of the data acquisition system depend to a large extent on the final design of the different subdetector electronic components, most of which are not fully defined today. Therefore the DAQ system presented here will be conceptual, showing possible options and the feasibility of the system in general.

At the TESLA linear collider the operation conditions (see chapter 1) are different from those of accelerators currently operating or being constructed. The main parameters of the 500 GeV design, relevant for the DAQ system, are:

- a long time interval between two bunch trains of 199 ms,
- a separation of two bunches inside a train by 337 ns,
- a train length of 950 μs.

TESLA operation therefore results in bursts of 2820 bunch crossings (BX) with a duration of roughly 1 ms at 5 Hz frequency. This yields a BX rate of 3 MHz for 1 ms followed by a period of almost 200 ms without any interaction giving an integrated BX rate of 15 kHz. This burst structure leads immediately to the key element of the proposed DAQ system:

- no hardware trigger,

- dead time free pipelining of data for 1 ms,
- front-end pipeline ready for the next train within 200 ms, and
- event selection by software.

6.1 Technologies

The fast development in the computing and network area makes it almost impossible to predict the technology which will be used to build a DAQ system in a few years from now. Here a short overview of possible scenarios is presented, based on the experience of currently running experiments and on studies for the experiments planned at the LHC.

It is assumed that due to the high integration of electronic components the subdetector front-end will be equipped with hit detection or zero suppression capability. For simplicity it is further assumed that digitising will be done at the detector level already, although one could think of transferring analog signals as well. It is most likely that in addition the number of readout channels will be reduced already at the detector level by multiplexing several detector channels into a common readout line. Examples of such readout electronics with the required capability are currently being built for the LHC experiments, or are proposed for the subsystems described in this report (see chapter 3.2 and [1]).

Taking current technology, the usage of fast (> 1 Gbit/s) serial line input is assumed from the subdetector to the data acquisition. The DAQ will be a multi-staged buffered system based on fast network components like Gbit switches and commodity hardware processing nodes like PCs.

A throughput of 300 MByte/s for a 4×4 switch based on Gigabit Ethernet has been demonstrated [2] and further development is ongoing to reach the goal of 500 Gbit/s throughput with 1000×1000 connections needed for the LHC experiments [3].

Data input rates of 100 MByte/s into commercial PCs have been reached and 500 MByte/s are envisaged for LHC experiments. Compared to LHC requirements the throughput for event building at TESLA is moderate and should not be a major concern in a few years time.

6.2 Conceptual Design

To achieve a dead-time free data acquisition under the TESLA operation condition, a trigger-free pipeline of 1 ms with readout of all data in the pipeline within 200 ms is proposed. The data throughput will be minimised at the subdetector level by using zero suppression or hit detection before sending the data to the readout units (RU) of the data acquisition system. The aim is to standardise the components to ease maintenance and to minimise cost.

Depending on the bandwidth available two scenarios are considered:

1. If the network bandwidth is sufficient to build a complete event within 200 ms, full event building of all subsystems for a complete train will be done in one step in an event finder unit (EFU). This needs up to 2 GByte/s event building capability into one event finder unit, but avoids moving data several times and makes event management and control easier.

2. If the network bandwidth does not fulfil the needs for full event building at once, parallel subdetector event building is possible with further pre-processing of subdetector data in the subdetector event building units (SEB), to reduce the data volume further before the full event is built. This implies a further level of event buffering to allow for the time needed to pre-process the data and implies moving information twice across the network.

A schematic view of the data acquisition for scenario 2 is shown in figure 6.2.1. [1]

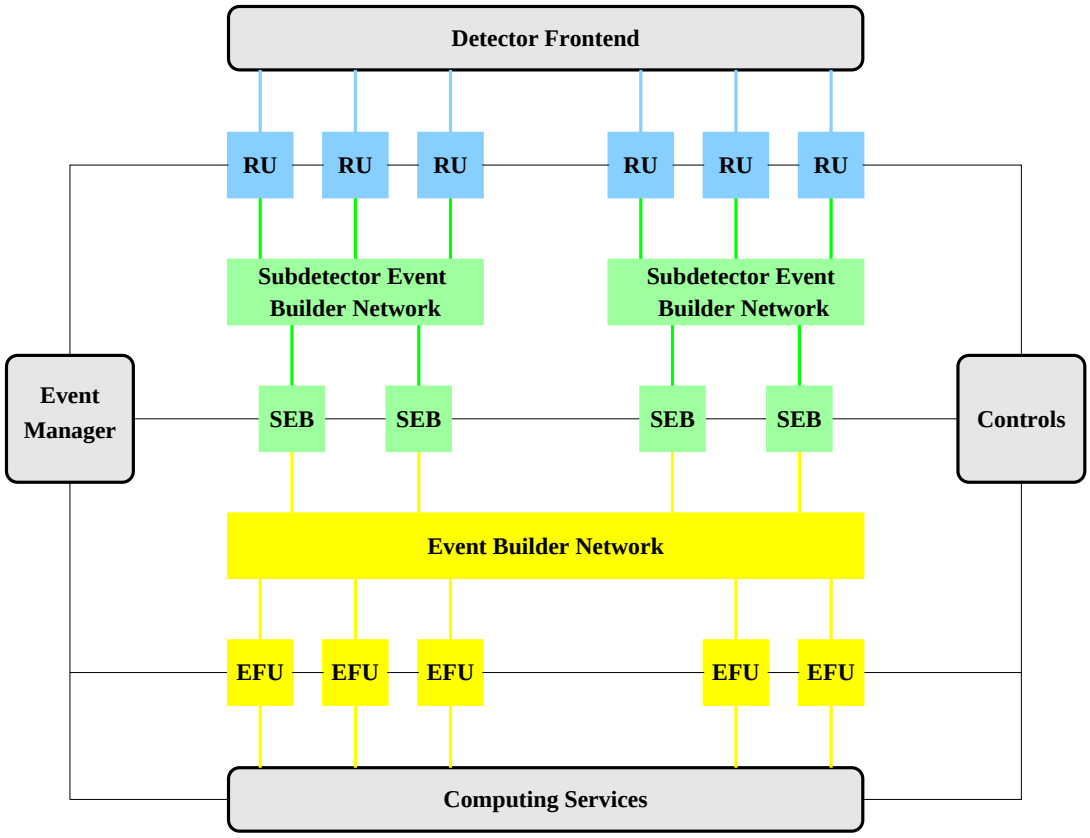

Figure 6.2.1: *Overall view of the trigger and DAQ concept.*

Comparing this design with recently built or just being built experiments, it is mainly the first level, hardware based, trigger which is omitted.

[1] For scenario 1 the subdetector building network is omitted and the functionality of the subdetector event builder units is implemented into the event finder units.

The subdetector specific part is realized in the front-end readout units which receive the detector data via a fast serial link. All readout units will be read by a fast subdetector event building network. For scenario 2 the data will be moved into subdetector event builder units. The data of a full train, i.e. for 2820 bunch crossings, will be read into one unit at a time to free the pipeline for the data of the next train. To achieve the necessary throughput, parallel building of the subdetector events is foreseen via separate subdetector event building units. To allow for variations on the readout time to more than 200 ms an implementation of multiple pipelines or pipelines with multiple train capacity can be foreseen. Subsequent trains can then be stored in the pipelines while the readout is going on in parallel.

The subdetector event builder will perform a further pre-processing of the data such as local pattern recognition or cluster finding to reduce the data volume further before the full event is built via a second fast network, the full event building network, into one event finder unit.

For scenario 1 the data will be read directly from the readout unit through the event builder network into the event finder unit. At the level of the event finder unit, the complete data of all bunch crossings within a train will be available for event processing. This is needed because some subsystems, like the vertex detector or the TPC, will have overlapping signals from consecutive bunch crossings.

Event selection is then performed in the event finder units. For each class of physics process a specific finder process will identify the bunches which contain event candidates and mark them as 'bunches of interest'. All data for these 'bunches of interest' will be fully processed and finally sent to the computing services which in this context means permanent storage and physics analysis infrastructure. By running all possible finders on all bunches and using the full data available, a maximum event finding efficiency is achieved.

The best strategy for applying these finders and processing the data depends on the topology of physics processes to be selected and their background processes. This has to be further studied and optimised based on full Monte Carlo simulations with the final detector and machine design.

By using a farm of finder units it is possible to build events from several trains in parallel. A buffering in the subdetector event units or in the readout units will be implemented in case the processing time varies such that the full event of the subsequent train could not be built immediately into a free event finder unit. The size of the event finder farm has to be such that the average processing time per train fits the train rate of 5Hz. If for example a farm of 500 PCs is considered, an average processing time per train of less than 100 seconds has to be achieved for 5 Hz running. If 5 high multiplicity events are found on average in a train this yields 20 seconds per event which is not unusual with processor farms used in current experiments. The number of processing units is expected to be on the order of 1000 for SEB and EFU each.

The proposed concept makes it possible to build a scalable system by adding more parallel subdetector builder units or event finder units if network bandwidth or processing power would limit data taking.

The use of off-the-shelf technology for the network and the computing units will

ease maintainability and allow to profit from the rapid development in this area. The system will also profit from the use of a common operating system like Linux and high level programming languages already at the event building and event finding stage, making the separation of on-line and off-line code obsolete and therefore avoids the need to duplicate or even rewrite code for on-line or off-line purposes. This results in a more efficient use of the common resources.

The impact of a 1 ms active pipeline without trigger interrupt and therefore no possibility of a fast clear or buffer flushing for the different subdetector pipelines has been studied and readout technologies able to cope with this have been proposed. For the vertex detector built in CCD technology [1] a column parallel readout at a speed of 50 MHz during the active pipeline has been proposed, to handle the expected data rates. For the TPC several designs are being studied which allow the collection of signals in an un-gated mode for the full time of the pipeline by limiting the ion feedback with grids or GEMs (see Chapter 2.3) and for the electromagnetic calorimeter built out of silicon tungsten a continuously running pipeline with hit detection and multiplexing is foreseen (see chapter 3.2).

6.3 Performance

Extensive calculations and simulations have been performed on physics and background rates (see Part III, and Chapter 7) throughout the ECFA/DESY study. Table 6.3.1 summarises the event rates for some selected physics processes [1].

process	cross-section [pb]	events per train
$e^+e^- \to e^+e^-$	628	4.2
$e^+e^- \to q\bar{q}$	2.7	0.02
$e^+e^- \to WW$	7.6	0.05
$e^+e^- \to t\bar{t}$	0.6	0.004
$e^+e^- \to \gamma\gamma \to q\bar{q}$	27000	184
$e^+e^- \to \gamma\gamma \to l^+l^-$	2100	14.3

Table 6.3.1: *Expected event rates at 500* GeV.

From the total hadronic cross section for e^+e^--annihilation about 0.1 events per train are expected whereas about 200 events per train will come from $\gamma\gamma$ reactions. The event size for a multi-hadronic event excluding background is estimated to be 200 kByte but for forward peaked low multiplicity $\gamma\gamma$ events it is much less.

The dominant source of data volume is the background from the beam beam in-

[1] A Luminosity of $L = 3.4 \times 10^{34}\,\mathrm{cm}^{-2}\mathrm{s}^{-1}$ is assumed, a detector acceptance cut of $\theta > 80$ mrad has been applied and for the $\gamma\gamma$ cross section W$>$ 2 GeV was used

teractions as described in section 7.1 and [4]. Table 6.3.2 summarises the dominant background processes which are relevant for the data volume.

background from	hits/BX VTX	tracks/BX TPC	cells/BX ECAL
pair production	568	5	5040
$\gamma\gamma$-hadronic reactions	16	1	100

Table 6.3.2: *Expected background rates at 500* GeV.

The main sources are the photons from pair production reaching the TPC and the ECAL and the hits produced by the pairs in the vertex detector. Although the $\gamma\gamma$-hadronic reactions here are treated as background the line between background and physics events will finally be drawn by the physics groups and a considerable fraction of these events will end up on mass storage for physics analysis. The background coming from $10^3 - 10^4$ neutrons reaching the TPC and the ECAL is negligible in terms of data volume as well as the background from beam induced muons which will be less then 0.1 muon per bunch crossing passing the TPC parallel to the beam-line.

The number of tracks and hits from background sources exceeds those from the physics processes by more than two orders of magnitude thus giving the bulk data for the DAQ system.

Table 6.3.3 summarises for the various subsystems the expected data volume (see also [5]). The numbers are based on the physics and background rates quoted in Tables 6.3.1 and 6.3.2.

component	channels [10^3]	Data volume per train [MBytes]
VTX	799 000	8
SIT	300	1
FTD	40 000	2
TPC	1 200	110
FCH	20	1
ECAL	32 000	90
HCAL	200	3
MUON	75	1
LAT	40	1
LCAL	20	1
total	$\sim$ 873 000	$\sim$ 220

Table 6.3.3: *Data Volume expected at TESLA*

component	units	price per unit [kEUR]	total [MEUR]
readout units	10000	1	10
readout crates	500	10	5
event building network			4
subdetector building units	1000	1	1
event finder units	1000	1	1
permanent storage			1
infrastructure			1
total sum			23

Table 6.3.4: *cost estimate for the data acquisition system*

The number of hits produced in a detector part by a traversing particle is taken from simulations and the data size per hit varies from 5 to 16 byte depending on the accuracy required for the time and charge measurement.

The event building will be performed at 1-2 GByte/s and an event finder output rate of 30 Hz is expected, including $\gamma\gamma$ physics processes as well as additional calibration and background events for cross checks. The event size varies from 0.2 MByte to 5 MByte depending on the amount of background included. Assuming background data to be suppressed the processed event size will be on average about 1 MByte which leads to 30 MByte/s output to mass storage. This results in a total data volume of roughly 300 TByte per year.

For TESLA operation at the Z mass with a luminosity of $L = 7 \times 10^{33}\,\mathrm{cm}^{-2}\mathrm{s}^{-1}$ the total hadronic annihilation cross section of $\sigma \sim 30\,\mathrm{nb}$ will results in an event rate of 210 Hz, which yields about 10 MByte additional data from physics events per train. The total input data volume for event building does therefore not change significantly. A possible reduction of the data volume coming from background processes at the lower energy is neglected here. The event finder output to permanent storage will then increase, due to the physics rate, to about 30 Hz and 300 MByte/s.

In conclusion the proposed DAQ system is capable to ensure data taking with maximum efficiency both for the high energy running as well as for the operation at the Z mass. The software event selection based on the full event data available will enable very efficient event recording for high as well as for low rate physics processes. Compared to systems built for the LHC experiments the proposed DAQ for TESLA is less demanding and key components like the fast switched network and the computing units are available already today.

6.4 Cost estimate

Due to the rapid development in computing and networking technologies, only a rough cost estimate can be performed by extrapolating from current hardware and prices.

Assuming the 10^9 channels multiplexed into 10^7 readout lines and 10^3 readout lines on average being handled by a readout unit, 10^4 readout units will be needed and will

be housed in 500 readout crates. Taking current prices for VME boards and VME crates 1000 EUR and 10000 EUR each is expected. It is assumed that the price per PC stays constant in the order of 1000 EUR per processor but with an increasing processing power and memory capacity. The development of networks will certainly be boosted further due to the large demands resulting from the Internet community and prices will decrease for larger switches. For each Gigabit connection of the event building network 1000 EUR is estimated and 4000 connections are envisaged.

Table 6.3.4 lists the major components of the DAQ system and the cost estimates with the above assumptions.

Bibliography

[1] C. Damerell. A CCD Based Vertex Detector for TESLA. *LC-DET-2001-023*, 2001. electronic document http://www.desy.de/~lcnotes/.

[2] M. Bellato. The CMS Event Builder Demonstration based on GigaEthernet Switched Network. In *Proceedings of CHEP 2000*, Padova, Italy, 2000.

[3] F. Meijers. Studies for the CMS Event Builder. In *Proceedings of DAQ 2000-Workshop at IEEE 2000*, Lyon, France, 2000.

[4] C. Hensel. Beam Induced Background at a TESLA Detector. *LC-DET-2000-001*, 2000. electronic document, http://www.desy.de/~lcnotes/.

[5] G. Eckerlin, R. Gerhards, R. Heuer, and P. L. Du. Concept of a Software Trigger for an Experiment at the TESLA Linear Collider. In *Proceedings of IEEE 2000*, Lyon, France, 2000.

7 Machine Detector Interface

The success of a particle physics experiment is very closely related to the interplay between the detector and the accelerator itself. Monitoring polarisation, luminosity and beam energy are not only needed for machine development but are also essential tasks for the experiment itself. Additionally the understanding of background sources resulting from the beams is necessary. The intense TESLA beams will be a large source of beam induced background. Efforts to reduce the different backgrounds are essential in the detector design. In addition, the monitoring of the background will be required for the running experiment.

7.1 Backgrounds and the Mask

A number of different background sources are present in the interaction region. The most severe ones come from beam beam interactions of the electron and positron beams themselves. The high charge density of the colliding beams produces strong electromagnetic fields which bend the trajectories of the particles of the oncoming bunch. This so called pinch effect increases in e^+e^- collisions the luminosity significantly, but on the other hand it induces an intense emission of hard beamstrahlung photons (at $\sqrt{s}$=500 GeV, $\approx 6 \cdot 10^{10}$ for each bunch crossing (BX) with a total energy of $\approx 2.6 \times 10^{11}$ GeV). These photons broaden the energy distribution of both beams. While the photons themselves disappear in the beam pipe they are a source of background from secondary effects. The main effects are e^+e^- pairs, hadronic background, neutrons, and radiative Bhabhas.

Other beam induced background sources like muons, synchrotron radiation induced background and beam gas scattering also have to be considered. Details on the different backgrounds are given in [1, 2, 3].

7.1.1 Motivation for the mask

One of the main background sources is the production of e^+e^- pairs with typical energies of a few GeV which stem from conversion of beamstrahlung photons in the high electromagnetic field densities of the colliding bunches. The effects of incoherent pair production[1] have been studied using the simulation tool GUINEA-PIG [2]. The numbers and the total energies of pairs produced in one BX are shown in table 7.1.1 for $\sqrt{s}$ of 500 and 800 GeV.

[1]The number of pairs produced via the coherent production mechanism is negligible [2].

	500 GeV	800 GeV
N_{pairs}/BX	129 000	153 000
E_{tot}/BX [TeV]	361	810

Table 7.1.1: *Number and total energy of pairs with energy $E \geq 5$ MeV produced in one BX, simulated with GUINEA-PIG [2].*

The e^+e^- pairs created by beamstrahlung at the interaction point (IP) curl up in the magnetic field of the detector coil and move longitudinally towards the quadrupoles of the final doublets. The boundary of the pair trajectories however is quite sharp. Figure 7.1.1 shows the xy profiles of electrons and positrons at the longitudinal position of z= +220 cm which is the position of the luminosity calorimeter LCAL (see Section 7.1.2).

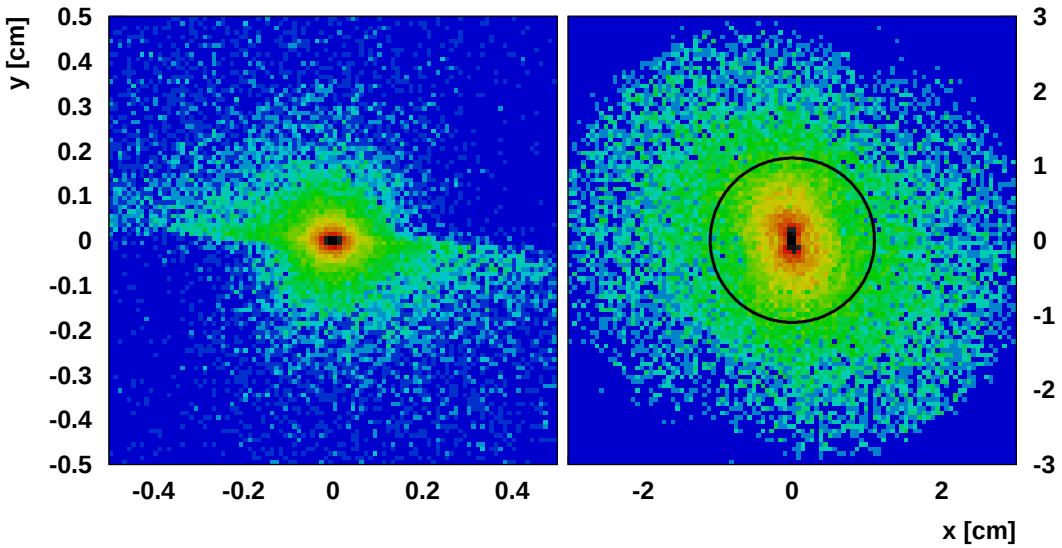

Figure 7.1.1: *xy profile of pairs (left: positrons; right: electrons) at z=+220 cm. The circle indicates the inner aperture of the LCAL. Note the different length scales and the logarithmic colour scale.*

On their way in +z direction, the electrons are defocused by the oncoming electron beam while the positrons are focused. This can be seen clearly by comparing the dimensions of the profiles. The roles of electrons and positrons are exchanged on the opposite side of the IP (where $z < 0$).

Most of the pair particles disappear through the beam pipe. A large number of those is deflected in the magnetic fields of the quadrupoles and may hit the beam pipe and the quadrupoles from inside. The absorption of the pair particles in front of and inside the quadrupoles creates a large number of secondary particles which are a major

background source for the detector. The detector has therefore to be shielded from these backgrounds. A system of tungsten shields has been designed which absorbs a large fraction of the pair particles and their secondaries.

7.1.2 Design of the mask

This system of tungsten shields, called the mask, will be installed around the final quadrupole doublet. The cylindrical mask will have a conical tip towards the IP which shields the tracking detectors from backscattered particles. The disc shaped tungsten shield (the so called inner mask) has an inner aperture which is smaller than the one of the quadrupoles, shielding the inner layer of the vertex detector from pairs and secondaries which are backscattered from the quadrupoles, and from synchrotron radiation photons produced further upstream. Graphite serves as a low Z absorber to reduce the backscattering of showers which develop when the pairs hit the tungsten shield. Additionally the graphite protects the vertex detector from neutrons originating from the final focus beam line upstream. Fig. 7.1.2 shows a drawing of the mask elements.

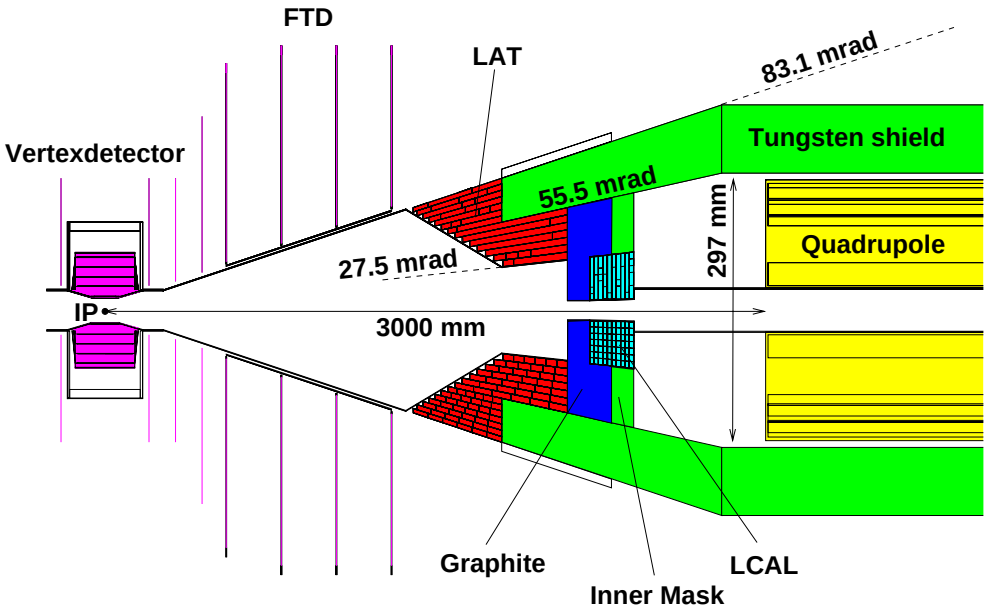

Figure 7.1.2: *Mask layout.* **LCAL***: Luminosity Calorimeter,* **LAT***: Low Angle Tagger,* **FTD***: Forward Tracking Discs. Note the different horizontal and vertical scales.*

Part of the mask will be equipped with two calorimeters to provide instrumentation for low angle measurements and beam diagnostics. The luminosity calorimeter **LCAL** is a radiation hard tungsten sampling calorimeter which can stand the high radiation environment near the beam pipe. This calorimeter is integrated into the inner mask

and serves as a collimator for the pairs and covers a polar angle region of $4.6 \leq \theta \leq 27.5$ mrad. As the number of impinging pairs, the deposited energy on the LCAL, and the azimuthal energy distribution are measures for the luminosity, the LCAL will be used as a pair monitor providing a fast signal for beam tuning (see section 7.4.4 in Part II). Additionally it provides a limited ability to detect high energy electrons at small angles.

The low angle tagger (LAT) is a silicon/tungsten calorimeter with a smallest inner diameter of 9.6 cm which lies outside the region of the intense beamstrahlung pairs (compare figure 7.1.1). It serves as a device for measurements of particles (e.g. Bhabha scattering) in the angular region of $27.5 \leq \theta \leq 83.1$ mrad. Additionally the tungsten in this calorimeter is part of the shield which protects the tracking detectors. The design and performance of both calorimeter is described in detail in section 3.5.

The space between the final quadrupole and the inner mask with the LCAL will be used for the installation of vacuum components, beam position monitors and flanges. The mask will also be instrumented with a laser interferometer for single beam profile measurements (see section 7.4.4 in Part II).

7.1.3 Background in the detector

The mask has a significant role in reduction of the different background sources. In the following the remaining influence of the different background sources on the detector is discussed.

7.1.3.1 Pair background

The background resulting from pairs has been simulated [4] using the GEANT 3 based detector simulation program BRAHMS [5] where the mask design is included in detail. The cut off energies down to which charged and neutral particles are tracked in GEANT were set to 10 keV. Figure 7.1.3 shows the tracks of 10 simulated pair particles and their secondaries hitting the mask and beam line elements. Clearly visible is the amount of secondary particles produced in the region of the LCAL and the quadrupoles.

LAT and LCAL A large part of the pairs is absorbed in the LCAL. Typical energies of 20 (35) TeV are deposited there per BX for $\sqrt{s} = 500$ (800) GeV. Due to the sharp envelope of the pair tracks, the LAT, which covers larger polar angles, receives a much smaller amount of energy in the range of a few GeV per BX. Details on the LAT and the LCAL are given in section 3.5.

Tracking detectors The part of the tracking system most susceptible to backgrounds is the vertex detector. The first vertex detector layer has to be close to the IP to provide the required vertex resolution. One limiting factor for the radius of the innermost layer is the expected background from beamstrahlung pairs. Figure 7.1.4 shows the number of hits expected per BX in the five layers of the vertex detector for a 3 T and 4 T magnetic field at $\sqrt{s}$ of 500 GeV and 800 GeV respectively.

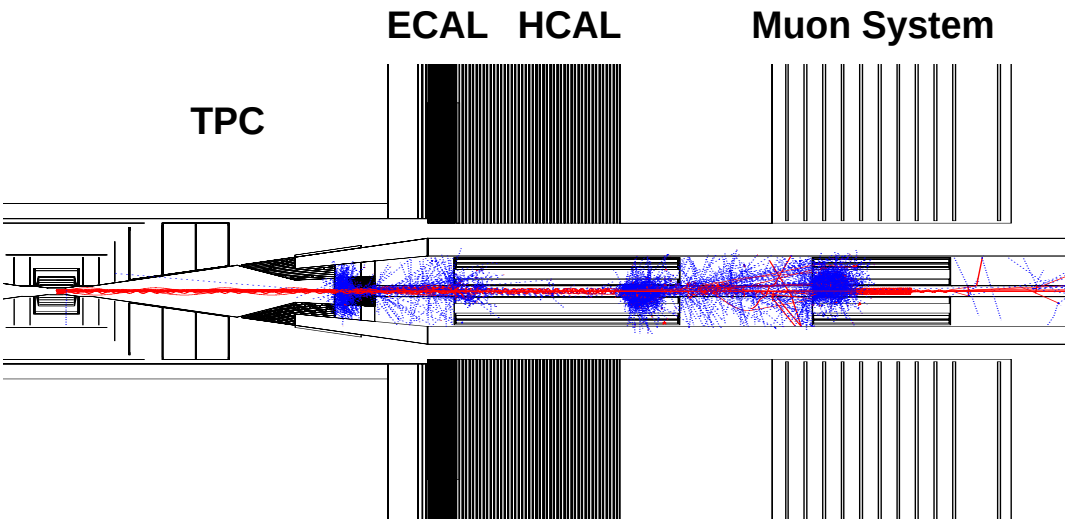

Figure 7.1.3: *Pairs from beamstrahlung hitting the mask elements. Only a very small fraction of pairs created in one BX is shown. Charged tracks are shown in red, photons in blue. Note the different scale in comparison to figure 7.1.2.*

Detector	500 GeV, 3 T	500 GeV, 4 T	800 GeV, 3 T	800 GeV, 4 T
TPC (tracks)	7	5	7	8
SIT 1	22	23	16	17
SIT 2	15	7	9	5
FTD 1	36	17	42	27
FTD 2	29	17	34	18
FTD 3	19	12	19	13
FTD 4	12	8	14	13
FTD 5	13	8	16	8
FTD 6	11	7	8	7
FTD 7	6	6	6	6
FCH (12 planes)	111	63	53	69

Table 7.1.2: *Charged hits per BX from pairs in the tracking detectors. The hits in the forward chamber (FCH) are summed over all 12 planes, for the TPC the number of charged tracks is shown.*

The number of hits on the inner vertex detector layer is less than 420 (610) with a 4 T (3 T) magnetic field at $\sqrt{s} = 800\,\text{GeV}$. This results in hit densities of less than 0.05 (0.07) hits per mm^2 which is far below critical background levels (section 2.1.2). Clearly a magnetic field of 4 T as planned for the detector coil (section 4) is a significant improvement over a 3 T field.

The other tracking detectors are less susceptible to background, however, the num-

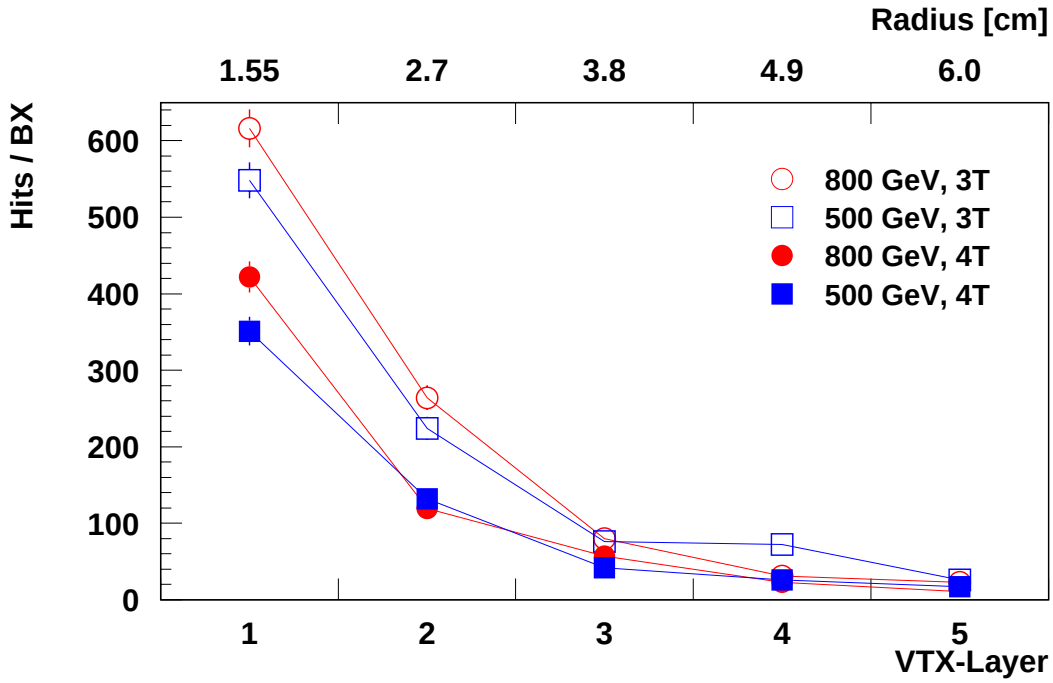

Figure 7.1.4: *Number of hits resulting from pair background in the five layers of the vertex detector for a magnetic field of 3 T (open symbols) and 4 T (filled symbols) and for $\sqrt{s}$ of 500 GeV (squared symbols) and 800 GeV (round symbols). The errors were assumed to be Poisson distributed.*

ber of background hits is also of importance there. Table 7.1.2 shows the number of charged hits in both layers of the Silicon Intermediate Tracker (SIT), the seven Forward Tracking Discs (FTD), and summed up for the 12 planes of the Forward Chambers (FCH). The number of charged hits and the resulting occupancies in all tracking detectors are acceptable.

The largest active tracking volume is the time projection chamber (TPC). The main background source with respect to the beamstrahlung are photons which are produced when the pair particles impinge on the LCAL/LAT, the beam pipe, or the mask (compare Fig. 7.1.3). A number of these photons enter the TPC volume and eventually convert into e^+e^- pairs. This leads to background tracks in the TPC. Additionally shower particles may back-scatter from the electromagnetic calorimeter (ECAL) into the TPC. These sources of background have been simulated and table 7.1.3 shows the results.

Fig. 7.1.5 shows the origin of photons which pass the inner radius of the TPC volume. The large peaks at $|z| \approx 220\,\mathrm{cm}$ correspond to the z position where the pairs hit the mask elements. The number of photons is comparable for $\sqrt{s}$ of 500 and 800 GeV.

The number of tracks in the TPC which result either from direct passage of charged particles or which stem from converted photons is given in Table 7.1.2. These numbers

	500 GeV		800 GeV	
	N	E_{tot} [GeV]	N	E_{tot} [GeV]
Photons from beam region	1325	3.11	1749	4.18
Photons from ECAL	11	0.02	10	0.02

Table 7.1.3: *Number and total energy of photons from pairs per BX with $E \geq 10\,keV$ which enter the TPC from the beam region or are backscattered from the ECAL.*

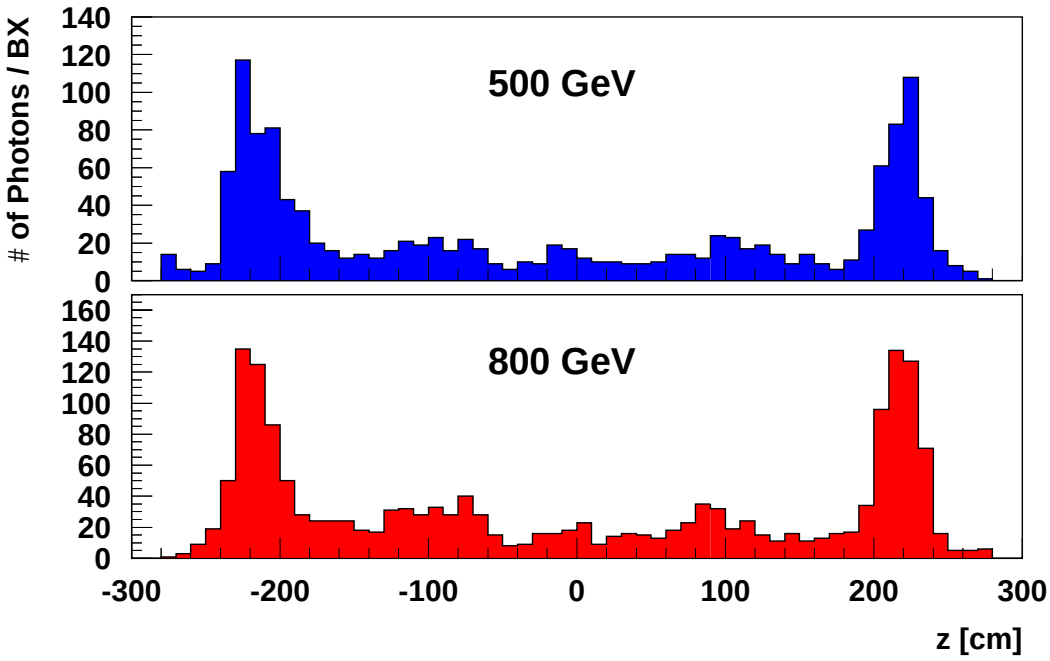

Figure 7.1.5: *Origin of photons from pairs which cross the inner TPC radius for a magnetic field of 4 T and the 500 GeV (top) and 800 GeV (bottom) option. The total number of photons is 1325 (1749) with total energies of 3.11 (4.18) GeV for $\sqrt{s} = 500$ (800) GeV.*

lead to occupancies on the TPC readout pads which are of the order of a few per–mill [6].

Calorimeters A large fraction of the photons entering the TPC is expected to eventually be absorbed in the electromagnetic calorimeter ECAL. In addition a large number of photons is produced when the pair particles hit the final quadrupoles (Fig. 7.1.3). As the calorimeters and the muon detection system surround the cylindrical tungsten mask, the energy which is leaking out of the mask has to be considered as a potential background source for the calorimeters as well. The result of a simulation is shown in figure 7.1.6. The total leaking energy is around 0.7 GeV per BX.

The numbers of electrons, positrons and photons originating from the sources mentioned and hitting the ECAL with energies larger than 3 MeV (which is approximately

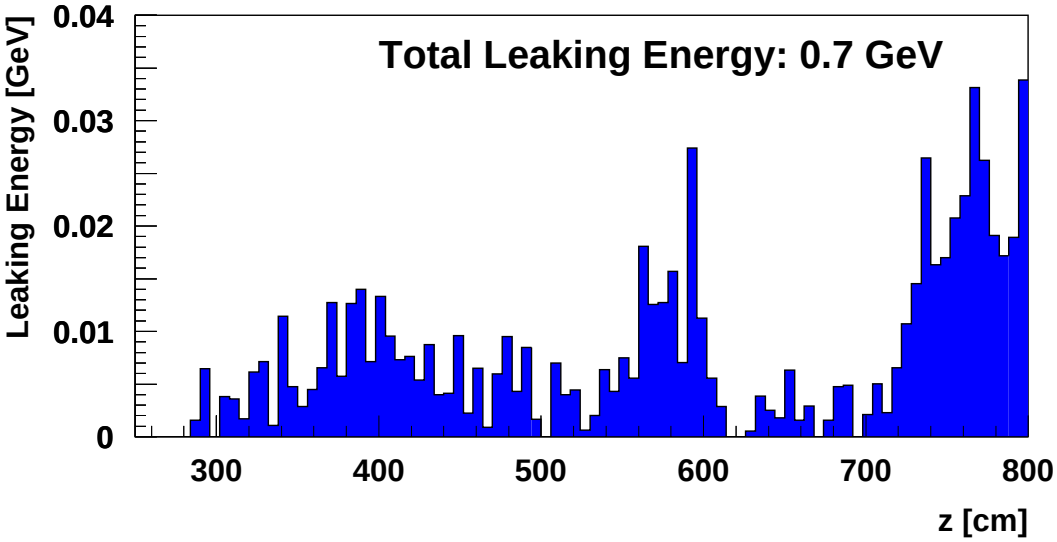

Figure 7.1.6: *Energy leaking out of the cylindrical tungsten shield by photons per BX (total number: 375) which are produced from pairs for $\sqrt{s} = 500\,GeV$ and 4 T magnetic field.*

the minimum energy to produce a hit in a ECAL cell) have been simulated and are summarised in table 7.1.4.

	500 GeV		800 GeV	
	N	E_{tot} [GeV]	N	E_{tot} [GeV]
ECAL barrel	101	0.63	152	0.87
ECAL endcap	91	1.29	117	3.97
Total	192	1.92	269	4.84

Table 7.1.4: *Number and total energy of pairs and their secondaries ($e^{\pm}, \gamma$) per BX which enter the ECAL with energies larger than 3 MeV.*

7.1.3.2 Hadronic background

The beamstrahlung photons may interact hadronically ($e^+e^- \rightarrow e^+e^-\gamma\gamma \rightarrow e^+e^-$ hadrons) which leads to background events in the detector. These hadronic reactions have been studied in detail [2, 7] for $\sqrt{s} = 500\,GeV$ using GUINEA-PIG and HERWIG 5.9 including multiparton interactions. A cut on the – with respect to the beam direction transverse – momentum of $p_t \geq 2.2\,GeV/c$ has been applied.

The number of hadronic events per BX is given in table 7.1.5. The total number sums up to 0.02 events per BX with an average (charged) multiplicity of 34.4 (17.4).

Type	events / BX [10^{-2}]	multiplicity	charged mult.	E_{tot} / BX [GeV]
direct	0.53	15.2	8.5	0.25
single resolv.	0.40	30.5	15.7	0.32
double resolv.	1.12	44.7	22.2	1.50
all	2.05	34.4	17.4	2.07

Table 7.1.5: *Number of direct, single resolved and double resolved hadronic interactions [7], multiplicities and energy for $p_t \geq 2.2\,GeV/c$.*

This leads to a total charged hit density of less than 3.4 (5) $\cdot 10^{-5}$ hits per mm^2 on the inner layer (summed over all layers) of the vertex detector. In the integration time of the TPC ($\sim$160 BX) around 110 charged tracks (incl. secondaries) will be superimposed to the physics events. The background events could fake real physics events but the time resolution of the TPC should allow to disentangle these tracks.

The total number of photons which stem from hadronic reactions and may eventually convert into charged particles inside the TPC is ≈ 7/BX with a total energy of 18.5 MeV. This can clearly be neglected as background source.

7.1.3.3 Radiative bhabhas

Another possible background source is the production of low energy particles via the beam-beam bremsstrahlung process $e^+e^- \rightarrow e^+e^-\gamma$. The high energy γ disappears through the beam pipe while the remnant beam particle (the so called radiative Bhabha) may be dumped in the mask or the final quadrupole doublet and will eventually produce electromagnetic showers and neutrons there. These secondary particles may scatter back into the detector. A detailed simulation [3] shows that the expected background in the detector is negligible. Details are given in table 7.1.6.

7.1.3.4 Neutron background

Neutrons are produced through photo-nuclear reactions from electromagnetic shower bremsstrahlung photons. Therefore any γ, e^+, or e^- hitting the mask or beam line elements further downstream is a potential source of neutrons. Additionally large numbers of neutrons are produced in the beam dump. Neutrons can scatter back into the detector region from these different neutron sources. The simulation of neutron production and the subsequent neutron tracking has been done for $\sqrt{s} = 500$ GeV using the program FLUKA99 [8, 9]. The results are described in detail elsewhere [3, 10].

Most neutrons are produced as secondary particles in the interaction of pairs with material in the beam-line (section 7.1.3.1). A total flux of the order of 10^9 neutrons per cm^2 and year, normalised to the silicon bulk damage by total non ionising energy loss of 1 MeV neutrons, is expected at the position of the vertex detector. The total numbers of neutrons depositing energy in the calorimeters are around 8000 (5000) per BX for the ECAL (HCAL) with total deposited energies of the order of 10 GeV. The number

of neutrons passing the TPC is around 15000 per BX. This contains neutrons which are reflected from the ECAL surface and pass the TPC more than once. Therefore this number depends on the albedo of the ECAL. A modification of the ECAL surface could reduce this number significantly. The neutron rates expected at the position of the SIT and the FTD are given in table 7.1.6.

The spent electron and positron beams also produce large numbers of neutrons in the main beam dumps 240 m downstream from the IP. The number of neutrons per BX radiating out of the concrete shield is small, but a significant number of neutrons travel back through the 1 m diameter entrance window of the dump. In total on each side (positron and electron beam dump) $2.7 \cdot 10^7$ neutrons leave the beam dump carrying a total energy of 1270 TeV, of which most are backscattered through the entrance window in the direction of the detector. The expected neutron background in the detector, however, is small. In total around 33000 neutrons per BX hit the iron yoke from the outside but less than 100 actually reach the HCAL. Less than one neutron per BX is expected from this source in the tracking detectors.

Beamstrahlung photons are another possible source of neutrons. Due to the design of the beam extraction system (compare section 7.6.2 in part II of this TDR) the number of neutrons produced by beamstrahlung photons hitting beamline elements is negligible [10]. The neutrons which are produced in the beamstrahlung dump 240 m downstream of the IP are well confined. Only very few neutrons leak back through the entrance window which is small (20 mm diameter) compared to the one of the main beam dump. No significant neutron background is expected in the detector from this source.

A total number of $2.8 \cdot 10^5$ neutrons with $E_{tot} = 1.3 \cdot 10^3$ GeV is produced by radiative Bhabhas. This leads to a small background contribution; details are given in table 7.1.6.

7.1.3.5 Muon induced background

Muons are produced in electromagnetic beam-nucleon interactions in the beam delivery system (BDS). Electrons from the halo of the beam interact with beam line elements and may produce muons. The production processes which have been investigated are the Bethe-Heitler process ($eA \rightarrow A\mu^+\mu^- e'$), direct annihilation ($e^+_{beam}e^- \rightarrow \mu^+\mu^-$), pion decay ($eA \rightarrow \pi^\pm + X$; $\pi^\pm \rightarrow \mu^\pm\nu$), and muons produced from secondaries in showers in the beam-line elements [3, 11]. Altogether 7×10^4 beam particles have to be lost to produce one muon in the detector.

If 10^4 beam particles are in the halo of the beam this results in 0.3 muons per BX. As the TPC (which covers roughly 1/4 of the detector cross section) samples around 160 BX the total number of muon tracks per TPC readout is expected to be 11.

A muon protection system can be installed to reduce the muon rates in the detector. A system consisting of 3 large magnetised iron spoilers would reduce the muon rate by a factor of $200 - 500$, a system of 20 toroids results in a gain of $1000 - 3000$.

Source	N_{tot} (E_{tot})	VTX (CCD) N_{hits}/mm^2	SIT N_{hits}	FTD N_{hits}	TPC	FCH N_{hits}	ECAL	HCAL
Beamstr. γ	$6.4 \cdot 10^{10}$ $2.6 \cdot 10^{11}$ GeV	No direct beamstrahlung background in detector						
Pairs (@ 4 T)	129 000 E=361 TeV	L 1: $36{\cdot}10^{-3}$ L 2: $3.1{\cdot}10^{-3}$ L 3: $0.7{\cdot}10^{-3}$ L 4: $0.3{\cdot}10^{-3}$ L 5: $0.2{\cdot}10^{-3}$	SIT 1: 23 SIT 2: 7	D 1: 17 D 2: 17 D 3: 12 D 4: 8 D 5: 8 D 6: 7 D 7: 6	$\mathrm{N_{tracks}} = 5$ $N_\gamma = 1336$ $E_{\gamma,total} =$ 3.13 GeV	63	$\mathrm{N}_{e^\pm,\gamma} = 1176$ $\mathrm{N}_{E>3\mathrm{MeV}} = 192$	n/s
Hadrons $p_t \geq 2.2$ GeV/c	0.02 events $E = 2.07$ GeV	L 1: $34{\cdot}10^{-6}$ L 2: $6.6{\cdot}10^{-6}$ L 3: $4.2{\cdot}10^{-6}$ L 4: $2.9{\cdot}10^{-6}$ L 5: $2.3{\cdot}10^{-6}$	n/s	n/s	$\mathrm{N_{tracks}} = 0.7$ $N_\gamma = 7.1$ $E_{\gamma,total} =$ 18.5 MeV	n/s	ECAL and HCAL: E_{tot}=6 GeV	
rad. Bhabhas	$3.9 \cdot 10^4$ $1.7 \cdot 10^6$ GeV	N_{hits}=2 (L 1)	negligible		$N_\gamma = 3$	negligible		
n from RB	$2.8 \cdot 10^5$ $1.3 \cdot 10^3$ GeV	$< 0.5 \cdot 10^8$ n/cm^2/y	n/s	n/s	110	n/s	90	3160
n from Pairs	70 000 E= 322 GeV	$\mathcal{O}(10^9)$ 1 MeV n/cm^2/year	439 both lay.	478 all discs	14551	n/s	$N_n = 8024$ $E_{tot} =$ 6.1 GeV	$N_n = 4669$ $E_{tot} =$ 8.5 GeV
n from BS+dump	see text	negligible						
Muons	$7 \cdot 10^4 \frac{N_e}{N_\mu}$	10^4 beam halo particles: Full detector: 0.3/BX; TPC: 11 Tracks / 160 BX.						
Sync. Rad.	$2.0 \cdot 10^{11}$ $2.0 \cdot 10^8$ GeV	60 γ/cm^2/BX	negligible					
Beam-Gas	$3 \cdot 10^{-3}$ 0.15 GeV	negligible						

Table 7.1.6: *Summary table of backgrounds for one BX at $\sqrt{s}$ =500 GeV. n/s: not studied.*

7.1.3.6 Synchrotron radiation induced background

Synchrotron radiation is produced by both beams in the magnetic fields of the last bending magnets and the final quadrupoles. The collimation system has been designed so that no direct synchrotron radiation can hit any part of the detector. Backscattered photons are however a potential background source. The main source for these photons is the first collimator at a distance of 19 m from the IP. The total number of synchrotron radiation photons hitting the first collimator is of the order of 10^{11} photons per BX. The calculation of backscattered synchrotron radiation [3] yields about 60 photons per cm^2 per BX in the vertex detector with the photon energies below 1 MeV. No backscattered photons reach the TPC or the ECAL.

7.1.3.7 Beam-Gas background

The vacuum system of the beam delivery system and the interaction region has been designed to maintain an average rest gas pressure of 10^{-8} mbar CO equivalence (compare section 7.2.8 in part II of this TDR). Simulations have been performed to study the effects of beam-gas interactions [3]. Tracking was performed through the last 600 m of the beam line including quadrupoles, collimators, mask, and the beam pipe itself. Assuming a residual gas pressure of $5 \cdot 10^{-9}$ mbar of CO, a number of $3 \cdot 10^{-3}$ electrons per BX leave the beam pipe near the IP which is negligible.

7.1.4 Background summary

The different background sources and the expected background rates in the detector are summarised in table 7.1.6. The detector is shielded well from all background sources. With respect to the chosen fine granularity of the detector elements the expected background rates are small. We expect no problems with the total background rate, the feasibility of recognising and subtracting the background, and with respect to radiation hardness of detector elements.

7.1.5 Cost

Table 7.1.7 gives a summary of the cost estimate for the mask elements.

7.2 Polarimeter

A full exploitation of the physics potential of TESLA must aim to employ polarised electron and positron beams with a high degree of longitudinal polarisation at full intensity. The technology of polarised electron sources of the strained GaAs type is well established [12, 1] and TESLA is therefore likely to deliver a state of the art polarised electron beam with about 80% polarisation from the very beginning. The prospects for the polarisation of the positron beam are under investigation. The proposed scheme of Balakin and Mikhailichenko [13, 14, 1] to upgrade the envisaged wiggler type positron

Source	Cost estimate [kEUR]
Tungsten (material)	1200
Tungsten (processing)	250
Contingency	50
Total for one side	1500
Total for both sides	3000

Table 7.1.7: *Cost estimate for the mask elements. A price of 100 EUR/kg for tungsten has been assumed. The cost for the mask calorimeters LCAL and LAT are given in section 3.5.*

source of TESLA for the generation of polarised positrons will require R&D before it can be implemented. A positron polarisation of 45-60% is expected (see section 4.3.7 in Part II of this TDR).

Equally important to the generation of high beam polarisation will be its precise measurement and control. The quantity of basic interest is the longitudinal spin polarisation of the two beams at the interaction point. Since a precise polarisation measurement at the e^+e^- interaction point itself is either impossible or difficult, the point of measurement should be chosen such that beam transport and beam-beam interaction effects are either negligible or small and well quantified. Other important factors relate to the level of radiation backgrounds and to the technical infrastructure and accessibility.

In the following, we shall give a brief description of the TESLA Compton Polarimeter. A detailed description is given in [15, 16]. The concept of the polarimeter is based on the well established laser backscattering method, as it was already envisaged in the TESLA CDR [1, 17]. The proposed location of the Compton IP, where the laser beam crosses the electron or positron beam, is 630 meters upstream of the center of the e^+e^- detector, near the end of the BDS tuning segment. Although the polarisation vector experiences large rotations (due to the g-2 effect) as the beam traverses the ± 3 mrad bends of the BDS, the beam and spin directions at the chosen polarimeter site are precisely aligned, except for a parallel offset, with the e^+e^- interaction and detector axis. A polarisation measurement at the proposed upstream location will therefore provide a genuine determination of the quantity of interest, as long as beam-beam effects are negligible or correctable. This is indeed the case. We estimate the beam-beam induced depolarisation at TESLA to be 0.5%.

We have also considered the possibility of downstream polarimeter locations, which would in principle permit to investigate beam-beam effects experimentally, as was done with the SLD Compton polarimeter at SLAC. However, the envisaged geometry of the extraction beamline at TESLA appears to be unfavourable for beam polarimetry.

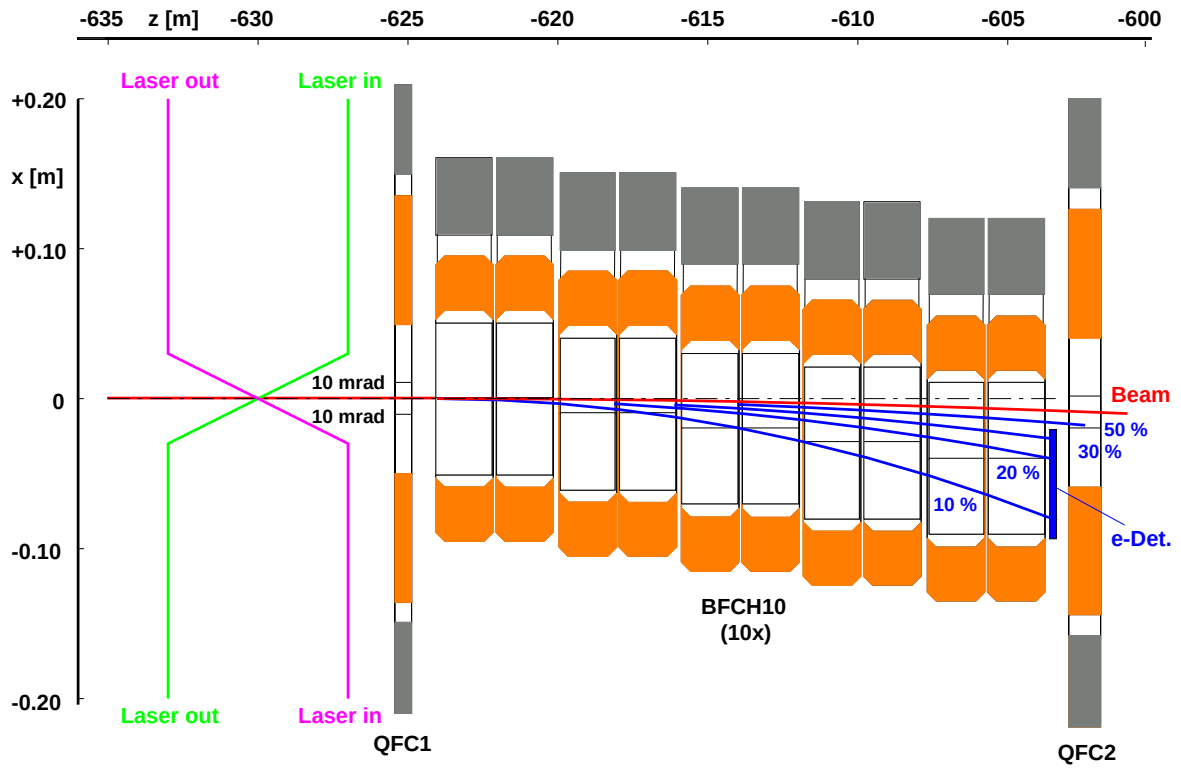

Figure 7.2.1: *Plan layout of the Compton polarimeter.*

7.2.1 Compton polarimeter

The long straight tuning section of the BDS is foreseen for general beam diagnosis and is also ideally suited for high quality beam polarisation measurements. Figure 7.2.1 shows a plan view layout of the Compton Polarimeter. The laser beam crosses the electron or positron beam with a small crossing angle of 10 mrad at z = -630 m, just upstream of 10 C-type dipole magnets (BFCH0) which bend the beam horizontally by 0.77 mrad. The transverse placement of the individual dipoles has been adjusted to accept a large fraction of the recoil electron spectrum. The electron detector is a segmented gas Cerenkov counter, similar in design to the one in use at the SLD polarimeter [18]. An optional calorimetric photon detector can also be employed further downstream.

The energy spectrum, the associated spin asymmetry and the scattering angles of the Compton scattered electrons and photons are shown in Fig. 7.2.2 for a beam energy of 250 GeV and a green frequency-doubled YAG or YLF solid state laser (photon energy 2.33 eV). This configuration allows for good coverage of the most interesting part of the electron spectrum with the spectrometer described earlier. In order to accomplish this also for much higher or lower beam energies, it will be advantageous to change the wavelength of the laser. At a beam energy of 400 GeV, the laser should be operated at the fundamental infrared wavelength (1.165 eV = 1064 nm). At the Z-pole (45.6 GeV), fourth harmonic UV operation (4.66 eV = 266 nm) will be advantageous. The corresponding spectra and other relevant details can be found in [15].

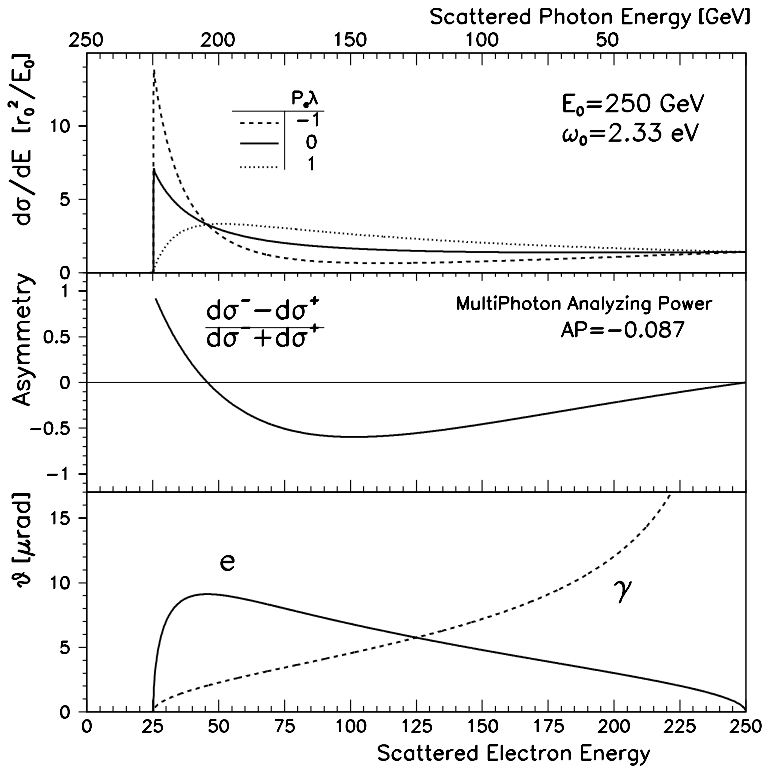

Figure 7.2.2: *Energy spectrum (top), spin asymmetry (middle) and scattering angles (bottom) of Compton scattered electrons and photons.*

Since the optical elements of a laser beam line can only be optimised for a specific wavelength, one should preinstall multiple laser beam lines in the tunnel, as indicated in Fig. 7.2.1, if such a large change of the beam energy must be accomodated with minimal polarimeter downtime.

The longitudinal polarisation of the electron beam is determined from the asymmetry of two measurements of Compton scattering with parallel and antiparallel spin configurations of the interacting electron and laser beams. In order to achieve good statistical precision in a short time, the laser should ideally be pulsed with a temporal profile that matches the pulse and bunch pattern of the TESLA linac.

A laser system with such exceptional properties is not commercially availible, but has been developed at Max Born Institute for the Tesla Test Facility (TTF) photo injector gun at DESY, where it has been in operation since some time [19, 20]. This multi-stage laser system employs Nd:YLF and operates at a fundamental wavelength of 1047 nm in the infrared, which is converted in two steps to 2nd and 4th harmonic, for a final wavelength of 262 nm in the UV. The laser has delivered up to 250 μJ (IR) and 50 μJ (UV) per bunch, with associated pulse widths σ_t of 16 and 8 ps.The mean IR power is ≤ 2 W.

A variant of this TTF laser system would also be well suited for the Compton polarimeter. The luminosity that can be achieved with such a laser is typically six orders

of magnitude higher than with a cw laser of similar average power. The statistics of Compton produced events is very high, about 10^3 per bunch and 10^7 per second, for the conditions listed in Table 7.2.1 and Fig. 7.2.2. Not all of this will be detected, nevertheless, it is clear that statistical errors will not matter in comparison with systematic errors. We expect a performance similar to the SLD Compton polarimeter, with an overall precision of $\Delta P/P \sim 0.5\%$ for the measurement of the beam polarisation.

	e^+/e^-–beam	laser beam
energy	250 GeV	2.3 eV
charge or energy/bunch	$2 \cdot 10^{10}$	35 μJ
bunches/s	14100	14100
bunch length σ_t	1.3 ps	16 ps
average current(power)	45 μA	0.5 W
$\sigma_x \cdot \sigma_y$ (μm)	$10 \cdot 1$	$50 \cdot 50$
beam crossing angle	10 mrad	
luminosity	$1.5 \cdot 10^{32}$ cm^{-2}s^{-1}	
cross section	$0.136 \cdot 10^{-24}$ cm^2	
events produced/s	$0.2 \cdot 10^8$	
events produced/bunch	$1.4 \cdot 10^3$	
ΔP/P stat. error/s	negligible	
ΔP/P syst. error	$\sim 0.5\%$	

Table 7.2.1: *Compton Polarimeter Parameters at 250 GeV*

7.2.1.1 Cost of Compton polarimeter

The estimated cost of the Compton Polarimeter, based on year 2000 prices, is summarised in Table 7.2.2. This cost table is figured on the assumption that the laser and the electronics and data acquisition system (DAQ) will be located in a dedicated surface building (Polarimeter Lab) at z = -615 m in close vicinity to the polarimeter site in the tunnel. It provides access to all critical laser and electronic elements and minimises the length of the laser beam transport and the cables. This scenario is therefore strongly preferred for technical as well as economical reasons. The incremental cost of an optional second laser beamline, which may be desirable to accommodate very different electron beam energies with minimal polarimeter downtime, would be 150 kEURper polarimeter.

7.2.2 Møller polarimeter

A different beam polarimeter concept based on Møller and Bhabha scattering has been investigated [21]. As this method employs a thin ferromagnetic foil target in the beam line, it could not operate in conjunction with physics data taking, but only

	Cost Estimate (kEUR)
Surface Building	250
Laser	400
Vertical Shaft	25
Laser Beamline and Optics	125
Vacuum Chambers	75
e-Detector	50
Cables	10
Electronics and DAQ	165
Total for one beam	1100
Total for both beams	2200

Table 7.2.2: *Cost estimate for Compton Polarimeters*

intermittently, if it is located upstream of the e^+e^- detector. In principle, it could be located downstream in the extraction beam line, but it would have to confront the very difficult conditions in this area and a feasible solution has to be found. The polarimeter is based on a new target concept [22] which allows to obtain a systematic uncertainty below 1%. With this precision it can be used to check regularly the absolute calibration of the Compton polarimeter.

7.3 Energy Spectrometer

The measurement of the top quark mass with an error of less than 100 MeV (which is comparable to the error resulting from theory) requires the knowledge of the beam energy of both beams (e^+ and e^-) with a precision of $\Delta E/E \leq 10^{-4}$. We propose two different designs for an energy measuring device, a magnetic spectrometer and a setup which makes use of Møller scattering. The second alternative could be combined with a Møller polarimeter.

7.3.1 Requirements

Since a linear accelerator has no depolarising resonances, the method of resonant depolarisation (e.g. used at LEP) cannot be used to calibrate a beam energy spectrometer. A calibration can only be done at the – due to the precise LEP measurements well-known – mass of the Z. Therefore a method should be preferred which can provide an absolute measurement of the beam energy.

The energy spectrometer cannot be installed in the extraction beam line as the beam is very hard to control in this region and high background is expected there. Thus we propose to use up to 50 m of free space in one of the straight sections of the final focus beam line. More space (≈ 100 m) is available in the last 300 m before the IP but a very large background from beamstrahlung originating from the IP is expected there.

7.3.2 Magnetic spectrometer

Magnetic spectrometers with energy resolutions of a few 10^{-4} have been used for precision energy measurement at LEP [23] and SLC [24]. We propose a design which is similar to the LEP spectrometer (fig. 7.3.1).

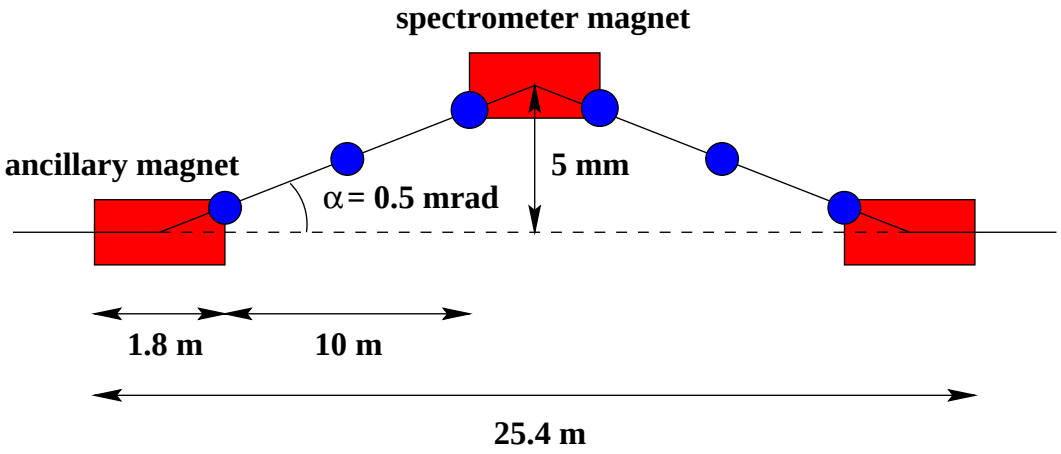

Figure 7.3.1: *Magnetic spectrometer. The circles indicate the beam position monitors (BPMs). Not to scale.*

The setup for TESLA should consist of a magnetic chicane of two deflection magnets (B = 0.37 T/m) and one spectrometer magnet with a magnetic field of B = 0.74 T/m and a length of 1.8 m for all magnets. The field of the spectrometer magnet has to be mapped to a resolution of $\Delta B/B \leq 3 \cdot 10^{-5}$ which has shown to be feasible at the LEP energy spectrometer [23]. Three beam position monitors (BPMs) on each side of the spectrometer magnet are foreseen to measure the beam deflection angle ($\theta = 0.5$ mrad @ 400 GeV) with high precision. The beam energy is then given by

$$E_{beam} = \frac{ec \int Bdl}{\theta} \ . \tag{7.3.1}$$

A spatial resolution of better than 1 μm is required for the BPMs (comparable to the BPMs used at the LEP spectrometer [23]). The BPM offset can be measured by switching off the magnets and using the calculable ballistic path of the beam. As the range of the BPMs might not be large enough to cover the then expected beam displacement of ≤ 5 mm the position of BPMs will be re-adjusted mechanically with a position accuracy of better than 1 μm.

We estimate the energy resolution of such a magnetic spectrometer to be a few 10^{-4}. This can be improved by using BPMs with a resolution of ≈ 100 nm, e.g. cavity type BPMs. An energy resolution of $\Delta E/E \approx 10^{-4}$ is then feasible.

7.3.3 Møller (Bhabha) scattering

For electroweak precision measurements at TESLA in the vicinity of the Z mass peak an accuracy in the energy calibration of 10^{-5} is needed (see Part III, Chapter 5). Møller scattering has been studied as a possibility to measure the beam energy at LEP to a resolution of a few 10^{-5} [25, 26]. The advantage of this method is the use of a physical scattering reaction which does not disturb the beam like using a bend. Our proposal foresees to use a hydrogen gas jet as electron target. Fig (7.3.2) shows the conceptual setup of a Møller scattering spectrometer which can be installed in the electron linac. A similar setup can be used to detect Bhabha scattering in the positron beam.

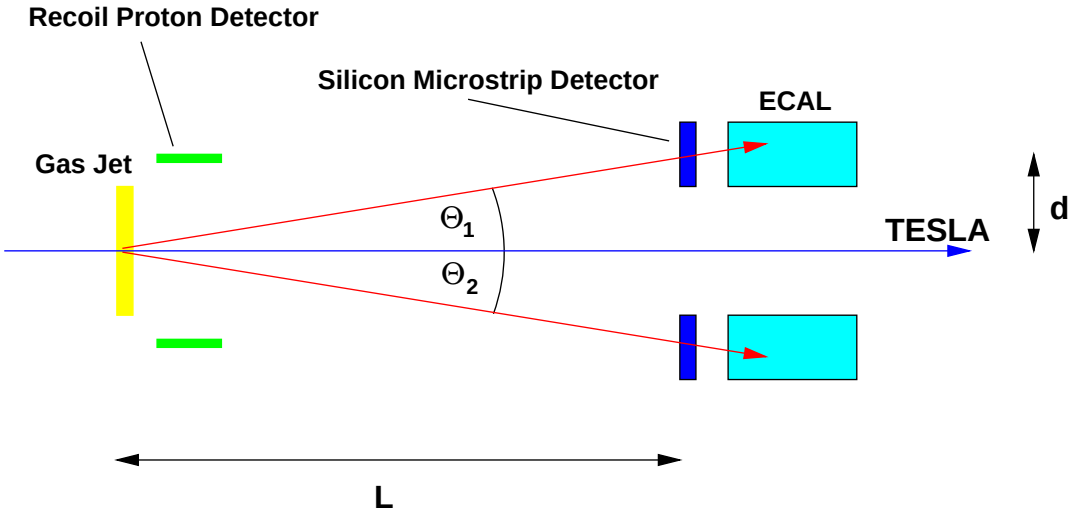

Figure 7.3.2: *Møller spectrometer. Not to scale.*

With a gas jet of a few 10^{14} atoms per cm^2 (typical for a cluster jet target, compare e.g. [27]) luminosities in the order of $10^{31}\,cm^{-2}\,s^{-1}$ will be reached. The scattered electrons will be measured near the symmetric angle (where $\theta_{cms} = 90°$) in a detector setup of silicon microstrip detectors in combination with high resolution electromagnetic calorimeters. The beam energy can be calculated from a precision measurement of the scattering angles. The determination of the energies of the scattered electrons allows a measurement independent on transverse beam displacements. The expected resolution can be improved significantly, however, by an additional measurement of the transverse beam positions. This could be realised by detecting the recoil protons of elastic electron-proton scattering in a dedicated detector close to the target [26].

The accuracy of the energy measurement depends linearly on the precision of the angle measurement. A precision aim of $\Delta E/E \approx 10^{-5}$ requires a resolution in the angular measurement of the same order. With typical distances of $L \approx 20\,m$ and $d \approx 20\,cm$, this requires accuracies of $\Delta L \approx 150\,\mu m$ and $\Delta d \approx 1\,\mu m$ (refer to Fig 7.3.2). It has been shown [26] that (for LEP energies) errors originating from binding effects of the electrons, finite energy resolutions of the calorimeters and radiative corrections are small enough that an overall error on the energy measurement of a few 10^{-5} can be

reached.

The Møller scattering method should reach a precision of 10^{-5} in a *relative measurement* when it is cross calibrated using the well known Z mass [26].

7.3.4 Cost

The estimates for the magnetic and the Møller scattering energy spectrometer are summarised in table 7.3.1.

Source	Magnetic Spectrom. [kEUR]	Møller Scatt. [kEUR]
Magnet	200	-
Field mapping	200	-
Cluster Jet Target	-	750
Instrumentation	300	500
Mechanics	300	300
Total for one beam	1000	1550
Total for both beams	2000	3100

Table 7.3.1: *Cost estimate for the magnetic and the Møller scattering energy spectrometers.*

Bibliography

[1] R. Brinkmann, G. Materlik, J. Rossbach, and A. Wagner (eds.). *Conceptual Design Report of a 500 GeV e^+e^- Linear Collider with Integrated X-Ray Laser Facility*, DESY 1997-048, ECFA 1997-182, 1997. DESY. http://tesla.desy.de/TTF_Report/CDR/TTFcdrTab.html.

[2] D. Schulte. Study of Electromagnetic and Hadronic Background in the Interaction Region of the TESLA Collider. *TESLA 97-08*, 1996. electronic document http://tesla.desy.de/TTF_Report/TESLA/TTFnot97.html.

[3] O. Napoly, I. Reyzl, and N. Tesch. Interaction Region Layout, Feedback and Background Issues for TESLA. In E. Fernández and A. Pacheco (eds.), *Proceedings of the Worldwide Study on Physics and Experiments with Future Linear e^+e^- Colliders*, Sitges, Spain, 1999. Universitat Autònoma de Barcelona.

[4] K. Büßer. Mask Design and Background Studies for TESLA. In *Proceedings of the Linear Collider Workshop 2000*, Fermilab, Batavia, IL, USA, 2000. http://www-lc.fnal.gov/lcws2000.

[5] T. Behnke, G. Blair, M. Elsing, K. Mönig, and M. Pohl. BRAHMS: A Monte Carlo for a Detector at a 500/800 GeV Linear Collider. *LC-TOOL-2001-005*, 2001. electronic document http://www.desy.de/~lcnotes/.

[6] M. Schumacher. A TPC with GEM Readout for TESLA. In *Proceedings of the Linear Collider Workshop 2000*, Fermilab, Batavia, IL, USA, 2000. http://www-lc.fnal.gov/lcws2000.

[7] C. Hensel. Beam Induced Background at a TESLA Detector. *LC-DET-2000-001*, 2000. electronic document http://www.desy.de/~lcnotes/.

[8] A. Fassò et al. FLUKA: Present Status and Future Developments. In A. Menzione and A. Scribano (eds.), *Proc. IV Int. Conf. on Calorimetry in High Energy Physics*, 493, La Biodola, Italy, 1993. World Scientific.

[9] A. Ferrari et al. The Physics of High Energy Reactions. In A. Gandini and G. Reffo (eds.), *Proc. of Workshop on Nuclear Reaction Data and Nuclear Reactors Physics, Design and Safety*, 424, Miramare-Trieste, Italy, 1998. World Scientific.

[10] G. Wagner. Neutron Background Studies at the TESLA Collider. *LC-DET-2001-048*, 2001. electronic document http://www.desy.de/~lcnotes/.

[11] H. J. Schreiber. Muon Background. In *7th Workshop of the 2nd ECFA/DESY Study of Physics and Detectors for a Linear Electron-Positron Collider*, Hamburg, Germany, 2000. http://www.desy.de/~ecfadesy/transparencies/Det_HJSchreiber1.pdf.

[12] R. Alley et al. The Stanford Linear Accelerator Polarized Electron Source.

Nucl. Instrum. Meth., A365:1–27, 1995. electronic document.

[13] V. E. Balakin and A. A. Mikhailichenko. The Conversion System for Obtaining High Polarized Electrons and Positrons. *INP 79-85*, 1979.

[14] K. Flöttmann. Investigation Toward the Development of Polarized and Unpolarized High Intensity Positron Sources for Linear Colliders. *DESY-93-161*, 1993.

[15] V. Gharibyan, N. Meyners, and K. P. Schüler. The TESLA Compton Polarimeter. *LC-DET-2001-047*, 2001. electronic document http://www.desy.de/~lcnotes/.

[16] K. P. Schüler. Polarimeter Studies for TESLA. In *Proceedings of the Linear Collider Workshop 2000*, Fermilab, Batavia, IL, USA, 2000. http://www-lc.fnal.gov/lcws2000.

[17] G. Bardin et al. Compton Polarimeter Studies for TESLA. *TESLA 97-03*, 1997. http://tesla.desy.de/TTF_Report/TESLA/TTFnot97.html.

[18] M. Woods. The Scanning Compton Polarimeter for the SLD Experiment. *SLAC-PUB-7319*, 1996. electronic document.

[19] I. Will, P. Nickles, and W. Sandner. A Laser System for the TESLA Photo-Injector. Internal Design Study, Max-Born-Institut, Berlin, 1994.

[20] S. Schreiber, D. Sertore, I. Will, A. Liero, and W. Sandner. Running Experience with the Laser System for the RF Gun Based Injector at the TESLA Test Facility Linac. *Nucl. Instrum. Meth.*, A445:427–431, 2000. electronic document.

[21] G. Alexander and I. Cohen. Møller Scattering Polarimetry for High Energy e^+e^- Linear Colliders. *LC-DET-2000-046*, 2000. electronic document http://www.desy.de/~lcnotes/.

[22] L. V. de Bever, et al. A Target for Precise Møller Polarimetry. *Nucl. Instrum. Meth.*, A400:379–386, 1997. electronic document.

[23] B. Dehning. Status of the LEP2 Spectrometer Project. In *Proceedings of EPAC 2000*, Vienna, Austria, 2000.

[24] J. Kent et al. Precision Measurements of the SLC Beam Energy. *SLAC-PUB-4922, LBL-26977*, 1989. electronic document.

[25] P. Galumian, C. Joseph, J. P. Perroud, M. T. Tran, and M. Werlen. A Method for Precise Calibration of Electron Beam Energy. *Nucl. Instrum. Meth.*, A327:269–276, 1993.

[26] C. Cecchi, J. H. Field, and T. Kawamoto. Beam Energy Measurement at LEP2 using Møller Scattering. *Nucl. Instrum. Meth.*, A385:445–455, 1997. electronic document.

[27] H. Dombrowski, et al. The Münster Cluster Target for Internal Storage Ring Experiments. *Nucl. Instrum. Meth.*, A386:228–234, 1997. electronic document.

8 Detector Integration

In this section a concept is presented for the experimental hall and for a procedure to install, service and access the detector. Particular emphasis has been given to the development of a concept which allows the access to the inner part of the detector, without removing the detector from the beam line.

The size of the detector and these requirements lead to the following experimental hall dimensions:

- hall width in beam direction 30 m,
- hall length perpendicular to the beam 82 m,
- beam height 8 m above the floor,
- crane hook 19 m above the floor.

The beamline divides the hall into a long 66 m section and a short 16 m section. The long section will allow detector assembly, detector maintenance or detector upgrade with the interaction region shielded by movable 2 m thick concrete blocks. Commissioning of the linac and machine studies are therefore completely independent of the detector assembly status in the parking position. The length of the short section is defined by the open position of the detector in the interaction region to allow access to the vertex region. Two cranes with a capacity of 80 tons each are foreseen for the handling of heavy items. Fig. 8.0.1 shows a sketch of the detector assembly arrangement in the parking position with the installation area shielded against radiation from linac operation by a system of concrete blocks.

8.1 Detector Mechanical Concept

The main design criteria when developing the mechanical concept of the detector were to allow easy access to the innermost parts of the detector without moving the whole detector into the parking position. To this end the detector has been divided into five parts moving independently on air pads. The central yoke ring holds the coil cryostat with the calorimeter and the central tracking chamber inside. The four corner half-shells close the iron return yoke. The vertex detector and inner tracker are fixed to the central beampipe. This concept allows access to the vertex and inner tracking systems while the detector is in the interaction region with the central detector beampipe still connected to the linac machine vacuum. The main idea behind this concept is that after opening the yoke and removing the calorimeter endcap, the TPC is moved in the beam direction by about one length, sliding over the mask system. In this way access is possible to the innermost Si tracking detectors, the mask system and the beampipe

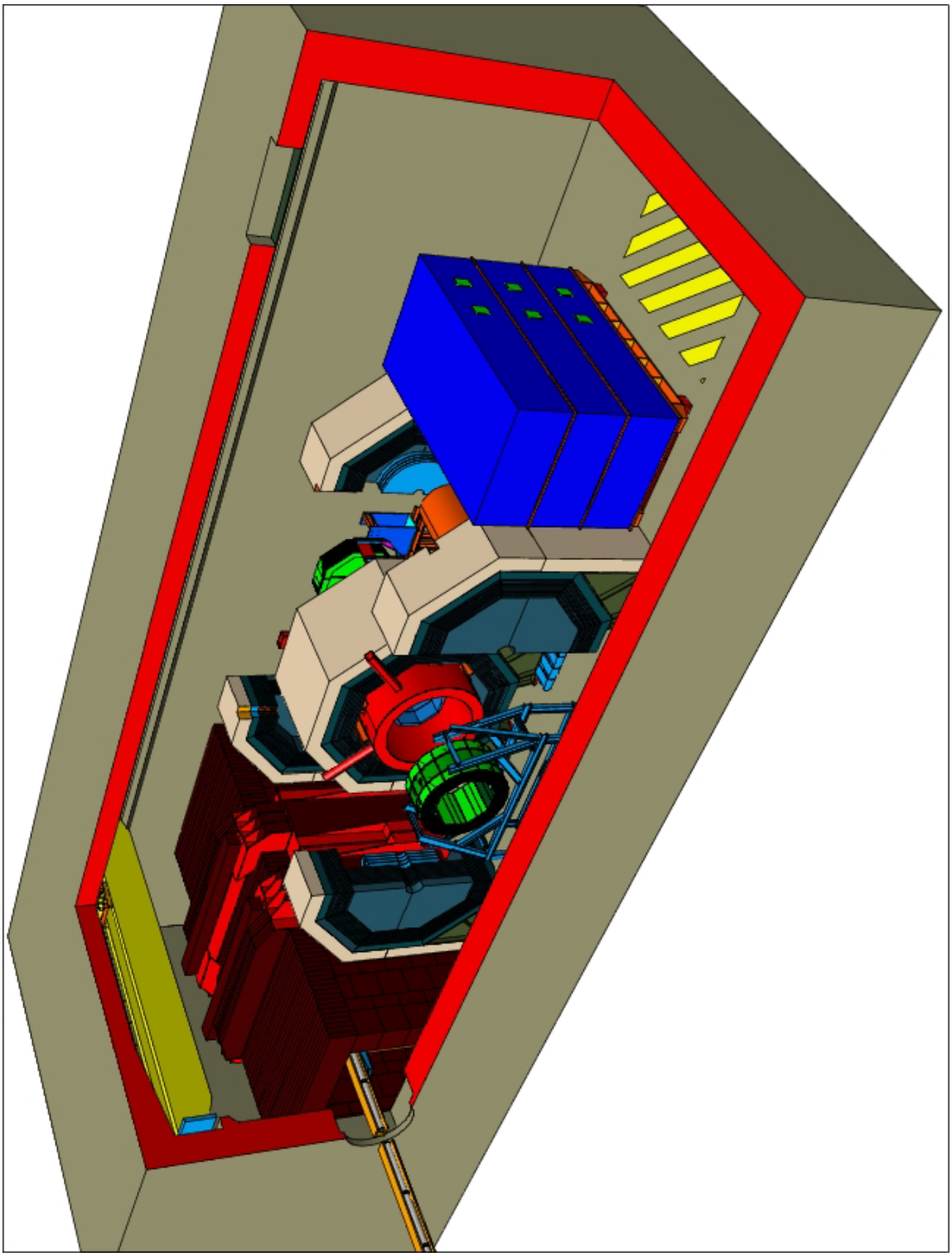

Figure 8.0.1: *View of the detector hall with the detector in the parking position. The beam line is shielded with concrete blocks, so that the machine operation and the detector work can proceed in parallel.*

in the interaction region. Fig. 8.1.1 shows the detector in the open position with the four half shells opened and the TPC removed in the beam direction to clear the central beampipe section.

A particularly difficult part of the mechanical design is the support and control of the tungsten tube which is used as a shield and as a support for the final focusing quadrupoles. During normal operation the tube is supported at its two ends, outside the detector through the cantilever system shown in Fig. 8.1.2, and inside the detector through a system of spokes to the cryostat of the coil. The distortion of the tungsten tube in this situation is shown in Fig. 8.1.2, indicating, that the mask bends at most $250\,\mu$m . The situation is very different during the opening of the detector. The support at the tip of the mask has to be released. As a result the tip of the mask will sag by around 20 mm. This is counteracted by a system of cantilevers, so that the tip at the mask remains stable, thus making sure that the inner detector which is in part suspended from the mask is not destroyed. During movement of detector parts an active system has to ensure that the tip of the mask does not move.

The technical solutions for the mechanical detector concept and the different assembly and maintenance scenarios including support and moving mechanisms are described in detail in reference [1, 2].

The detector is designed to be self-shielding. A layer of concrete about 1 m thick is added on the outside of the muon filter to stop slow neutrons. The machine sections between detector and linac-tunnel are shielded by movable concrete blocks. The detector electronics are located in a 3-story trailer coupled to the detector at a fixed distance. Fig. 8.1.3 is an isometric view of the detector in the beam position (with one detector quadrant cut out and part of the shielding left out to show the structure of the detector arrangement).

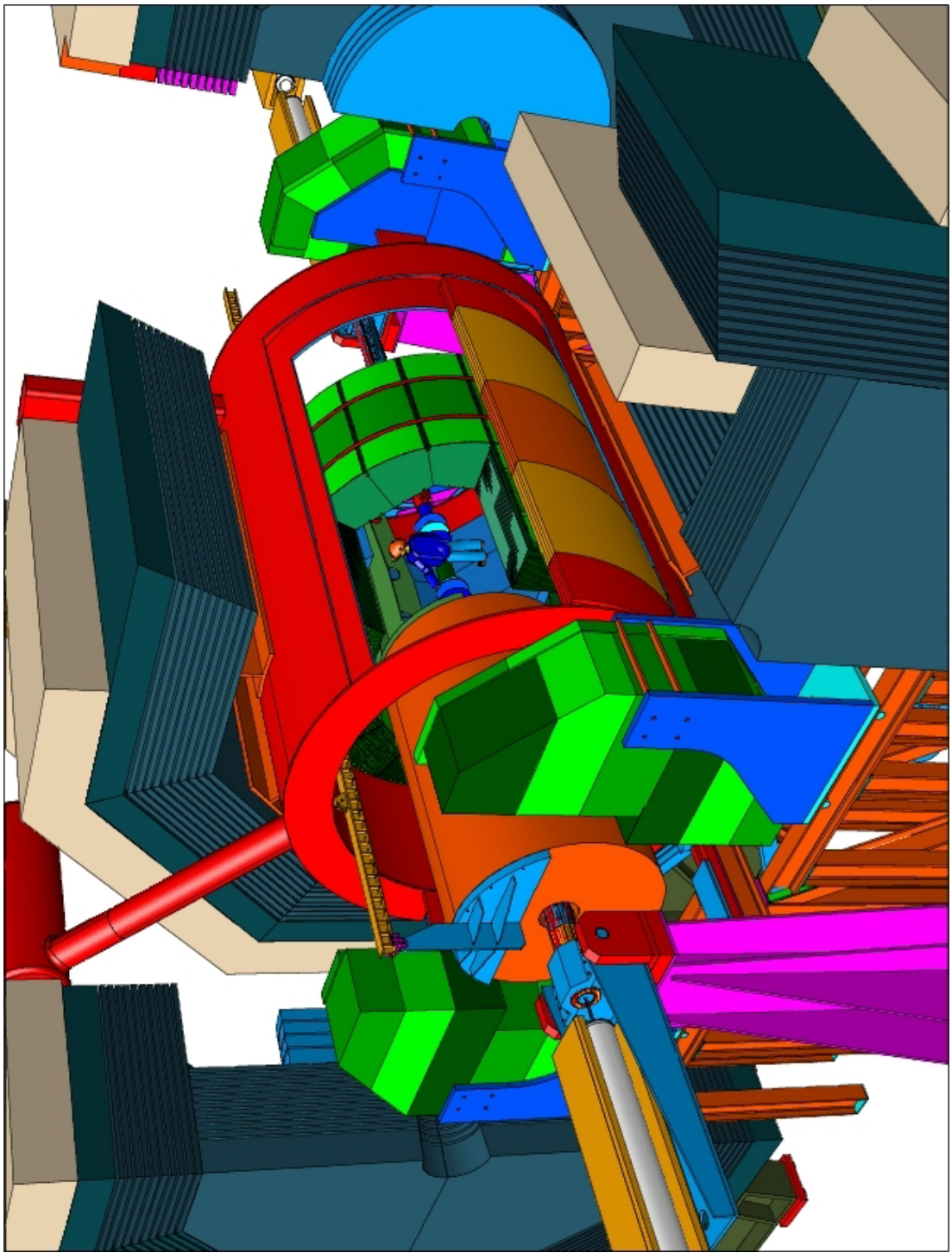

Figure 8.1.1: *View of the detector in the service position in the beam line. The yoke has been opened, and the endcap HCAL has been removed with special tooling. The TPC has been moved in the direction of the beam to clear the inner detectors and to allow access to them.*

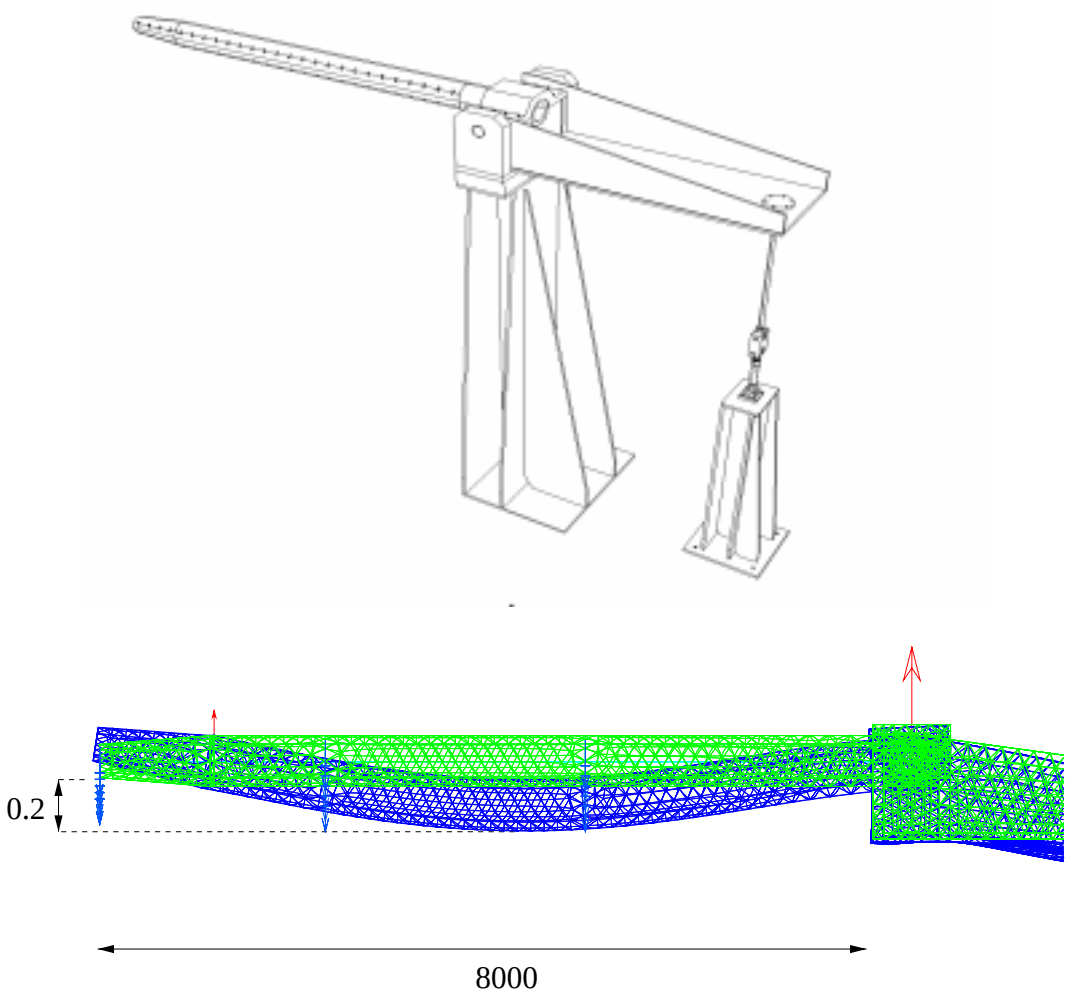

Figure 8.1.2: *Top: View of the mask and its support and cantilever structure. Bottom: Results from a finite-elements calculation showing the deformation of the mask during normal running operations. Scales are in mm. The mask is shown in the running position, where it is suspended from the tip and at the base.*

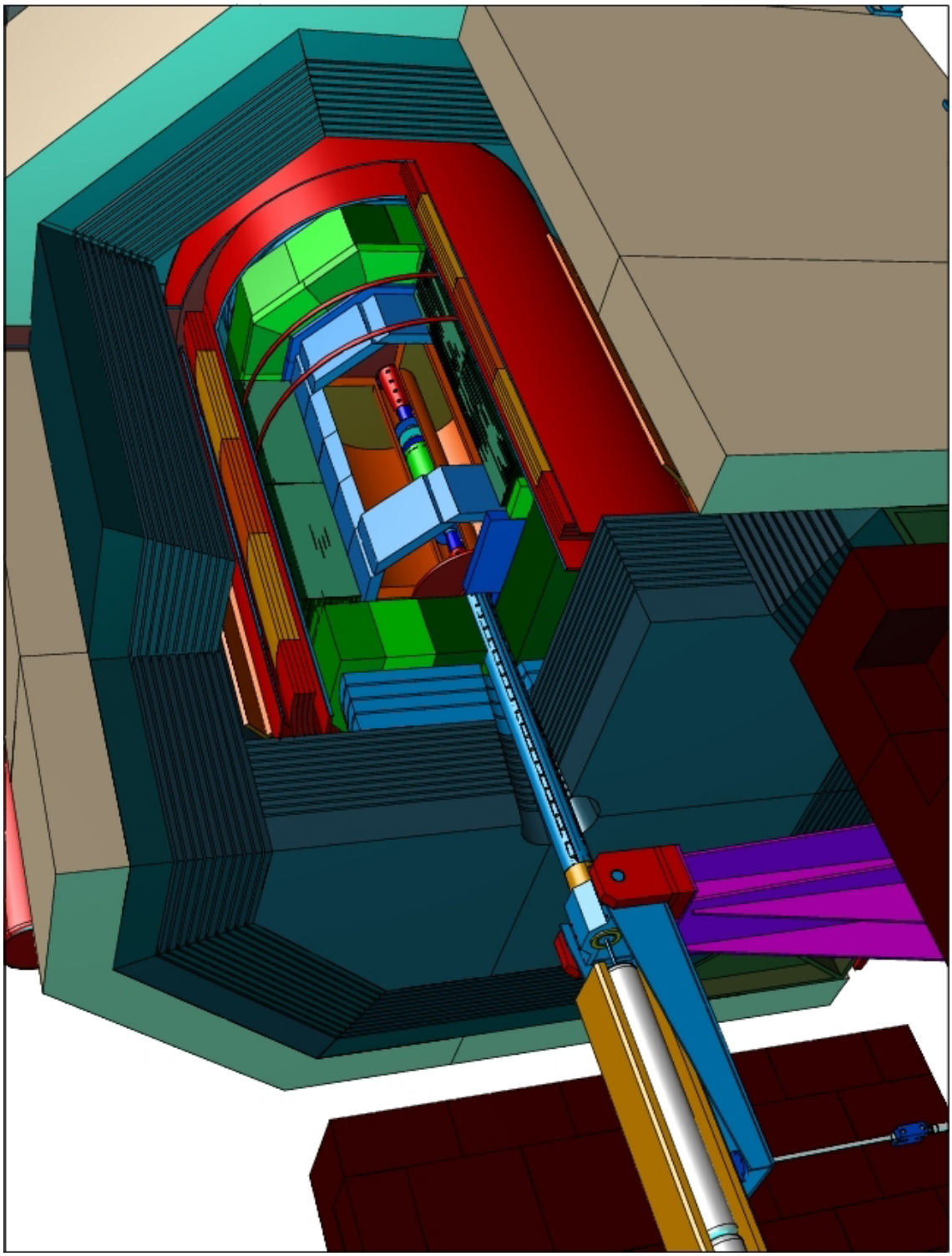

Figure 8.1.3: *View of the detector in the beam position.*

Bibliography

[1] N. Meyners, K. Sinram, et al. Mechanical Concept of the TESLA Detector. *LC-DET-2001-045*, 2001. http://www.desy.de/~lcnotes electronic document.

[2] P.Hassler et al. The Mechanical Design of the HCAL Detector for TESLA. *LC-DET-2001-046*, 2001. http://www.desy.de/~lcnotes/ electronic document.

9 Detector Performance

In the relevant detector subsections the technical performances of the different components are shown. As explained in Chapter 1 the four main requirements of the detector are an excellent momentum resolution, flavour tagging capability, energy flow reconstruction and hermeticity .

This section summarises the performance of the detector system for a set of benchmark physics reactions characteristic for the diversified TESLA physics programme.

9.1 Simulation Tools

To assess the performance of the detector two types of simulation programs have been written. For detailed detector studies a full simulation program, BRAHMS, based on GEANT3 [1] has been developed [2], which produces hits in the different subdetectors. These hits are reconstructed with a pattern recognition and track fitting software, largely based on code used by the LEP experiments [3, 4]. To allow physics studies with high statistics the outcome of the full simulation is parameterised in a fast simulation program, called SIMDET [5]. This program outputs measured tracks and calorimeter clusters which are subsequently used in the physics studies.

9.2 Momentum Resolution

For the model independent analysis of the Higgs cross section, branching ratios and mass, using the recoil mass against a leptonic Z-decay (see Part III, Chapter 2), it is important to have very good resolution on the reconstructed Z- and recoil-mass to minimise the background. The momentum resolution reached by the detector in the central region is $\Delta 1/p = 5 \cdot 10^{-5}\,(\,\mathrm{GeV}/c)^{-1}$. Figure 9.2.1 shows the generated and reconstructed Z-mass and recoil mass at $\sqrt{s} = 350$ GeV. Due to the large natural width of the Z the generated and reconstructed mass are practically indistinguishable. The resolution on the recoil mass for single events is 1.2 GeV/c^2. The long tail to larger masses is due to initial state radiation and beamstrahlung. The width of the reconstructed distribution is similar to the generated one, which is caused by a 0.1% beam energy spread. Therefore also here the degradation of the signal due to the detector is modest.

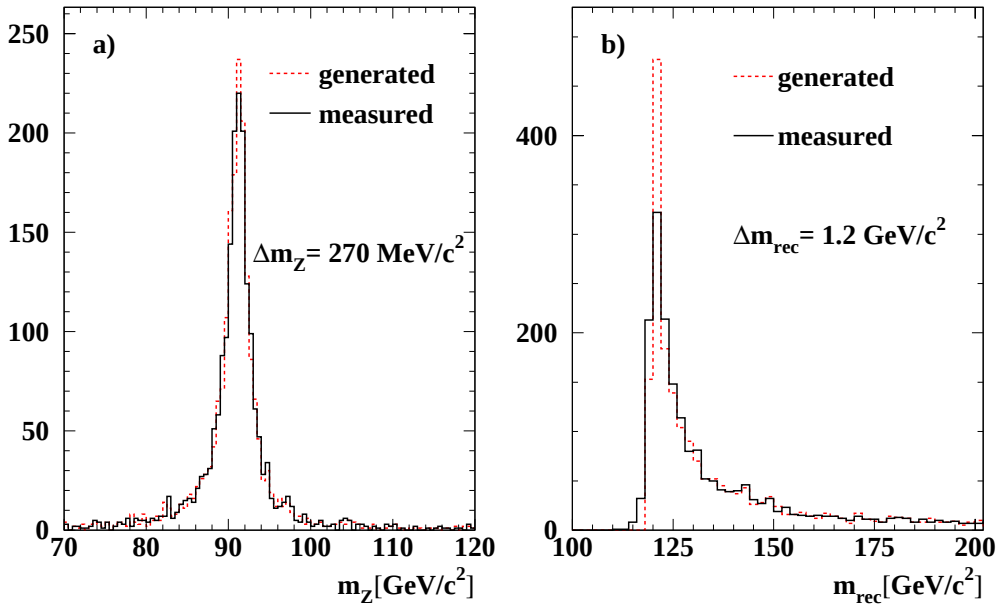

Figure 9.2.1: *a): Generated and reconstructed Z-mass and b): recoil-mass for* $e^+e^- \rightarrow ZH \rightarrow \ell^+\ell^-H$ *events at* $\sqrt{s} = 350$ *GeV* ($m_H = 120$ *GeV*/c^2).

9.3 Flavour Tagging

For many analyses the performance of the flavour tagging is of utmost importance. A light Higgs-boson decays predominantly into $b\bar{b}$ and top quarks decay in almost all cases into a b-quark and a W-boson. In some analyses multi-b final states, like $t\bar{t}H$ or ZHH, need to be separated from a large background. This requires a very high b-tagging efficiency combined with a large rejection power against light and c-quarks. In addition the measurement of the branching ratio of the Higgs into c-quarks requires an efficient c-tagging with a very high rejection of b-quarks. Figure 9.3.1 shows the efficiency–purity curves for b– and c–tagging for jets from Z-decays [6]. The b-purity stays above 90% for efficiencies up to 80% and also c–purities of $> 90\%$ can be reached with around 30% efficiency. As indicated by the blue filled circles especially the rejection of b-jets, needed for the Higgs branching ratio measurement, can be kept high up to very high efficiencies. These are large improvements compared to what has been achieved with present detectors. It has been checked that the performance of the flavour tagging is essentially independent of the jet-energy up to at least 200 GeV.

Figure 9.3.2 shows the precision that is reachable on the Higgs branching ratios with the proposed detector [8]. The separation between $H \rightarrow b\bar{b}$, $H \rightarrow c\bar{c}$ and $H \rightarrow gg$ is entirely due to the capability of the flavour-tagging.

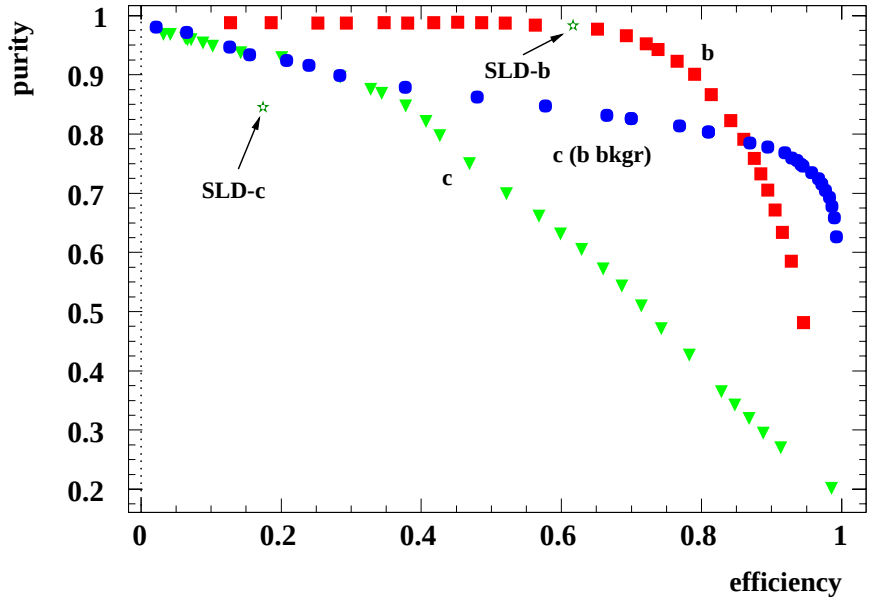

Figure 9.3.1: *Efficiency versus purity of the b- and c-tagging for jets from Z-decays. The green triangles are for the natural flavour composition. For the blue bullets the uds-background has been suppressed artificially to indicate the tagging performance in the Higgs branching ratio measurement. The green stars show the working points of the SLD R_b, R_c analyses [7].*

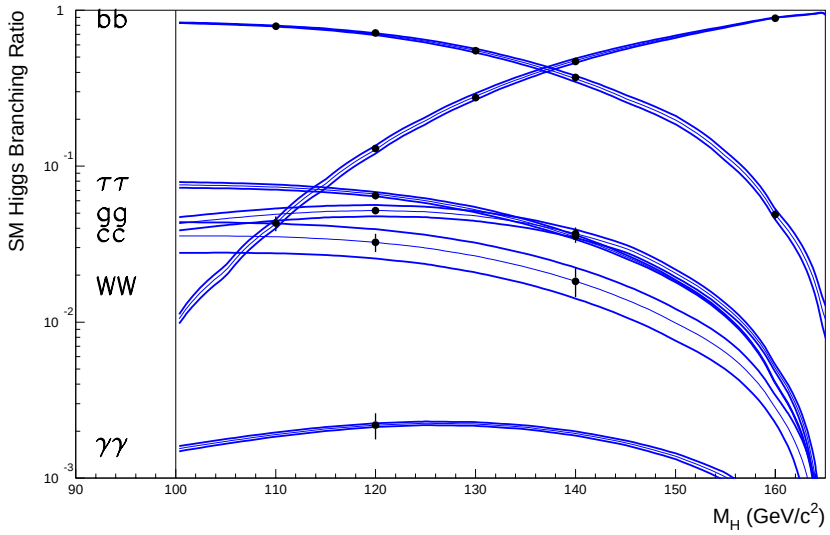

Figure 9.3.2: *Possible precision of the Higgs branching ratio measurement as a function of the Higgs mass. For details see Part III, Chapter 2.*

9.4 Energy Flow

The third important task of the detector is the accurate measurement of the energy flow. The energy flow algorithm has to provide an optimal estimate on the energy and direction of partons, mainly to measure jet-jet invariant masses and to estimate the momentum of unseen particles like neutrinos. Unlike at LEP, constrained fits are only of limited use, since the initial state is less well defined because of beamstrahlung and since many interesting channels end up in multi-jet final states where fewer constraints are present. The resolution needed can only be reached by adding the momenta of the charged particles, measured in the tracking system, to the energies of the neutrals, measured in the calorimeters. To achieve this goal sophisticated software is needed to separate overlapping showers from charged and neutral particles. At present a jet energy resolution of $\Delta E/E = 33\%/\sqrt{E}$ is reached [4], compared to $\Delta E/E = 60\% \cdot (1 + |\cos\theta|)/\sqrt{E}$ which has been achieved at LEP [9]. This is a remarkable improvement made possible by the high granularity of the detector. The present energy flow software does not yet use a true three dimensional reconstruction and better methods are known. The goal of $\Delta E/E = 30\%/\sqrt{E}$ should thus be reachable with the calorimeters presented in chapter 3. Due to the high granularity of the detector no dependence of the resolution on the polar angle is expected. The energy flow performance of the detector at present is given in Fig. 9.4.1, which shows the difference between the generated and the reconstructed visible mass in hadronic Z-decays at rest. The jet-jet mass resolution in the central part is 3.1 GeV.

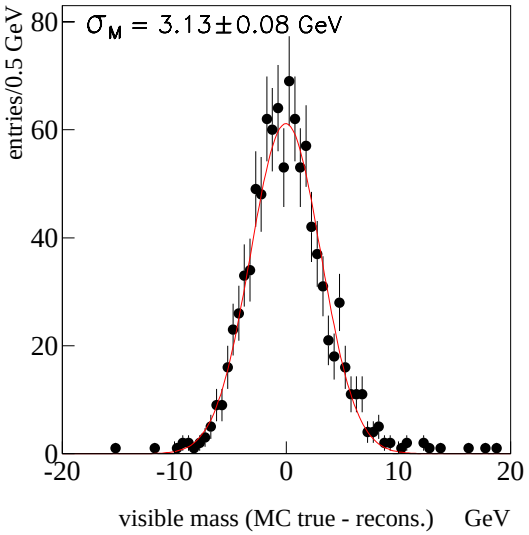

Figure 9.4.1: *Mass resolution for hadronic Z-decays at rest.*

Some interesting physics signals decay through intermediate resonances, which in turn decay hadronically. To identify them, a good jet-jet mass resolution is important. One example is the measurement of the trilinear Higgs coupling from the process

$e^+e^- \to ZHH$ [10]. A signal of about 0.5 fb has to be separated from a huge background. One handle is the jet-jet mass resolution to identify two Higgs- and one Z-boson. Having reconstructed six jets a distance of the event to a signal event can be defined as Dist $= \sqrt{(m_{12}-m_H)^2+(m_{34}-m_H)^2+(m_{56}-m_Z)^2}$. This variable is in general larger than zero and exactly zero only when the invariant masses of all three jet pairs are exactly equal to the expectation for the signal. The width of the distribution for the signal is given by the energy flow resolution of the detector. Figure 9.4.2 shows this distance variable for simulated signal and background events for the energy flow resolution as reached at LEP and for the TESLA goal. The separation improves significantly with the better resolution. Figure 9.4.3 shows the achievable significance for several assumptions on the resolution. This measurement is only possible if the energy flow performance is extremely good. At least $\Delta E/E \approx 35\%/\sqrt{E}$ is needed to establish the signal with an integrated luminosity of $1\,\mathrm{ab}^{-1}$.

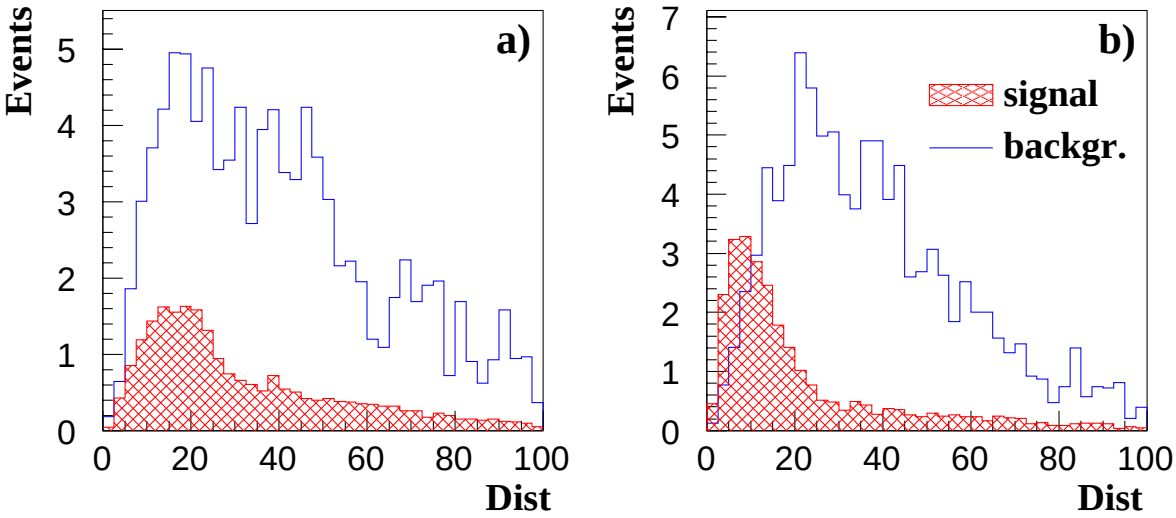

Figure 9.4.2: *Distance variable for signal and background assuming a):* $\Delta E/E = 60\%(1+|\cos\theta_{\mathrm{jet}}|)/\sqrt{E}$ *or b):* $\Delta E/E = 30\%/\sqrt{E}$. *For details see text.*

If no elementary Higgs exists the structure of the mechanism that provides electroweak symmetry breaking can be accessed analysing WW scattering in events of the type $e^+e^- \to \nu\overline{\nu}WW$ and $e^+e^- \to \nu\overline{\nu}ZZ$. To do this analysis not only backgrounds need to be suppressed but also the two types of reactions need to be separated. Due to the two neutrinos escaping detection no constrained fits of the events are possible so that the mass resolution is purely given by the resolution of the detector. Figure 9.4.4 shows the reconstructed masses for the two types of events with $\Delta E/\sqrt{E} = 30\%$ and $\Delta E/\sqrt{E} = 60\%$ [11]. Figure 9.4.5 shows the dilution factor, d, as a function of the cut on the average mass of the two two-jet systems for both energy resolutions. This factor gives an indication of the loss in statistical precision due to the selection efficiency

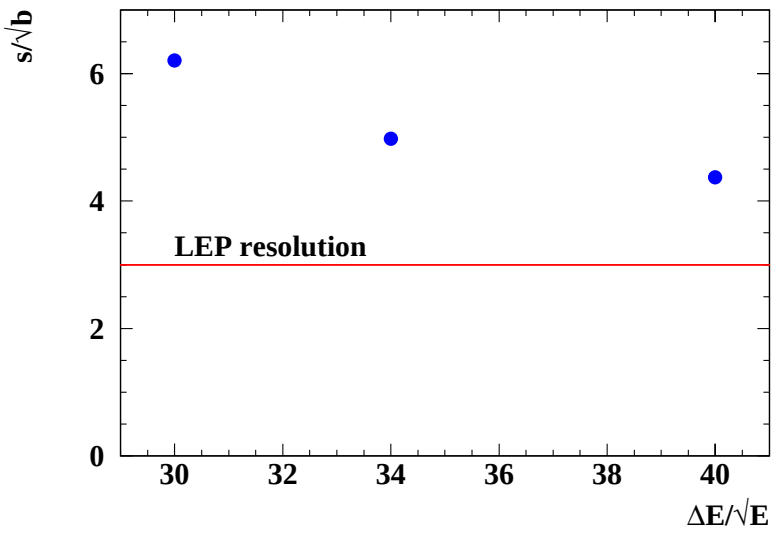

Figure 9.4.3: *Obtainable significance for the ZHH signal as a function of the energy flow resolution for an integrated luminosity of 1 ab^{-1}. The horizontal line is the significance for the energy resolution reached at LEP ($\Delta E/E = 60\%(1 + |\cos\theta_{\mathrm{jet}}|)/\sqrt{E}$).*

and the non-zero background from the other channel. The improvement going from $\Delta E/\sqrt{E} = 60\%$ to $\Delta E/\sqrt{E} = 30\%$ is equivalent to an increase of 30%-40% in the luminosity, which is important for an analysis which is largely statistics limited.

In models with gauge mediated Supersymmetry breaking a long lived neutralino can decay inside the detector into a photon and an invisible gravitino. These events are characterised by a photon that is not pointing back to the interaction point. Using the high granularity of the SiW-calorimeter the direction of an isolated photon can be measured with a precision of $\Delta\Theta = (8 + 68/\sqrt{E})$ mrad (see Fig. 9.4.6). For a 20 GeV photon this corresponds to an impact parameter resolution at the IP of about 4 cm.

9.5 Hermeticity

Supersymmetric events are often characterised by a large missing energy, carried away by the undetectable lightest Supersymmetric particles. For this reason these events are easily confused with two-photon reactions where the electrons are lost in the acceptance hole around the beam direction. Since the transverse momentum of the two-photon event has to be balanced by the outgoing electrons, the veto angle for the electron translates directly into the sensitivity to events with missing p_t. One of the main reasons to instrument the mask is therefore to reduce the acceptance hole for energetic electrons as much as possible. As an example Fig. 9.5.1 shows the reconstructed transverse momentum of muon pairs from two photon interactions with and without the instrumented mask, compared to a possible smuon signal from Supersymmetry if the mass difference between the smuon and the lightest neutralino is very small. The sensitivity in the mass difference increases by more than a factor two if the veto angle

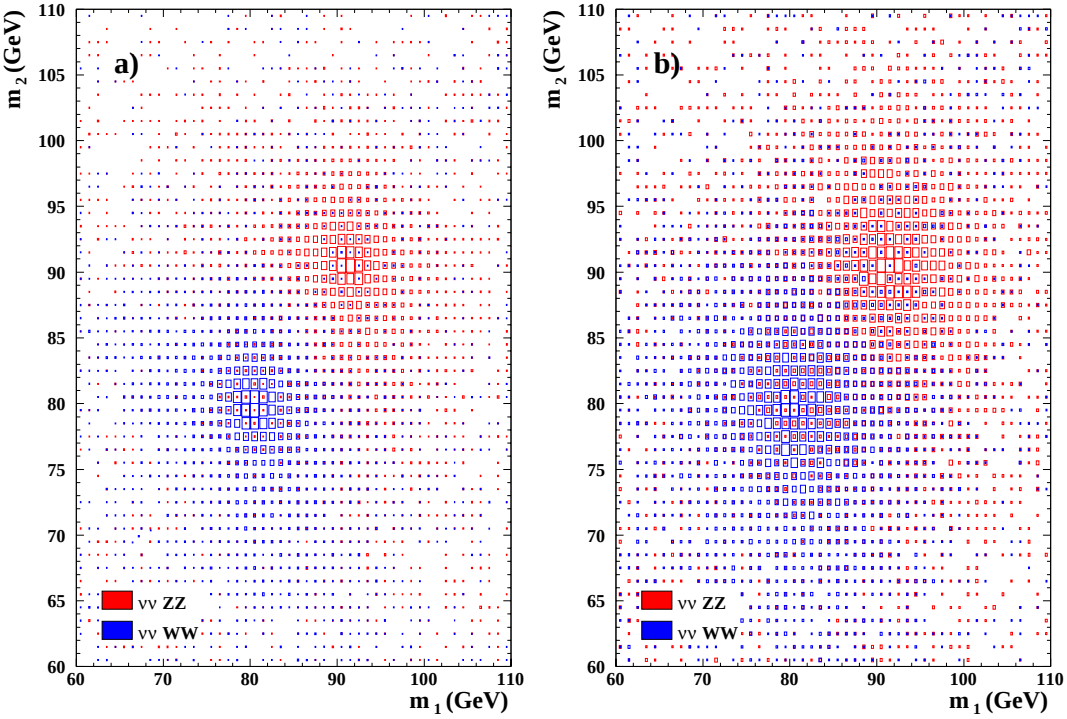

Figure 9.4.4: *Reconstructed masses for* $e^+e^- \to \nu\overline{\nu}WW$ *events and* $e^+e^- \to \nu\overline{\nu}ZZ$ *events for a)* $\Delta E/\sqrt{E} = 30\%$ *and b)* $\Delta E/\sqrt{E} = 60\%$.

for electrons can be brought down from 83 mrad to 25 mrad with the help of the LAT.

Another important task of the LAT is the measurement of the absolute luminosity. The luminosity at an e^+e^--collider is most conveniently measured from Bhabha scattering in the forward region which is a high cross section QED process. Due to the steep angular dependence ($d\sigma/d\theta \propto 1/\theta^3$) the most important requirement for a precise luminosity measurement is an excellent position resolution to define the inner acceptance border. Using SiW calorimeters at LEP a precision of $< 0.1\%$ has been reached and there is no reason why this should not also be possible with the LAT [12].

9.6 Other Topics

For many analyses like threshold scans or high precision measurements in the continuum a good knowledge of the luminosity spectrum is required. This spectrum can be measured from the acolinearity of Bhabha events in the forward region [13]. In the same analysis also the beam energy spread can be measured.

Figure 9.6.1 shows the differential luminosity reconstructed from Bhabha events in the FTD [14]. Without including the beam energy spread a small dilution due to detector resolution can be seen, however the smearing due to the beam energy spread is much larger than detector effects. Already with $3\,\text{fb}^{-1}$ the average fractional centre of mass energy after beamstrahlung, $\sqrt{s'/s}$, can be measured to $5 \cdot 10^{-5}$, better than

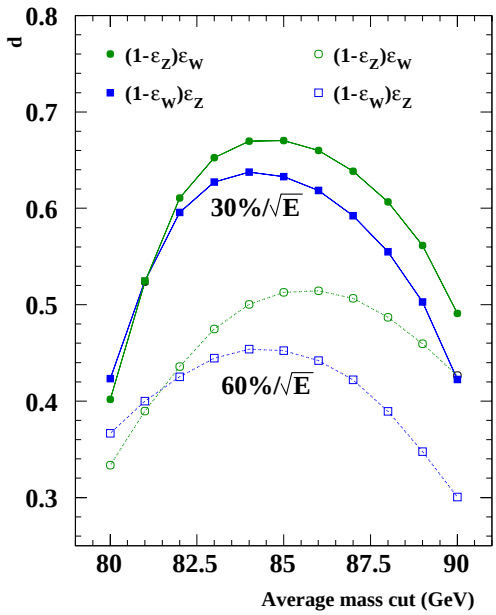

Figure 9.4.5: *Dilution factor d for* $e^+e^- \to \nu\overline{\nu}WW$ *and* $e^+e^- \to \nu\overline{\nu}ZZ$ *as a function of the cut on the average invariant mass for* $\Delta E/\sqrt{E} = 30\%$ *and* $\Delta E/\sqrt{E} = 60\%$.

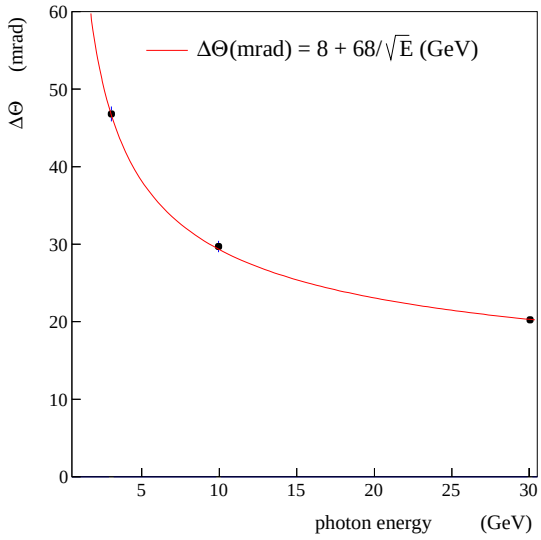

Figure 9.4.6: *Directional resolution of the Calorimeter for isolated photons as a function of the energy.*

the precision on the beam energy. The error on the fraction of events in the peak at $\sqrt{s'} = \sqrt{s}$ is $5 \cdot 10^{-3}$ with this luminosity. As an example, the top-pair cross section near threshold is $< 0.5\,\text{pb}$ resulting in at most a few thousand events per scan point, so that this accuracy is also largely sufficient.

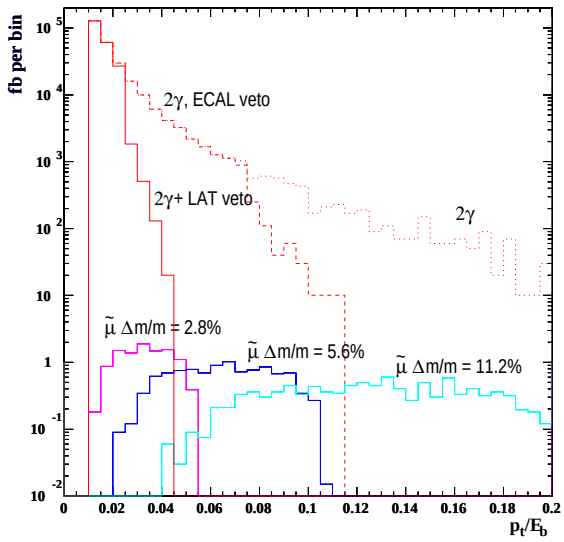

Figure 9.5.1: *Reconstructed transverse momentum distribution for muon pairs from smuon production with a small mass difference, Δm, to the lightest neutralino compared to the background from two–photon interactions with different angle cuts on the outgoing electron. The simulation was done with $\sqrt{s} = 189$ GeV and $m_{\tilde{\mu}} = 90$ GeV. However all cross sections follow approximately the same scaling if $\Delta m/m$ and $m_{\tilde{\mu}}/\sqrt{s}$ are kept constant.*

Another important task of the detector is particle identification, especially to separate leptons from hadrons. Leptons in jets can identify semileptonic b- and c-decays and help to tag the quark charge. Isolated leptons signal W- and Z-decays and measure the W-charge without ambiguities. Isolated pions can stem from τ-decays and in many analyses it is important to separate τ's from electrons and muons. Figure 9.6.2 shows the efficiency to identify isolated electrons and pions with the ECAL and muons and pions with the digital HCAL. Since the output of the identification algorithms are binary the misidentification efficiency in the wrong channel is one minus the efficiency in the correct one. For momenta above 3 GeV isolated electrons, muons and pions can be separated with an efficiency of more than 99%.

If TESLA runs on the Z-peak with large luminosity (GigaZ) CP-violation in the B-system can be analysed [15]. For the measurement of $\sin 2\alpha$ from $B^0 \to \pi^+\pi^-$-decays the decays $B^0 \to \pi^+\pi^-$ and $B^0 \to K^+\pi^-$ need to be separated. Figure 9.6.3 shows that this separation can be done with a very high purity using only the invariant mass resolution of the detector and the remaining background can be rejected using the dE/dx measured in the TPC.

9.7 Conclusions

The detector for the e^+e^--interaction region has been optimised to fulfil the requirements set by the physics goals of the project: hermetic tracking down to 100 mrad with excellent momentum and angular resolution, unprecedented flavour tagging capa-

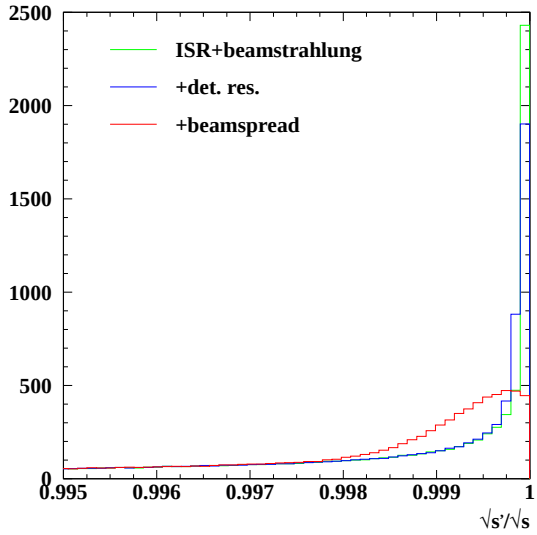

Figure 9.6.1: *Differential luminosity reconstructed in the forward region in the ideal case, including detector effects and beam energy spread.*

bilities, and hermetic calorimetric coverage down to 25 mrad, with high granularity to reconstruct the energy flow in multi-jet final states.

The detector can be used over the full TESLA energy range, i.e. 90 GeV to $\sim$ 1 TeV making it cost effective and reducing simultaneously the systematic uncertainties in the measurement of the energy dependence of physics observables.

In this section the performance of the detector has been demonstrated using a few challenging physics reactions. As seen in these examples the analyses are in general not limited by the detector and the detector resolution affects the expected results only marginally. However the detector cannot be downgraded substantially without losing important physics opportunities.

The total cost of the detector will be in the range of 160-280 MEUR. The exact price depends on the technology option chosen, which can be decided only after intense further development work and simulation studies.

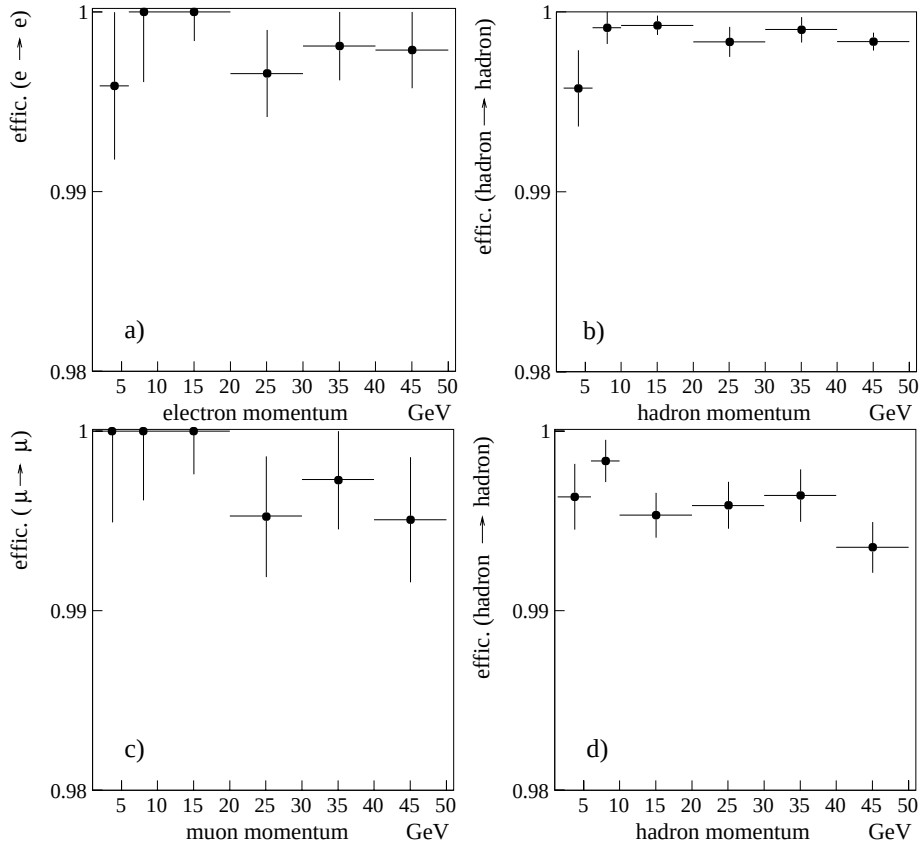

Figure 9.6.2: *Identification efficiency for isolated electrons (a) and hadrons (b) with the ECAL and muons (c) and hadrons (d) with the HCAL.*

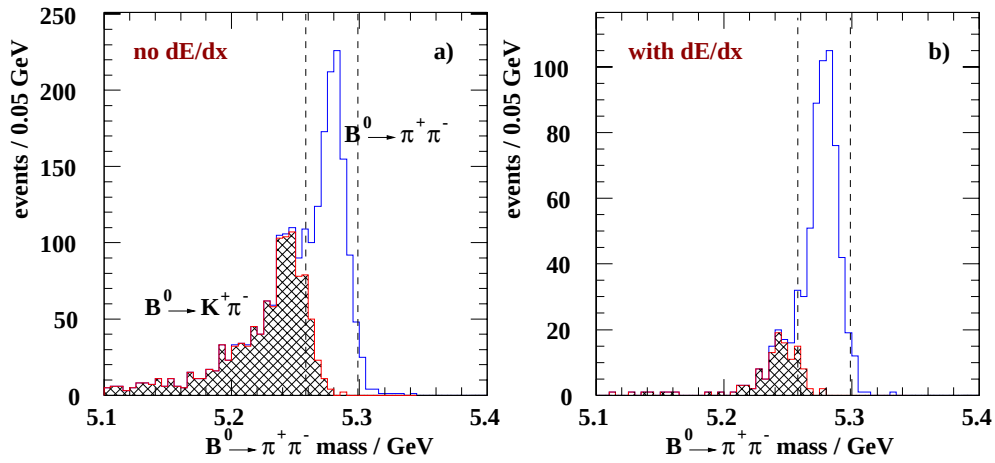

Figure 9.6.3: *Two particle invariant mass spectrum assuming the pion mass for* $B^0 \to \pi^+\pi^-$ *and* $B^0 \to K^+\pi^-$ *decays without (a) and with (b) a cut on dE/dx in the TPC.*

Bibliography

[1] S. Giani et al., GEANT detector description and simulation tool, CERN program libray long writeup W5013.

[2] T. Behnke, et al., BRAHMS: A Monte Carlo for a Detector at a 500/800 GeV Linear Collider, *LC-TOOL-2001-005*, 2001. http://www.desy.de/~lcnotes electronic document.

[3] T. Behnke et al. Performance study of the proposed TESLA detector using a realistic track reconstruction package, *LC-DET-2001-029*, 2001. http://www.desy.de/~lcnotes electronic document.

[4] P. Gay, Energy flow. In *Proceedings of the Linear Collider Workshop 2000*, Fermilab, Batavia, IL, USA, 2000. http://www-lc.fnal.gov/lcws2000.

[5] M. Pohl, H. J. Schreiber. SIMDET-Version 3 A parametric Monte Carlo for a TESLA Detector, DESY 99-030.

[6] S. M. Xella Hansen, D. J. Jackson, R. Hawkings, and C. J. S. Damerell. Flavour Tagging Studies for the TESLA Linear Collider. *LC-PHSM-2001-024*, 2001. http://www.desy.de/~lcnotes electronic document.

[7] D. Su, R_b, R_c measurements at SLD and LEP-I, *SLAC-PUB-8668*, 2001.

[8] M. Battaglia and K. Desch. Precision Studies of the Higgs Boson Profile at the e^+e^- Linear Collider. 2001. hep-ph/0101165.

[9] ALEPH Collaboration: D. Buskulic et al., Nucl. Instrum. Meth. A360:481, 1995. electronic document.

[10] C. Castanier et al., Higgs self coupling measurement in e^+e^- collisions at center-of-mass energy of 500 GeV, *LC-PHSM-2000-061*, 2000. http://www.desy.de/~lcnotes electronic document.

[11] R. Chierici et al. Strong Electroweak Symmetry Breaking Signals in WW Scattering at TESLA, *LC-PHSM-2001-038*. http://www.desy.de/~lcnotes electronic document.

[12] K. Büßer, M. Paganoni. The measurement of Luminosity at TESLA, *LC-DET-2001-044*, 2001. http://www.desy.de/~lcnotes electronic document.

[13] M. N. Frary, D. J. Miller, Monitoring the Luminosity Spectrum, DESY-92-123A (1992) 379.

[14] K. Mönig, Measurement of the Differential Luminosity using Bhabha events in the Forward-Tracking region at TESLA, *LC-PHSM-2000-060*, 2000. http://www.desy.de/~lcnotes electronic document.

[15] R. Hawkings, K. Mönig, EPJdirect C8:1, 1999.